THE EFFECTS OF METALLURGICAL VARIABLES ON THE MECHANICAL PROPERTIES OF HIGH-CHROMIUM CAST IRONS

Suleyman Bulent Biner

Submitted for the degree of
Doctor of Philosophy

The University of Aston in Birmingham

September 1981

TITLE: EFFECT OF METALLURGICAL VARIABLES ON THE MECHANICAL PROPERTIES OF HIGH-CHROMIUM CAST IRONS

NAME: Suleyman Bulent Biner

DEGREE: Ph.D.

YEAR: 1981

SUMMARY

The use of high-chromium cast irons for abrasive wear resistance is restricted due to their poor fracture toughness properties. An attempt was made to improve the fracture characteristics by altering the distribution, size and shape of the eutectic carbide phase without sacrificing their excellent wear resistance. This was achieved by additions of molybdenum or tungsten followed by high temperature heat treatments. The absence of these alloying elements or replacement of them with vanadium or manganese did not show any significant effect and the continuous eutectic carbide morphology remained the same after application of high temperature heat treatments.

The fracture characteristics of the alloys with these metallurgical variables were evaluated for both sharp-cracks and blunt notches. The results were used in conjunction with metallographic and fractographic observations to establish possible failure mechanisms. The fracture mechanism of the austenitic alloys was found to be controlled not only by the volume percent but was also greatly influenced by the size and distribution of the eutectic carbides. On the other hand, the fracture mechanism of martensitic alloys was independent of the eutectic carbide morphology. The uniformity of the secondary carbide precipitation during hardening heat treatments was shown to be a reason for consistant fracture toughness results being obtained with this series of alloys although their eutectic carbide morphologies were different. The collected datawere applied to a model which incorporated the microstructural parameters and correlated them with the experimentally obtained valid stress intensity factors.

The stress intensity coefficients of different short-bar fracture toughness test specimens were evaluated from analytical and experimental compliance studies. The validity and applicability of this non-standard testing technique for determination of the fracture toughness of high-chromium cast irons were investigated. The results obtained correlated well with the valid results obtained from standard fracture toughness tests.

KEY WORDS: High-chromium cast irons, fracture, eutectic carbide, heat treatment, compliance

CONTENTS

LIST OF TABLES

LIST OF FIGURES

LIST OF PLATES

ACKNOWLEDGEMENTS

I would like to express my thankfulness to Dr. R.S. Jackson, Professor J.T. Barnby and Dr. R.W. Durman for their guidance, invaluable discussions and constant encouragement during the period this work was carried out.

I would like to record my thanks to Bradley and Foster Limited for providing the samples and the Turkish Iron and Steel Works for the financial support which enabled me to carry out this research.

I would like to thank the staff and technicians of the Department of Metallurgy and Materials Engineering for their help and special mention is due to Mrs. Howell for typing the thesis.

I wish to acknowledge my indebtedness to my wife Zulal without whose encouragement and support this work would not have been possible.

I INTRODUCTION

Many types of cast ferrous alloys are used for applications in grinding, crushing, mineral handling and earth moving industries. An assurance of freedom from premature failure is vital, since such failure can be costly not only in replacement and repairs but also in lost production during unscheduled shutdowns.

Wear resistance usually increases with hardness but this is accompanied by brittleness, which can cause failure of the components during abrasive wear. Thus in selection of materials for use in a variety of abrasive wear conditions a compromise is necessary between directly conflicting properties of hardness and resistance to brittle fracture (fracture toughness).

Experience has shown that wear rate is more accurately assessed by service trials than by laboratory wear tests. Progress in this aspect has led to reliable classification of many types of alloys in terms of wear rate. The problem of fracture, however, appears to be somewhat neglected. Arbitrary measurements of toughness were made from obser-vations during the wear programmes but results obtained are not quantitative, poorly sensitive to metallurgical variables and lack reproducibility.

The application of fracture mechanics to wear-resistant cast materials makes it possible to relate this material property to metallurgical variables very accurately. The

concept of fracture mechanics recognises that the majority of structural components will contain minute cracks or defects. The fracture toughness of a material is the property which relates these defects to the applied stress which causes failure of the components in a brittle manner. In practice fracture toughness is generally expressed in the form of critical stress intensity factor K_{IC} (where subscript I refer to the opening mode of the crack) and failure occurs when this stress intensity is exceeded at the crack tip or defect. This is a material property which is independent of crack length, applied stress or specimen geometry. Therefore, it is directly applicable to structural design and the determination of acceptable stress levels and discontinuity sizes.

Since K_{IC} is a material property it can also be directly related to the micro-structural characteristics of the alloys, in the light of current theories and practice of micro-mechanism of fracture. These allow a better understanding of the failure mechanism of the alloys and can also be used as guide lines for the research and developments of new alloys.

II DEVELOPMENT AND PERFORMANCE OF HIGH-Cr WHITE CAST IRONS FOR ABRASION RESISTANT APPLICATIONS

The first commercial use of white cast iron as a wear resistant material started early in this century. Unalloyed white irons of this type were used in the as-cast condition, where microstructure is graphite-free containing iron-carbide (Fe_3C) surrounding a relatively soft pearlitic matrix.

In the early 1930's serious attempts were made to add alloying elements to white cast irons and as a result the different grades of Ni-hard were established by adding up to 5% Ni and 3% Cr. These alloys are suitable for cupola melting and their microstructure consists of 40-50% eutectic carbides $(Fe, Cr)_3C$, high carbon twinned martensite and residual austenite. They are in growing use where high abrasion resistance is required from the components used in the as-cast condition. These irons, together with the more recently developed Ni-hard 4 alloy are covered by British Standard 4844 Pt.2.

At the same time, mainly in America work has been carried out in the development of high-Cr white cast irons. The cast irons with 1.5 - 3% C and 10 - 30% Cr contain eutectic carbides $(Fe,Cr)_7C_3$, within an austenite matrix and consequently relatively high toughness is combined with their wear resistant properties. These alloys have been made more widely available by the increased use of electric melting and their characteristics were outlined by B.S.4844 Pt. 3 and ASTM No. A552 type 2.

The rate of metal removal and degree of impact involved in earth moving, mineral handling, crushing and grinding processes characterises the type of wear, which has been classified into three broad categories by Avery [1].

1. Gouging or grooving wear: Such abrasion occurs when abrasive particles penetrate the working surface with considerable force and tear relatively large particles from the wearing surface. Severe impact often accompanies gouging abrasion and may be a major factor in the selection of wear-resistant materials. This type of wear occurs in earth moving plant, hammer mill heads and jaw crushers.

2. High-stress abrasion (grinding): Grinding occurs when two wearing surfaces rub together in gritty environments with sufficient force to produce a crushing action on the abrasive entrapped between the two surfaces. In this wear process the level of stress involved is significant in governing the choice of materials, and this is the kind of wear to which track shoes and roll and jaw crushers are subjected.

3, Low stress scratching abrasion or erosion: This type of wear occurs as a result of the contact between relatively freely moving abrasive particles and wearing surfaces. The stresses are insufficient to cause penetration of the working surface or

crushing of the abrasive. Shovels, truck bodies, chutes and grizzly screens are subjected to this kind of wear.

In the first class of wear, which involves very high impact stress levels, 12% austenitic manganese steels have been used satisfactorily. The low yield point (350 N/mm^2) leads to high plasticity and toughness, while the ability to work harden in service from an initial hardness of about 200 Hv to 450-550 Hv on the working surface gives a reasonable degree of wear resistance. Although its resistance to fracture in the most severe conditions is excellent the use of these steels in many applications is limited by bowing and distortion of working parts due to low yield properties.

For the third class of wear, due to very low working stress levels, toughness is not important and brittle high-carbon unalloyed white cast irons have been used extensively.

The second type of wear, which takes place between these two extremes of the wear process (class I and class II), has a very wide field and the most difficult problem is the selection of materials for the wide range of applications. In this field and in some cases for class I abrasive wear, the high-Cr cast irons containing 15% Cr and 2.4 - 3.5 % C have been found to be particularly attractive because, apart from the economy of their alloy content,

they exhibit better wear resistance than 25 - 28% Cr added high-Cr cast irons. The considerable tonnages of steel castings which had good toughness but lacked adequate abrasion resistance have been replaced by these types of alloys. The 15% Cr alloyed white cast irons can be used in either the as-cast condition when a predominantly austenitic matrix structure is obtained or alternatively can be air-hardened to give martensitic and fine secondary carbides.[2,3]

The aim of this work is to improve the toughness characteristics of this particular high-Cr cast iron microstructure of which consists of continuous net-work of eutectic carbides $(Fe,Cr)_7C_3$ within the austenitic matrix. During the work it was believed that improved fracture toughness and mechanical properties could be achieved by altering the distribution, size and shape of the very hard and brittle eutectic carbide phase within the microstructure, without sacrificing the hardness. In order to obtain these structural changes, metallurgical variables such as alloy additions and application of heat treatments were investigated. The observed variations of toughness with these metallurgical factors were related and correlated with the micro-structure of the alloys in the light of micro-mechanism of fracture.

2.1 Fe-Cr-C System

Early studies on the Fe-Cr-C ternary system were made by Murakami et al [4], Tofaute et al [5] and Kinzel and Craft [6]. The liquidus surface and some isothermal sections of the system were established in the work of Bungardt [7], and it was shown that the M23C6 carbide phase field joins to the austenite phase field and the M7C3 carbides will be produced as a result of peritectic reaction. Later, the investigations of Griffing et al [8] and Jackson [9] indicated that the M23C6 carbide phase field joins the ferrite phase field rather than austenite phase field and the M7C3 carbides form as a result of eutectic reaction. Also in Jackson's work it was pointed out that there are large temperature differences in the designation of the invarient planes.

Recently some work has been done on the different isothermal section of the system. Woodyatt and Klauss [10] established the isothermal section of the system at 870°C. It was observed that the M23C6 carbides were in equilibrium with both austenite and ferrite phases, whereas the M7C3 and M3C carbides are only in equilibrium with austenite. Their results also showed that the M7C3 and M3C carbides are stoichiometric with respect to carbon, which was also the conclusion drawn in Jackson's work. Benz and co-workers [11] and other investigators [12,13,14] studied the isothermal sections of the system between 900°C and 1150°C using thermodynamic analysis and other experimental

techniques. Although there are slight differences in the chemical composition of the phases in the data which they established, it was basically shown that the M23C6 carbides in equilibrium with the austenite as well as the ferrite phase field.

No work has yet been done on the liquidus surface of the system since Jackson's work. On consideration of the information obtained from the studies of the isothermal sections of the system, it is assumed that the M23C6 carbides on the liquidus surface make a conjunction with the austenite phase field at higher-Cr levels than those in the liquidus surface as established by Bungardt. The estimated liquidus surface of the system is given in Figure 1. The figure shows that a composition close to the iron-chromium side of the diagram should give a primary precipitation of ferrite. A primary precipitation of austenite will occur in alloys with a carbon-chromium content within the area A, B, C, D and E. A peritectic line A-B runs between the liquidus surface bordering on ferrite and on austenite. At point B this peritectic line meets an eutectic line between the liquid, the austenite and M23C6 carbides. An eutectic line between the liquid austenite and M23C6 carbides starts from the 4-phase plane at point C. The quarternary equilibrium at C is the starting point of an eutectic reaction between liquid austenite and the M7C3 carbide phase field. A new liquid austenite and M3C carbides starts at point D. The reactions and their approximate compositions are summarised in Table I. The isothermal section of the system at 870°C and the vertical section for 15% Cr are given in Fig. 2 and Fig. 3 respectively.

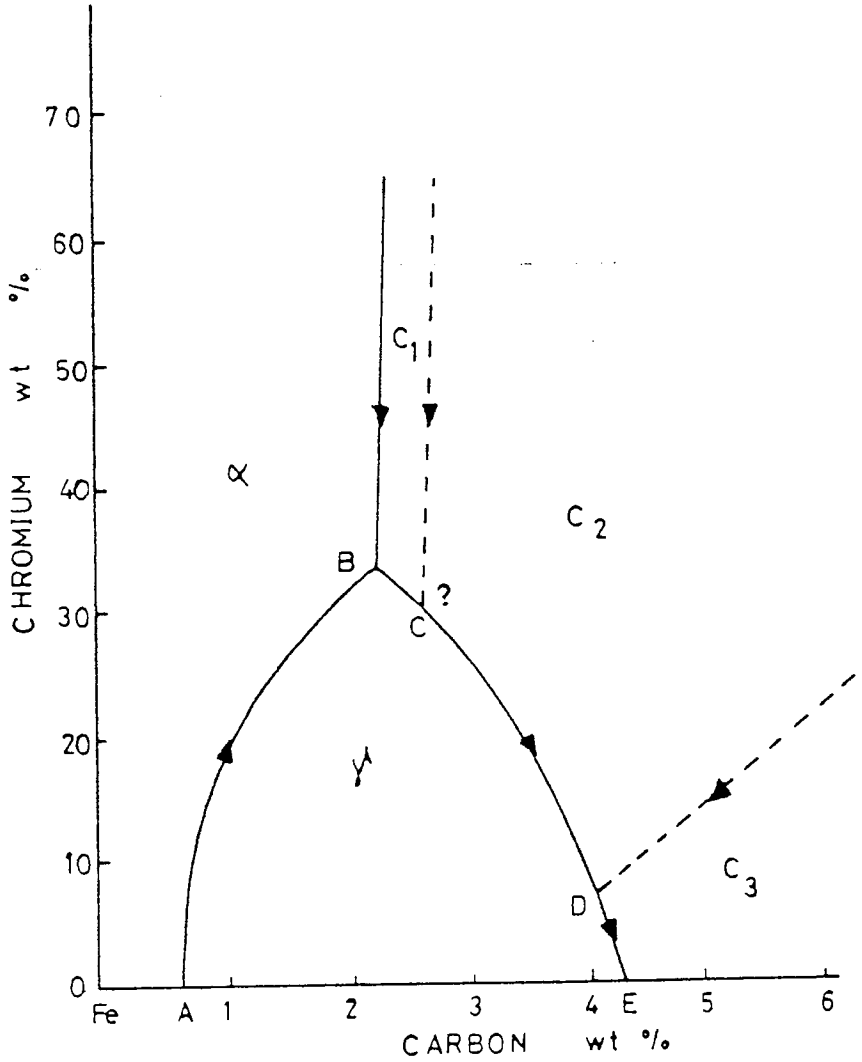

FIGURE 1: Estimated liquidus surface of Fe-Cr-Carbide system

where:

α	:	Ferrite phase
γ	:	Austenite phase
C_1	:	$(Fe,Cr)_{23}C_6$ phase
C_2	:	$(Fe,Cr)_7C_3$ phase
C_3	:	$(Fe,Cr)_3C$ phase

Reaction	Point in Fig. 1	Temp °C	Cr% by weight	C% by weight
$L + \alpha \rightarrow \gamma + M_{23}C_6$	B	1292	34	2.4
$L + M_{23}C_6 \rightarrow \gamma + M_7C_3$	C	1255	(30-31)?	(2.9-3.0)?
$L + M_7C_3 \rightarrow \gamma + M_3C$	D	1184	15.0	6.8

TABLE I: Summary of reactions which occur on the liquidus surface of Fe-Cr-Carbide system

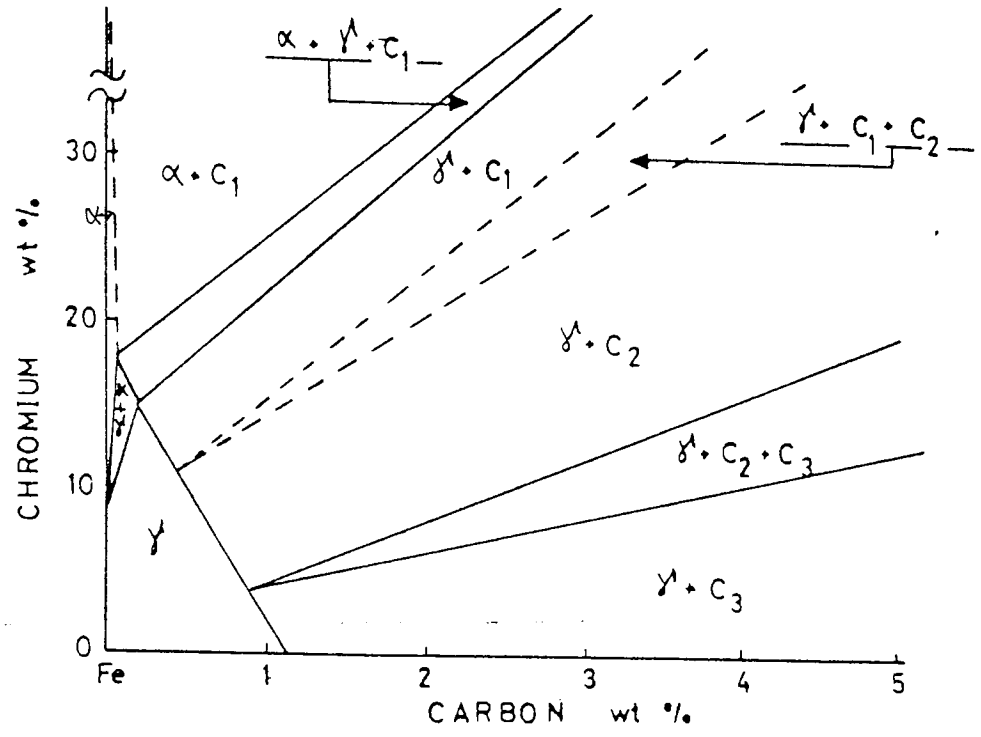

FIGURE 2: Isothermal section of Fe-Cr-C system at 870°C (10)

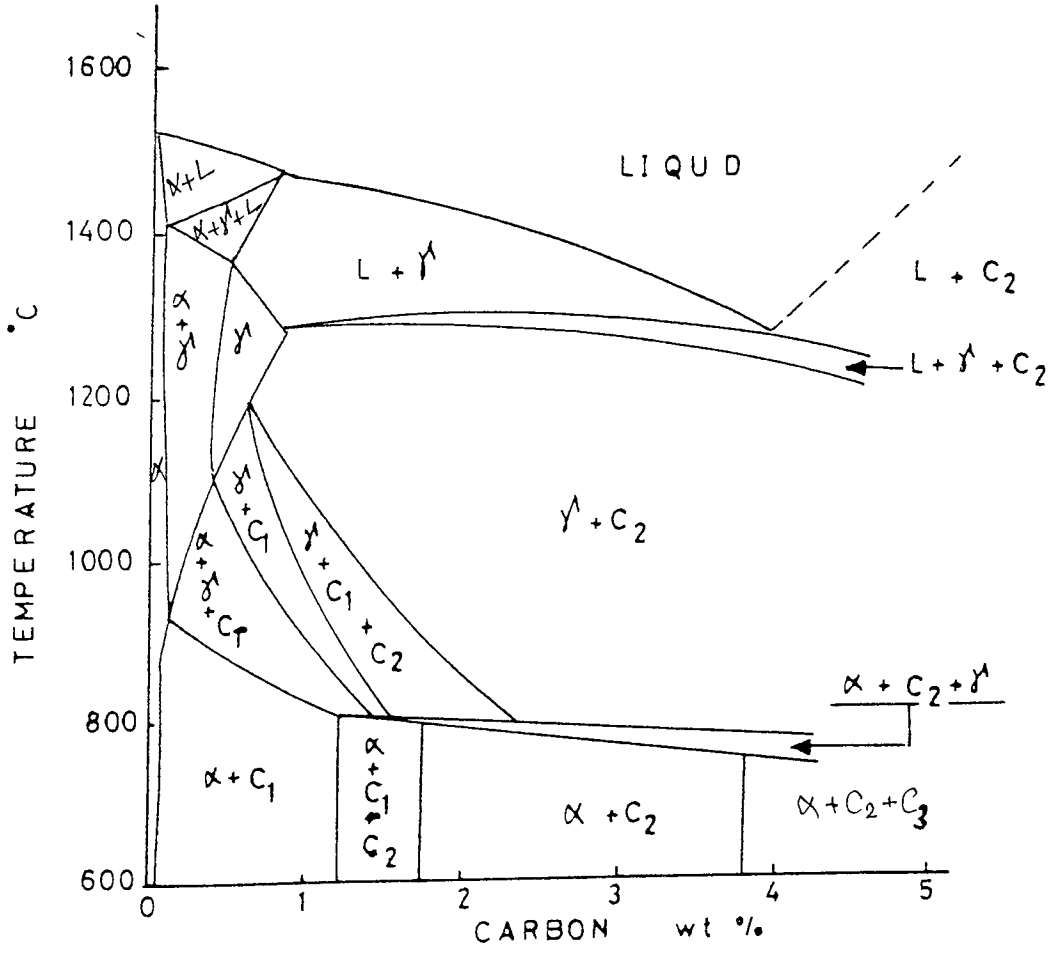

FIGURE 3: 15%Cr vertical section of Fe-Cr-C system (7)

The effects of the solidification rates were studied by Frederikson and Remaus [15]. It was observed that during solidification a primary precipitation of austenite is kinetically favoured by increasing the cooling rate, since growth of the carbides is interface controlled.

During cooling to room temperature, very often the eutectic austenite around the carbides transforms into martensite. This is a result of an increase in M_S temperature due to depletion of carbon and chromium by massive carbides [15].

It was shown by Jackson [3] that under equilibrium conditions and in the absence of other alloying elements, the high temperature austenite transforms by a peritectic reaction at 795°C to soft ferrite and less corrosion resistant M23C6 carbides. The product of this reaction is an irresolveable granular pearlite. The balance of ferrite and addition of small quantities (up to 1.5%) of stabilising elements enables the austenite to be retained in the meta-stable state at room temperature and appearance of the M23C6 can be suppressed. This is an important factor when high-Cr cast irons are used in the as-cast condition since it is now well established that the wear rate of pearlitic high-Cr cast iron is much faster than that of austenitic high-Cr cast irons.

2.2 Properties of Alloy Constituents

2.2.1 The properties of the carbide phase in high-Cr cast irons

Abrasion resistance is almost entirely dependent upon the hardness of the material. 12% Mn steels are an exception to this rule. In a two phase structure such as in white and high-Cr cast irons, the hardness of the carbide phases may be of great significance since plain iron-carbide (Fe_3C) has a hardness of the order of 1000 Hv which is much the same as quartz. The matrix hardness also is significant. If the matrix hardness is very much lower than that of the carbides preferential wear may occur. For comparison the hardness of minerals, iron-phases and carbides are given in table II.

Cr itself forms three carbides in the Cr-C binary system which are designated as Cr3C, Cr7C3, Cr23C6 in the work of Goldschmidt [16]. Their crystal structure is summarised in table III. In the Fe-Cr-C ternary system a certain quantity of Fe atoms substitute for Cr atoms in the Cr-carbides and very often they are called complex carbides and designated as M3C, M7C3 and M23C6 carbides. The solubility limits of Fe in these carbides were determined as below in the work of Woodyatt [10]

Carbide	Fe solubility %
M3C	75.2 to 93.3
M7C3	0.0 to 58.2
M23C6	0.0 to 42.8

Mineral	Hardness Hv	Material or Phase	Hardness Hv
Gypsum	36	Ferrite	70 - 200
Calcite	140	Pearlite (unalloyed)	250 - 320
Fluorite	190	Pearlite (alloyed)	300 - 460
Apatite	540	Austenite (12% Mn)	170 - 230
Felspar	600 - 750	Austenite (high-Cr)	300 - 600
Flint	950	Martensite	500 - 1010
Quartz	900 - 1280	Cementite	840 - 1100
Topas	1430	Cr-carbide (M7C3)	1200 - 1600
Dimond	10.000	Mo-carbide (Mo2C)	1500
		W-carbide (WC)	2400
		V-carbide (VC)	2800
		Ti-carbide (TiC)	3200
		B-carbide (B_4C)	3700

TABLE II: The hardness comparison between minerals, materials and phases (47).

When high-Cr cast irons are alloyed with other alloying elements such as Mo, W, V and Mn a certain amount of these alloying elements dissolves in the complex metallic carbides, but the solubility limits of these alloying elements in the complex carbides have not yet been determined and it is also still under question whether these alloying elements replace Cr atoms or Fe atoms.

It was mentioned by Rothery [17] that the solubility of W in $M_{23}C_6$ carbides is limited and that when it exceeds 8 atoms out of 92 Cr atoms there is a phase change from $M_{23}C_6$ to the M_6C structure.

$Cr_{23}C_6$	Complex face centred cube with 116 atoms per unit cell (92 Cr atom and 24 C atom). Edge of unit cube : 10.638 Kx
Cr_7C_3	Hexagonal with 80 atoms (56 Cr and 24 C atoms) per unit cell. Per unit cell: a = 2.821 Kx $c/_a$ = 0.324
Cr_3C	Orthorhombic with 20 atoms (12 Cr and 8 C atoms) Per unit cell: a = 2.821 Kx, b = 552 Kx, c = 11.46 Kx.

TABLE III Crystal properties of Cr-Carbides [16]

2.2.2 The Mechanical Behaviour of Retained Austenite

High ductility can be associated with high strength in austenitic steels undergoing phase transformation during plastic straining, and this has been studied extensively in TRIP (transformation induced plasticity) steels, high-Cr and stainless steels [18-23].

It is well established that shear-band intersections can be very effective strain induced-martensite nucleation sites [24,25]. The operative shear-bands can be in the form of e´(hcp) martensite, mechanical twins or dense stacking fault bundles, all being promoted by low austenite stacking fault energy. An extensive investigation of the strain induced transformation behaviour of 304 stainless steel by Angel [26] has shown that transformation curve (amount of martensite as a function of plastic strain at constant temperature) is sigmoidal in shape, generally reaching saturation below 100%. Although a parabolic relationship was observed in the work of Garberich et al[27]. Measurements on the steels which deform homogeneously appear to support the sigmoidal shape [24,28].

The complex inter-relationships between applied stress, plastic strain and martensite transformations have been studied extensively by Bolling and Richman [29-32]. They defined a temperature M^{σ}_{s} (lying above M_s temperature), below which yielding under applied stress is initiated by the onset of martensite formation, and above which yielding under appliedstress is initiated by regular slip processes in the parent phase.

These relationships are given schematically in Fig. 4. At temperatures under M^{σ}_{s} the yielding which accompanies the martensitic transformation which occurs below the regular yield stress (σ_{ys}) of the austenite. It was concluded that nucleation under these conditions is stress-assisted, and takes place at pre-existing nucleation sites or embryos in the parent austenite which trigger the spontaneous transformation on cooling. Nucleation is assisted by the thermo-dynamic effect of applied stress. In the stress-assisted transformation regime, the required initiating stresses are in the elastic range (below σ_{ys}) but increase with increasing temperature. Above M^{σ}_{s} the applied stress must reach or exceed σ_{ys} in order to initiate the martensite transformation. In the temperature range above M^{σ}_{s} the stresses at which transformation is initiated lie significantly below the relatively steep stress-assisted transformation line extrapolated up from below M^{σ}_{s}. It was postulated that plastic deformation at σ_{ys} and above introduces new highly potent sites which allow nucleation at appreciably lower stresses than in the case of stress-assisted nucleation and therefore nucleation above M^{σ}_{s} was considered to be strain induced.

In the work of Antolovich and Singh[33 and 34] the contribution of the martensite formation to the fracture toughness was calculated using fracture mechanics concepts and theoretically obtained values gave good correlation with experimental observations. They used crack extension force rather

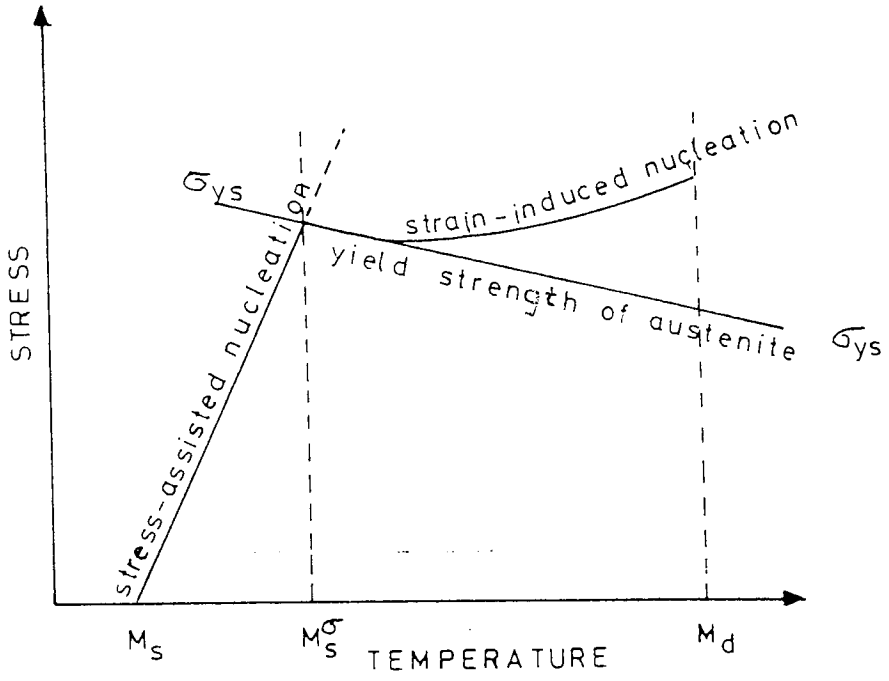

FIGURE 4: Schematic representation of inter-relationship between stress assisted and strain-induced nucleation of martensite in Fe-Ni-C alloys (29)

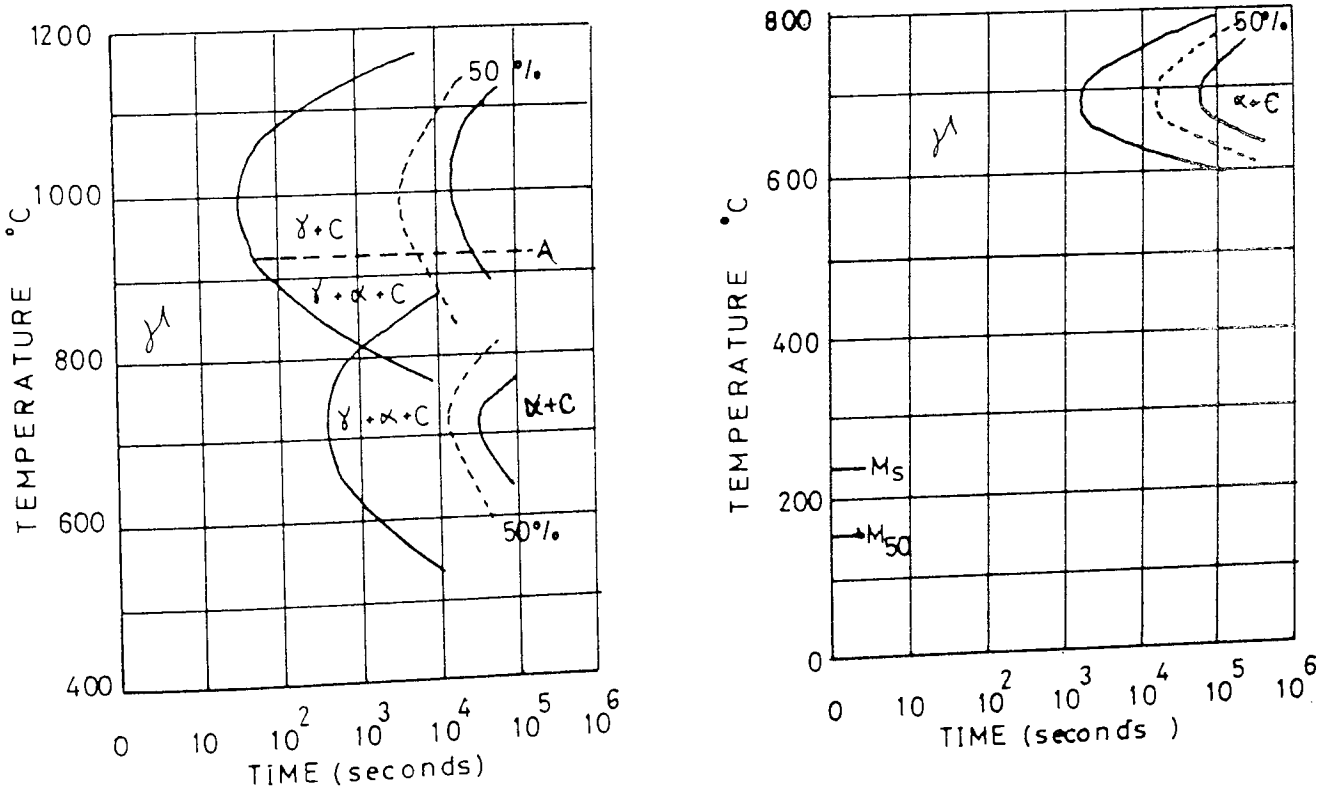

FIGURE 5: A: Isothermal transformation of austenite
B: Isothermal transformation of destabilised austenite (39

than stress intensity since the energy approach is more straight forward. For simplicity the martensite zone was idealised as an ellipse with a semi-major axis of h units and a semi-minor axis of βh units, and it was postulated that:

$$\Delta G^{A \rightarrow M} : A.a.F(a/W) \quad \text{.....(1)}$$

where

$\Delta G^{A \rightarrow M}$: strain energy observed by the martensite formation

$$A : \frac{e_{IS}\ \bar{V}_M \cdot \beta\alpha^2 \cdot P^4}{\sqrt{3} \cdot \bar{\sigma}_M^3\ t^4\ W^4} \quad \text{.....(2)}$$

e_{IS} : invariant shear strain associated with transformation

$\bar{V}_M$: average volume fraction of martensite in the martensite zone

β and α: Constants

P : P_Q failure load of the test piece

t : specimen thickness

$\bar{\sigma}_M$: tensile stress at which martensite forms

W : specimen width

$$F(a/W) = 2Y^4 + 4Y^3\ a\ \frac{\partial Y}{\partial a} \quad \text{.....(3)}$$

Y : dimensionless K calibration of the specimen

a : crack length

They concluded that the high toughness of TRIP steels can be attributed to the formation of martensite from austenite during the fracture process which absorbs energy that would otherwise be available for crack extension.

The phase transformation during plastic straining enhanced the ductility and toughness properties with high strength in austenitic steels. Bressanelli and Moskowitz [23] suggested that the amount of martensite formed during necking in austenitic steel would enhance ductility, while Rosen et al [35] argued that it was not the total amount of martensite but its distribution which was important in governing the ductility of the material. Fatigue crack propagation has also been studied in austenitic stainless steel [36] and the crack growth rate was found to be relatively low when martensite was produced at the crack tip. On the other hand, low cycle fatigue life was observed to be independent of the extent of martensitic transformation in TRIP steels [37].

2.3 Heat Treatment and Decomposition Mechanism of the Austenitic Matrix

Very often high-Cr cast irons are subjected to heat treatment in order to obtain a hard matrix for better wear resistance. The effects of heat treatments and the decomposition mechanism of the austenitic matrix can be summarised as follows.

2.3.1 Isothermal Decomposition of the Austenite

More detailed investigations have been carried out by Maratray and Nanot [38,39] and several isothermal transformation diagrams have been published for a wide range of high-Cr cast irons of different compositions. According to their published data, the austenitic matrix is stable at low and high temperatures but subject to decomposition at intermediate temperatures. Isothermal decomposition of austenite occurs in two temperature ranges, the schematic transformation diagrams are given in Fig. 5a. According to Maratray and Nanot at about 975 $\pm$ 25°C precipitation of secondary carbides can be observed and this area can be divided into two sections: the one above the A3 point corresponds to the transformation

$$\gamma \rightarrow \gamma + M7C3$$

the other below the A3 point corresponds to the 3 transformations

$$\gamma + M23C6 \rightarrow \alpha + M7C3$$

$$\gamma + M7C3 \rightarrow \alpha + M3C$$

$$\gamma + M3C \rightarrow \alpha + \text{graphite}$$

The second C shaped transformation range has a maximum rate of about 650 to 700°C. The product of transformation here is very fine pearlite. Precipitation of secondary carbides changes the composition of the austenite and thus alters its transformation characteristics (Figure 5b).

2.3.2 Secondary Carbide Precipitation

Although very extensive work has been done for the precipitation and growth kinetics of secondary carbides in Cr-steel and austenitic stainless steels, very limited information has been found in the literature concerning secondary carbide formation in the structure of high-Cr cast irons. The carbide precipitation retards the pearlite transformation, makes possible a bainitic transformation for some compositions and permits a martensitic transformation in all high-Cr cast irons.

A number of experimental papers given as data reject or confirm that the secondary M7C3 carbides precipitate by in-situ mechanism or separate nucleation [40,41,42]. Kolosova [43] confirmed that the M7C3 carbides can precipitate by either the mechanism of separate nucleation directly from a solid solution or by the in-situ mechanism from M3C carbides depending on the alloy composition and temperature. The same results were indicated in the work of Japrie et al [44].

Some work was carried out by Maratray and Nanot [39] on the formation of secondary carbides in high-Cr cast irons and it was confirmed that the M7C3 carbides precipitate at temperature above A3. On the other hand the M23C6 carbides have been observed after being held between A1 and A3 for various periods of time. But it is uncertain whether the M23C6 carbide is only formed within this temperature range and it is stable if held at this temperature for longer

periods of time. According to their work, at the beginning the precipitation is very fine, dense and randomly located around the primary eutectic carbides and some grain boundaries. The temperature has a major effect on the coarsening of precipitates, it starts around the eutectic carbides then progresses and occurs within the austenite grains, along the preferred crystallographic planes.

The formation of carbides M23C6 has been studied by some investigators [45-47]. Although earlier investigations were concerned with the process of precipitations at the grain boundaries, it has been shown recently that the M23C6 carbides can also precipitate inside the grains. However growth kinetics and the shape of the precipitated particles is still under discussion [46,48].

2.3.3 Martensitic Transformations

As a result of the wide range of uses for quenched high-Cr cast irons in practice, extensive work has been carried out to investigate the martensitic transformation characteristics of these types of alloyed cast irons. According to the work of Maratray and Nanot [39] and Fairhurst and Rohrig [49] the martensitic transformations are closely related to the precipitation of secondary carbides. It was observed that it was impossible to obtain martensite without prior carbide formation but also the temperature at which precipitation occurs determines the formation temperature of the martensite,

the amount of martensite formed and its hardness. According to the data the increase in M_s temperature reveals increasing matrix impoverishment in chromium and carbon as the temperature of precipitation of secondary carbides is lowered. It was observed that the M_s temperature is largely independent of the amount of secondary carbides precipitated at any one temperature since the dominant factor for the M_s temperature is the lowest carbon area present in the matrix. Precipitation of more carbides at the same temperature apparently does not alter this microsegregation of carbon. Therefore the composition of the martensite depends only on the temperature at which secondary carbides are precipitated. For a given destabilisation temperature, the amount of martensite formed increases with the amount of secondary carbides.

Recently, the effects of destabilising temperature and soaking time on the martensite formation were studied by Fredrikson and Remaus [15]. According to their results the hardness of the martensite is mainly dependent on the carbon content, while the amount of martensite is dependent on the chromium content of the matrix. The amount of alloying elements in the matrix could be increased by raising the destabilising temperature for given alloy composition. This fact was explained with consideration of isothermal sections of the Fe-Cr-C system. A high destabilising temperature gives a low percentage of hard martensite and a high percentage of retained austenite

results in a low overall hardness value. If the destablising temperature is low, the martensite formed is soft and the percentage of retained austenite is small which also means low hardness values for the product. They concluded that the overall hardness of a product could be achieved either by austenizing at high temperatures than quenching to a temperature below the M_f (which means well below the room temperature), or by decreasing the chromium content which gives a higher carbon content in the matrix.

The effect of the overall carbon content on the formation of martensite in high-Cr cast irons has been studied by Rozhkova et al [50]. It was observed that carbon greatly reduces the temperature and extent of martensite formation. Raising the carbon content of the alloy (12-14% Cr) from 1.96% to 3.57% C lowers M_s temperature by 130°C (from 200°C to 70°C), due to this decrease in M_s temperature the amount of retained austenite increases from 7% to 38% within the matrix. The effect of the carbon content on the martensite formation according to Rozhkova et al [50] is shown in Fig. 7.

The rates of precipitation of secondary carbides are relatively rapid, carbides continue to precipitate when sections over a certain size are quenched and the pearlite transformation takes place. In order to obtain a fully martensitic structure for a given section thickness, it is necessary to balance the chemical composition of

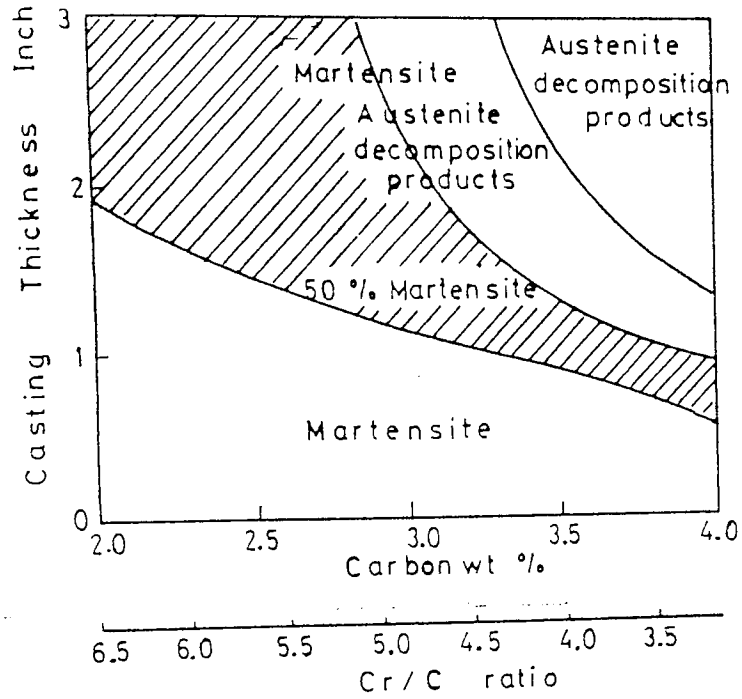

FIGURE 6: Effect of the Cr/C ratio and section thickness on the hardenability of high-Cr cast irons (49)

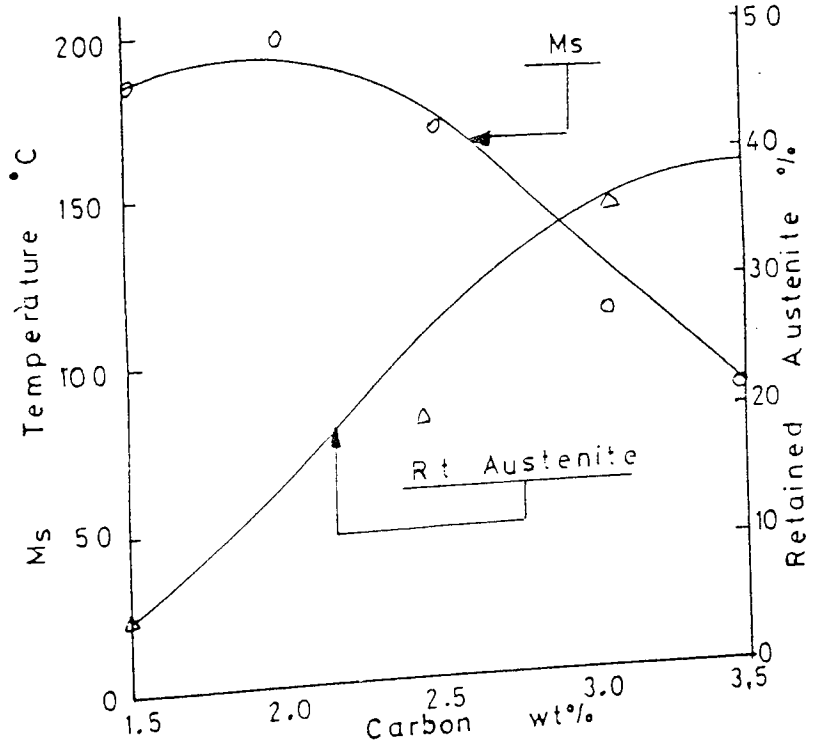

FIGURE 7: Effect of the carbon % on the M_s temperature and hardenability of 17.5%Cr high-Cr cast iron (50)

alloys [49]. The effects of other alloying elements on the martensite transformation characteristics of high-Cr cast irons are given in section 2.4. The influence of the Cr/C ratio and section thickness of casting on the amount of formed martensite is given in Fig. 6. In practice the hardening procedure involves raising the temperature to between 950 and 1000°C, destablisation and soaking for quenching are usually carried out at the same temperature and combined in one operation. This is followed by forced air quenching, since liquid quenchants, such as oil, water or salt solution may invoke too great a risk of cracking. Also it was observed that the castings with low Cr/C ratio can only be hardened by oil quenching even in sections as small as half an inch thick [51].

After martensitic transformation the retained austenite within the matrix is not completely stable. By re-heating the alloy to 400-600°C some destabilisation of retained austenite is produced so that it transforms to martensite on cooling to room temperature [49].
It was observed that the secondary hardening can cause a decrease in hardness if there are very small amounts of retained austenite after the hardening process. However, with large amounts of retained austenite, secondary hardening results in a greater degree of hardness than that of the as-quenched condition.

2.3.4 Bainitic Transformations

It was concluded by Maratray and Nanot [39], that the bainitic transformations take place only after destabilisation and only if the Cr/C ratio of the alloy is not too high. According to their work, with a destabilisation treatment of 20 minutes at 1000°C, alloys having a Cr/C ratio less than 5.2 are capable of transforming to bainite under isothermal conditions. Under continuous cooling conditions, the bainitic transformation is formed in a more restricted range of alloys and the amount of bainite formed is considerably less than that formed after isothermal transformation. Low hardenability alloys which are capable of transforming to bainite under isothermal conditions do not show a bainitic transformation under continuous cooling because of the rapidity of pearlitic transformation and slowness of the bainitic transformation. It was also mentioned that Mo increases bainite transformation and permits this type of transformation to occur with higher Cr/C ratio values. (e.g. with 2% Mo bainitic transformation can occur with a Cr/C ratio of about eight.)

2.3.5 Homogenisation of High-Cr Cast Irons at Elevated Temperatures

Although some studies have been carried out [52-54] there is relatively limited information available in the literature concerning the structure and properties of the high-Cr cast irons which are obtained by applying high temperature homogenisation heat treatments.

Earlier attempts were made by Boyes [52], in order to determine the structure stability of a series of ferritic high-Cr cast irons (27-33% Cr and 1.1-2.2% C), at elevated temperatures. According to his results, no evidence of eutectic carbide instability was found except for marked spheroidization at temperatures of 1100°C and over. It was also indicated that ferritic high-Cr cast irons may be susceptible to sigma phase formation when they are subjected to heating at intermediate temperatures. The formation of the sigma phase is favoured by high-chromium and low carbon contents, but rapid resolution occurs when the heating temperatures reach 1000°C and above. Silicon, manganese and phosphorus have also been found to have a marked influence in promoting sigma phase formation and should therefore be kept as low as possible.

Similar investigations were carried out on the austenitic high-Cr cast irons (15% Cr and different carbon levels) by Durman [53]. According to his results, during homogenisation at 1150°C, a large proportion of the eutectic carbides were taken into the solid solution. The remaining free carbides became spheroidised and the interdentritic network tended to break down into isolated particles. It was observed that about 50% of the original eutectic carbides were dissolved during high temperature heat treatment and it was found that the solution of carbides was a function of time at elevated temperatures.

Fredrikson and Remaus [15] carried out their investigations on an austenitic high-Cr cast iron which has higher chromium level (26% Cr 2.5% C). In their work the spheroidisation of eutectic M7C3 carbides was observed at 975°C, while M23C6 carbides were completely dissolved in the matrix. For some reason this marked spheroidisation of the eutectic carbides was reached at lower temperatures than those previously mentioned in two other studies.

It was mentioned in the work of Silman et al [54] that white cast irons alloyed with V, Cr, Mn in certain combinations permits simplication of the high temperature heat treatment (the chemical compositions of the alloys were not given in their published data). According to their results annealing at 1050°C causes the boundary network to break up and separate carbides to form, and this leads to some increase in the mechanical properties.

2.4 Influence of Alloying Elements on the Properties of High-Cr Cast Irons

High-Cr cast irons are characterised by a micro-structure of eutectic carbides of the M7C3 type surrounded by a matrix that is predominantly austenitic in the as-cast condition or martensitic following the heat treatment. A martensitic matrix usually offers better resistance to abrasive wear especially for those conditions involving repeated impact [2]. However a metastable austenitic

matrix may offer comparable or superior abrasion resistance in some applications. Pearlite is undesirable in the matrix of either as-cast or heat treated irons, since it has been found that it decreases abrasion resistance when present in significant amounts [3]. Although the high-Cr cast irons respond favourably to heat treatment, the austenite or decomposition products of austenite are retained to room temperature within the micro-structure in the large sectioned components. Also complex shaped components are susceptible to cracking during the hardening heat treatment process. Therefore it is very often desirable to use these irons in the as-cast condition; consequently the as-cast stability of the matrix (retardation of the pearlite transformation) becomes an important factor and for heat treated high-Cr irons full hardenability becomes an important consideration for large sectioned components.

In order to achieve the desired micro-structure and mechanical properties in as-cast or heat treated conditions high-Cr cast irons are very often subjected to alloying with other alloying elements besides chromium and carbon. Several European, Canadian and American producers and investigators have dealt with additions of molybdenum, nickel, manganese and copper. Russian investigators have carried out their studies on high-Cr cast irons alloyed with vanadium, tungsten and manganese singly or in combination and occasionally with titanium, yttrium, cerium and calcium.

During the survey of available literature very limited information has been obtained for some of the alloying elements whereas the data for others is well established. It can be concluded from the data available that the main purpose of alloy additions to the high-Cr cast irons was only to improve the properties of the matrix. For some reason very little attention was paid to determination of the structural and chemical variations of the eutectic carbide phase by alloying.

2.4.1 Molybdenum Additions

Molybdenum is one of the alloying elements which has a wide range of uses in the production of high-Cr cast irons due to its delaying effect on the pearlite transformation. The effects of molybdenum additions on the hardenability of high-Cr cast irons were studied by Cias [55], the addition of Mo in amounts of up to 2.9% widened up the time ranges of martensitic transformation and delayed the appearance of pearlite within the matrix. The effect of Mo additions on the hardenability of high-Cr cast irons is given in Fig. 8. These effects of molybdenum additions were found to be amplified by increasing manganese content and by individual additions of up to 2% nickel or copper. It was also observed in the work of Norman et al [56] that the effectiveness of molybdenum additions is greater at low carbon levels than higher carbon levels in the as-cast condition.

According to the work of Kitigora [57], the addition of 5-20% Mo changes the nature of the carbides and (Cr,Fe,Mo)7C3 carbides are finer and more evenly distributed. It was also observed that the structure of the matrix also varied with increasing Mo content; with 5% Mo the matrix was fully austenitic and with 10-20% Mo the matrix consisted of austenite and martensite (base metal in his work was 15.5-20% Cr and 2.5-4.2%C).

Studies were carried out by Maratray and Nanot [39] in order to determine the distribution of Mo among the carbides and matrix in the range of up to 3.5% Mo for different Cr/C ratio cast irons. According to the work, the Mo content of the eutectic carbides (M7C3) increased as the Mo content of the alloy was raised, and maximum of around 3% Mo concentration has been observed, but no conclusion was reached as to whether Mo replaced Fe or Cr atoms in the structure of eutectic carbides. Their X-ray analysis demonstrated that the cubic Mo_2C carbides were present within the matrix for all Mo levels, and microprobe analysis of these cubic carbides indicated the absence of any other metallic material such as Cr or Fe. They concluded that, on average, about half of the Mo in the alloy would be expected to be present in the form of Mo_2C, the other half would be divided between the M7C3 carbides and matrix equally.

Recently the Fe-Cr-Mo-C system was reinvestigated (isothermal sections in the temperature range of between 800-1100°C) by Waldenstrom [58] andfive phases were observed in together with austenite. These were M23C6, M7C3, M6C, (ξ-carbide) and M3C. It was found that ξ-carbides and cementite have the same carbon content but the solubility of Mo in the ξ-carbide is much higher, and ξ-carbides form at higher Mo and Cr contents which indicates that Mo has a very strong preference for its own carbides Mo_2C and among them the ξ-carbides is the one which is stablised by Cr. It was observed that the stabilising effect of Mo on M7C3 is not very strong in comparison with M23C6 and also indicated that Mo has a very strong tendency to dissolve in many carbides, but in most cases there seems to be an upper limit to the Mo content, however no tendency for an upper limit was observed for Mo in the M7C3 and M3C carbides.

2.4.2 Manganese Additions

A well known property of manganese as an alloying element is that of an austenite former. Manganese by itself is a very weak carbide former and a relatively potent carbide stabiliser. Although it was shown in the work of Norman et al [56] and Farge et al [57] that manganese additions were most beneficial in suppressing the formation of pearlite in the low alloyed white cast irons, it was observed in the work of Gurlach [60] that it was less effective than nickel and also that manganese and copper were comparable in their effects on pearlite suppression

Manganese appeared to be the most potent supplementary additions to the 2.9% C, 17.5% Cr and 1.5% Mo base alloy in the work of Cias [55]. Manganese additions of 2% or more than its standard level are more effective in extending the time range of the martensitic transformation and in delaying the appearance of pearlite transformation than the addition of about 2% nickel or 2% copper, to the same alloy. The effect of manganese additions on the hardenability of 17.5% Cr added to high-Cr cast iron is given in Fig. 9. It was observed in the work of Levi et al [61] that with a Mn content of 4.5-5.2% it is possible to obtain a fully martensitic structure which has a hardness of over 60 R_C for massive sections up to 150 mm thick. However, increased manganese content causes a decrease in the hardness of the alloys and this effect can be explained in terms of increased content of retained austenite due to the austenite field bordering action in ferrous alloys with increasing manganese content. It was mentioned by Cias [55] that the hardness of the alloys which contain large amounts of manganese can be brought up to high hardness levels only under very slow cooling conditions. The variation of hardness with increasing manganese content in a high-Cr cast iron is given in Fig. 10.

According to the results of Tyspin et al [62] the greatest hardenability of high-Cr cast irons can be achieved by combining alloying with manganese and molybdenum. This is more effective than adding each element separately. Their phase analysis indicated that part of the molybdenum is

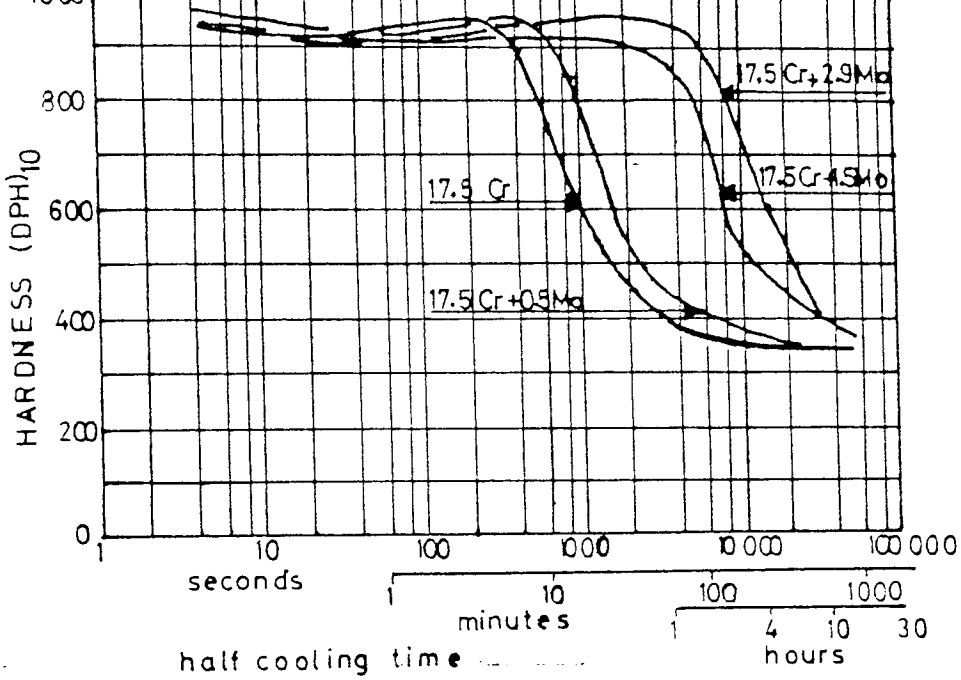

FIGURE 8: Effect of Mo on the hardenability of 17.5%Cr and 2.9%C high-Cr cast iron (55)

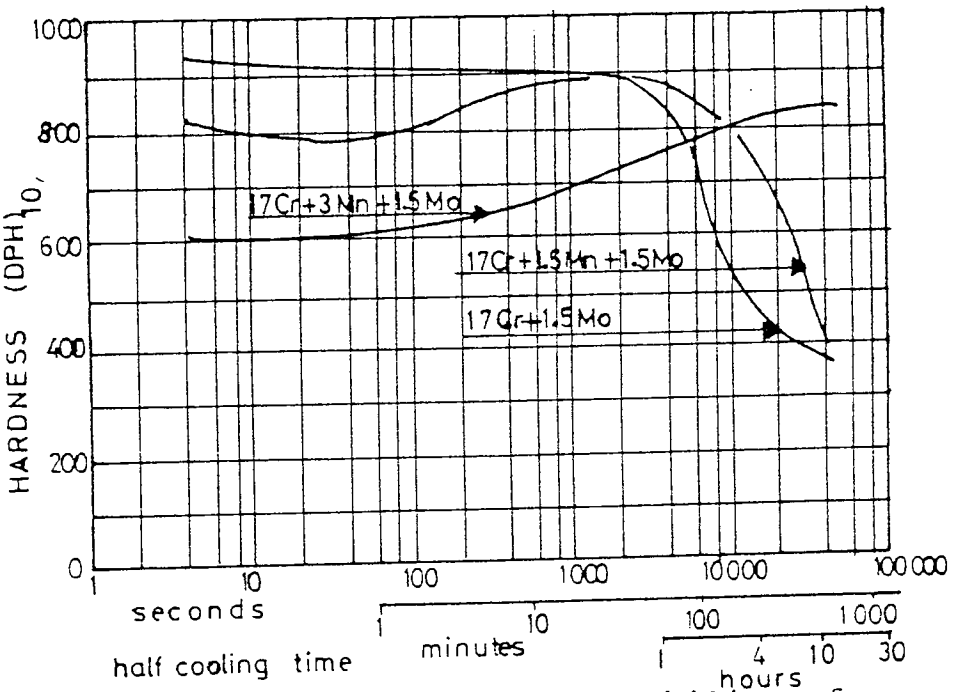

FIGURE 9: Effect of Mn on the hardenability of 17.5%Cr, 1.5%Mo and 2.9%C high-Cr cast iron (55)

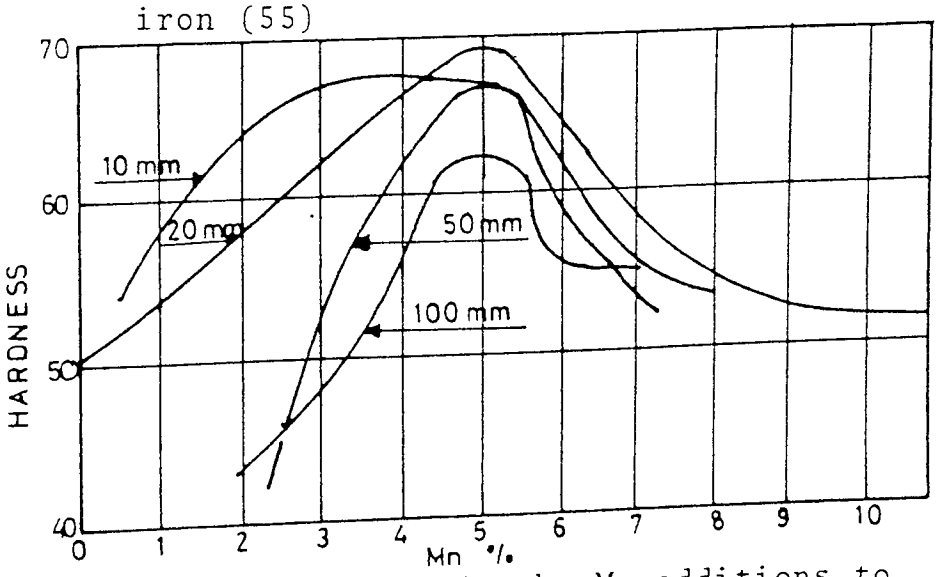

FIGURE 10: Hardness variation by Mn additions to

combined with eutectic carbides, therefore small single additions of Mo have little effect on the hardenability.

2.4.3 Nickel and Copper Additions

It was observed in the work of Gurlach [60] that the alloyed high-Cr cast irons exhibited a decrease in the value of as-cast hardness and abrasion-resistance with increasing nickel and copper content. It was found that in combination with molybdenum, nickel was most beneficial in suppressing the formation of pearlite in as-cast conditions.

The effects of nickel additions on the hardenability of 15% Cr-3%C-Mo high-Cr cast irons were studied by Cox [63]. It was shown that Ni can be used satisfactorily for very large castings without raising the problem of retained austenite, and that by adding 2% Ni and 0.25% Mo, makes it possible to air-harden castings which were at least 200 mm in thickness. It is concluded that the addition of nickel is particularly useful, since this element does not lower the M_s as much as manganese or molybdenum does and it concentrates in the austenite phase so that it acts in a very effective way on the hardenability. According to the work of Cias [55], as far as the delaying effect of nickel and copper on the pearlite transformation is concerned, their effects are comparable for lower molybdenum additions but at higher contents of the molybdenum the effect of nickel becomes progressively stronger.

2.4.4 Vanadium Additions

The effect of vanadium additions up to 5% on the properties of an as-cast high-Cr cast iron (15% Cr 2.9% C) was studied by Stefanescu [64]. It was observed that by increasing vanadium content, the austenite dendrites were refined during solidification and the micro-structure at room temperature consisted of very evenly distributed eutectic carbides and vanadium carbides (VC) within a very fine pearlite. The refining of austenite dendrites during solidification was explained by means of cooling curves. It was concluded that the eutectic temperature is decreased by additions of molybdenum and is raised when vanadium is added. The additions of up to 5% vanadium to high-Cr cast irons increased the values of tensile and bending strengths slightly, but for some reason wear resistance under dry friction conditions was decreased.

It was shown in the work of Parrent et al [64] that when 15% Cr cast irons were alloyed with around 6% vanadium, they exhibited better mechanical properties than unalloyed ones, better wear resistance was also observed due to the presence of vanadium carbides (VC) which are harder than eutectic M7C3 carbides. After hardening heat treatment for some reason vanadium alloyed irons exhibited a reduction in the value of bending and impact strength whereas their hardness increased by only around 2%.

2.4.5 Cerium, Calcium, Yttrium and Titanium Additions

It is well known that the Mg and Ce additions do not show the same effects on high-Cr cast irons as they do when added to grey cast irons in order to obtain nodular graphite. Some studies were carried out by Russian investigators [66-68] in order to determine the variations in the structure of white and alloyed high-Cr cast irons. According to their results [66] the most important factor as regards the structure of unalloyed white cast irons treated with cerium was the growth mechanism and associated structure of austenite and eutectic carbide colonies, under conditions of increasing super-cooling. Because of the solubility of cerium in the eutectic liquid the cerium accumulates ahead of the growth fronts on the eutectic colonies and prevents co-operatively growing austenite. Therefore variation of eutectic structure from honeycombs to plate-like structure was observed. Due to very low or non solubility of the cerium in the micro-structural constituents of white cast irons, it was mainly associated with non-metallic inclusions in the pearlite, on the boundaries between pearlite and eutectic carbides. Their results showed that when more than 0.2% Ce was added, complex eutectic inclusions of rare-earth metals were formed and properties of castings were lowered.

The influence of calcium and yttrium additions on the properties of high-Cr cast irons (1.8-2.5% C, 11-20% Cr, and 3-5% Mn) was investigated by Baranow et al [67] and it

was observed that the effect of modification was to raise the structure stability by absorption of the modifier at the external and internal boundaries of the crystal and at the defects of the crystal lattice. Normalising the casting at 900-1050^{o}C caused an initial coagulation of eutectic (M7C3) carbides with a partial solution of secondary carbides in austenite. The optimum modifier content was determined as being less than 0.4%.

In the work of Kitaigore [57] Ti was observed as a very strong carbide forming and deoxidising element. Studies were carried out within the range of alloy compositions: 2.4-3.2% C, 6% Cr, 2.5-8% Ti and 1% Mo by Ryabstsev et al [66]. It was concluded that the optimal amount of carbon content in the alloys depends on the Ti content and that it should be above the stoichoimetric level. The best results were obtained for wear resistance due to the presence of hard and strong Ti-carbides in combination with Cr-carbides. It was observed that during high temperature heat treatment of alloys up to melting point, Ti-carbides did not dissolve whereas Cr-carbides went into solution.

III DEVELOPMENTS IN FRACTURE MECHANICS

3.1 Energy Balance Approach

The energy balance approach to the study of the fracture phenomenon in cracked bodies was originally proposed by Griffith [69]. His theory was based on the assumption that unstable crack growth would occur when the "strain energy release rate" exceeded the rate of absorption of energy as new fracture surfaces were formed. By considering an ellipsoidal crack in unit thickness infinite body, (see Fig. 11), Griffith proposed that the total energy U in the system may be given by

$$U = \bar{U} + S + W \qquad \ldots\ldots\ldots(4)$$

where $\bar{U}$: elastic energy of an infinite body which is not dependent on presence of the crack.

S : increase in elastic surface energy

W : decrease in elastic energy due to introduction of a crack.

the increase elastic surface energy is given by

$$S = 4a\gamma_e \qquad \ldots\ldots\ldots(5)$$

where γ_e : the surface energy of the material

$4a$: surface area of the crack faces

and energy release rate

$$W = -\frac{\sigma_{app}^2 \pi a^2}{E} (1-\nu^2) \text{ (for plane-strain)} \ldots(6)$$

where σ_{app} : Applied stress

E : Young's modulus

ν : Poisson's ratio

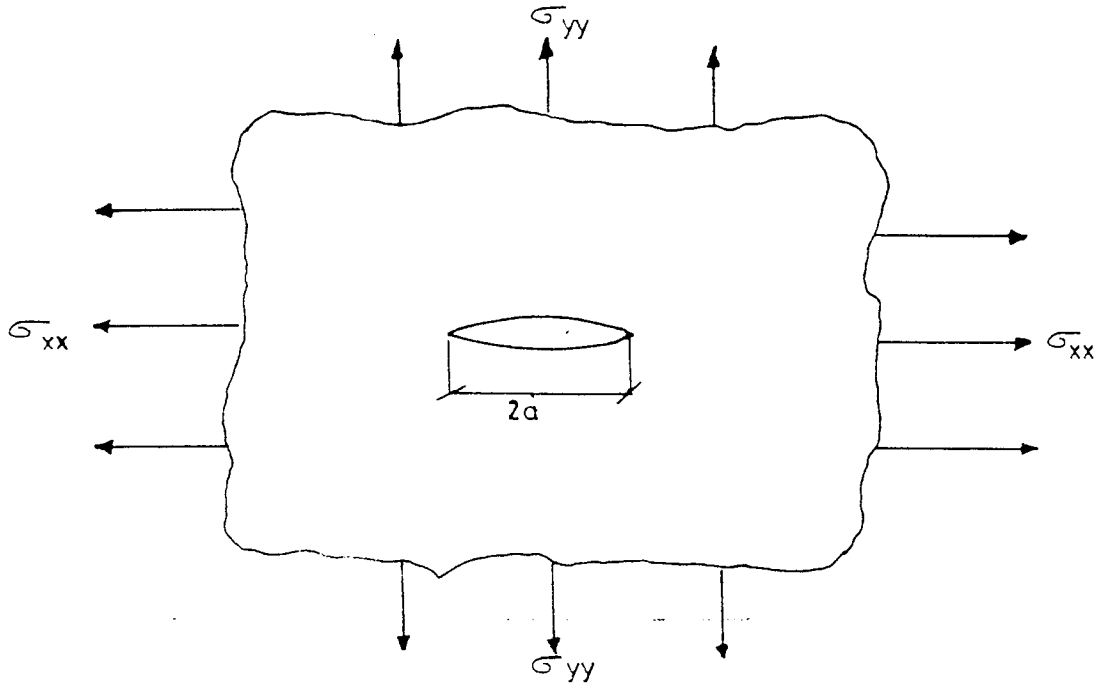

FIGURE 11: Through thickness crack in an infinite plate

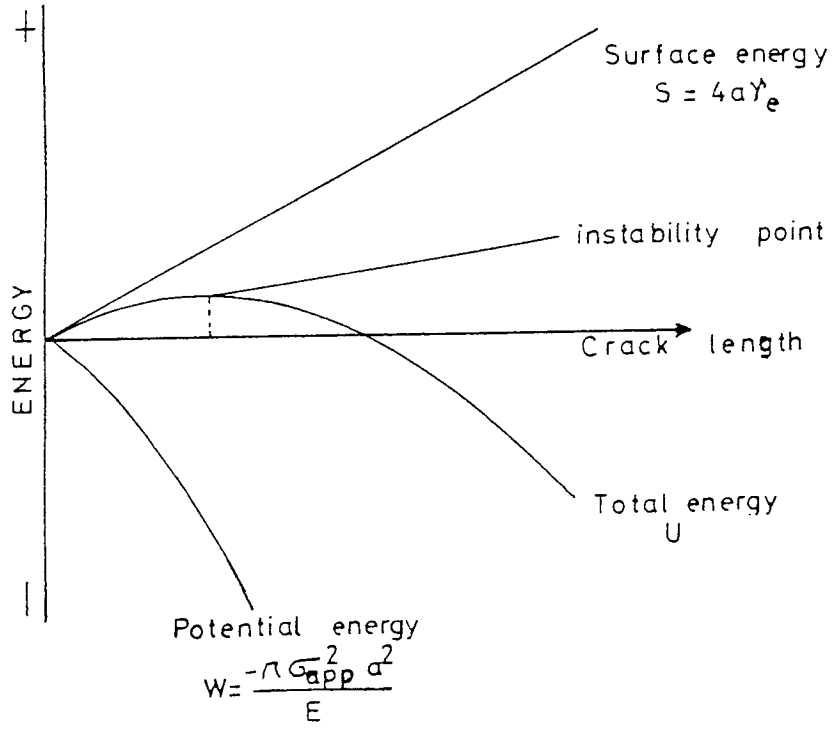

FIGURE 12: Energy balance of a crack in an infinite plate

Variation in the values of these expressions with crack length is given in Fig. 12. It can be seen that total energy U is a maximum when

$$\frac{dU}{da} = \frac{dS}{da} + \frac{dW}{da} = 0 \qquad \text{.....(7a)}$$

or

$$\frac{d}{da}\left(\frac{\sigma_{app}^{2}\,\pi\,a^{2}}{E}(1-\nu^{2})\right) = \frac{d}{da}\,(4a\gamma_e) \qquad \text{.....(7b)}$$

which leads to

$$\sigma_{app}\cdot\sqrt{a} = \left(\frac{2E\gamma_e}{\pi(1-\nu^2)}\right)^{\frac{1}{2}} \qquad \text{.....(8)}$$

and by re-arranging equation (8)

$$G = \frac{\sigma_{app}^{2}\,\pi a}{E}(1-\nu^{2}) = 2\gamma_e \text{ (for plane-strain) ..(9)}$$

where G represents the strain energy release rate.

Although the work of Griffith on hard glasses was very encouraging at the instant of fracture a constant value of $\sigma_F\sqrt{a}$ was obtained for a range of crack lengths but most materials do not behave in an entirely elastic manner, and normally some plastic deformation occurs at the crack tip prior to crack extension. Irwin [70] and Orowan [71] suggested a modification of the original theory so that limited plastic deformation γ_p could be accommodated by the theory, i.e.

$$G = \frac{\sigma_{app}^{2}\,\pi a}{E}(1-\nu^{2}) = 2\gamma_e + 2\gamma_p \qquad \text{.....(10)}$$

Irwin [70] proposed an alternative interpretation of critical strain energy release rate. He defined as a material property G_c which is total energy absorbed during cracking, per unit increase in crack length for unit thickness. Thus G_c is equivalent to $2\gamma_e$ when only the creation of new surface energy is required at the new crack surfaces, but where extensive energy is consumed in plastic deformation at the crack tip G_c also includes this according to equation (10).

3.2 Stress Intensity Factor Approach

This interpretation was originally developed by Irwin[72,73] considering the analyses of Westergaard [74], Irwin noted that the stresses in the vicinity of a crack tip could be expressed in the following form

$$\begin{vmatrix} \sigma_{xx} \\ \sigma_{yy} \\ \tau_{xy} \end{vmatrix} = \frac{K\cos^{\phi/2}}{\sqrt{2\pi r}} \begin{vmatrix} 1 - \sin^{\phi/2} \sin^{3\phi/2} \\ 1 + \sin^{\phi/2} \sin^{3\phi/2} \\ \sin^{\phi/2} \cos^{3\phi/2} \end{vmatrix} \quad \ldots\ldots(11)$$

where r, and ϕ are the cylindrical polar co-ordinates of a point with respect to the crack tip (see Fig. 13).

Irwin also demonstrated that the strain energy release rate or crack extension force G could be defined with K according to the following relationship

$$G_c = \frac{K_c^2}{E}(1-\nu^2) \quad \text{(for plane-strain)} \quad \ldots\ldots(12)$$

This relationship shows that if fracture (proceeded by limited plastic flow) may be characterised by the attainment of critical crack extension force G_c then this is

equivalent to characterising the fracture event by the attainment of a critical stress environment. The material property governing the fracture may therefore be stated as a critical stress intensity factor K_c, and the Griffith solution can be expressed by

$$\sigma_F = \sqrt{\frac{E G_c}{\pi a (1-\nu^2)}} = \frac{K_c}{\sqrt{\pi a}} \quad \ldots\ldots\ldots (13)$$

At the fracture stresses the quantities G_c and K_c are material properties expressing the resistance of the material to fracture. Generally K_c is preferred because it is independent from Young's modulus as a scaling factor.

3.3 Linear Elastic Fracture Mechanics

In metallic materials, the plastic zone forms where microscopic yielding has taken place in the vicinity of the crack tip due to high elastic stress. The plastic zone prepared the way for fracture by initiating the microstructural damage. This process consumes most of the energy during fracture. Although the plastic zone forms ahead of the crack tip, if the size of the body is much larger than plastic zone, the effects of such small scale yielding on the elastic stress field approximate to Irwin's plasticity correction (through equation (10)) and then the theories of linear elastic fracture mechanics (L.E.F.M.) can be applied to design problems. Assuming that the stresses ahead of the crack tip are less than the yield stress (σ_{ys}), the radius of the plastic zone may be given by

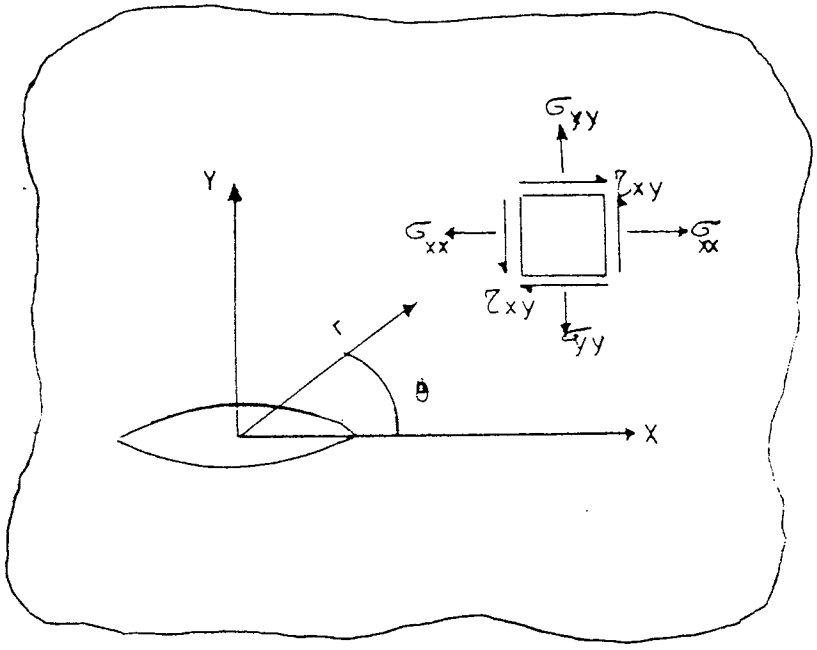

FIGURE 13: Stresses near a crack tip

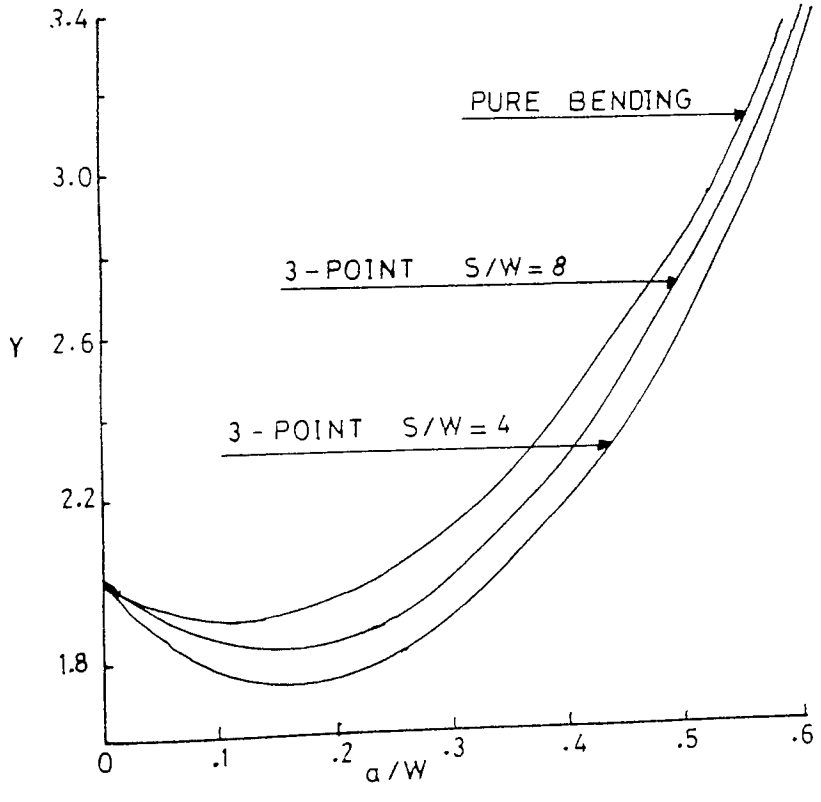

FIGURE 14: K calibration for Bend specimens

$$r_y = \frac{1}{2\pi}\left(\frac{K_{IC}}{\sigma_{ys}}\right)^2 \quad \text{(for plane-stress)} \quad \ldots(14a)$$

$$r_y = \frac{1}{5.6\pi}\left(\frac{K_{IC}}{\sigma_{ys}}\right)^2 \quad \text{(for plane-strain)} \quad \ldots(14b)$$

3.3.1 Dimension effect

Equation (10) could be written as

$$K_C = Y.\sigma_F\sqrt{a} = Y'\sigma_F\sqrt{a} \quad \ldots\ldots\ldots(15)$$

Here Y is a geometrical constant of value $\sqrt{\pi}$ in Griffith's equation and Y′ is a similar constant incorporating the $\sqrt{a}$. Variation of the geometry of the problem simply changes Y. For a given class of geometry Y depends on the ratio of crack length to gross width $^a/_w$, and a plot of Y versus $^a/_w$ as in Fig. 14 is called a K calibration curve. If K_{IC} value of a material is evaluated for one geometry, that of a laboratory test piece, then the results can be used to predict the fracture stress of an engineering structure or component once the K calibration curve is known.

3.3.2 Thickness effect

K calibration curves account for two dimensional features of the geometry, but thickness also introduces a pure size effect and this is treated by measurement of K_{IC} with thickness. In thin sheets in tension and containing through cracks, the condition is plane-stress which means that, all crack tip stresses lie in the plane of the sheet and stress in the thickness direction is almost zero. The tension stress in the yield zone is equal to the uniaxial yield-stress and fracture occurs by local shearing through the yield zone. Crack faces are therefore at 45^o to gross tensile direction.

As the thickness of the plate is increased, stresses are developed in the thickness direction as well as in the width and tension direction. These stresses arise because the region very close to the crack tip undergoes a large elastic or plastic stretch whereas outside this region the stretch is small. Very close to the crack tip the material therefore wishes to undergo a large Poisson contraction in the two directions perpendicular to the axis of the gross applied stress. Material remote from the crack tip resists this contraction and produces tensile constraint stress in the thickness and width directions, as shown in Fig. 15. Under these triaxial stress conditions the resolved shear components of σ_{yy} are reduced and yielding cannot take place until σ_{yy} reaches a value of nearly three times the uniaxial yield stress (σ_{ys}). The result of the higher σ_{yy} at yield is a smaller yield zone than that for plane stress conditions, as shown in Fig. 16.

In thick plates there is no constraint stress at the side free surfaces, so that near these surfaces the conditions are similar to plane-stress for thin sheet. As thickness is increased or decreased the plane-stress region remains unchanged but the plane-strain zone occupies a larger and larger proportion of the thickness as the thickness is increased. Since the plane-strain zone consumes much less energy than its plane-stress counterpart there is a decrease of G_{IC} or K_{IC} with increasing thickness, as shown in Fig. 17.

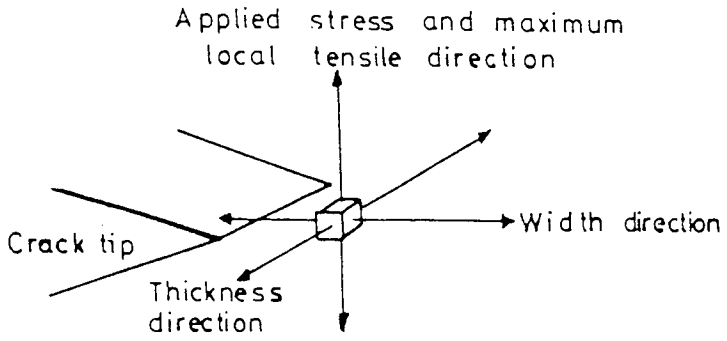

FIGURE 15: The direction of tensile constraint stresses ahead of the crack tip (75)

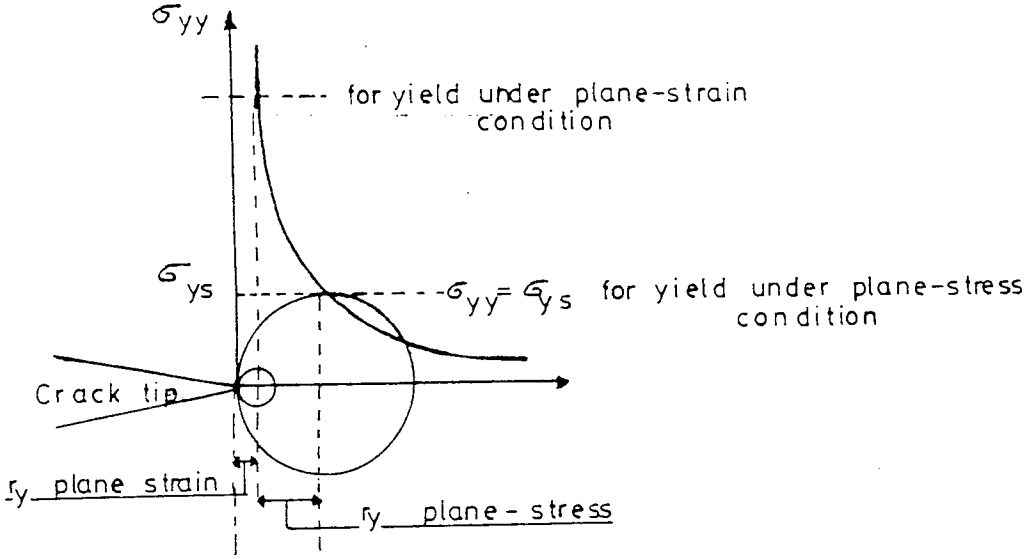

FIGURE 16: Variation of σ_{yy} tensile stress component with plane-strain conditions (75)

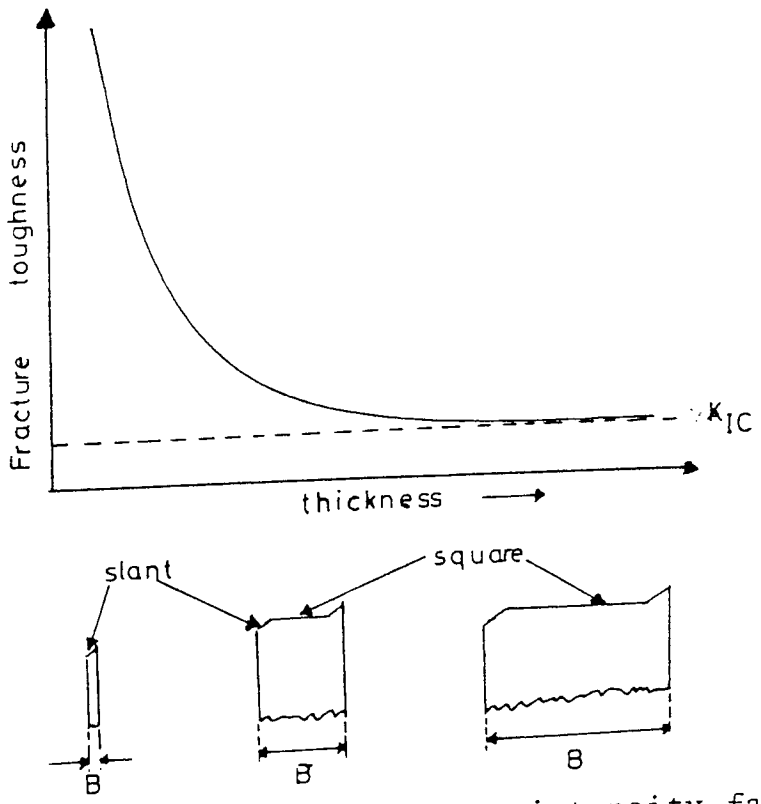

FIGURE 17: Variation of stress intensity factor and fracture profiles with thickness of the test piece

In practise to ensure that the stress intensity factor is obtained in plane-strain conditions, standards [76,77] specify that the value of thickness of the test specimen should be greater than

$$B > 2.5 \left(\frac{K_{IC}}{\sigma_{ys}}\right)^2 \qquad \ldots\ldots\ldots (16)$$

3.4 Elastic-Plastic (Yielding) Fracture Mechanics

Standard procedures of L.E.F.M. lead to the measurements of consistant values of plane-strain fracture toughness K_{IC} of relatively tough materials. It is however necessary to use test pieces of dimensions so large that either they are impractical to test or the test piece may not be representative of behaviour of the sections actually used in service. There is consequently much interest in the possibility of making alternative measurements using small test pieces which will still reflect the material property. The concept of yielding fracture mechanics enables the fracture toughness of a material to be assessed after gross plastic deformation has taken place. Two main procedures are currently in use, namely:

a - Crack opening displacement (C.O.D.)

b - J-integral analysis (J)

3.4.1 Crack Opening Displacement (C.O.D.)

The "strip yield" model for the extent of plastic deformation at the tip of the crack was proposed by Dugdale [78] and at the same time by Barenblatt [79]. Also another alternative method using the dislocation theory was presented

by Bilby, Cottrell and Swinden [80]. The plasticity at the tip of a central crack (length = 2a) in an infinite plate was represented by a notional increase in the crack length to some value 2c with the faces of the crack over distance (c-a) from both ends partly restricted from opening by restraining stresses (t). These restraining stresses were equated to the material yield stress σ_{ys} and a relationship was obtained for the length 2c in which notional plastic zone is extended in terms of the real crack length 2a and applied stress σ (see Fig. 18). This relationship is given by:

$$\frac{a}{c} = \text{Cos}\left(\frac{\pi\sigma}{2\sigma_{ys}}\right) \qquad \ldots\ldots\ldots(17)$$

from this it can be seen that as $\sigma \to \sigma_{ys}$ the value of $(a/c) \to 0$, i.e. $c \to \infty$ and yielding spreads across the finite plate.

Wells [81] noticed that in practice the tip of the slot subjected to plastic deformation opened with a near square contour, giving a definite tip opening. He proposed that crack opening displacement which was denoted as δ was a measure of crack tip deformation and that fracture might occur when the critical value of this parameter δ_c was reached.

Experimentally and theoretically Well's proposal was supported by Burdekin and Stone [82] and the values of δ derived by:

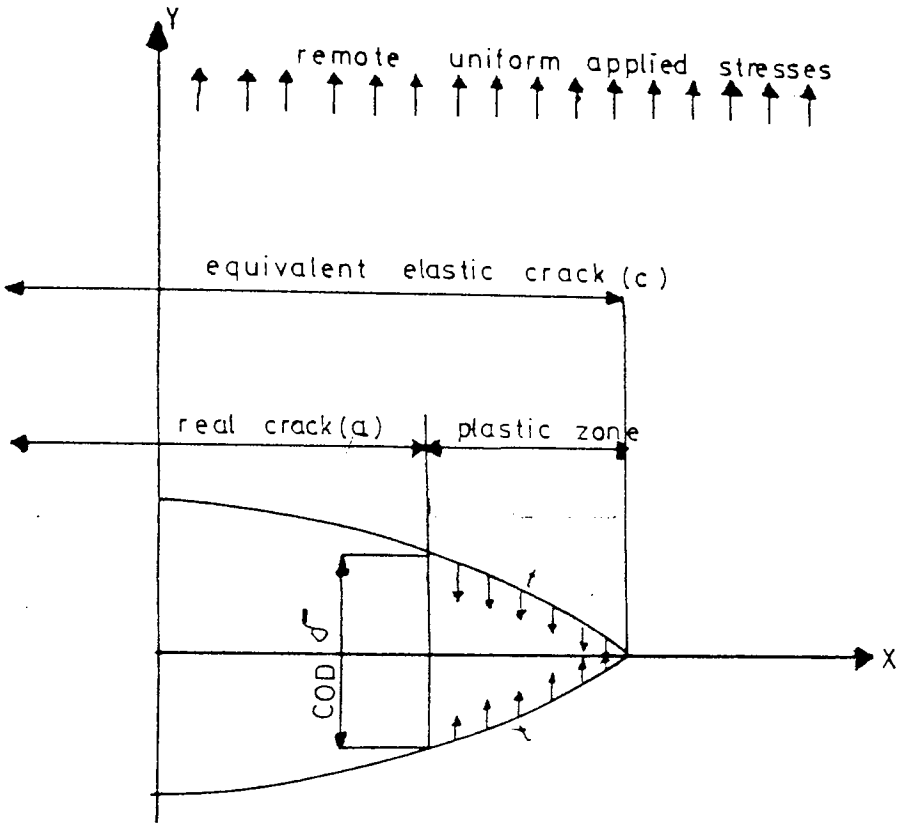

FIGURE 18: Dugdale's strip-yield model for crack tip plasticity (78)

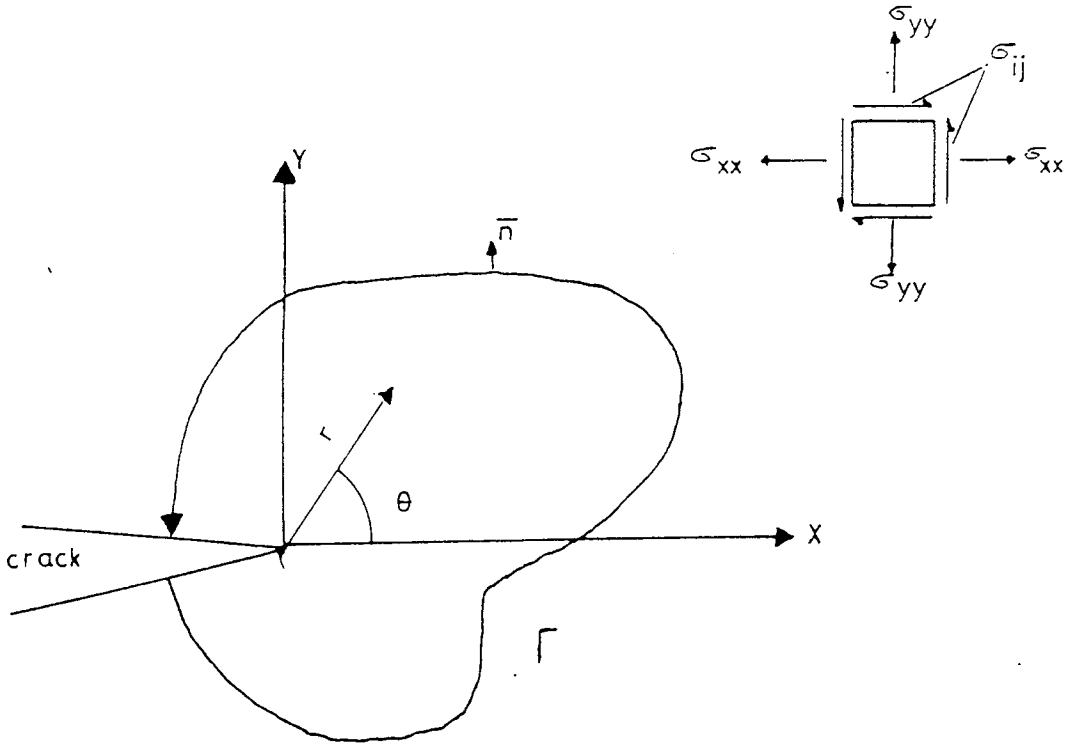

FIGURE 19: Crack tip co-ordinate system and arbitrary line J-integral contour (88)

$$\delta = \frac{8\sigma_{ys}}{\pi E} \ln \left(\sec \frac{\pi\sigma}{2\sigma_{ys}}\right) \quad \text{.....(18)}$$

by expanding the log sec term it was found that

$$\delta = \frac{\pi\sigma^2 a}{E\sigma_{ys}} \left[1 + \frac{\pi 2}{24} \left(\frac{\sigma}{\sigma_{ys}}\right)^2 + \ldots\ldots\right] \quad \text{.....(19)}$$

3.4.1.1 Correlation between C.O.D., G and K

In L.E.F.M. conditions for the infinite plate with centre crack (length = 2a)

$$G = \frac{K^2}{E} = \frac{\pi\sigma^2 a}{E} \quad \text{.....(20)}$$

as can be seen, the first term of the equation (19) corresponds to

$$G = \sigma_{ys}.\delta \quad \text{.....(21)}$$

If the plastic zone correction factor for plane-stress is used so that effective crack length $2c = 2\ (a+r_y)$, where r_y plastic zone size for plane stress condition (equation 11a) then the modified L.E.F.M. expression is:

$$G = \frac{\pi\sigma^2 a}{E} \left[1 + \frac{1}{2} \left(\frac{\sigma}{\sigma_{ys}}\right)^2 + \ldots.\right] \quad \text{.....(22)}$$

which together with equation (21) differs from equation (19) by a very small amount in the coefficient of the second term. Various attempts were made at a later stage to represent the plane strain by:

$$G = M\sigma_{ys}.\delta \quad \text{.....(23)}$$

where M at present is the subject of much controversy, owing to the discrepancies between theoretical and experimental values. Generally M is taken as 1 in plane-stress and 2 for

plane-strain. Equation (23) can be re-arranged for K_{IC} plane strain conditions, as

$$K_{IC} = \sqrt{\frac{M.E.\sigma_{ys}\,\delta_c}{(1-\nu^2)}} \qquad \ldots\ldots\ldots(24)$$

The critcal value of C.O.D. δ_c as a material property is defined as the initiation of growth from a pre-existing crack.

3.4.1.2 Limitations of C.O.D. as a fracture criteria

The difficulties, both theoretical and experimental, with C.O.D. characterisation of fracture toughness are summarised in the work of Eftis and Liebowitz [83]. The most important limitation of the C.O.D. concept is that the onset of crack extension does not necessarily signify unstable crack propagation leading to failure in an unstable manner, since it is possible that slow crack growth can be sustained by increasing loads. Measurements of critical C.O.D. at the onset of fast fracture after significant slow crack growth could in principle be considered but sizeable slow crack growth invalidates use of equation (17), since the strip yield model is based on the assumption that the plastic yield strip thickness along the plane of the crack is constant, whereas experimental data shows that the plastic zone grows both in length and breadth with crack extension.

On the other hand, when general yield precedes fracture it is no longer possible to relate critical C.O.D. values to load and crack size, even approximately since equation (18) will no longer make any physical sense. C.O.D. must then simply be regarded as a quantity which provides some inform-

ation on the character of the material tested, particularly as to its ductility at the root of a crack, and perhaps as a qualitative indication of its resistance to fracture. In this regard the application of C.O.D. must be empirical, similar to applications of results of charpy tests.

The experimental observations are that critical values of δ for a given material, section thickness and temperature appear to be approximately the same regardless of whether crack growth commences from pre-yield or post-yield state and irrespective of specimen configuration and crack sizes. The reason for these observations may be a result of the critical values of δ since they are quite small (the order of 10^{-3} cm) and gross differences in local crack tip stresses and strains in pre-yield and post-yield situations may be reflected by small differences in crack opening displacements.

3.4.2 J-Integral Analysis

The theoretical foundation for the path independent energy line integral (J - Integral) was introduced to fracture mechanics by Rice [84]. The energy line integral (J) is applicable to elastic or elastic-plastic materials when treated by a deformation theory of plasticity and its path independent nature allows an integration path, taken sufficiently far from the crack tip, to be substituted for a path close to the crack tip region. It is defined for two dimensional problems and it is possible to define an energy line integral (J) on any curve, as is shown in Fig. 19, surrounding the crack tip, starting from the lower

surface and ending on the upper surface of the crack such that J is given by [84]:

$$J = \int_{\Gamma} W dy - T \left(\frac{\partial u}{\partial x}\right) ds \qquad \text{.....(25)}$$

where: Γ : path surrounding the crack tip

W : strain energy density given by

$$W = w(\varepsilon_{m,n}) = \int_{o}^{e_{min}} \sigma_{ij} . d\varepsilon_{ij}$$

T : Traction vector defined by the outward normal $\bar{n}$ along Γ, $T_i = \sigma_{ij} . \bar{n}_{ij}$

u : displacement vector

s : arc length along Γ

For the J-integral to have validity as a failure criterion it must be assumed that there is a crack tip stress-strain singularity for large scale yielding. The works of Hutchinson [85], Rice and Rosengreen [86] support this assumption and these singularities were expressed as

$$\sigma \alpha \frac{1}{r^{N/N+1}} \sigma(\theta) \qquad \text{.....(26a)}$$

$$\varepsilon^p \alpha \frac{1}{r^{1/N+1}} \varepsilon(\theta) \qquad \text{.....(26b)}$$

where N is the strain hardening exponent. For the linear elastic condition N = 1, therefore the elastic-plastic equation (26) reduces to the equation (11).

3.4.2.1 Energy Rate Interpretation

Energy balance calculations by Irwin [73] show that the Griffith type fracture criteria for crack extension in linear elastic solids depends on local conditions at the crack tip. It has been pointed out by Rice [87] that local conditions also govern the inelastic crack tip deformation. Therefore the path independent energy line integral (J) must be related to energy balance considerations, and may be interpreted as the potential energy difference between two identically loaded bodies having neighbouring crack sizes. This is stated mathematically as

$$J = -\frac{du}{da} \qquad \text{.....(27)}$$

where u : potential energy

a : crack length

In the linear elastic case and also for small scale yielding, J is therefore equal to G, the crack driving force. In the general elastic-plastic problem, loses its physical significance as a crack driving force. One of the restrictions involved in the useage of the deformation theory is that unloading is not permitted since deformation is not reversible. In plane-stress conditions materials exhibit significant subcritical crack growth prior to any crack extension which necessarily implies unloading near the crack tip. Since unloading is not permitted, J-Integral may be interpreted as the energy available for crack extension and refers to crack initiation rather than propagation.

Experimental evidence in support of the J-Integral as a parameter for describing fracture has been produced by Landes and Begley [88]. They have also shown that for two independent geometries (a centre cracked panel and bend bar) the differences in slip line were of no consequence and both geometries gave the same value of J_{IC} [88].

J_{IC} is simply related to the parameters of linear elastic fracture mechanics as given below:

$$J_{IC} = G_{IC} = \left(\frac{1-\nu^2}{E}\right) K_{IC}^2 \quad \text{(for plane-strain)} \quad ..(28)$$

In order for the J-Integral analysis to be valid the thickness limitation of the test pieces is given by [88]

$$B > 25.0 \left(\frac{J_{IC}}{\sigma_{ys}}\right) \quad .....(29)$$

3.4.2.2 Limitations of J-Integral as a Fracture Criteria

Fracture toughness evaluation under plane-stress conditions where slow stable crack growth precedes fast fracture clearly limits the applicability of the J-integral as a measure of fracture toughness since it is possible that slow-crack growth can be sustained by increasing loads. Measurements of J_{IC} at the onset of fast fracture after significant slow crack growth could not in principle be considered since crack growth induces stress relaxation within the yield zone ahead of the crack tip and invalidates the usage of the deformation theory.

Although computational results have shown that J-integral is still valid when the plasticity spreads to the far boundary (general yield-situation) and remains path independent from the far field to the near crack tip region, exact theoretical proof to establish such independence has not yet been put forward [83,89].

Because of the mathematical difficulties associated with general elastic-plastic analysis of the opening mode cracked body problem, the methods which are mentioned here make use of some particular aspect which enables the elastic-plastic problem to be treated as if it were a modified or equivalent elastic one. All of them suffer limitations of one kind or another as to suitability for fracture toughness evaluation in situations where there is a possibility of extensive crack-tip plastic yield and sustained sub-critical crack growth prior to fast fracture. Despite the limitations, the methods of yielding fracture mechanics are able to offer quantitive values which can be used for the assessment of working stress levels and critical flaw sizes in the design of engineering components.

3.5 Test Methods for Measuring Fracture Toughness

The techniques which are used for determining K_{IC} under linear elastic conditions are well established and documented (ASTM E-399) (B.S.5449). Also techniques to evaluate the toughness for conditions at which excessive plastic deformation or general yielding take place prior to fast fracture have been developed (J-Integral, R-Curve and C.O.D. techniques) [90,91,92].

The recommended testing practise for linear elastic and elastic-plastic conditions includes the process of introduction of a sharp-crack into the test pieces. For most of the metallic materials this sharp-crack is generated by fatiguing until a crack of adequate length is developed from the base of the pre-machined notch. However, for brittle metallic materials (i.e. hard steels, alloyed cast irons) and for non-metallic brittle materials (i.e. glasses and ceramics) a satisfactory crack generating process has not been developed. Many types of specimens, such as the single edge notch bend specimen, the double torsion specimen, the double cantilever beam specimen and the surface flawed specimens are currently used. These specimens have either blunt notches in comparison with a sharp crack or cracks are produced by wedge loading or by local thermal shock. Specimens with blunt notches could over-estimate the K_{IC}. Pre-cracked specimens are difficult to prepare in a reproducible manner and it is very often difficult to distinguish and to measure the initial crack length on the fracture surface after testing.

To overcome these difficulties test specimens with a chevron notch were first used by Nakajama [93] and later by Tattersal and Tappin [94]. Their specimens have a square cross-section and contain a chevron notch at mid span and are loaded either in three point bending or four point bending. The authors suggested that,using a specimen with a chevron notch, during loading the crack initiates

at a low load level so that the associated energy release rate G is too low to maintain continuing crack growth. Therefore additional load is necessary for crack extension. They worked on the necessary energy for crack extension. This energy was normalised with respect to the generated crack area and then termed the "work of fracture" or "fracture toughness". However later on some difficulties were experienced when attempting to obtain stable crack growth during testing [95,96].

Barker [97] suggested using the recorded maximum load for fracture toughness (K_{IC}) determinations by using calibrated specimens. According to his published data [98] during the test the initiated crack reaches a constant critical length at the maximum load independent of the specimen material and this enables determination of the fracture toughness of the materials for linear elastic conditions according to the given equation (30) as long as scaled specimen dimensions are in accordance with calibrated specimen dimensions:

$$K_{IC} = \frac{P_{max} A}{B^3/2} \qquad \text{.....(30)}$$

where A = constant

B = specimen width

P_{max} = maximum recorded load during the test.

This suggested method has the advantage that a sharp crack is produced during loading and therefore neither fatigue pre-cracking nor measurements of critical crack length

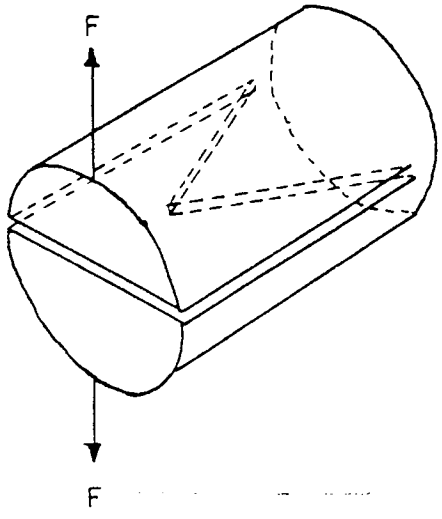

FIGURE 20: a: Short-Rod fracture toughness specimen

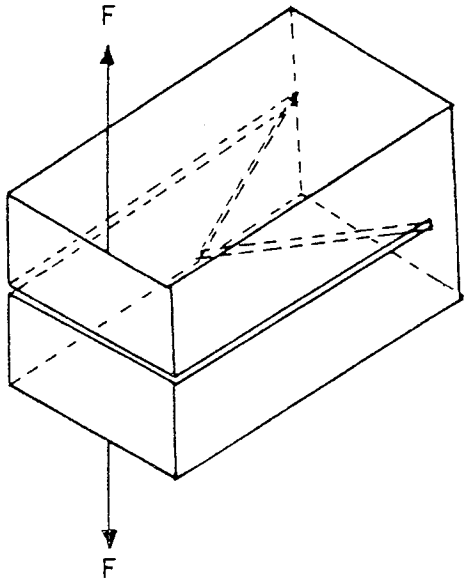

FIGURE 20: b: Short-Bar fracture toughness specimen

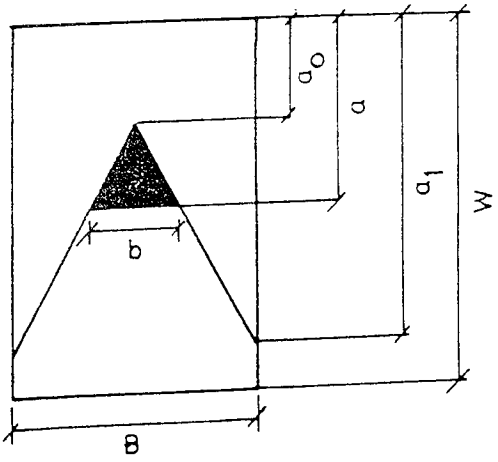

FIGURE 20: c: Chevron notch detail of short-bar/rod fracture toughness specimens

are required. It is necessary only to determine the maximum load.

Barker used a specimen with a circular cross-section (short-bar specimen (Fig. 20a)) of fixed overall geometry and obtained a relationship between P_{max} and K_{IC} by comparing with materials of known K_{IC} values determined by standard methods. Thus he arrived at the value of A which is given equal to 22. Barker also used a specimen with rectangular cross-section (short-bar specimen, (Fig. 20b)) designed in such a way that the same maximum load is obtained as for the short rod specimen [99].

To obtain the relationship between fracture toughness and maximum load for the short-bar specimens Srawley et al[100] used an analytical expression of the compliance calibration of straight through cracks using the assumption that the change of compliance with crack length for a specimen with a chevron notch is the same as that for a specimen with a straight-through crack.

Barker was also able to evaluate the toughness of metallic materials for elastic-plastic conditions using a short-bar/rod technique [101]. He adopted a plasticity correction factor which is determined during testing, and adjusted the compliance due to plastic deformation ahead of the running crack.

Short rod/bar fracture toughness techniques have been gaining popularity due to their simplicity and applicability to both plastic-elastic and elastic behaving materials using very small scale test pieces. Although it is a new technique and the theoretical and experimental data have not been well established, especially for elastic-plastic cases, it is under review of the ASTM sub-committee (102).

IV THEORETICAL CONSIDERATIONS

Engineering fracture mechanics describe the brittle fracture of a body in terms of stress-intensity or fracture toughness K_{IC}, the body failing when this stress intensity is exceeded at the crack tip. In the previous chapter, the current theories and methods of measuring toughness of materials were described. In recent years, a considerable amount of work has been carried out in order to correlate the stress intensity factor or toughness of materials with their micro-structures. The majority of the work has been conducted with medium and low strength steels in specimens containing notches rather than sharp-cracks. The reason for this is that more is known about the elastic-plastic stress distribution as related to the fracture mechanism in notched specimens than for pre-cracked specimens.

4.1 Crack Nucleation

The studies of Barnby [103,104] and others for pearlitic and austenitic steels have shown that the fracture nucleation occurs in the second phase particles as a result of the local stress around slip-lines in the matrix. Smith and Barnby [105] modified the dislocation model of Stroh [106] for fracture initiation in two phase materials. Consideration of dislocations piled-up against a barrier such as a carbide in Fig. 22 leads to the following equation for shear stress to cause failure of the carbides.

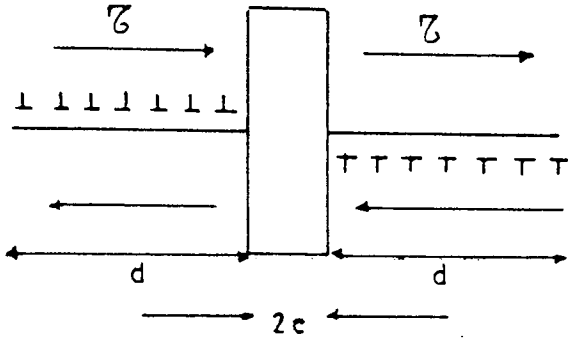

FIGURE 22: Dislocation pile-up against grain boundary carbide (105)

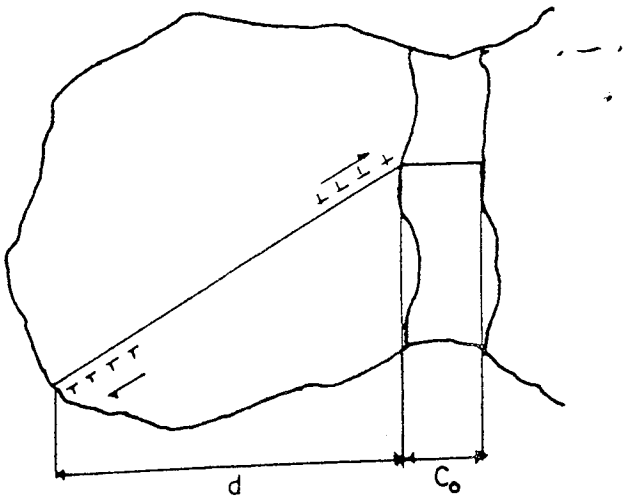

FIGURE 23: Smith's model for cleavage fracture (111)

$$\tau_{eff} > \left(\frac{2c}{d}\right)^{\frac{1}{2}} \left[\frac{2\gamma\mu}{\pi(1-\nu^2)d}\right]^{\frac{1}{2}} \quad \text{.....(31)}$$

where τ_{eff} : effective shear stress

γ : crack surface energy

μ : matrix shear modulus

c : carbide width

ν : Poisson's ratio

d : length of dislocation pile-up.

Another model for crack initiation in two phase alloys was proposed by Lindley, Oates and Richards [107]. The model assumes that the carbides act as long thin fibres which are loaded elastically when the matrix around them deforms plastically, and which crack when the matrix strain reaches a critical value. The stress in the carbides (length = l, thickness = t) is given simply by Hookes law:

$$\sigma_c = \varepsilon_M \cdot E_c \quad \text{.....(32)}$$

where σ_c : stress in the carbide

ε_M : strains in the matrix

E_c : Young's modulus of carbide.

For larger strains in the matrix, the maximum stress in the carbide film for a given aspect ratio l/t is given by equation

$$(\sigma_c)_{max} = \frac{1}{t} \cdot \tau_M \quad \text{.....(33)}$$

where τ_M is the shear strength of the matrix. The stress in the carbide will increase with strain if τ_M is raised by work hardening. According to this model, thin carbides

are easier to crack than thick ones, also spheroidal carbides are less brittle for equivalent thickness than plate-like carbides or rods since a spheroidal particle is not subjected to significant fibre-loadings.

4.2 Propagation of Nucleated Micro-Cracks and Critical Tensile Stress Criterion

Fracture may be considered to be nucleated when a critical value of effective shear stress is attained: this corresponds to a critically potent density of newly-created slip dislocations which serve to fracture carbides, either by stress induced at the end of a pile-up (Smith-Barnby Model) or plastically straining the matrix and producing sufficient stress in the carbides by a fibre-loading mechanism (Lindley-Oates and Richards Model).

According to the work of Smith and Barnby [108] once the crack is formed equal lengths of slip-lines cancel out leaving an unpropagated crack. Unbalancing will cause the crack to propagate into the matrix on the weaker side, and this will lead to a decrease in the total energy of the system provided that the surface energy encountered by the growing crack remains constant. The condition under which the nucleated micro-crack will spread given as

$$\tau_{eff} > \left[\frac{\pi\gamma\mu}{2(1-\nu^2)d}\right]^{\frac{1}{2}} \qquad \ldots\ldots\ldots (34)$$

The important stress causing the brittle fracture is therefore predicted to be the effective shear stress and this implies that fracture is nucleation controlled. The number of dislocations which are sufficient to nucleate a crack is also given by:

$$n = \frac{\pi 2\gamma}{2\tau_{eff} b} \qquad \text{.....(35)}$$

where b is Burger's vector of dislocation.

Another dislocation mechanism for cleavage fracture allowed growth to be the controlling factor by providing an easy nucleation process was proposed by Cottrell [109]. According to his work, the value of the local tensile stress σ_{yy} needed to propagate a nucleated micro-crack is given by:

$$\sigma_{yy} = \frac{2\mu\gamma}{K^s_y} d^{-\frac{1}{2}} \qquad \text{.....(36)}$$

Cottrell applied this expression to explain the experimental results of tensile specimens in various grain sizes. It was shown that the nucleated crack does not spread until the local tensile stress σ_{yy} attains a critical stress-level, σ_F thus:

$$\sigma_{yy} > \sigma_F = \frac{2\mu\gamma}{K^s_y} d^{-\frac{1}{2}} \qquad \text{.....(37)}$$

where d : grain size

K^s_y : the gradient of Hall-Petch yielding relation.

Cottrell's model therefore emphasises the role of tensile stress and explains the effects of grain size and yielding parameters on the fracture. Later it was shown by McMahon and Cohen [110] that the carbides within the micro-structure

play an important role. They carried out their tests on tensile specimens of identical yield and flow properties but containing different size carbides. Their results showed that coarse carbides promoted brittle fracture, while fine carbides allowed the material to fail by void coalescence in a ductile manner.

It is widely accepted that carbides provide a low surface energy phase as predicted by the Smith-Barnby model, which is necessary for propagation-controlled brittle fracture. Smith [111] proposed a theoretical model of brittle fracture of mild steel based on a crack nucleation mechanism. A grain boundary carbide particle is cracked by an impinging dislocation pile-up and the micro-crack so formed subsequently propagates as a Griffith defect under the combined influence of the pile-up and applied stress. By considering the change in energy with crack length the critical fracture stress was calculated to be given by:

$$\left(\frac{Co}{d}\right)\sigma_F^2 + \tau_{eff}^2\left\{1 + \frac{4}{\pi}\left(\frac{Co}{d}\right)^{\frac{1}{2}}\frac{\tau_i}{\tau_{eff}}\right\}^2 > \frac{E\gamma_p}{\pi(1-\nu^2)d} \quad \ldots(38)$$

where:
- τ_i : lattice friction stress
- τ_{eff} : effective shear stress
- γ_p : effective surface energy of matrix or plastic work term
- E : Young's modulus
- ν : Poisson's ratio
- d : grain size
- C_o : carbide thickness

4.2.1 Quantitive Determination of Critical Fracture Stresses

The value of the critical tensile stress σ_F which is required to propagate a nucleated micro-crack in a notched bar has been obtained by employing stress analysis based on slip-line theory or finite element analysis.

In the work of Wilshaw, Rue and Tetelman [112] a theoretical model for predicting elastic-plastic stress distribution in notched bar for plane-strain conditions was developed by combining the elastic solutions of Nueber [113] with the slip-line field solutions of Hill[114]. The model enables one to calculate the plastic zone size ahead of the notch as a function of externally applied bending moment, yield stress and geometrical factors. They found good agreement between theoretical predictions and experimentally measured plastic zone sizes in notched bars of a high-nitrogen steel. Their model is given in detail in section 7.4.

Notch-root true principal strain ε_{yy} was determined by the surface groove method in the work of Tetelman and Mohamed[115], and in the work of Wilkins by using finite element techniques [116]. The results have shown that the notch root strain is constant over most of the notch root radius, and both experimental and analytical studies have indicated that ε_{yy} varies hyperbolically with distance beneath the notch. It appears that the ε_{yy} values at the surface in the work of Tetelman et al [115] are lower than the results obtained from finite-element analysis due to problems associated with the visioplastic method at large strains [117]. The

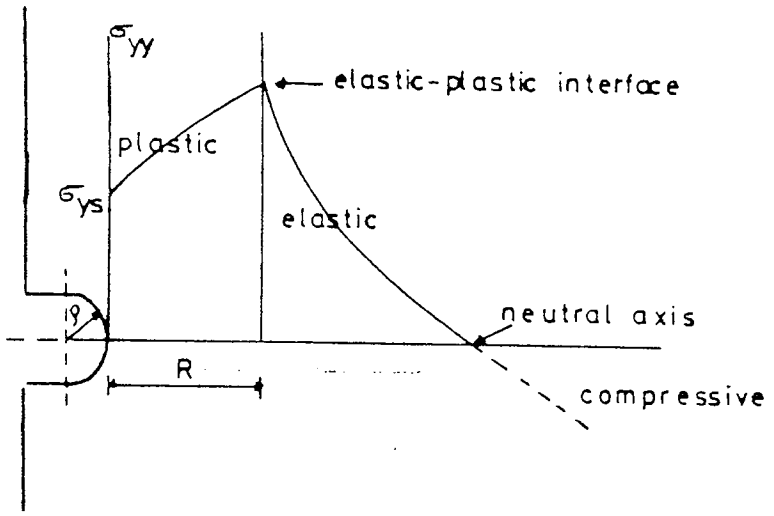

FIGURE 24: Distribution of tensile stress σ_{yy} ahead of a notch in the elastic-plastic bending case (112)

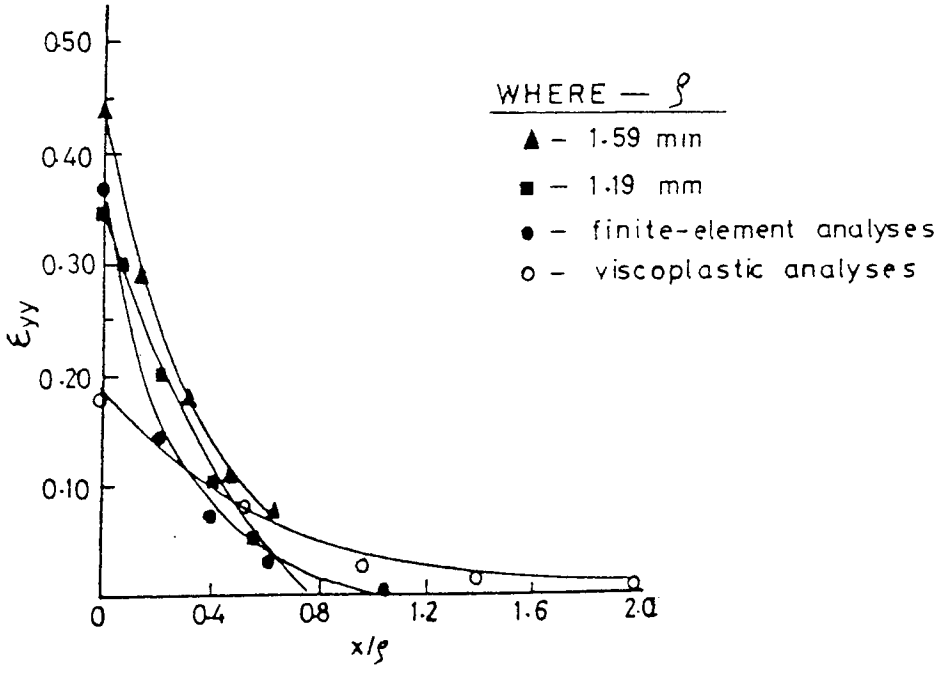

FIGURE 25: Variation of principal strain ε_{yy} ahead of the notch at fracture for various notch root radii (117)

variation of principal stress and strain distribution in a notched bending bar is shown in Fig. 24 and Fig. 25 respectively.

The elastic-plastic stress analyses which allow for linear work hardening for a notched bar were carried out by Griffith and Owen [118] using finite element techniques. In their work it was shown that the maximum tensile stresses do not occur at the elastic-plastic interface but at some distance behind the elastic-plastic interface. It was also shown that the stress intensification (σ_{yy}/σ_{ys}) in slip-line theory is over estimated at low loads and under estimated near to general yielding. This discrepancy between the two methods is given in Fig. 26 and Fig. 27.

4.2.2 Micro-Structural Significance of Critical Fracture Stresses

Equation (38) shows the value of σ_F in the tensile stress level required to propagate a nucleated micro-crack in a grain boundary carbide through the matrix. For a given material, it was shown that critical tensile stress does not change for a wide temperature range (-200 to 50°C) [118]. The value of effective surface energy or plastic work terms γ_p which appears to give a reasonable agreement between the carbide size, grain size and σ_F on the basis of equation (38) was found to be 12-22 J/m^2 for ferrite. These values of γ_p are substantially greater than the true surface energy of iron (2 J/m^2). The reason for this apparent increase was shown to be due to the very limited movement of the crack tip dislocations which do plastic work. Therefore some of

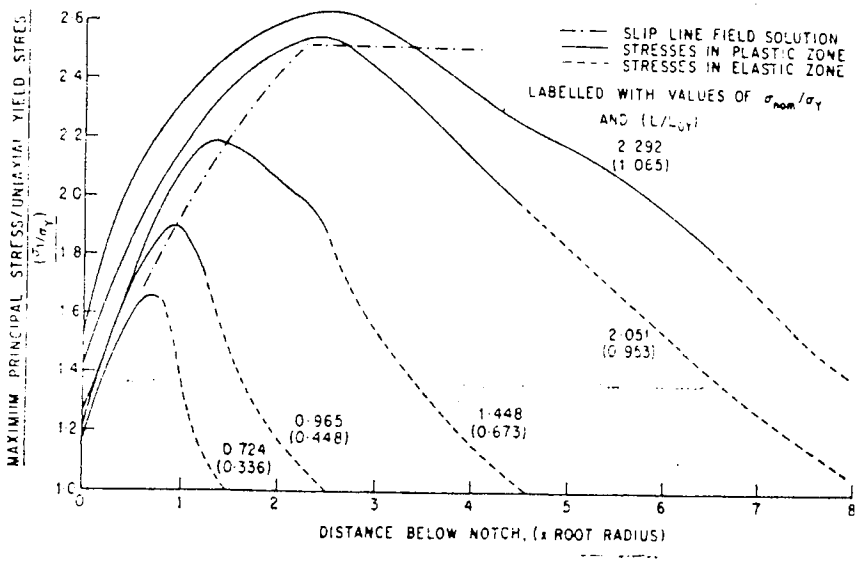

FIGURE 26: Distribution of tensile stress (σ_{yy}) acting directly ahead of a round notch (13)

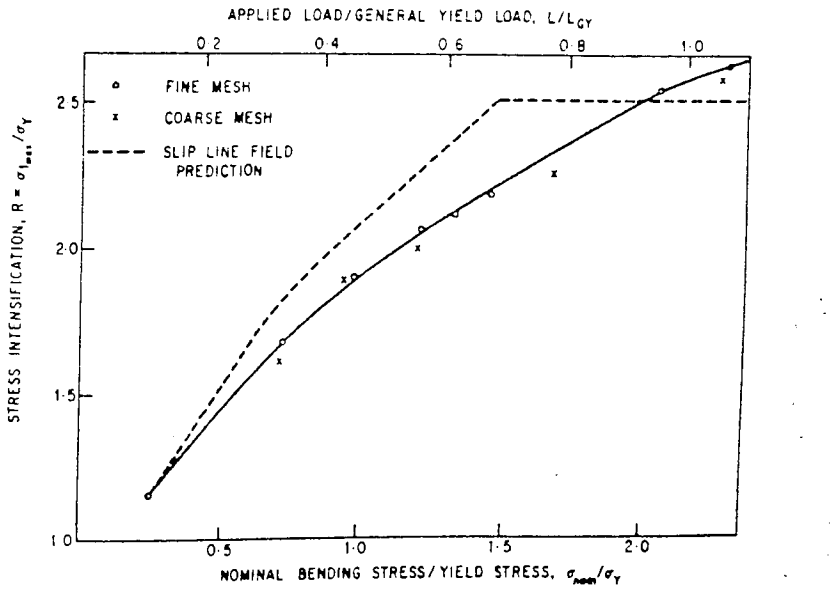

FIGURE 27: Variation of stress intensification with applied load ahead of a round notch (13)

the applied potential energy is dissipated as plastic work before the nucleus starts to propagate through the matrix [119].

Figure 28 shows the results obtained by a number of authors giving the value of σ_F as a function of the reciprocal square root of grain size ($d^{-\frac{1}{2}}$). It is clear that critical fracture stress increases quite markedly with ($d^{-\frac{1}{2}}$). The grain size dependence of σ_F was argued by Curry and Knott [120]. According to their work the first side of equation (38) predicts that fracture stresses depend on ferrite grain diameter. If the effective shear stresses τ_{eff} is written as $K^S_y d^{-\frac{1}{2}}$ where K^S_y in the gradient of Hall-Petch yielding relationship, the fracture criterion can be re-arranged as

$$\sigma_F^2 + \left(\frac{K^S_y}{C_o}\right)^2 \left[1 + \frac{4}{\pi} C_o \frac{\tau_i}{K^S_y}\right]^2 > \frac{4E\gamma_p}{\pi(1-\nu^2)C_o} \quad \ldots.(39)$$

This equation predicts that the only parameter affecting the critical fracture stress is the carbide width since σ_F is independent of grain size. They concluded that the carbide thickness is the only controlling factor and this existing anomoly (due to equation (39)) between the experimental observations of grain size dependence of brittle fracture stress in the mild steels may be removed simply by taking account of the observed increase of the carbide thickness by increasing grain size.

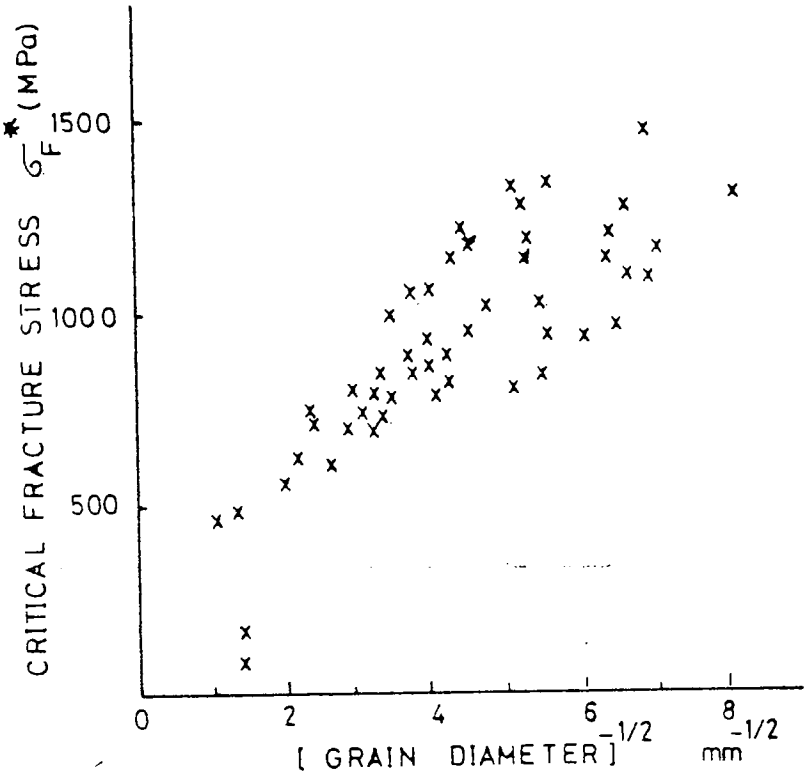

FIGURE 28: Variation of experimental values of σ_F^* with grain size. Data for mild steel (120)

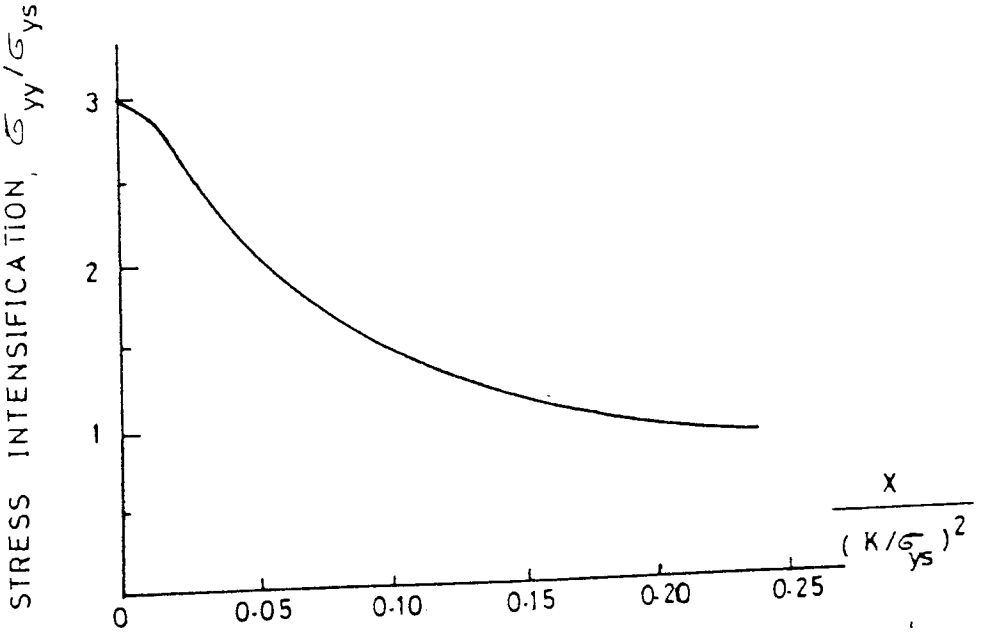

FIGURE 29; Distribution of tensile stress (σ_{yy}) acting directly ahead of a sharp crack in plane-strain for small scale yielding conditions (122)

4.2.3 Relationship between Critical Fracture Stress and Fracture Toughness

The elastic-plastic stress distribution analyses ahead of a sharp crack by Hutchinson [121], Rosengren and Rice [122], Rice and Tracey [123], made it possible to relate local criteria to macroscopic fracture behaviour. As mentioned earlier, the critical fracture stresses are determined from notched bend specimens. The stress distribution ahead of a loaded crack tip differs in two important ways from that in the notched bend bars (Fig. 29). First, the maximum tensile stress elevation is higher ahead of the crack tip. Secondly the maximum stresses vary rapidly with distance ahead of the crack tip whereas they are substantially constant over microstructurally significant distances below the notch root.

Dimensional considerations show that if fracture from a sharp crack is to occur at a critical stress intensity factor, then the attainment of a critical local tensile stress is not a sufficient criterion. It was postulated by Rice, Ritchie and Knott [124] that unstable fracture occurs when the maximum principal stress $(\sigma_{yy})_{max}$ ahead of the sharp crack tip equals or exceeds the critical tensile stress (σ_F^*) value over a micro-structurally significant size (a characteristic distance). Considering the position and magnitude of the stress intensification ahead of the sharp crack for failure, they concluded that the characteristic distance is a fixed distance and its magnitude is of the order of two-grain size, referring back to Smith's model [111]. They found good agreement between theoretical and experi-

mentally K_{IC} values for a high-nitrogen steel. It was also mentioned that this model is only applicable to materials which fail below general yielding since after general yielding unstable fracture is controlled by critical strain rather than critical stress. Thus, use of this model involves determining σ_F^* and employing a suitable characteristic distance representative of the micro-structure and fracture micro-mechanism involved. The characteristic distance has been generally found to be a small multiple of the grain size [125,126]. Ritchie et al [127], [128] recently used this model to explain quasi-cleavage and intergranular fracture of AISI 4340 steel and also for prediction of fracture toughness of neutron irradiated SA 533B.1 steel

Curry et al [129] discussed the characteristic distance and proposed a statistically based analysis of brittle fracture in quenched and tempered steels by considering the initiation of micro-cracks at carbide particles. The probability $P(f,r_o)$ of a cracked carbide particle being subjected to a sufficiently high-stress to cause fracture is estimated as

$$P(f,r_o) = SP(r_o)\, X^2\, n_A \qquad \text{.....(40)}$$

where $P(r_o)$ is the probability of the carbide particle having width r_o, X is the distance ahead of the crack tip over which a carbide particle of width r_o would cause fracture. n_A is the density of the carbide and S is the

shape factor. The critical fracture conditions are defined by summing $P(f,r_o)$ over all carbide widths and setting this sum equal to unity. The equation arranged to predict the fracture toughness K_{IC} is given as:

$$K_{IC} = M \sigma_y (n_A \cdot \varepsilon_{r_o})^{\frac{1}{4}} \quad \text{.....(41)}$$

where M : is a constant to allow for shape and orientation effect.

It has been shown recently by Curry [130] that the two models are dimensionally equivalent. A characteristic distance can always be found to represent the full statistical competition between different sized crack nuclei and it has to be determined empirically since no simple relationships exist between the fracture and observable micro-structural parameters.

Another approach which correlates the K_{IC} with critical tensile stress σ_F and micro-structural features was suggested by Tetelman et al [131]. They obtained a relationship which correlates the stress intensity factor for a notch of radius ρ

$$K_{IC_{(\rho)}} = 2.89 \sigma_{ys} \left[\exp((\sigma_F^*/\sigma_{ys}) - 1) - 1\right]^{\frac{1}{2}} \sqrt{\rho} \quad \text{...(42)}$$

It was observed that for a further decrease in notch root radius to below a critical value (ρ_o), the apparent toughness $K_{IC(\rho)}$ became equal to the K_{IC} value of the material, which is normally determined using a fatigue pre-

cracked specimen. It was concluded that the effective or limiting root radius (ρ_o) is a measure of the extent of the process zone ahead of the crack, over which critical stress must exist to cause failure. This limiting root radius is related to the micro-structural features which control the fracture. According to their suggestion (ρ_o) can be substituted for micro-structural parameters such as grain size, slip or twin band spacing, carbide spacing, etc.

V TOUGHNESS CHARACTERISTICS OF HIGH-Cr CAST IRONS

During the course of this work limited information was found concerning the fracture toughness characteristics of high-Cr cast irons or similar hard steels. This lack of information is mainly due to the difficulty of pre-cracking brittle materials in a controlled manner. It is generally accepted that during fatigue pre-cracking of brittle materials unstable crack propagation will occur immediately on crack initiation.

Extensive work was carried out by Durman [53]. His investigation was based on austenitic cast irons containing 15% Cr and different levels of carbon. According to his results the variation in carbon content can be shown to be a major factor influencing the fracture process. About 1.5% C level was found to be particularly important. It was concluded that the toughness of high-Cr cast irons with a carbon content above this value is controlled by the volume fraction of the continuous eutectic carbides and is insensitive to the matrix characteristics. In Durman's work, the grain size dependence of fracture toughness of high-Cr cast irons was also shown. An increase from 26 to 35 $K_{si}(in)^{\frac{1}{2}}$ was observed over the complete range of grain sizes representing sand castings in 6 in. section to chill casting in $\frac{1}{2}$ in. section (see Fig. 30). It was observed that after being hardened there is little variation in the toughness values over a wide range of carbon contents (see Fig. 31). It was concluded

that the following treatments have resulted in an improvement in the fracture toughness of low carbon alloys.

1. Reducing the volume fraction of eutectic carbides in austenitic alloys from the level at which a continuous carbide network is formed.

2. Decreasing the grain size of the alloys for a given carbon content

3. Increasing the tempering temperature of martensitic alloys

4. Annealing at high temperatures

5. Deformation of the as-cast structure

The purpose of the first work of Diesburg [132] was to show that the plane-strain fracture toughness test can be applied to determine the fracture toughness characteristics of white cast irons, rather than simply to study the toughness variation of white cast irons. According to his work the plane-strain fracture toughness test can be applied, but certain relaxations of the requirement which were outlined by ASTM-E399 are necessary for testing.

In his other works [133-135] a wide range of high-Cr cast irons were investigated. It was concluded that an increase in the carbon content reduces the toughness of both hardened and as-cast high-Cr cast irons. On the

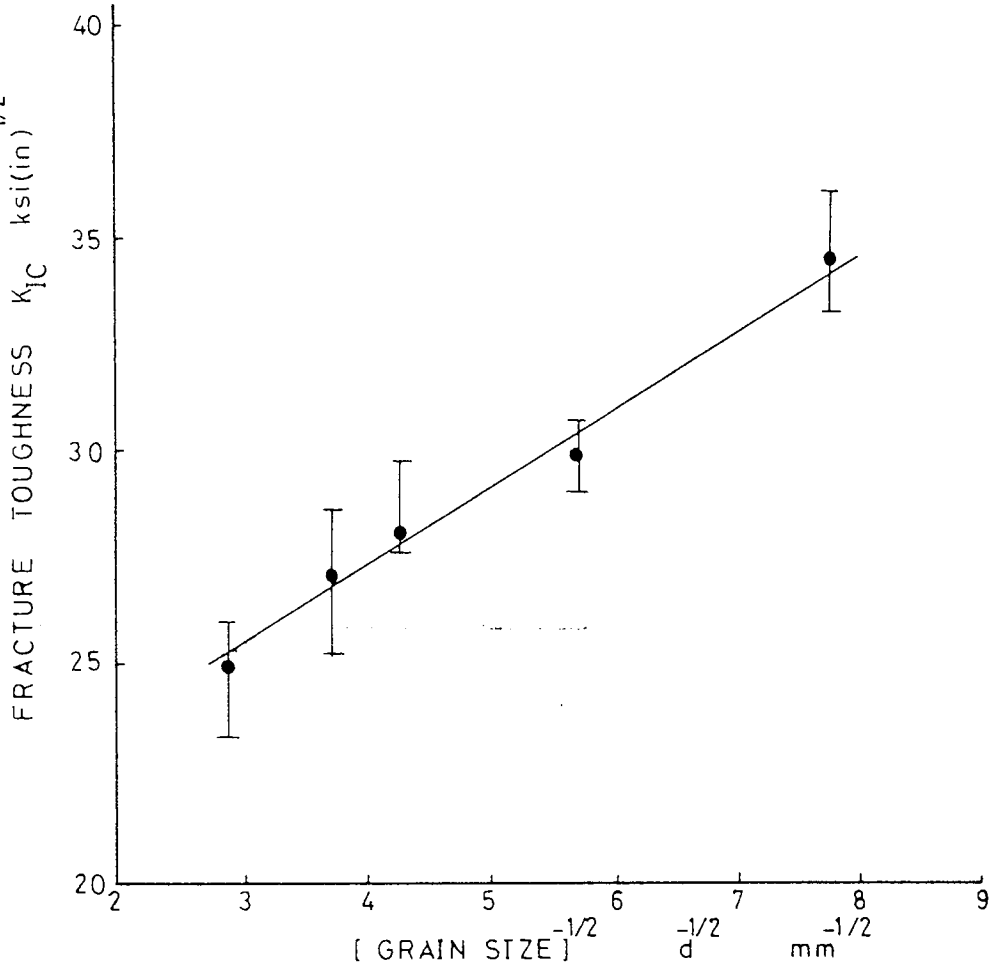

FIGURE 30: Grain size dependence of fracture toughness of high-Cr cast irons (53)

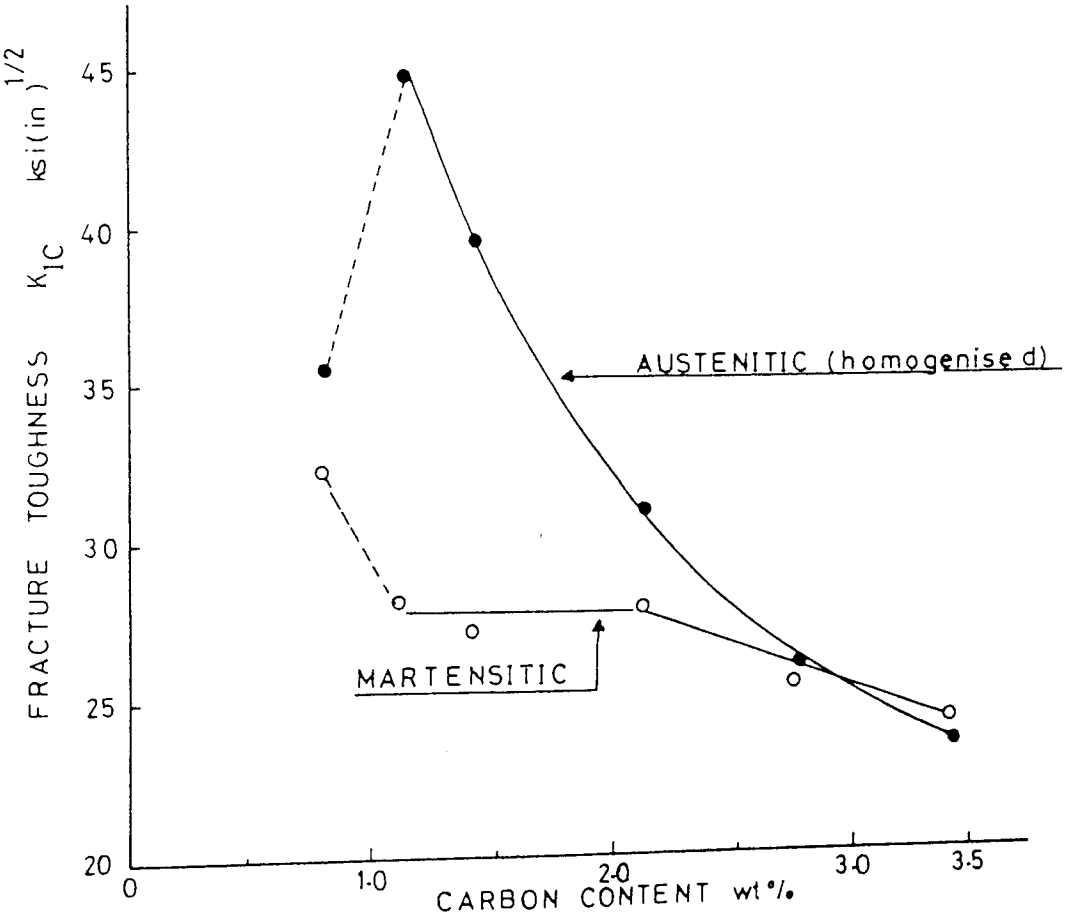

FIGURE 31: Fracture toughness variation of high-Cr cast irons with carbon content of the alloys (53)

other hand, hardening heat treatments improved only the compressive properties, which in turn resulted in increased resistance to rolling fatigue.

The variation of compressive properties of high-Cr cast iron (17.5% Cr, 1.5% Mo and 1% Cu) with carbon content of the alloys is given in Fig. 32.

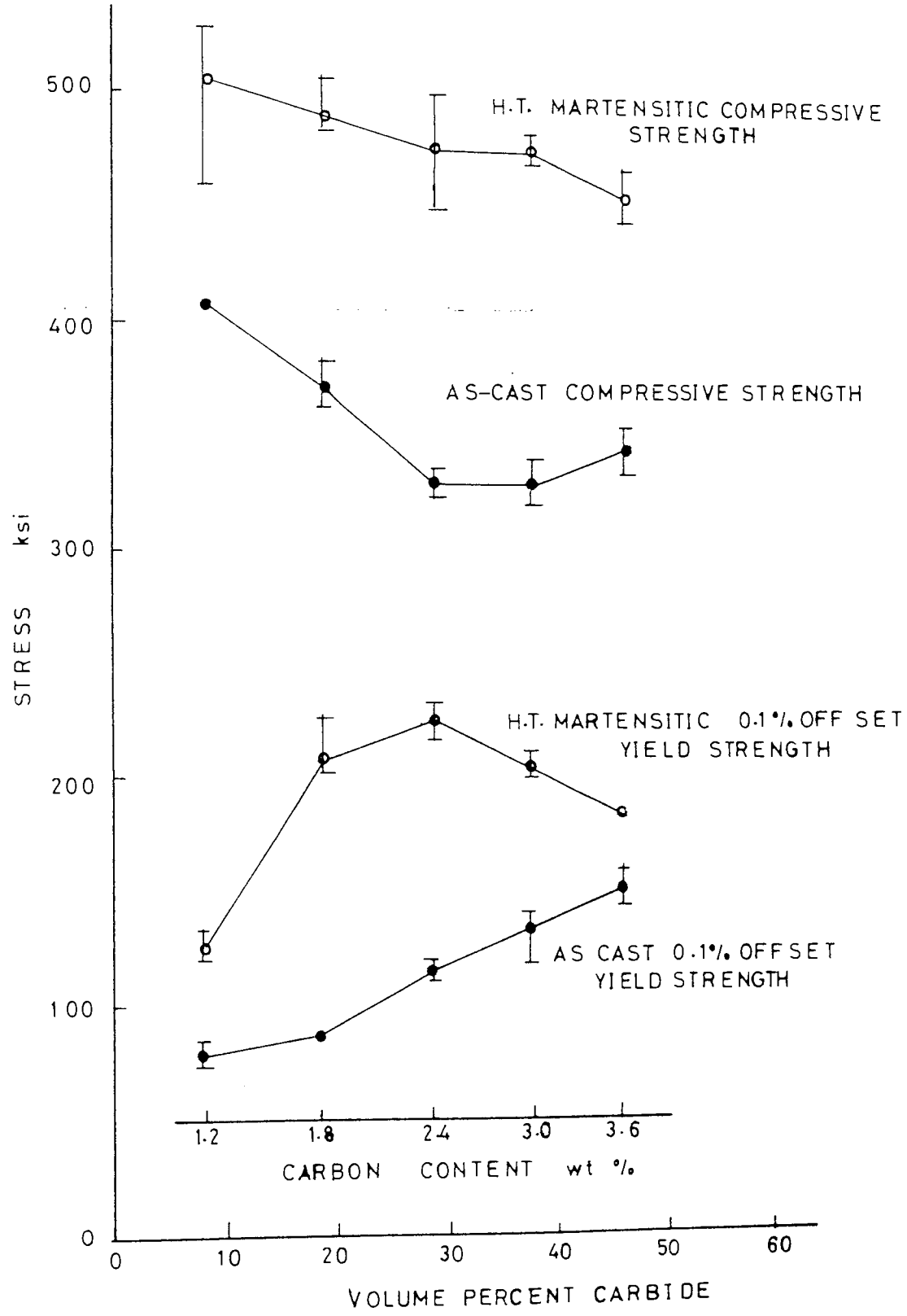

FIGURE 32: Variation of mechanical properties of high-Cr cast irons with carbon content of the alloys (135)

VI EXPERIMENTAL DESIGN AND PROCEDURES

6.1 Aim and Programme of the Project

The high-Cr cast irons comprise a micro-structure of very hard eutectic carbide particles (20-40% in volume) surrounding a matrix that is predominantly austenite or martensite following the heat treatments. Although these hard eutectic carbides improve the abrasive wear resistance, they are detrimental to the fracture toughness. Their low toughness properties quite often restrict the usage of these alloys for wide range of wear applications.

The aim of this research is to improve the toughness and other mechanical properties of the widely used 15% Cr and 3% C containing alloy. During the work it was believed that the fracture toughness values could be improved by altering the distribution shape and size of the eutectic carbides within the micro-structure, without sacrifice to hardness or abrasive wear resistance. Also particular attention was paid to reaching the desired properties in a way which could be applied easily in industrial practise.

Due to the nature of the alloys expensive and time-consuming machining techniques were inevitable. Therefore before starting any mechanical testing, the metallurgical condition (i.e. composition, heat treatment procedures) which give the desired micro-structural variations were pre-determined. Thus, the studies were directed to establishing the effects of possible variables. Four

different levels of vanadium, manganese, molybdenum and tungsten additions were made singly to a 15% Cr and 3% C containing base alloy. The melts were prepared in the 10 lb. laboratory arc-furnace, then the programmed high temperature heat treatments were applied and extensively studied by means of metallographic techniques.

After considering the results obtained from these metallographic studies the fracture toughness testing programme was designed to evaluate the effects of these metallurgical variables on the fracture toughness values and hence optimum conditions. It was also hoped to establish the possible interrelationship between the micro-structure and fracture toughness of the high-Cr cast irons. For this purpose the notch bend tests were undertaken for the selected micro-structure and the toughness values. The test data obtained were processed using the slip-line theory and the results were used in conjunction with the data obtained from the metallographic studies for better understanding the failure mechanism of the alloys.

During the course of work extensive studies were carried out to seek the adaptation of the new fracture toughness testing techniques in order to measure this property in a cheap and quick way and to use this technique not only for research and development purposes but also for routine quality control checks in the production of these alloys. For this purpose compliance studies were undertaken

experimentally and analytically to evaluate the stress intensity coefficients of different geometries of the short-bar fracture toughness test specimens. The fracture toughness results obtained were compared and correlated with the results from standard testing technique.

6.2 Experimental Procedures

6.2.1 Material Preparation

The alloys used during the first metallographic studies were melted in 10 lb. laboratory arc-furnace and bars $\frac{3}{4}$ inch in diameter and 7 inches in length were cast in green sand moulds. The composition of the alloys is listed in table 4.

For fracture toughness tests plates 18 x 45 x 180 mm and bars 20 x 15 x 300 mm were cast in green sand moulds. The composition of these alloys is given in table 5 and were melted in a 50 kg industrial induction furnace. The melts were prepared from commercial grade pig irons, high-quality steel scrap and ferro-alloys.

A swirl gate was incorporated into the running system to eliminate slag from the top surface of the castings and sufficient riser and feeder systems were attached to the moulds of the pair of plates and bars, to avoid possible shrinkage and gas porosity defects in the castings. Pouring temperature was controlled in the hand ladle and kept at about 1450^{o}C for all castings. The castings were

allowed to cool to room temperature in the moulds in order to avoid any residual stress and hot-cracks. The feeder and runner systems were then removed by knock-out or cutting by abrasive wear wheels. The quality of castings were examined by x-ray radiography.

6.2.2 Heat Treatments

All the heat treatments were carried out in a Scott-Vatt vacuum furnace. Heat was applied when the value of the vacuum reached 10^{-4} Torr in the furnace. Due to the small capacity of the furnace it was only possible to charge four fracture toughness specimens at a time, therefore care was taken to keep the heat treatment conditions identical for the other specimens in the same batch throughout the work.

The high temperature heat treatments were carried out at 1180^{o}C. This temperature was reached in three hours heating period followed by the soaking periods, then samples were quenched to room temperature by blowing argon gas into the furnace. The typical cooling rate obtained from this temperature is given in Fig. 33.

The all-hardening heat treatments were carried out in the previously mentioned furnace using an austenitising temperature of 975^{o}C and argon quenching to room temperature. The hardened specimens were tempered in an air-circulated furnace at 250^{o}C for two hours followed by air cooling.

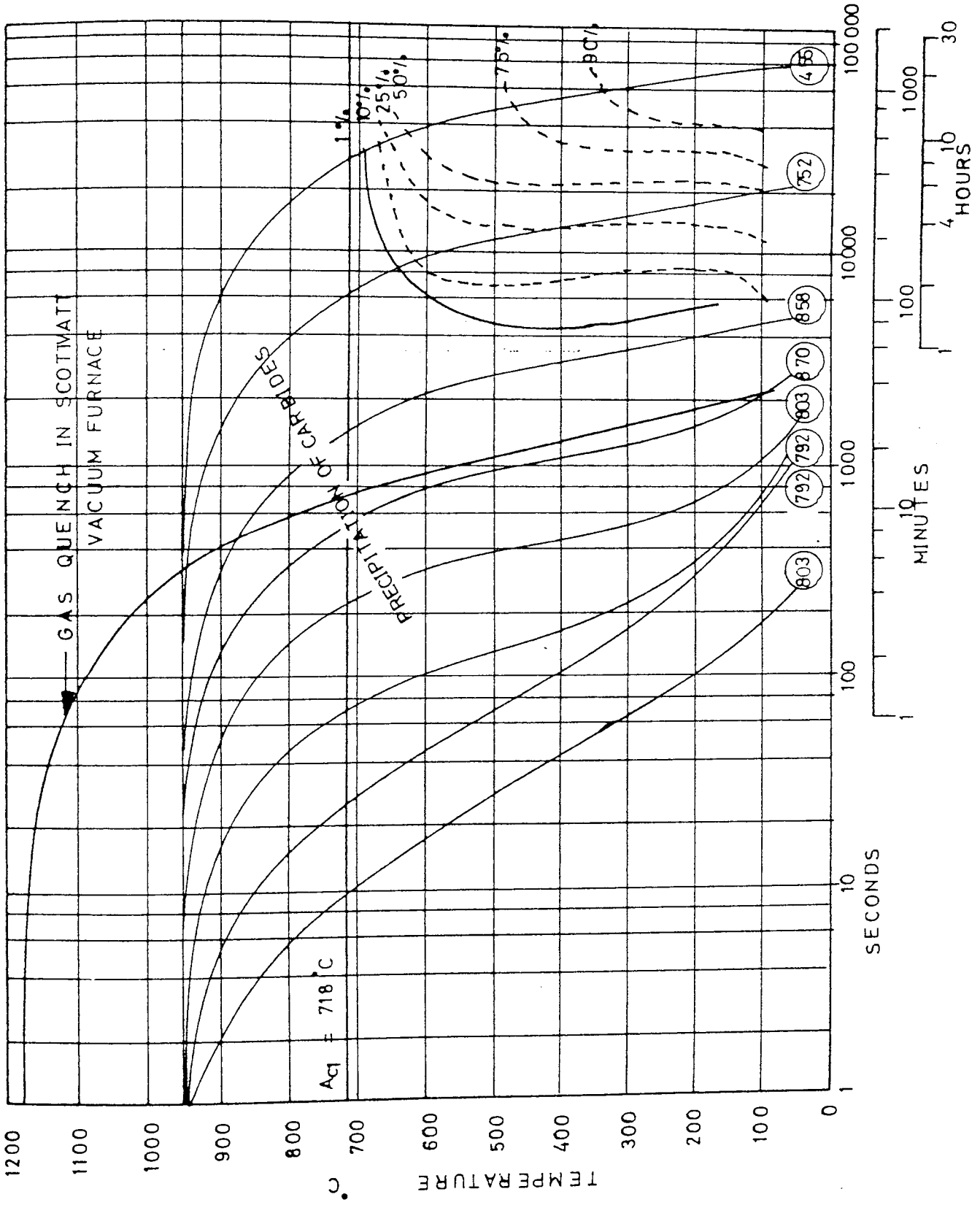

FIGURE 33: Cooling curve of the specimens from 1180°C Superimposed on the continuous cooling transformation diagram for the 15%Cr-2%Mo and 3.3%C containing high-Cr cast iron. (Austenised at 955°C for 20 minutes)

The numbers in circles give the Vickers hardness [49].

6.2.3 Fracture Toughness Testing

6.2.3.1 Specimen Details and Preparation

Three point bend test pieces, the dimensions and notch configuration of which are given in Fig. 34, were used for fracture toughness tests. The samples were obtained from the cast plates or bars by grinding, this being the only means of shaping. The notches were either machined by grinding with abrasive wheels which were the same shape as the notch or by using an erosion discharge machine with copper former electrodes which have the same dimensions as the notch. The machined sample surfaces were polished to 6 micron diamond paste to eliminate the marks which were left during the grinding process. After the notch five lines (1 mm away from each other) were marked on the polished side surface of the samples in order to follow growing cracks with the aid of low magnification binoculars during the fatigue pre-cracking.

6.2.3.2 Fatigue Pre-cracking

Fatigue pre-cracking was carried out on a 50 KN capacity hydraulic fatigue machine at frequency 30 Hz or on a 20 KN capacity Amsler vibrophore fatigue machine at frequency about 80-90 Hz. The specimens were tested in three point bending with support span four times of the width. Fatigue crack initiation and crack growth were detected using the electrical potential method. A D.C. current of 20 amps was passed along the specimen and the potential differance over a fixed gauge length close to the notch was measured using 0.15 mm diameter Nichrome wires which were spot

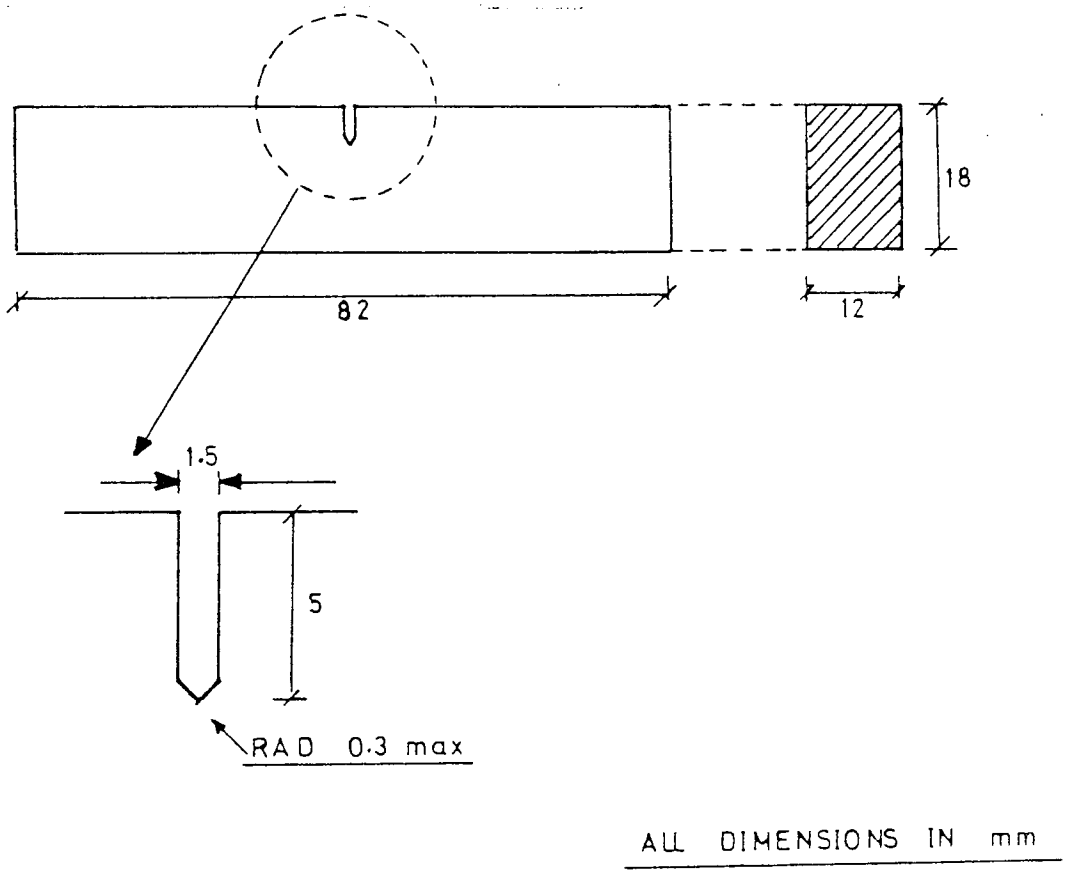

FIGURE 34: Dimensions and notch detail of three-point bend fracture toughness specimens

welded diagonally to the corners of the notch on the top surface of the specimen. By backing off the major proportion of the resultant potential between the two probes the micro-potential was measured and recorded against the time by using a chart recorder. The chart recorder was set up to give a 50 micro-volt full scale deflection and the speed of the chart was adjusted depending on the crack growth rate, in order to obtain reasonable micro-volts versus number of cycles recorded.

According to the recommendation laid down in ASTM-E399 the final portion of the fatigue crack should be grown more than 50.000 cycles to ensure that a sharp-crack tip is introduced. Also $K_{F(max)}$ (maximum stress intensity factor during the fatigue pre-cracking) should not exceed 70% of K_Q value. Therefore the fatigue-cracks were grown in two stages; after the notch about 2.5 mm crack in length was grown at higher loads, then the loads were reduced for the final portion (about 1.5 mm) in accordance with the standards. The final K_F values of tests are given in the results section and the final portions of the cracks were grown between 150.000 and 350.000 cycles.

6.2.3.3 Testing

The fracture tests of the pre-cracked specimens were carried out on 5 ton capacity Instron testing machine at a constant cross head displacement rate of 0.1 mm/minute. The three point bend rig was used, span length four times that of the width and specimens were supported on free rollers. In order to measure the load-load point displacement (L-L.P.D.) a transducer was mounted on the top ram as

developed by Barnby and Daimalani [136].

Before starting any test, recorders and equipment were warmed up for at least one hour, then the load cell of the equipment and the recorders were calibrated. It was necessary to calibrate the clip gauge and transducer so as to find the magnification given by each and to find out at which portion they were linear. The clip gauge was directly calibrated with a point micrometer and transducer was calibrated with the help of strain gauge. Each time two knife edges were attached to the specimen at the correct distance (in the linear portion of the clip gauge) with the help of a mild steel gauge. Crack initiation was determined by the electrical potential method and 20 amps D.C. current was applied to the ends of the specimen.

During the test in order to obtain the following graphs four recorders were used.

1. Load vs. clip-gauge opening displacement (x-y recorder)
2. Load vs. load point displacement (x-y recorder)
3. Load vs. time (chart recorder)
4. Potential drop vs. time (chart recorder)

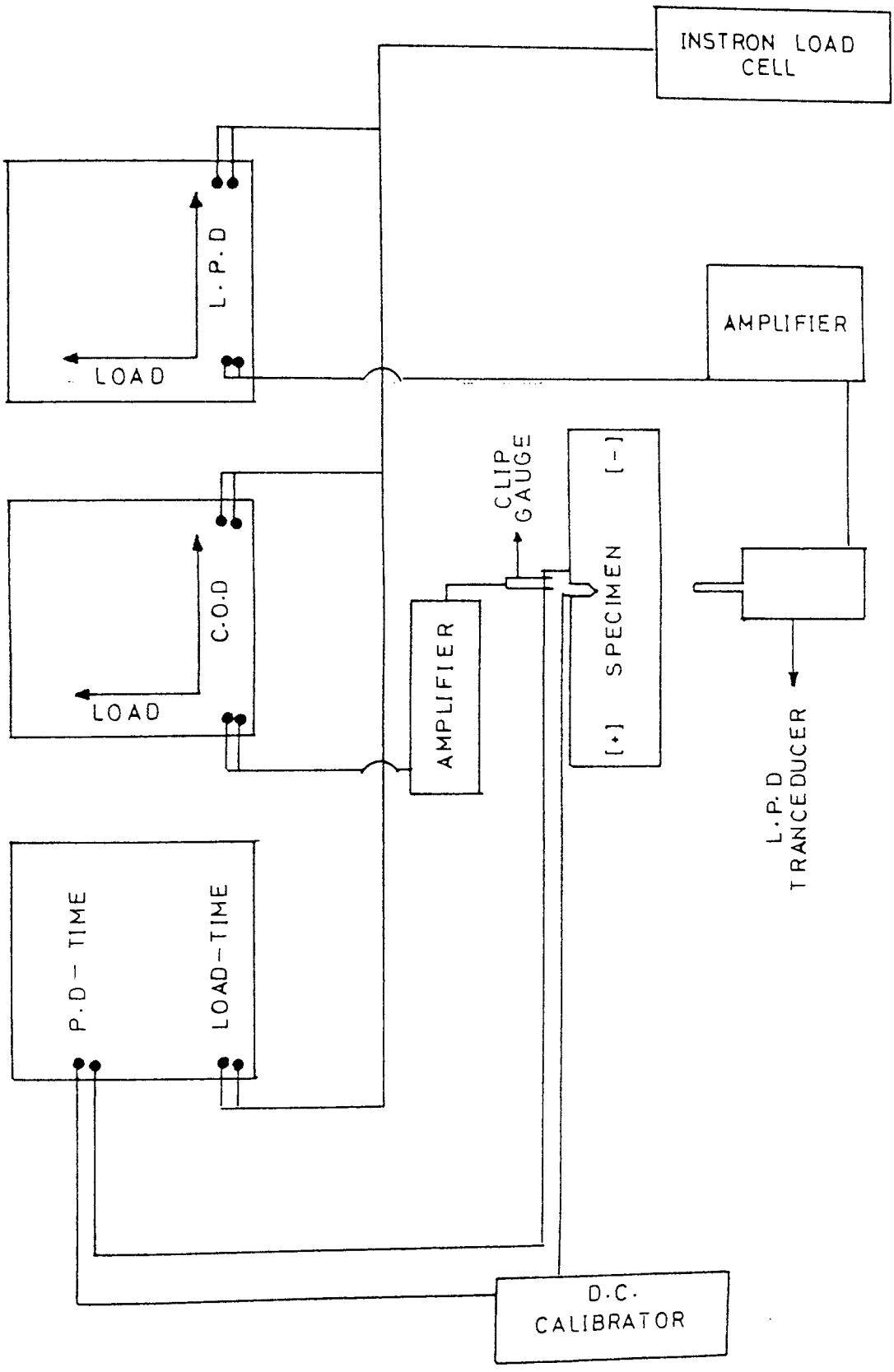

FIGURE 35: Schematic instrumentation diagram for fracture toughness testing

6.2.4 Non-Standard Short-Bar Fracture Toughness Testing

6.2.4.1 Compliance Measurements

Compliance measurements were made for three different configurations of short-bar fracture toughness specimen. Dimensions of each type are shown in Fig. 36. Ideally the material used for compliance measurements should be homogeneous isotropic and have a wide range of linear elastic behaviour. The experimental determination of compliance is made by extending a slot (representing the crack) in the specimen by a small increament and for each slot length measuring the displacement for per unit of applied load.

The compliance specimens were manufactured from perspex after polishing the surfaces of the specimen to 6 micron diamond grade, the specimens became completely transparant and this enabled direct viewing of the chevron slot (see plate 1). The slot representing the crack was extended using fine tooth jewellery saw giving a slot width less than 0.25 mm width and its length was determined from the specimen surface using a travelling microscope with $\pm$ 0.05 mm accuracy.

The specimens were pulled in tension with the help of a pair of grips, using a 5 ton capacity Instron tensile testing machine. Before commencing any test the 10 kg load cell, the x-y plotter and the clip-gauge amplifier were stabilised for at least one hour then the load cell and plotter were calibrated. Specimens were loaded up to 3 kg load with 0.1 mm/min constant cross-head displacement. For each increase in crack lengths the displacements were monitored directly from the

FIGURE 36: Dimensions of short-bar compliance test specimens

TYPE I

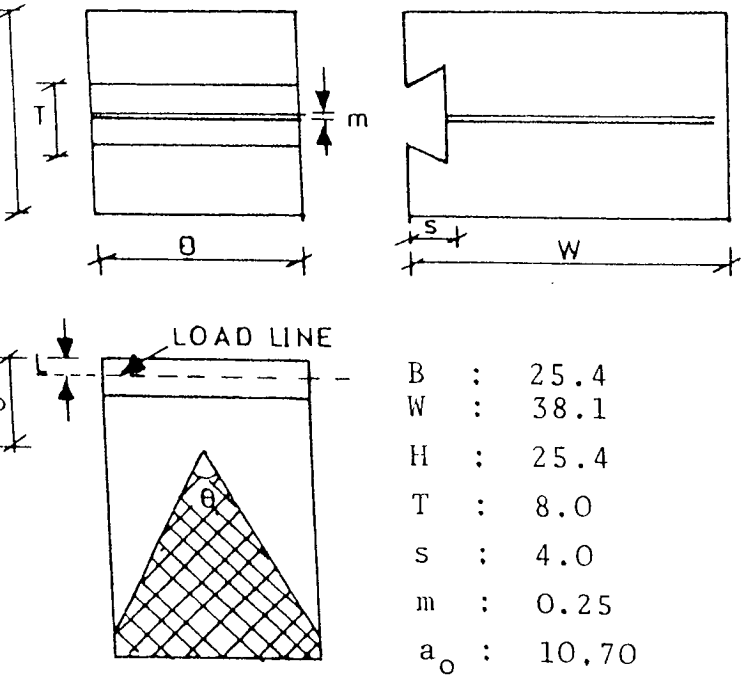

B	:	25.4
W	:	38.1
H	:	25.4
T	:	8.0
s	:	4.0
m	:	0.25
a_o	:	10.70
L	:	1.75
θ	:	58.0°

TYPE II

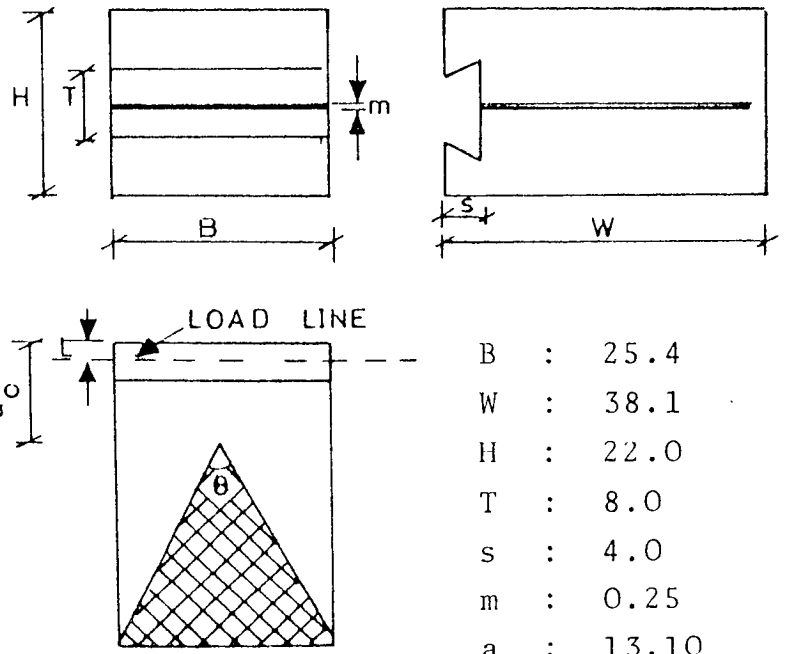

B	:	25.4
W	:	38.1
H	:	22.0
T	:	8.0
s	:	4.0
m	:	0.25
a_o	:	13.10
L	:	1.75
θ	:	55.0°

TYPE III

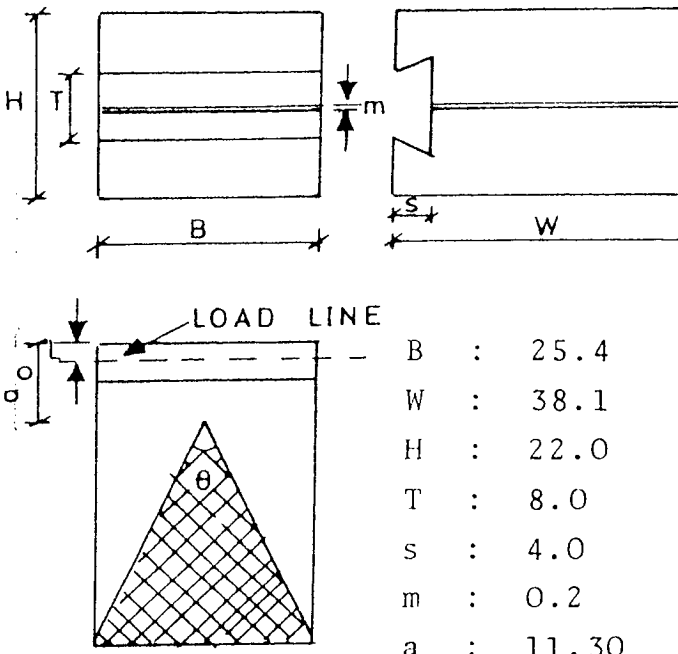

B	:	25.4
W	:	38.1
H	:	22.0
T	:	8.0
s	:	4.0
m	:	0.2
a_o	:	11.30
L	:	1.75
θ	:	52.0°

ALL DIMENSIONS IN mm

(not scale)

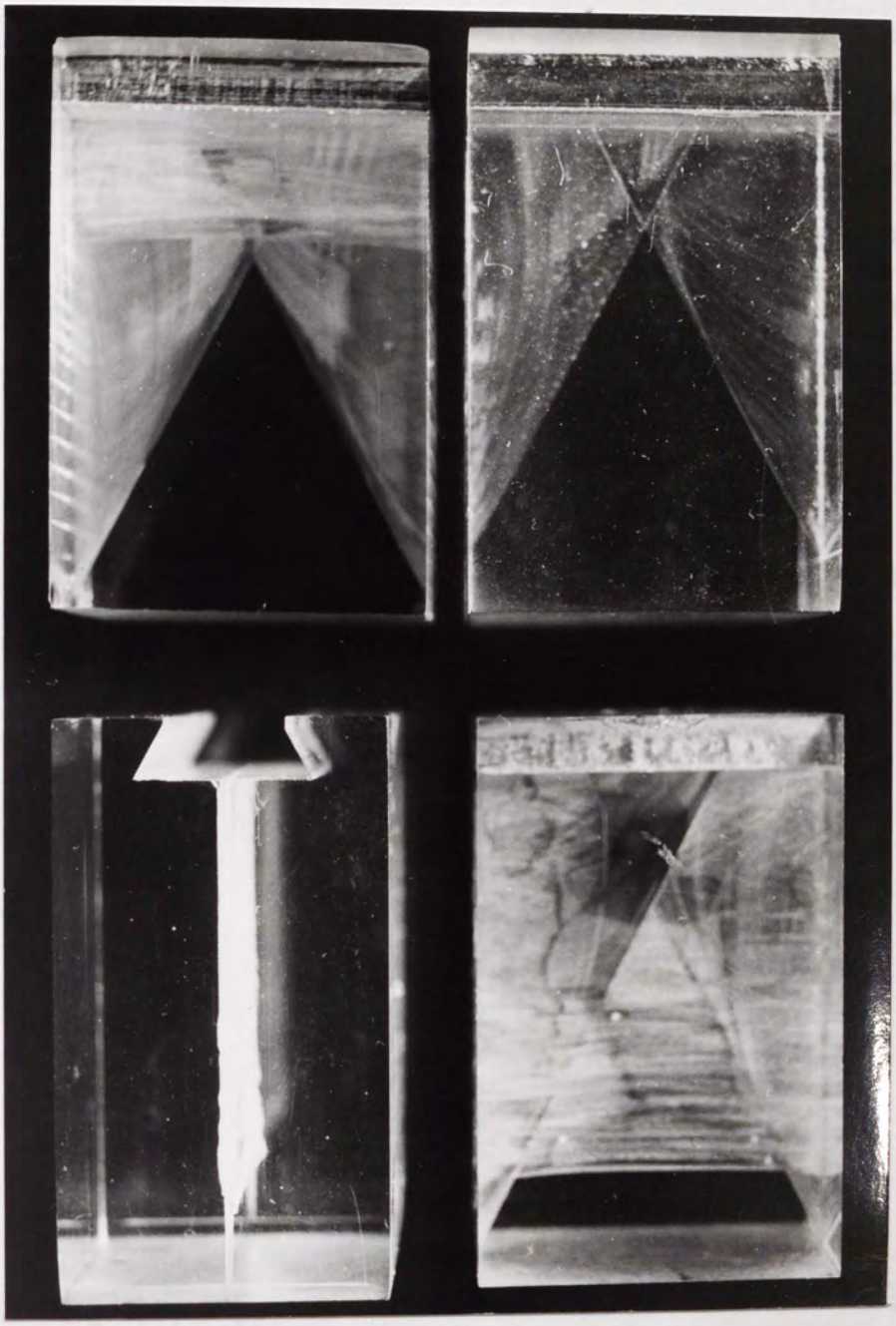

PLATE 1: General appearance of short-bar compliance test specimens

specimen using a calibrated clip-gauge which was attached to the specimen very close to the loading line with the help of two knife edges.

For each crack length average displacement measurements taken from loading and unloading curves were repeated five times for each crack length and tests were at least duplicated on different specimens of that type. All dimensions of the specimen and crack length were normalised to the loading line and Young's modulus for perspex was taken as $E = 2480\ N/mm^2$.

The obtained experimental results were reported as non-dimensional C.E.B. and a/W values in tables 26-28, where:

$$C = d\delta/dP$$

δ : elastic mouth opening displacement

P : load

E : Young's modulus

B : specimen width

a : crack length from loading line

W : specimen length from loading line

6.2.4.2 Determination of Fracture Toughness by Short-Bar Specimens

6.2.4.2.1 Specimen Design and Preparation

Short-bar specimens dimensions and chevron notch configurations of which are given in Fig. 37 were used for fracture toughness tests. The 12 x 12 x 18 mm square sectioned short-bar specimens were obtained from broken halves of the previously tested three point bend fracture toughness test specimens.

FIGURE 37: Dimensions of short-bar fracture toughness test specimens

TYPE I

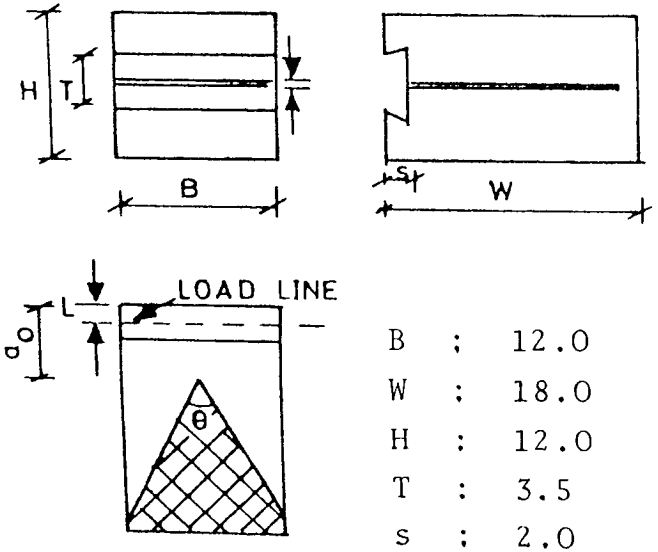

B	:	12.0
W	:	18.0
H	:	12.0
T	:	3.5
s	:	2.0
m	:	0.25
a_o	:	5.40
L	:	0.75
θ	:	58.0

TYPE II

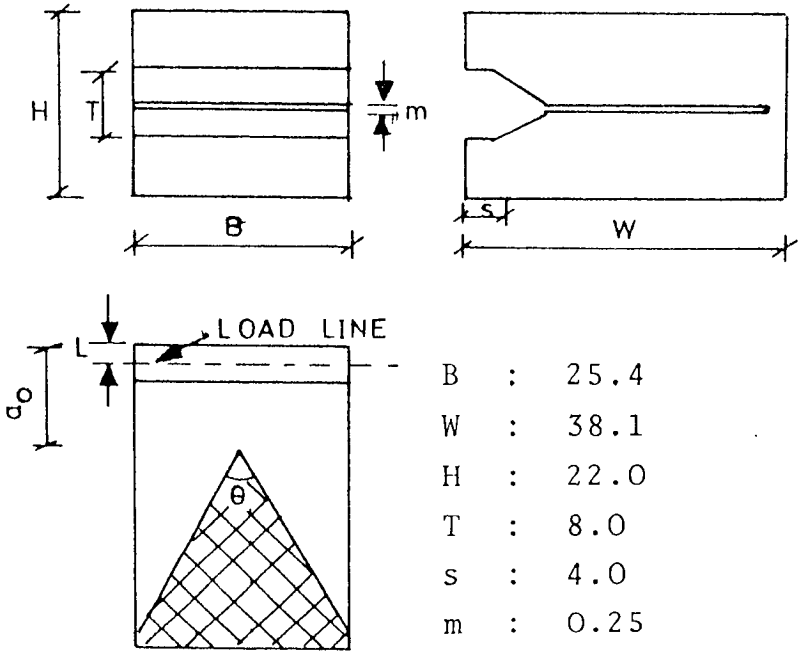

B	:	25.4
W	:	38.1
H	:	22.0
T	:	8.0
s	:	4.0
m	:	0.25
a_o	:	13.10
L	:	1.75
θ	:	55.0°

TYPE III

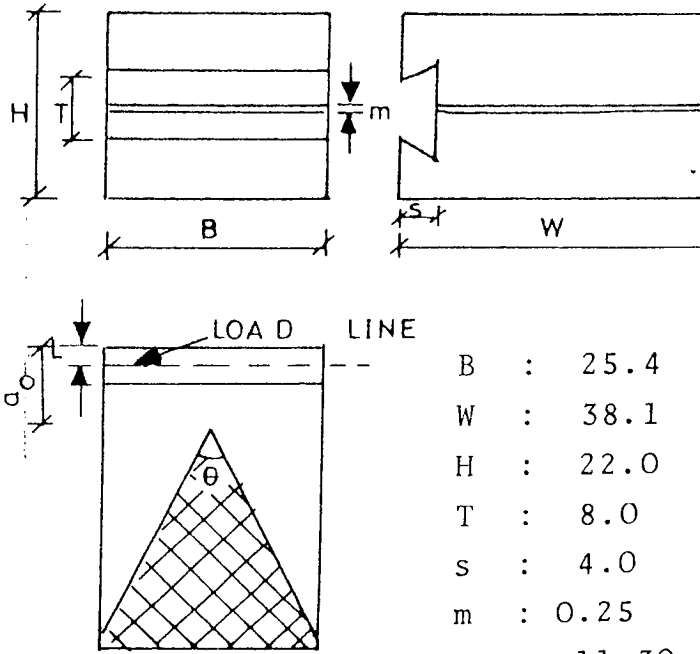

B	:	25.4
W	:	38.1
H	:	22.0
T	:	8.0
s	:	4.0
m	:	0.25
a_o	:	11.30
L	:	1.75
θ	:	52.0

ALL DIMENSIONS IN mm

(not scale)

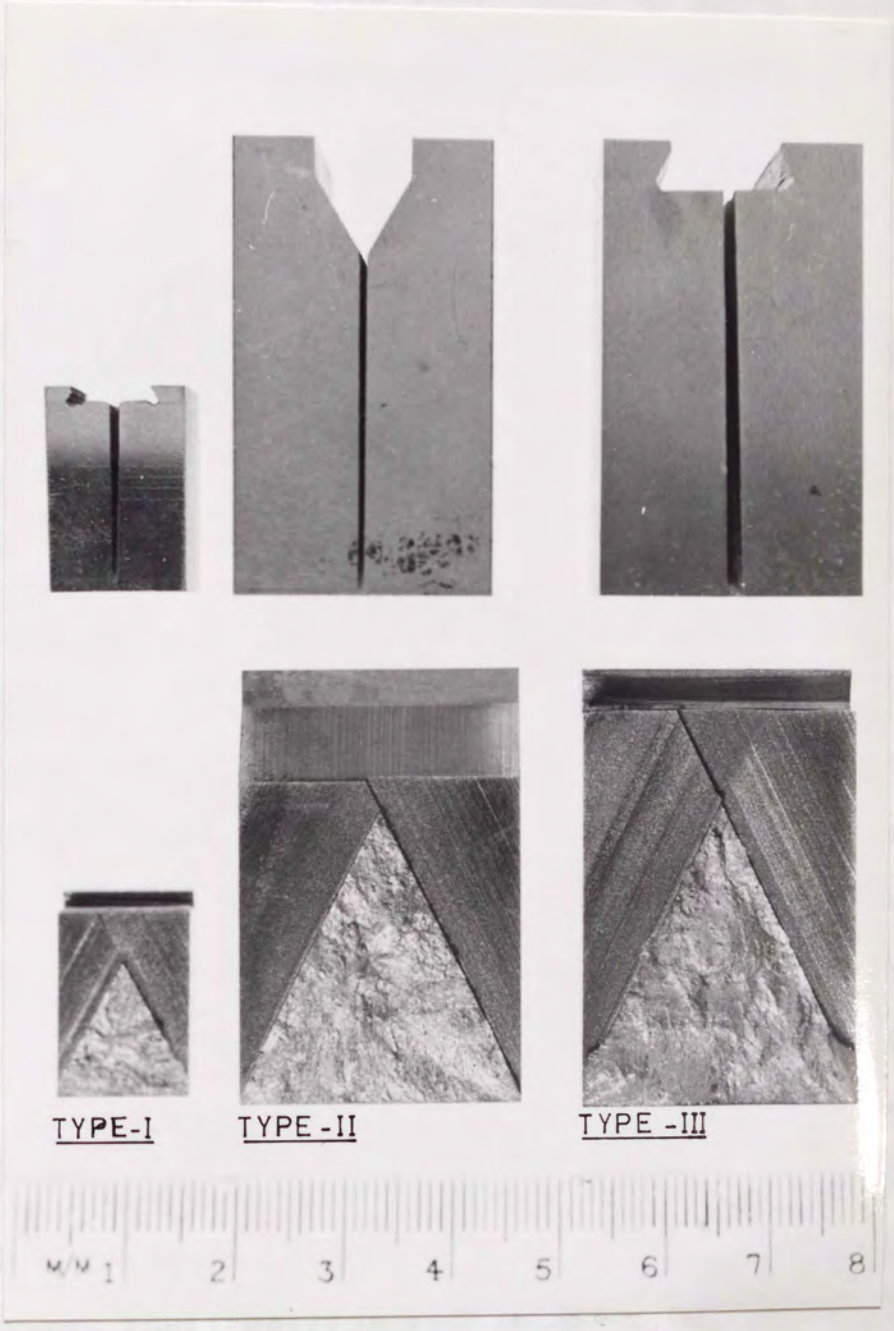

PLATE2: General appearance of short-bar fracture toughness test specimens and chevron notch detail

The rectangular sectioned short-bar specimens were cut from broken halves of the 26 x 45 x 200 mm thick three point bend fracture test specimens. All outer dimensions of the specimens were obtained by grinding process. The chevron notches and grip slots were machined by using a wire cutter device on an electrical discharge machine. Rigs were designed for holding the samples to obtain the required angle cuts.

In order to avoid any question which may arise from directionality the chevron notches in the short-bar fracture specimens were machined in the same direction as the notches in the three-point bending fracture toughness test specimens.

6.2.4.2.2 Testing

The short-bar specimens were pulled in tension using a 5 ton capacity Instron tensile testing machine with the same speed used during the three point bending fracture tests. The load versus mouth opening displacement records were obtained from a calibrated clip-gauge which was attached to maraging steel grips. Of these three rectangular specimens were pulled by using a Fractometer II which is designed and patented by Terra-Tek Inc. for fracture toughness measurements from short-bar/rod specimens.

Before commencing any test the machines and the x-y plotter were stablised and then calibrated. The tests using the Fractometer II were carried out following the instructions provided with the machine.

6.2.5 Slow Notch Bending Tests

6.2.5.1 Specimen Design and Preparation

The 9.5 x 9.5 x 55 mm square sectioned specimens were shaped by grinding from cast bars after the application of the heat treatments. The notches with 45 degree included angle with 2 mm constant depth and varying root radii were machined with abrasive wheels which were of the same shape as the notches. Particular attention was paid to avoiding grinding cracks at the bottom of the notches and this was achieved by taking very small cuts at each pass and using a stream of coolant. The side surfaces of the machined samples were polished to 6 micron grade diamond paste to eliminate the marks which were left during the grinding process. The notch depth and root radii were measured using a shadow-graph. Tracings were obtained from this instrument at x 100 magnification and were then compared with standard root radii circles.

6.2.5.2 Testing

The specimens were loaded at constant 0.1 mm/minute cross-head displacement in three point bending without any fatigue pre-cracking. The span width ratio was 4:1 and specimens were supported on free rollers. Load-load point displacements were monitored with a transducer which was attached to the top ram and records were obtained using a x-y plotter.

At the initial tests the potential drop technique was used to determine the crack initiation load with similar setting-up procedure, as described in section 6.2.3.3. During the

test the reference potential would increase when the crack initiated since initiation of the cracks occurred spontaneously at the attainment of the maximum load (see Fig. 44) this method was omitted and the only load-load point displacement records were required as test data.

6.2.6 Mechanical Testing

6.2.6.1 Determination of Tensile Properties

Several No. 11 Hounsfield tensile testing samples were machined from the broken halves of the three-point bend fracture toughness specimens and pulled using Instron tensile testing machine. Invalid results were always obtained since all the samples were broken from the shoulders where the grips held the specimens. In order to obtain meaningful results, related to the yielding properties of the selected alloys, cylindrical test pieces 4.5 mm in diameter and about 9 mm in length were prepared and 0.02% yield stress was evaluated from stress versus strain curves of the comparison tests of these cylindrical test pieces. In order to avoid any sinking of the samples into the top and bottom rigs, hardened steel plates were used. No attempt was made to determine the ultimate tensile stresses or reduction in area and in length since these were expected to be inaccurate from comparison tests.

6.2.6.2 Hardness Measurements

Vickers hardness (Hv) measurements were taken on the polished surfaces of the fracture toughness specimens, under the 30 kg load. The values given are an average of at least eight readings.

6.2.7 Metallographic Studies

6.2.7.1 Micro-Probe Studies

The composition of the carbides and matrix phases of the alloys were determined using a Cambridge micro-probe analyser. A (PET) crystal spectrometer was used for $CrK\alpha_1$, $MoL\alpha_1$, $VK\alpha_1$ and $WK\alpha_1$ readings and a (LiF) crystal spectrometer was used for $FeK\alpha_1$ and $MnK\alpha_1$ readings. All examinations were carried out with an operational potential of 15 Kv. The counting time for all measurements was 10 seconds. Quantitative analyses were made by the standard procedure, to correct the atomic number effects, x-ray absorbtion and secondary fluorescence corrections were made with a package computer programme. The carbon content of the carbide phases was determined by subtracting the sum of the measured alloy contents from one hundred.

6.2.7.2 Metallographic Examinations

Normal metallographic techniques were used extensively. The etchant found to be most successful on the alloys studied was Picrāl, a saturated solution of picric acid in alcohol acidified with 4% hydrochloric acid. This solution stains austenite a light yellow colour, martensite brown and leaves carbides and ferrite unattacked.

Although several etchants and etching techniques were applied, difficulty was always experienced obtaining a good contrast between the carbides and the matrix phase. Therefore quantitative metallographic studies could not be carried out using the quantitative electron-microscope available. Micro-structural parameters were determined with an optical

microscope by using the linear intercept method. The studies were carried out at a magnification of x 1000 in 50 fields and two planes of the selected samples. The magnification of the microscope was always checked before commencing any study with the help of a graticule. The parameters were obtained from these studies as:

Volume % of eutectic carbides : $V = L_c/L$

Mean Free path between the eutectic carbides : $L_o = \left[(1-V)/Nc\right] * L$

Mean size of the carbides : $C_o = \left[V/Nc\right] * L$

Density of the carbides : Nc

where:

L : Total length of the unit length random test lines.

L_c : Total length of the unit length random test lines intercepted by carbide particles

Nc : The number of carbides intercepted by total unit length of random test lines

VII DATA ANALYSES

7.1 Determination of K_{IC} Values from Load-Crack Opening Displacement Records

It was impossible to distinguish the fatigue crack tip from the fast fracture surface except for martensitic high-Cr cast irons. During the construction of potential drop calibration curve on the heat-tinted samples, the crack fronts were found to be straight lines, (see plate 3), therefore fatigue crack lengths including the notch were measured from the polished side surfaces of the samples. The average of two readingswas taken as the crack length of the samples. The measurements of the crack lengths were performed with a light microscope within the error $\pm$ 0.05 mm before commencing the fracture tests.

A typical load-crack opening displacement graph is presented in Fig. 38. The examination of the curves did not show any distinct pop-in behaviour. It was necessary to construct the 5% offset line to determine the critical load PQ. After determining the P_Q values with this method from given equation below the K_Q values (the provisional value of K_{IC}) were obtained.

$$K_Q = \frac{6 * Y * P_Q * \sqrt{a}}{B * W} \qquad \text{.....(44)}$$

where P_Q : critical load

B : Breadth of the specimen

W : Width of the specimen

a : crack length including the notch

Y : Stress intensity coefficient and may be given for 4:1 span length as below

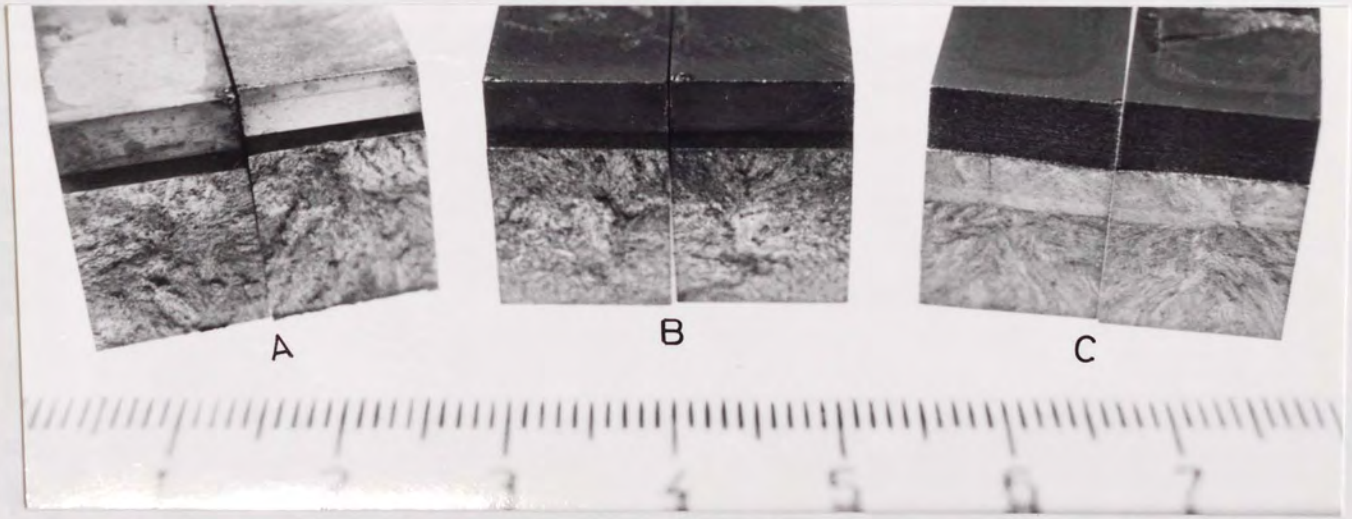

PLATE 3: General appearance of three point bend specimens

A - austenitic

B - austenitic heat tinted at 550^{o}C

C - martensitic

Note: Appearance of the fatigue-crack tip in austenitic samples

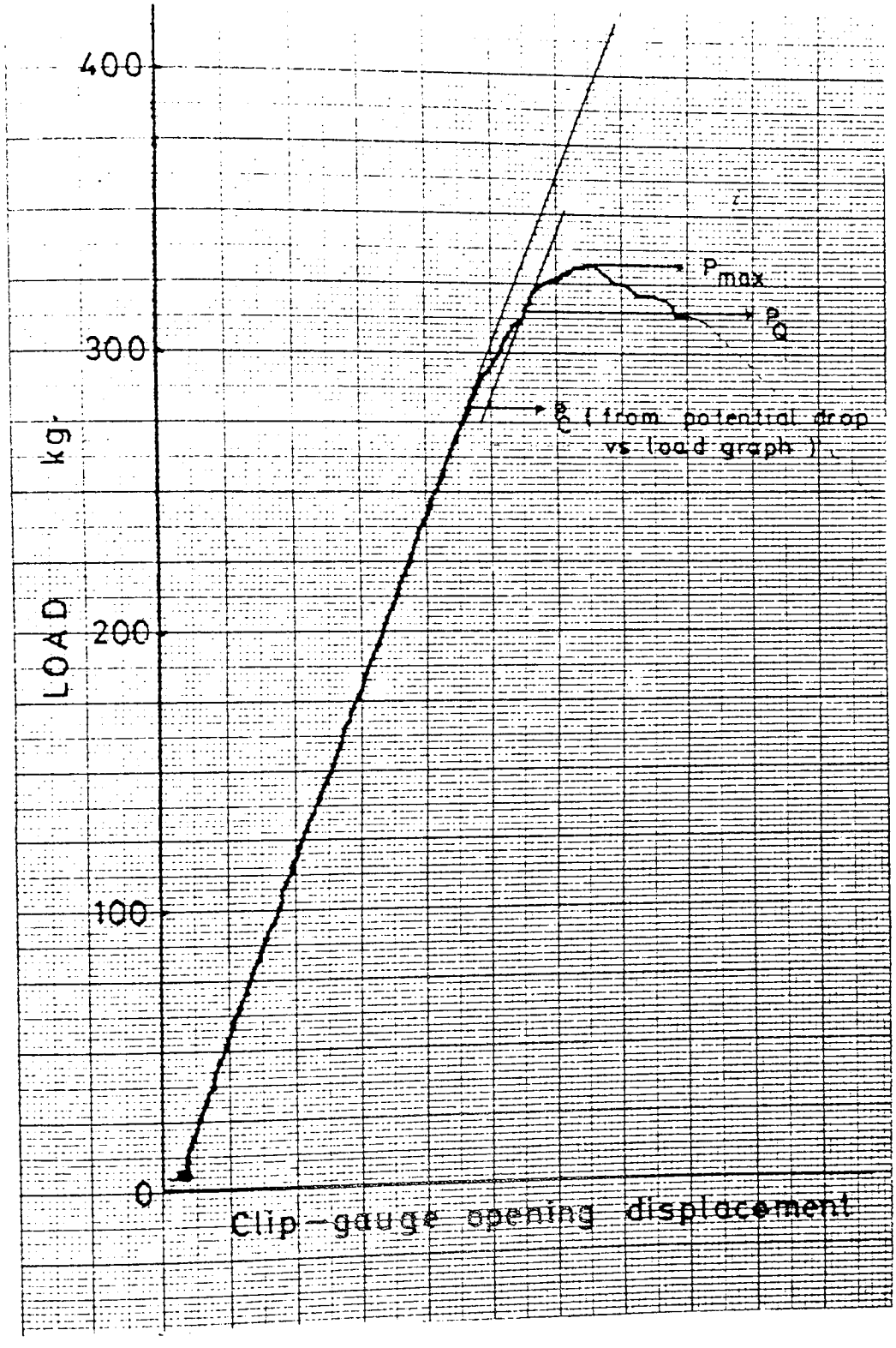

FIGURE 38: Typical load vs clip-gauge opening displacement record obtained from three-point fracture toughness tests

$$Y = \frac{[1.99-2.15(a/W)+6.08(a/W)^2-6.63(a/W)^3+2.7(a/W)^4]}{[(1.0*2(a/W)) \cdot (1.0-(a/W))^{3}/2]} \quad \ldots\ldots\ldots(45)$$

The maximum fatigue stress intensity (K_F) was calculated from equation (44) except that the final fatigue load P_F was substituted for P_Q values. Four criteria were put forward to check the validity of the K_Q values as K_{IC} values, these are:

1. P_{max}/P_Q ratio must not exceed 1.10

2. Limiting thickness criteria which is
$$B > 2.5 \left(\frac{K_{IC}}{\sigma_{ys}}\right)^2$$

3. The departure from linearity at 80% P_Q must be less than 25% of that P_Q

4. The ratio of K_Q/K_F must not exceed 70% K_Q

After all these requirements of validity criteria were met the K_Q values were reported as valid K_{IC} values.

7.2 Determination of J-Integral Values from Single Load-Load Point Displacement Records

An experimental method for determining the value of J has been presented by Begley and Landles [88]. Although their procedure gives accurate results, several specimens are required in order to obtain the value of J, as J_{IC}. Rice, Paris and Murkle [137] have suggested a method of estimating J_{IC} from single L-L.P.D. records; according to their work the strain energy of cracked specimen may be given by:

$$U_{TOTAL} = U_{NO\ CRACK} + U_{CRACK} \quad \ldots\ldots\ldots(46)$$

This may also be written as:

$$\delta_{TOTAL} = \delta_{NO\ CRACK} + \delta_{CRACK} \quad \ldots\ldots\ldots(47)$$

According to Rice et al the relationship between J and the uncracked ligament length, for the case of three point bending, may be given for unit thickness by:

$$J = \left(\frac{2}{W-a}\right) \int_{o}^{\delta_{CRACK}} P.d\delta_{CRACK} \quad \ldots\ldots\ldots(48)$$

The value of δ_{CRACK} may be directly obtained from equation (47)

$$\delta_{CRACK} = \delta_{TOTAL} - \delta_{NO\ CRACK} \quad \ldots\ldots\ldots(49)$$

where δ_{TOTAL} is the displacement at crack initiation from the L-L.P.D. record of a pre-cracked specimen and $\delta_{NO\ CRACK}$ is the elastic displacement of the un-cracked specimen. For three point bending $\delta_{NO\ CRACK}$ may be determined from beam theory, i.e.

$$\delta_{NO\ CRACK} = \frac{P_c * L^3}{48 * E * I} \quad \ldots\ldots\ldots(50)$$

where P_c : Critical load at crack initiation

L : span length and equal to 4W

E : Young's modulus

I : Second moment of area and is given by

I : $\frac{BW^3}{12}$

therefore $$\delta_{NO\ CRACK} = \frac{16 * P_c}{E * B} \quad \ldots\ldots\ldots(51)$$

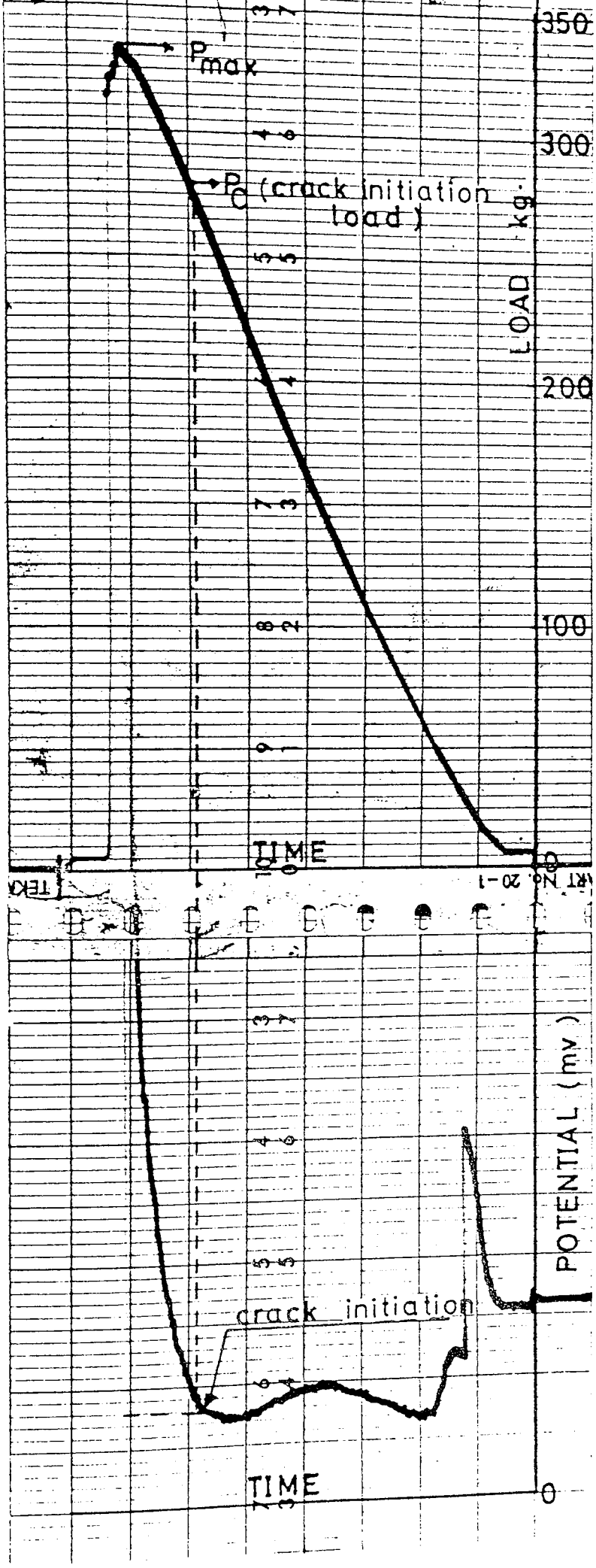

FIGURE 39: Determination of critical crack initiation load (P_C) from load vs time and potential-drop vs time records

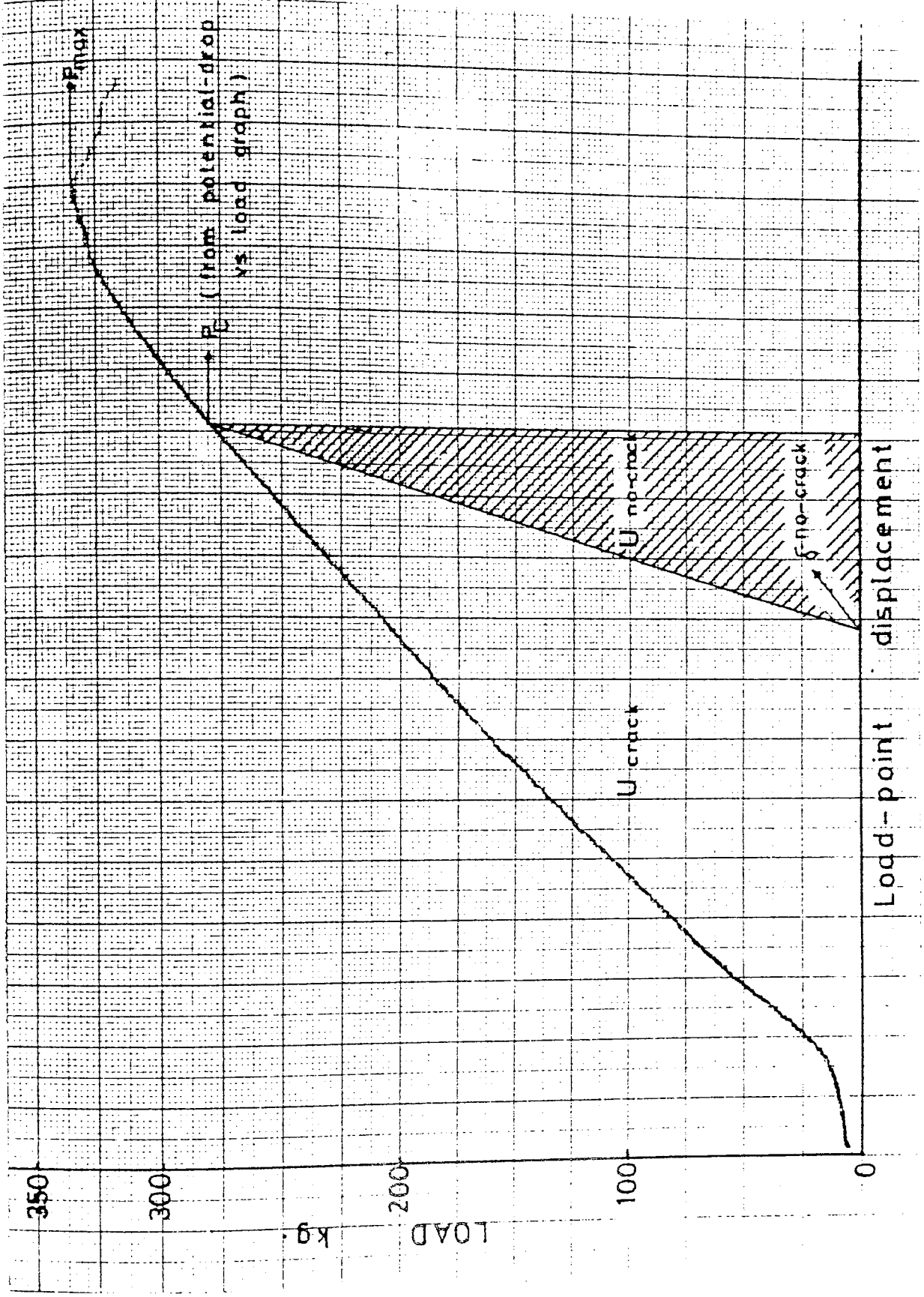

FIGURE 40: Typical load vs load point displacement record obtained from three-point bending fracture toughness tests and determination of the J values

For calculation of J_{IC} values from load-load point displacement records the procedure was as follows. The crack initiation load which is the critical load P_c was determined from the time-load and time-potential drop records. The P_c value was taken as the point at which the potential drop curve deviated from linearity (see Fig. 39). Then the value of P_c was plotted on the graph of load-load point displacement and the area under the curve U_{TOTAL} and $U_{NO\ CRACK}$ were calculated taking into account the amplication of the actual displacements and load values on the graphical-record. The critical value of J was calculated according to the equation suggested by Rice et al [137]:

$$J = \frac{2U_{CRACK}}{B(W-a)} \qquad \text{.....(52)}$$

where U_{CRACK} is the appropriate energy, equivalent to the difference between the total area under the load-load point displacement record (up to critical load) and the area contributed by the uncracked specimen (see Fig. 40). The J_{IC} values were then converted to the K_{IC} values by using the expression:

$$K_{IC} = \sqrt{\frac{J_{IC} * E}{(1 - v^2)}} \qquad \text{.....(53)}$$

7.3 Data Analyses of Short-Bar Fracture Toughness Tests

7.3.1 Determination of Stress Intensity Coefficients and Compliance Functions of Short-Bar Fracture Toughness Test Specimens

7.3.1.1 Analytical Approach

Blumh [138] suggested a slice model in order to obtain analytically the compliance functions of chevron notched bending test pieces. In this study analytical complicance

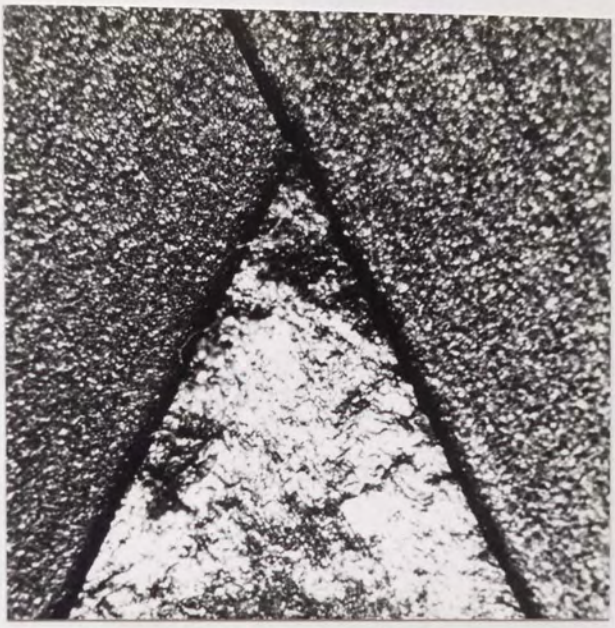

FIGURE 41: Chevron notch tip detail after spark-machining

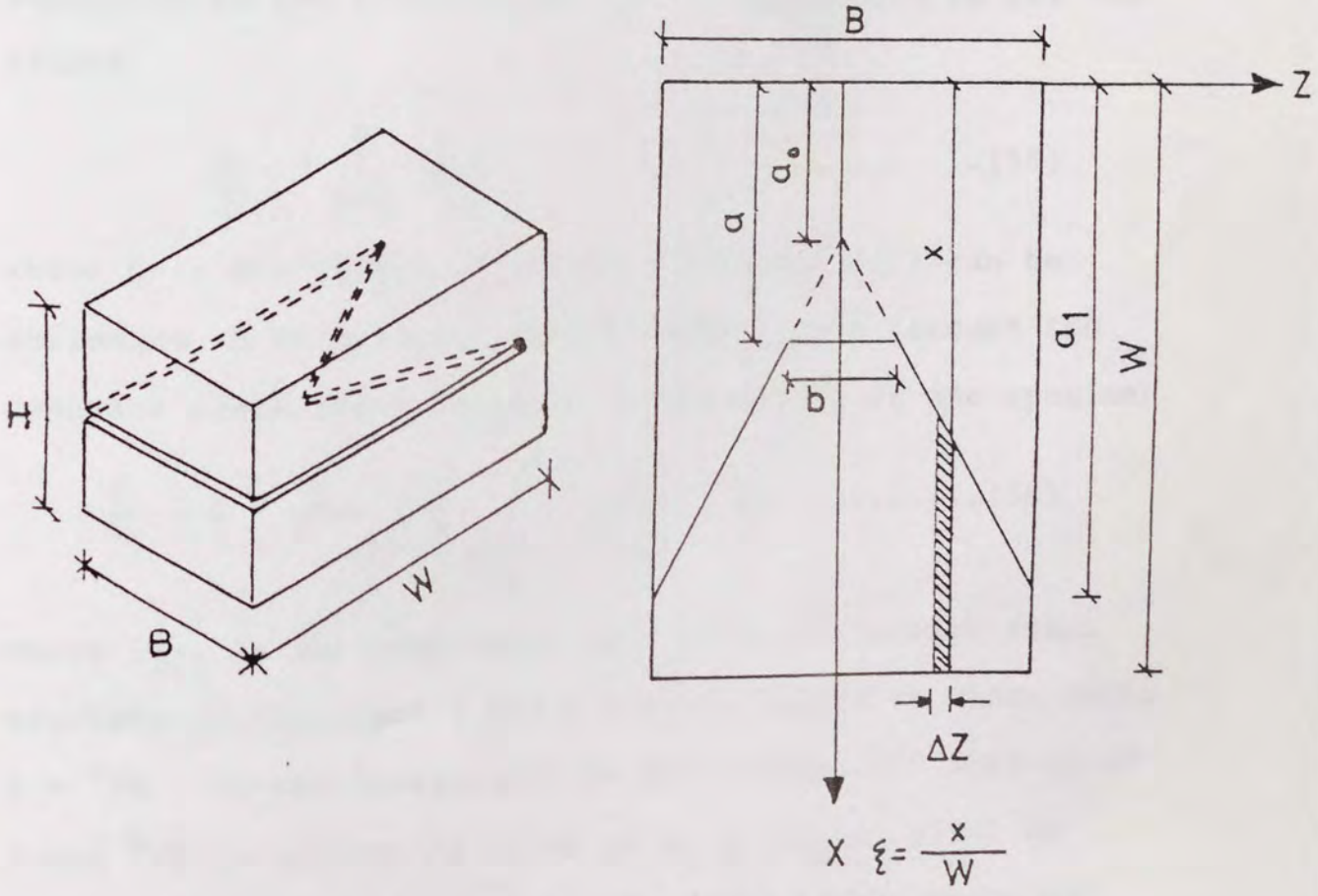

FIGURE 42: Fracture plane of a short-bar specimen showing the notations used in Blumh's slice model

studies of short-bar specimens were carried out by combining Blumh's slice model with the analytical expression of a straight-through crack for short-bar specimens as suggested by Srawley et al [100].

The method of Blumh can be explained with the help of Fig. 42. The specimen is divided into a number of slices of thickness Δz. The compliance of a slice with crack length x is given by:

$$C_s = C_{(\xi)} \cdot \frac{B}{\Delta z} \qquad \ldots\ldots\ldots(54)$$

where $C_{(\xi)}$ is the compliance of the straight-through crack specimen of thickness B and crack length to width ratio $\xi = x/W$. The total compliance C_T may be expressed by the summation of the recriprocals of the compliance of all the slices

$$\frac{1}{C_T} = \sum_{i=1}^{n} \left(\frac{1}{C_s}\right)_i \qquad \ldots\ldots\ldots(55)$$

where n is the number of slices. Equation (55) can be expressed in an integral form by taking into account the constant crack front length b in the centre of the specimen

$$\frac{1}{C_T} = \frac{b}{B} - \frac{1}{C_{(\alpha)}} + \frac{2}{B} \int_{b/2}^{B/2} \frac{1}{C_{(\xi)}} \cdot dz \qquad \ldots\ldots\ldots(56)$$

where $C_{(\alpha)}$ is the compliance of a straight through crack specimen of thickness B and the crack length to width ratio $\alpha = a/W$. If the integration is taken along (ξ) instead of z and b/B is written in terms of a, a_o, a_1 as given in equation (57) then the total compliance of the short-bar

specimen can be re-written in the following form:

$$\frac{b}{B} = \frac{(a/W) - (a_o/W)}{(a_1/W) - (a_o/W)} \qquad \ldots\ldots\ldots(57)$$

$$\frac{1}{C_T} = \left[\frac{(a/W) - (a_o/W)}{(a_1/W) - (a_o/W)}\right] \frac{1}{C_{(\alpha)}} + \frac{1}{(a_1/W) - (a_o/W)} \int_{(a/W)}^{(a_1/W)} \frac{1}{C_{(\xi)}} d(\xi)$$

$$\ldots\ldots\ldots(58)$$

According to Blumh the interlamellar shear stress increases the stiffness of the slice. The same qualitative effect is achieved by attributing to the slice an effective thickness $\Delta z'$ greater than the actual thickness and defined by the relation

$$\Delta z' = k.\Delta z \qquad \ldots\ldots\ldots(59)$$

where $k > 1$, thus the equation (58) can be replaced by

$$\frac{1}{C_T} = \left[\frac{(a/W)-(a_o/W)}{(a_1/W)-(a_o/W)}\right] \frac{1}{C_{(\alpha)}} + \frac{k}{(a_1/W)-(a_o/W)} \int_{(a/W)}^{(a_1/W)} \frac{1}{C_{(\xi)}} d\xi$$

$$\ldots\ldots\ldots(60)$$

During the analytical studies the compliance of the straight-through cracks was calculated using the analytical expression of stress intensity coefficients suggested by Srawley et al in the following form

$$Y = \frac{F(a/W)}{1-(a/W)^{3/2}} \qquad \ldots\ldots\ldots(61)$$

where $F(a/W) = \ell n(\exp F_1 + \exp F_2)$ $\ldots\ldots\ldots(62)$

$$F_1 = \sqrt{\left(\frac{W}{H}\right)^3 * 12 * (1-(a/W))^3}\ \left(1 + \frac{0.679}{(a/H)}\right) \ldots(63)$$

$$F_2 = \frac{2.702}{(a/W)} + 1.628 \qquad \ldots\ldots\ldots(64)$$

and non-dimensional compliance for straight-through crack can be written as

$$C_{(\alpha)} = 2 \int_{0}^{(a/W)} Y^2 d(a/W) \quad \ldots\ldots\ldots(65)$$

Thus, analytical compliance values of short-bar specimens were obtained combining equation (60) and equation (65), solving the equation numerically using the finite differances method with $a/W = 0.005$ intervals in a computer programme.

7.3.1.2 Analysis of the Experimental Compliance Data of the Short-Bar Specimens

From the measured values of compliance as a function of a/W a smooth curve can be drawn through the data points, enabling the rate of change of compliance to be determined. The most common method is third to fifth degree polynomial curve fitting. The major disadvantage of this process is the resulting error in differentiating.

Ryder et al [139] have proposed an analytical procedure for obtaining the stress intensity coefficients from the experimental compliance results using a three parameter fit. It was proposed that

$$C.E.B. = \exp(\exp.(F(a/W))) - 2.71828 \quad \ldots\ldots(66)$$

where

$$F(a/W) = e + (v - e)(-\ln(1 - (a/W)))^{1/k} \quad \ldots(67)$$

equation (66) can be re-written by combining the equation (67) in the following form

$$\ell n(\ell n(C.E.B. + 2.71828)) = e + (v-e)(-\ell n(1-(a/W)))^{1/k} \quad ..(68)$$

and in the short form

$$y = e + (v - e)\, x^{1/k} \quad .....(69)$$

where $$y = \ell n(\ell n[C.E.B. + 2.71828)) \quad .....(70)$$

and $$x = -(\ell n(1-(a/W))) \quad .....(71)$$

and equation (69) can be re-written in the form of a linear function

$$\ell n(y-e) = \ell n(v-e) + \frac{1}{k}\, \ell n(x) \quad .....(72)$$

From equation (72) it is possible to determine the three parameters since (v-e) is the intercept and $^1/k$ is the slope of the linear function.

In the original procedure the value of e is given by

$$e = \ell n(\ell n(C.E.B. + 2.71828))$$

when a/W approaches zero. In this work since a/W values are started from the initial chevron depth $[a_o]$, e values were determined by trying several e values till a maximum correlation coefficient was obtained in the linear regression analysis of the equation (72) with the experimental points in a computer programme.

7.3.1.3 P_{max} and K_{IC} relation for short-bar specimens and evaluation of stress Intensity Coefficients from Compliance Studies

The relation between P_{max} and K_{IC} can be obtained using the energy approach of Fracture Mechanics. The energy release

rate for extension of the crack by Δa can be expressed in terms of compliance in the following way

$$\Delta U = \frac{P^2}{2W} \cdot \frac{dC}{d(a/W)} \Delta a \qquad \ldots\ldots\ldots(74)$$

The energy for crack extension is also given by

$$\bar{\Delta W} = G_{IC}\, b.\Delta a = \frac{K^2_{IC}}{E}\, b.\Delta a \qquad \ldots\ldots(75)$$

During crack extension

$$\Delta U = \bar{\Delta W}$$

and

$$K_{IC}^2 = \left[\frac{P^2}{2Wb} \frac{d(CE')}{d(a/W)} \right] \qquad \ldots\ldots\ldots(76)$$

where $E' = E$ for plane stress and $E' = E/(1-v^2)$ for plane strain. By using the geometric relation equation (57) the equation (76) can be re-written for short-bar specimens in the following form

$$K_{IC} = \frac{P}{B\sqrt{W}} \left[\frac{1}{2} \left(\frac{(a_1/W)-(a_o/W)}{(a/W)-(a_o/W)} \right) \cdot \frac{d(CE'B)}{d(a/W)} \right]^{\frac{1}{2}} = \frac{P.Y^*}{B\sqrt{W}} \qquad \ldots(77)$$

with

$$Y^* = \left[\frac{1}{2} \left(\frac{(a_1/W)-(a_o/W)}{(a/W)-(a_o/W)} \right) \cdot \frac{d(CE'B)}{d(a/W)} \right]^{\frac{1}{2}} \qquad \ldots\ldots\ldots(78)$$

Equation (66) is very convenient in that it enables the compliance to be differentiated mathematically. Thus

$$\frac{d(CEB)}{d(a/W)} = \exp.(\exp.(F(a/W)))\exp.(F(a/W)).F'(a/W) \qquad \ldots(79)$$

where

$$F'(a/W) = \frac{v-e}{k} \left[-\ell n(1-(a/W)) \right]^{(\frac{1}{k}-1)} \left[\frac{1}{1-(a/W)} \right] \qquad \ldots(80)$$

Thus the stress intensity coefficients of each short-bar specimen geometry were obtained by combining equation (78) with equation (79) using the pre-determined compliance functions from experimental compliance tests. According to Srawley et al [100] for a given geometry of short-bar specimen maximum load (P_{max}) occurs when Y* has its minimum value. The variation of Y* values with $^{a}/_{W}$ for each specimen geometry was determined by solving equation (78,79) with intervals $^{a}/_{W}$ = 0.005 in a computer programme.

7.3.2 Determination of Fracture Toughness Values from Load-Mouth Opening Displacement Records of Short-Bar Tests

A typical load versus mouth opening displacement curve from short-bar fracture toughness tests is given in Fig. 43. As can be seen from the graph, after the maximum load the specimens failed in a completely unstable manner.

The K_{ICSB}^{*} values were obtained from equation (30) by determining the value of the constant [A] from the stress intensity coefficient of that type of short-bar specimen geometry in the following way

$$K_{ICSB} = \frac{P_{max} \cdot A}{B^{3/2}} \qquad \text{.....(30)}$$

and

$$A = Y^{*}_{(min)} / (W/B)^{\frac{1}{2}} \qquad \text{.....(81)}$$

where B : specimen width

W : specimen length (from loading line)

P_{max} : Maximum load on the load-mouth opening displacement record

---

* Toughness values using the short-bar technique are denoted as K_{ICSB} in order to distinguish from the standard K_{IC} results.

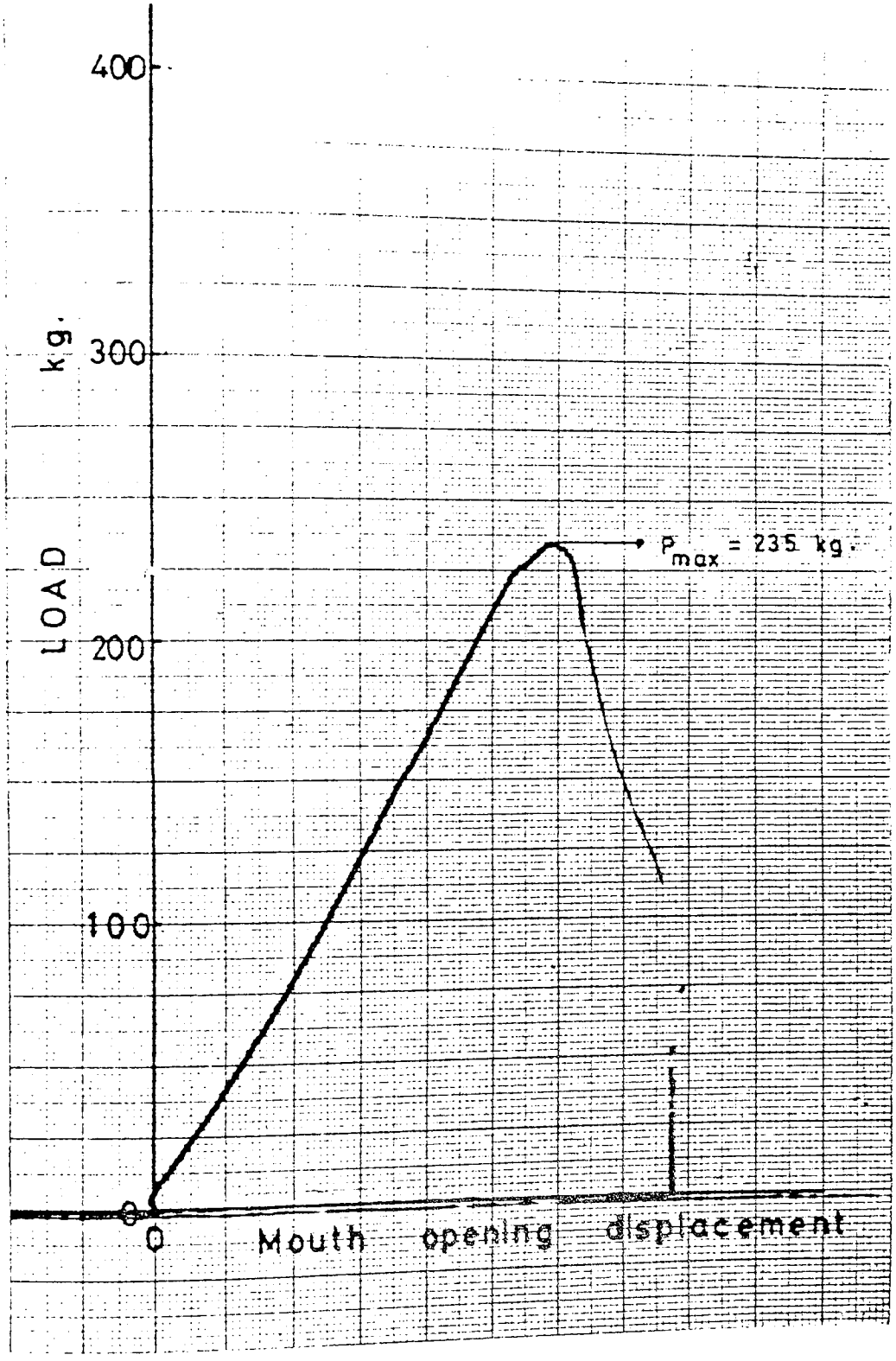

FIGURE 43: Typical load vs mouth opening displacement record obtained from short-bar fracture toughness tests of high-Cr cast irons

Y^*_{min} : Minimum stress intensity coefficient for given short-bar specimen geometry.

7.4 Determination of Critical Fracture Stress and Notch Toughness of the Alloys from Slow Notch Bending Tests

A typical load versus load point displacement record from a notch bend specimen is given in Fig. 44. As can be seen, no yielding has occurred prior to failure of the specimen and crack initiation occurred spontaneously at the attainment of the maximum load, therefore the maximum recorded loads were taken as failure loads.

The critical fracture stresses (σ^*_F) of the alloys were determined from the model which was suggested by Tetelman and co-workers [112]. The model predicts the elastic-plastic stress distribution of notched bars in plane-strain bending and is based on the elastic solutions of Neuber [113] and the slip-line solutions of Hill [114].

According to work of Tetelman et al, the stress distribution beneath the notch is a unique function of plastic zone size and tensile stress (σ_{yy}) acting ahead of the notch can be determined by the condition that the sum of internal bending moments resulting from the tensile stress $\sigma_{yy(x)}$ must be equal to the external applied bending moment.

The elastic-plastic stress distribution ahead of the notch is shown schematically in Fig. 45 with a solid curve. For rigid perfectly plastic materials the tensile stress along

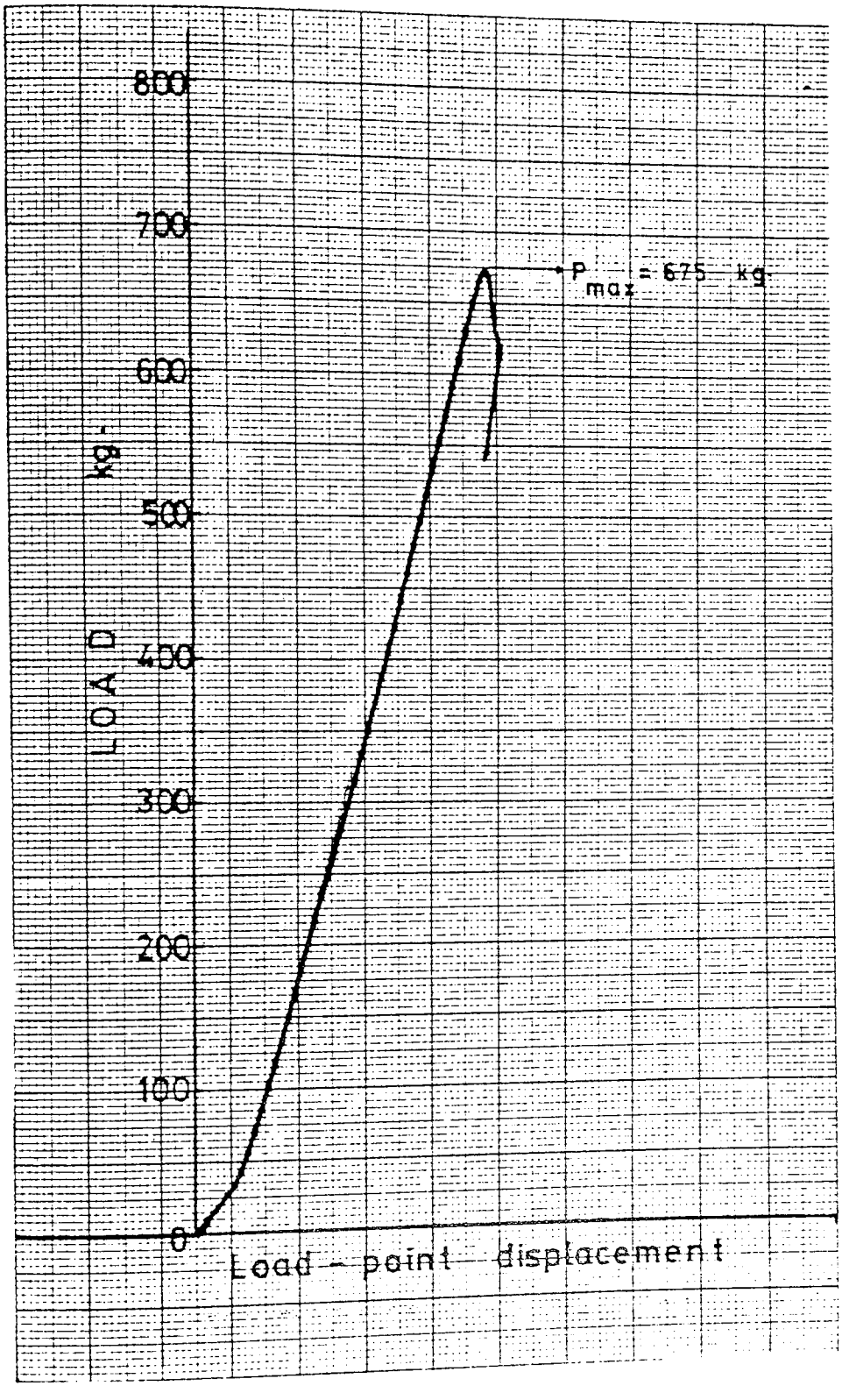

FIGURE 44: Typical load vs load point displacement records obtained from notch bending tests

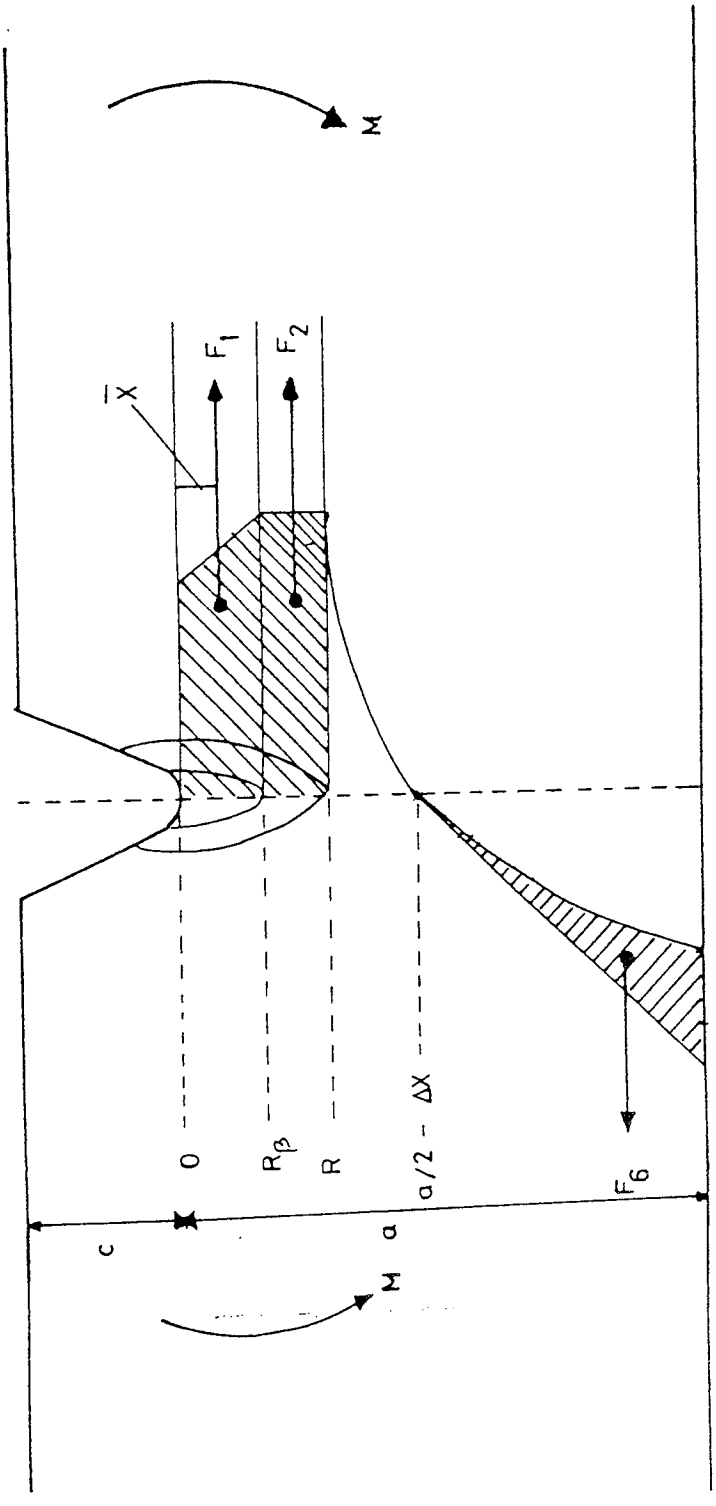

FIGURE 45: Schematic elastic-plastic stress distribution for a notched bar in plane-strain bending (112)

the net section within the plastic zone ($x<R_\beta$) is given by Hill as

$$\sigma_{yy(x)} = \sigma_{ys}\left[1 + \ell n(1 + x/\rho)\right] \quad x < R_\beta \quad \ldots(82)$$

where R_β is plastic zone size at maximum constraint. The maximum tensile stress occurs at the elastic-plastic interface

$$\sigma_{yy_{(max)}} = \sigma_{ys}\left[1 + \ell n(1 + R/\rho)\right] \quad R<R_\beta \quad \ldots(83)$$

The parameter inside the square brackets is measure of triaxiality and is known as the plastic stress concentration factor. Equations (82) and (83) are only valid while the plastic zone remains within the points of tangency between the notch root radius and the flank angles. Beyond this region the maximum stress remains constant at its maximum value which depends only on the flank angle:

$$\sigma_{yy_{(max)}} = \sigma_{ys}\left[1 + \pi/2 - \frac{w}{2}\right] \quad R_\beta<x<R \quad \ldots\ldots(84)$$

Beyond the plastic zone, stresses are elastic and decrease sharply.

a. The Elastic Moment

For a hypothetical notch with notch root radius $\rho^*(R)$ and notch depth C + R the nominal stress σ_N^* which is required to produce the elastic stress distribution is given by

$$M^* = \frac{\sigma_N^*}{6}(a - R)^2 \qquad \ldots\ldots\ldots(85)$$

M* is the applied bending moment per unit thickness to produce this nominal bending stress. Since stress is continuous at the elastic-plastic interface, the maximum

stress at the elastic, plastic stress is also given by equation (83) and is equal to:

$$\sigma_N^* = \sigma_{ys}\left[1 + \ell n(1 + R/\rho)\right] / K_{\sigma(R)}^* \quad \ldots\ldots(86)$$

and substituting into equation (85)

$$M^* = \sigma_{ys}\left[1+\ell n(1+R/\rho)\right](a-R)^2 / 6K_{\sigma(R)}^* \quad R<R_\beta \quad \ldots(87)$$

where $K_{\sigma(R)}^*$ elastic stress concentration factor of a hypothetical notch of depth C + R and root radius $\rho_{(R)}^*$ and its value equal to

$$K_{\sigma(R)}^* = K_\sigma \cdot \frac{1}{(1-2R/a)} (1 + 4R/\rho)^{-\frac{1}{g}} \quad \ldots\ldots(88)$$

where g : 2 for elastic

g : 2.5 for elastic-plastic

a : remaining ligament depth after notch

K_σ : Elastic stress concentration factor after Nueber and equal to

$$K = 1 + \frac{(K_{Deep} - 1)(K_{shallow} - 1)}{\sqrt{(K_{Deep} - 1)^2 . (K_{shallow} - 1)^2}} \quad \ldots\ldots(89)$$

where $K_{shallow}$: $1 + 2\sqrt{c/\rho}$ $\ldots\ldots\ldots\ldots(90)$

and K_{Deep} : $\dfrac{2((a/\rho) + 1) - \alpha_1\sqrt{(a/\rho) + 1}}{\frac{4}{\alpha_2}((a/\rho) + 1) - 3\alpha_1}$ $\ldots\ldots(91)$

where $\alpha_1 = \dfrac{2((a/\rho) + 1)\sqrt{a/\rho}}{((a/\rho) + 1) \arctan(\sqrt{a/\rho}) + \sqrt{a/\rho}}$ $\ldots(92)$

and $\alpha_2 = \dfrac{4(a/\rho)\sqrt{a/\rho}}{3\left[\sqrt{a/\rho} + ((a/\rho) - 1) \arctan(\sqrt{a/\rho})\right]}$ $\ldots(93)$

b. Plastic Moment

In order to maintain the equilibrium of force, the tensile forces in the plastic region must be balanced by equivalent forces in the in the comparison region and so they proposed that

$$F_6 = -(F_1 + F_2) \quad \text{.....(94)}$$

where $$F_1 = \int_0^{R_\beta} \sigma_{ys}\left[1 + \ell n(1 + {}^{x}/\rho)\right] . dx \quad x<R_\beta \quad \text{...(95)}$$

and $$F_2 = (R-R_\beta)\sigma_{ys}\cdot\left[1+\ell n(1+R_\beta/\rho)\right] \quad \text{.....(96)}$$

For $R<R_\beta$ is replaced by R so that $F_2 = 0$

The total moment of elastic-plastic distribution is equal to the applied moment M required to produce it and M is simply equal to M* plus the couple generated by the Force F_1, F_2, F_6 and is given by

$$M = M^* - F_1\bar{x} - F_2\left\{R-\frac{R-R_\beta}{2}\right\} + F_6\left\{a - \tfrac{1}{3}(a/2 + \Delta x)\right\} \quad \text{...(97)}$$

where $\bar{x}$ = centre of logarithmic slip region.

Using the equations (87, 94, 95), the equation (97) can be re-arranged to relate the plastic zone size to the applied moment. This relationship depends upon geometrical parameters, yield stress and two unspecified parameters which are Δx and g. According to the work of Tetelman et al the values of these parameters are given as below

$$o < \Delta x < {}^{a}/6$$

g = 2 for elastic case

g = 2.5 for elastic-plastic case

By taking the maximum loads from load-load point displacement records as the failure loads of the specimens, the critical plastic zone size R_F^* (plastic zone size at fracture) was calculated by solving equation (97) numerically with R = 2 micron intervals in a computer programme. Then critical plastic zone size was related to the critical fracture stress which is ($\sigma_{yy} = \sigma_F$) through equation (82). Also in the same computer programme the nominal bending stress (σ_N), general yielding stresses (σ_{Gys}) were calculated from equations (98) and (99) respectively

$$\sigma_N = (6 * M)/(B + a^2) \quad \text{.....(98)}$$

$$\sigma_{Gys} = 2.184 * \sigma_{ys} * (1-(c/W))^2 \quad \text{.....(99)}$$

where M : applied bending moment

B : specimen breadth

a : remaining ligament depth

c : notch depth

W : specimen width

σ_{ys} : 0.02% yield stress

7.5 Electrical-Potential Method for Determining Initiation and Propagation of the Cracks

The electrical potential technique for determining crack initiation and propagation is now well established [140,141]. Basically the technique involves applying a large D.C. current to the ends of the specimens and monitoring the change in electrical potential between two poles attached to each side of the crack or notch.

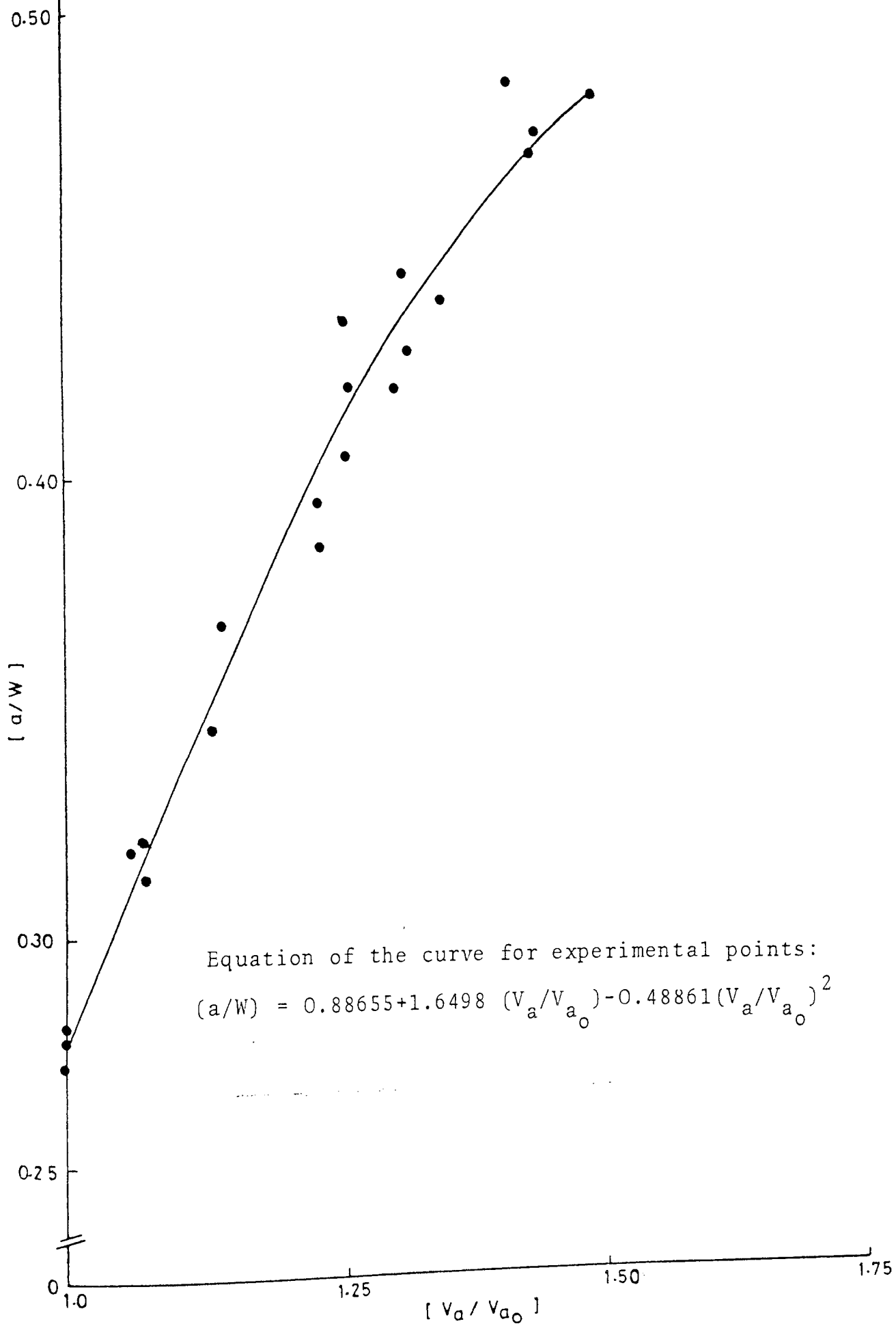

FIGURE 46: Experimentally obtained electrical potential calibration curve

where:

a : crack length (including the notch)
W : specimen width
V_a : instant voltage at a given crack length
V_{a_o} : reference initial voltage

The sensitivity of the method depends on several factors such as specimen size, crack length, magnitude of the applied D.C. current and probe spacing. The calibration curve is constructed as V_a/V_{ao} versus a/W where V_a instant voltage, V_{ao} initial voltage, a (crack length including the notch) and W width of the specimen. The calibration curve which was used during the tests is given in Fig. 46 and shows $\pm$ 0.3 mm maximum variation from actual measured crack lengths.

7.6 Determination of Fatigue-Crack Growth Rates

Fatigue crack growth rates of the alloys were determined using a computer programme. The data obtained from the true-reference potential records were input as pairs of potential readings and numbers of cycles, from this data crack lengths were calculated from the equation of potential calibration curve, then da/dN was calculated by a finite difference method. For each instantaneous value of crack length the ΔK value was calculated using equations (44) and (45). The crack growth rates were calculated only for the first load which was used during the pre-cracking of the toughness samples. Linear-regression analyses were made on the linear portion of the da/dN versus ΔK graphs.

VIII RESULTS

Each aspect of the work is considered as a separate experiment and tabulated in the following form:

Table 4 Chemical analysis of the castings for primarily metallographic studies to determine the effects of high temperature heat treatments and alloy additions on the eutectic carbide morphology.

Table 5 Chemical analysis of the castings for the fracture toughness testing programme.

Table 6 The composition of the carbides and matrix phases of the alloys determined from electron-microprobe studies.

Table 7 The micro-structural parameters of the alloys determined from metallographic studies.

Tables 8-19 Fracture toughness test data of the alloys for the studied metallurgical variables (includes the hardness and tensile stress values of the alloys).

Tables 20-25 Notch bending test data of the alloys for the studied metallurgical variables.

Tables 26-28 Experimental compliance data for three different short-bar fracture toughness test specimens.

Table 29 Comparison of the experimentally obtained compliance results with the result obtained from Blumh's slice model.

Table 30 The curve fitting parameters of the Ryder's exponential solution for the experimental compliance data.

Table 31 The experimentally and analytically determined minimum stress intensity coefficients of short-bar specimen geometries and corresponding critical crack lengths.

Tables 32,33 Test data of short-bar fracture toughness measurements of high-Cr cast irons.

Table 34 Fatigue-crack growth data of a series of high-Cr cast iron.

Key for the designations of the alloys which were used throughout the work

As : As-cast

Mo : Molybdenum series

V : Vanadium series

Mn : Manganese series

W : Tungsten series

M : Martensitic

HT : High-temperature heat treated

The first numbers appearing in the designations give the holding periods at 1180^{o}C. The second number after letters indicate the approximate addition level and roman numbers designate the number of the test specimen. The four number containing designations, the first four numbers indicate the heat treatment temperature. The second number from the last in notch bend specimens designate the type of the notch. For example:

8HT2MoI : 8 hours high temperature heat treated, 2% molybdenum containing alloy. Fracture toughness test specimen number one.

12M2Mo1.I : 12 hours high temperature heat treated, 2% molybdenum containing martensitic alloy. Notch bend specimen with 0.3 mm notch root radius.

ALLOY DESIGNATION	C	Si	S	P	Mn	Ni	Cr	Cu	Sn	Al	Mo	W	V
1C	0.77	0.44	0.037	0.028	0.49	0.09	15.4	0.13	< 0.01	< 0.01	-	-	-
2C	1.81	0.41	0.035	0.024	0.57	0.18	15.1	0.15	"	"	-	-	-
3C	2.74	0.37	0.033	0.028	0.58	0.09	15.8	0.12	"	"	-	-	-
1 Mo	2.79	0.69	0.037	0.031	0.52	0.11	14.2	0.10	"	"	1.25	-	-
2 Mo	2.69	0.53	0.033	0.030	0.58	0.10	14.6	0.10	"	"	1.76	-	-
3 Mo	2.60	0.61	0.033	0.031	0.63	0.10	13.8	0.11	"	"	2.74	-	-
4 Mo	2.79	0.52	0.041	0.030	0.51	0.09	14.6	0.11	"	"	3.71	-	-
1W	2.74	0.59	0.038	0.027	0.51	0.12	14.3	0.15	"	"	-	0.80	-
2W	2.60	0.65	0.033	0.030	0.62	0.11	14.6	0.13	"	"	-	2.50	-
3W	2.60	0.62	0.033	0.031	0.59	0.13	14.0	0.11	"	"	-	3.16	-
5W	2.60	0.61	0.034	0.029	0.54	0.14	14.9	0.09	"	"	-	5.12	-
1V	2.88	0.55	0.030	0.028	0.61	0.14	14.3	0.11	"	"	-	-	0.69
2V	2.60	0.61	0.030	0.027	0.57	0.12	14.6	0.10	"	"	-	-	1.11
3V	2.56	0.52	0.033	0.020	0.59	0.13	15.1	0.13	"	"	-	-	3.79
5V	2.60	0.64	0.034	0.027	0.61	0.13	1.0	0.13	"	"	-	-	5.03
2 Mn	2.79	0.51	0.030	0.024	1.52	0.14	15.4	0.11	"	"	-	-	-
3 Mn	2.67	0.56	0.035	0.030	2.71	0.17	15.5	0.13	"	"	-	-	-

Table (4): Chemical Analyses of the castings for metallographic studies

ALLOY DESIGNATION	C	Si	S	P	Mn	Ni	Cu	Cr	Sn	Al	Mo	W
15.3 (Base Alloy)	2.79	0.65	0.017	0.028	0.28	0.12	0.13	16.2	< 0.01	< 0.01	-	-
1 Mo	2.79	0.66	0.017	0.028	0.29	0.12	0.14	16.0	"	"	0.69	-
2 Mo	2.60	0.68	0.018	0.030	0.28	0.12	0.15	15.7	"	"	2.23	-
4 Mo	2.60	0.72	0.020	0.031	0.27	0.12	0.15	15.2	"	"	4.03	-
1W	2.79	0.62	0.016	0.028	0.31	0.12	0.15	15.5	"	"	-	1.15
3W	2.75	0.63	0.017	0.028	0.31	0.12	0.15	15.2	"	"	-	3.09
5W	2.70	0.65	0.017	0.034	0.31	0.12	0.16	14.8	"	"	-	5.63

Table 5: Chemical analyses of the castings for the fracture toughness programme

ALLOY	PHASES	Cr %	Fe %	Mo %	Mn %	C %
1 Mo	CARBIDE	42.96	45.56	2.20	0.67	8.61
	MATRIX	11.68	-	0.64	-	-
3 Mo	CARBIDE	44.14	41.73	3.67	0.70	9.26
	MATRIX	11.90	-	1.26	-	-
4 Mo	CARBIDE	44.10	40.89	4.80	0.67	9.54
	MATRIX	11.45	-	1.49	-	-

ALLOY	PHASES	Cr %	Fe %	W %	Mn %	C %
1W	CARBIDE	45.34	44.69	0.67	0.60	8.7
	MATRIX	12.21	-	0.28	0.60	-
3W	CARBIDE	44.93	42.89	2.14	0.76	9.28
	MATRIX	12.48	-	0.83	-	-
5W	CARBIDE	42.26	44.69	3.82	0.70	8.53
	MATRIX	11.70	-	1.45	-	-

ALLOY	PHASES	Cr %	Fe %	V %	Mn %	C %
1V	CARBIDE	45.26	41.97	3.66	0.79	8.32
	MATRIX	12.40	-	0.44	-	-
3V	CARBIDE	39.40	43.89	8.84	0.80	7.63
	MATRIX	12.10	-	1.19	-	-
5V	CARBIDE	37.51	41.30	12.69	0.71	7.79
	MATRIX	11.04	-	1.89	-	-

Table 6: Determined compositions of carbide and matrix phases in the alloys

Alloy	Volume %	Density	Mean Interparticle Spacing μm	Mean Carbide Size μm	K_{IC} $MN\,m^{3/2}$
AS 15.3.	27.11 ± 4.37	68 ± 13	9.13 ± 2.24	3.66 ± 0.68	20.58
4 HT 15.3	23.32 ± 1.21	70 ± 6	9.46 ± 0.92	3.73 ± 0.89	19.74
8 HT 15.3	25.5 ± 3.99	63 ± 5	11.96 ± 2.76	5.01 ± 0.79	18.61
24 HT 15.3	25.77 ± 4.21	59 ± 5	9.38 ± 0.75	3.59 ± 0.56	19.29
72 HT 15.3	25.89 ± 2.40	54 ± 9	14.01 ± 2.12	4.78 ± 0.43	25.78
AS 1 Mo	26.76 ± 4.37	65 ± 15	10.66 ± 2.15	3.81 ± 0.69	23.00
4 HT 1 Mo	26.01 ± 2.59	51 ± 8	13.04 ± 2.24	3.84 ± 0.78	25.91
12 HT 1 Mo	26.77 ± 4.17	50 ± 10	13.64 ± 1.13	4.2 ± 1.13	27.60
24 HT 1 Mo	24.96 ± 2.65	48 ± 6	14.65 ± 1.79	4.73 ± 1.02	26.32
72 HT 1 Mo	23.93 ± 1.98	42 ± 5	17.33 ± 3.12	5.38 ± 0.64	25.02
AS 2 Mo	24.33 ± 2.68	53 ± 13	13.02 ± 2.54	4.17 ± 0.91	24.4
4 HT 2 Mo	26.30 ± 3.45	42 ± 10	15.51 ± 2.89	4.89 ± 0.74	28.80
8 HT 2 Mo	24.73 ± 4.96	38 ± 7	19.46 ± 3.32	5.46 ± 1.26	30.13
12 HT 2 Mo	24.64 ± 3.75	43 ± 6	19.66 ± 3.32	5.79 ± 0.55	26.87
24 HT 2 Mo	23.34 ± 3.51	37 ± 6	19.47 ± 3.86	5.68 ± 1.01	27.75
72 HT 2 Mo	22.64 ± 3.68	27 ± 6	27.19 ± 5.52	8.82 ± 2.98	26.35
AS 4 Mo	23.42 ± 2.50	66 ± 8	10.67 ± 1.03	3.40 ± 0.28	23.80
4 HT 4 Mo	25.49 ± 3.14	33 ± 5	21.08 ± 3.67	6.19 ± 1.11	27.37
8 HT 4 Mo	24.3 ± 3.75	26 ± 5	23.89 ± 4.99	7.11 ± 2.21	26.34
12 HT 4 Mo	25.11 ± 5.12	28 ± 6	25.11 ± 5.13	8.74 ± 1.68	26.10
24 HT 4 Mo	22.99 ± 2.86	26 ± 3	26.52 ± 3.0	8.40 ± 2.10	23.98
72 HT 4 Mo	21.42 ± 3.21	22 ± 3	30.26 ± 4.11	11.26 ± 1.79	23.41

Table (7): The results obtained from quantitative metallographic studies

Specimen	B mm	W mm	a mm	P_{max} kg	P_Q kg	K_Q $MN/m^{3/2}$	P_{max}/P_Q	K_F $MN/m^{3/2}$	K_F/K_Q	σ_{ys} N/mm^2	Limit. Thick. mm	P_c kg	J (KJ/m^2)	$K_{Q(J)}$ $MN/m^{3/2}$	Hard. Hv30	K_{IC} $MN/m^{3/2}$
AS15.3.I	18.01	11.95	8.37	356	334	19.5	1.06	11.67	0.59	1350	0.91	285	1.23	16.48	637	20.58 ±1.08
AS15.3.II	18.0	11.96	9.05	357	340	21.66	1.08	14.44	0.66	1350	1.08	276	1.66	18.80		
AS1Mo.I	18.02	12.01	9.15	375	350	23.23	1.07	14.6	0.62	-	1.23	305	1.38	17.14	625	23.00 ±0.24
AS1Mo.II	18.04	12.04	8.90	375	360	22.76	1.04	13.91	0.61	-	1.19	280	1.21	16.34		
AS2Mo.I	18.01	12.01	8.95	410	385	24.67	1.06	16.76	0.68	1195	-	-	-	-	518	24.70 ±0.02
AS2Mo.II	18.03	11.97	8.80	422	393	24.71	1.06	15.01	0.60	1195	1.40	322	2.11	21.17		
AS4Mo.I	18.04	11.99	8.50	427	395	23.42	1.07	14.23	0.60	1167	1.26	377	1.88	20.54	503	23.80 ±0.36
AS4Mo.II	18.04	11.98	8.90	415	380	24.14	1.09	15.25	0.63	1167	1.30	354	1.73	19.65		
AS1W.I	18.07	11.95	9.00	3.50	339	21.96	1.02	14.21	0.64	-	1.10	304	1.14	15.98	595	22.14 ±0.18
AS1W.II	18.08	11.96	9.02	361	343	22.32	1.04	14.23	0.63	-	1.15	327	1.19	16.35		
AS3W.I	18.05	11.94	8.45	475	445	26.24	1.06	14.15	0.53	-	1.57	362	1.92	20.71	516	25.93 ±0.26
AS3W.II	18.06	11.94	8.75	443	415	25.72	1.07	14.87	0.57	-	1.53	389	2.24	21.83		
AS5W.I	18.00	11.98	8.95	386	361	23.18	1.06	15.45	0.66	-	1.24	327	1.42	17.86	494	23.09 ±0.10
AS5W.II	18.08	11.98	8.60	402	378	23.0	1.06	14.53	0.63	-	1.22	318	1.61	18.52		

Table 8; Fracture toughness test data and the results for the alloys in as-cast condition

Specimen	B mm	W mm	a mm	P_{max} kg	P_Q kg	K_Q $MN/m^{3/2}$	P_{max}/P_Q	K_F $MN/m^{3/2}$	K_F/K_Q	σ_{ys} N/mm^2	Limit. Thick. mm	P_c kg	J (KJ/m^2)	$K_{Q(J)}$ $MN/m^{3/2}$	Hard. Hv30	K_{IC} $MN/m^{3/2}$
4HT15.3.I	11.57	17.73	7.35	360	350	18.38	1.02	11.55	0.62	-	-	280	1.03	15.81	608	19.74 ±1.36
4HT15.3.II	11.71	17.75	9.24	320	295	21.10	1.08	15.73	0.74	-	-	275	1.30	16.79		
4HT1Mo.I	11.43	17.74	8.72	420	395	26.38	1.06	17.36	0.65	-	-	350	1.69	19.19	507	25.91 ±0.47
4HT1Mo.II	11.35	17.61	7.96	460	425	25.44	1.08	15.56	0.61	-	-	370	1.98	20.75		
4HT2Mo.I	12.11	17.60	7.95	565	525	29.43	1.07	14.57	0.49	-	-	430	2.52	23.40	505	28.80 ±0.63
4HT2Mo.II	11.21	17.62	8.97	420	390	28.17	1.07	18.78	0.66	-	-	360	2.17	21.74		
4HT3Mo.I	12.07	18.12	9.68	430	405	29.10	1.06	18.68	0.64	-	-	360	2.43	22.80	474	27.37 ±1.73
4HT3Mo.II	12.11	18.15	9.30	410	385	25.64	1.06	17.31	0.67	-	-	305	2.45	23.10		

Table 9: Fracture toughness test data and results for the alloys heat treated at 1180°C for 4 hours

Specimen	B mm	W mm	a mm	P_{max} kg	P_Q kg	K_Q $MN/m^{3/2}$	P_{max}/P_Q	K_F $MN/m^{3/2}$	K_F/K_Q	σ_{ys} N/mm^2	Limit. Thick. mm	P_c kg	J (KJ/m^2)	$K_{Q(J)}$ $MN/m^{3/2}$	Hard. Hv30	K_{IC} $MN/m^{3/2}$
8HT15.3.I	11.98	18.03	9.25	280	275	18.61	1.01	13.53	0.72	1011	0.81	-	-	-	596	18.61
8HT15.3.II	11.98	18.01	- Fractured during fatigue pre-cracking							-	-	-	-	-		
8HT1Mo.I	12.01	18.00	8.65	435	405	24.69	1.07	14.63	0.59	-	-	305	2.20	22.1	515	25.03 ±0.34
8HT1Mo.II	12.04	18.01	3.90	430	400	25.37	1.07	15.22	0.59	-	-	295	1.96	20.76		
8HT2Mo.I	11.99	18.05	8.45	540	510	29.95	1.05	15.27	0.50	928	2.08	440	3.25	26.98	478	20.13 ±0.18
8HT2Mo.II	11.98	18.04	8.45	550	515	30.30	1.06	15.30	0.50	928	2.08	460	2.89	25.40		
8HT4Mo.I	11.91	18.06	8.60	480	440	26.65	1.09	14.53	0.54	845	1.56	380	247	22.70	465	26.34 ±0.31
8HT4Mo.II	11.98	18.03	8.75	450	420	26.03	1.07	14.87	0.57	845	1.59	360	2.16	21.91		
8HT1W.I	11.90	18.00	7.90	490	450	24.46	1.08	14.60	0.59	-	-	-	-	-	516	24.26 ±0.20
8HT1W.II	11.91	18.02	8.10	460	430	24.07	1.06	15.69	0.65	-	-	360	1.61	18.96		
8HT3W.I	11.93	18.06	8.50	485	455	27.05	1.06	15.46	0.57	-	-	360	1.97	21.02	506	27.33 ±0.28
8HT3W.II	11.94	18.05	8.75	475	445	27.61	1.06	16.13	0.58	-	-	370	2.11	21.75		
8HT4W.I	11.98	18.04	8.65	535	505	30.73	1.05	15.82	0.51	-	-	450	3.08	26.23	448	30.38 ±0.35
8HT5W.II	11.98	18.07	8.30	565	525	30.03	1.07	14.87	0.49	-	-	475	3.26	26.96		

Table 10: Fracture toughness test data and results for the alloys heat treated at 1180°C for 8 hours

Specimen	B mm	W mm	a mm	P_{max} kg	P_Q kg	K_Q $MN/m^{3/2}$	P_{max}/P_Q	K_F $MN/m^{3/2}$	K_F/K_Q	σ_{ys} N/mm^2	Limit. Thick. mm	P_c kg	J (KJ/m^2)	$K_{Q(J)}$ $MN/m^{3/2}$	Hard. Hv30	K_{IC} $MN/m^{3/2}$
12HT15.3.I	11.70	17.69	8.49	360	330	20.79	1.09	13.86	0.66	-	-	290	1.20	16.04	592	20.74
12HT15.3.II	11.77	17.66	8.92	320	305	20.69	1.04	14.92	0.72	-	-	280	1.722	19.16		±0.05
12HT1Mo.I	11.88	17.70	8.04	535	495	28.42	1.08	16.07	0.56	-	-	470	2.361	22.43	513	27.6
12HT1Mo.II	11.90	17.61	8.14	495	455	26.78	1.08	16,48	0.61	-	-	395	2.120	21.26		±0.82
12HT2Mo.I	12.24	17.81	8.17	505	465	26.18	1.08	14.64	0.55	-	-	425	1.870	19.96	472	26.87
12HT2Mo.II	11.98	17.78	7.83	540	505	27.55	1.06	14.18	0.51	-	-	390	2.605	23.56		±0.69
12HT4Mo.I	12.04	16.44	6.70	540	500	25.70	1.07	13.36	0.52	-	-	420	2.964	25.13	462	26.1
12HT4Mo.II	11.98	17.85	8.05	505	472	26.50	1.07	15.72	0.59	-	-	-	-	-		±0.40

Table 11: Fracture toughness test data and results for the alloys heat treated at 1180°C for 12 hours

Specimen	B mm	W mm	a mm	P_{max} kg	P_Q kg	K_Q $MN/m^{3/2}$	P_{max}/P_Q	K_F $MN/m^{3/2}$	K_F/K_Q	σ_{ys} N/mm^2	Limit. Thick. mm	P_c kg	J (KJ/m^2)	$K_{Q(J)}$ $MN/m^{3/2}$	Hard. Hv30	K_{IC} $MN/m^{3/2}$
24HT15.3I	11.90	17.97	8.65	325	305	18.83	1.06	13.58	0.72	-	-	240	1.37	17.12	602	19.29 ±0.46
24HT15.3II	11.95	17.98	8.50	350	330	19.75	1.06	13.17	0.66	-	-	270	1.29	16.61		
24HT1MoI	12.00	18.00	9.25	425	390	26.44	1.08	17.63	0.66	-	-	330	2.45	22.87	515	26.32 ±0.13
24HT1MoII	11.98	18.01	8.30	485	455	26.19	1.06	14.96	0.57	-	-	360	2.16	21.50		
24HT2MoI	11.97	18.05	8.60	495	460	27.75	1.07	15.68	0.56	-	-	340	2.53	23.24	441	27.75 ±
24HT2MoII	11.99	18.01	Fractures during fatigue pre-cracking							-	-	-	-	-		
24HT4MoI	11.95	17.99	8.90	380	360	23.06	1.05	16.65	0.72	-	-	290	1.677	18.91	438	23.98 ±0.92
24HT4MoII	11.96	18.02	9.05	410	380	24.89	1.07	17.03	0.68	-	-	320	2.452	22.86		
24HT1WI	11.88	17.99	8.15	440	410	23.27	1.07	14.45	0.63	-	-	320	223	21.84	510	23.06 ±0.21
24HT1WII	11.89	17.99	8.90	380	355	22.85	1.07	16.74	0.73	-	-	325	2.07	21.03		
24HT3WI	11.93	18.05	8.0	425	395	25.62	1.07	16.86	0.65	-	-	340	2.30	22.16	475	25.32 ±0.30
24HT3WII	11.92	18.06	8.65	430	410	25.02	1.04	15.87	0.83	-	-	330	2.506	23.11		
24HT5WI	11.95	18.03	8.6	495	465	28.16	1.06	15.74	0.55	-	-	390	3.05	25.53	440	27.74 ±0.42
24HT5WII	11.96	18.03	8.95	460	425	27.32	1.08	16.71	0.61	-	-	360	2.67	23.86		

Table 12: Fracture toughness test data and results for the alloys heat treated at 1180°C for 24 hours

Specimen	B mm	W mm	a mm	P_{max} kg	P_Q kg	K_Q $MN/m^{3/2}$	P_{max}/P_Q	K_F $MN/m^{3/2}$	K_F/K_Q	σ_{ys} N/mm^2	Limit. Thick. mm	P_c kg	J (KJ/m^2)	$K_{Q(J)}$ $MN/m^{3/2}$	Hard. Hv30	K_{IC} $MN/m^{3/2}$
72HT15.3I	11.52	17.32	7.70	470	450	26.18	1.04	13.96	0.53	986	1.76	-	-	-	560	25.78 ±0.41
72HT15.3II	11.36	17.19	7.35	480	450	25.37	1.06	13.53	0.53	986	1.65	-	-	-		
72HT1MoI	11.93	17.96	8.55	455	420	25.46	1.08	15.76	0.61	-	-	360	1.668	18.85	475	25.02 ±0.44
72HT1MoII	11.94	17.95	8.85	470	385	24.58	1.06	14.04	0.57	-	-	370	2.097	21.14		
72HT2MoI	11.96	18.08	9.05	425	390	25.36	1.08	16.91	0.66	711	3.18	360	1.833	19.77	442	26.35 ±1.00
72HT2MoII	11.95	18.08	8.30	480	450	27.34	1.06	15.79	0.57	711	3.69	395	2.708	24.02		
72HT4MoI	11.96	18.02	8.45	440	410	24.31	1.07	16.54	0.68	737	2.72	-	-	-	422	23.41 ±0.89
72HT4MoII	11.95	17.91	8.05	430	405	22.52	1.06	15.57	0.69	737	2.33	-	-	-		
72HT1WI	11.85	17.97	8.90	420	400	25.90	1.05	16.83	0.65	-	-	380	1.881	20.02	465	25.62 ±0.30
72HT1WII	11.87	17.97	9.00	420	385	25.33	1.09	17.10	0.67	-	-	340	1.661	18.81		
72HT3WI	11.90	18.00	9.05	385	360	23.75	1.06	17.15	0.72	-	-	330	2.408	22.66	454	25.96 ±0.21
72HT3WII	11.89	18.03	8.95	450	415	26.16	1.06	18.01	0.68	-	-	370	2.008	20.69		
72HT5WI	11.71	17.83	8.43	430	405	24.85	1.06	17.18	0.69	-	-	-	-	-	431	24.28 ±0.57
72HT5WII	11.67	17.61	7.42	480	455	23.71	1.07	14.91	0.62	-	-	-	-	-		

Table 13: Fracture toughness test data and results for the alloys heat treated at 1180°C for 72 hours

Specimen	B mm	W mm	a mm	P_{max} kg	P_Q kg	K_Q $MN/m^{3/2}$	P_{max}/P_Q	K_F $MN/m^{3/2}$	K_F/K_Q	σ_{ys} N/mm^2	Limit. Thick. mm	P_c kg	J (KJ/m^2)	$K_{Q(J)}$ $MN/m^{3/2}$	Hard. Hv30	K_{IC} $MN/m^{3/2}$
M15.3.I	11.90	17.70	9.10	310	305	21.04	1.01	13.8	0.65	1305	0.64	280	1.636	18.67	770	21.63 ±0.60
M15.3.II	11.85	17.75	8.06	395	380	21.83	1.10	13.67	0.61	1305	0.70	340	1.302	16.66		
M1.Mo.I	11.90	17.76	8.22	315	315	18.49	1.00	11.74	0.63	-	-	245	1.290	16.58	853	18.93 ±0.44
M1.Mo.II	11.85	17.76	8.47	335	315	19.38	1.06	12.30	0.63	-	-	-	-	-		
M2.Mo.I	10.90	17.73	8.69	290	275	19.17	1.05	13.94	0.72	1310	0.53	225	1.160	15.72	842	21.24 ±2.07
M2.Mo.II	10.84	17.78	8.85	340	325	23.31	1.04	14.34	0.61	1310	0.80	270	1.658	18.80		
M4.Mo.I	12.42	17.31	7.98	355	345	19.55	1.02	11.33	0.57	-	-	280	1.630	18.64	859	18.83 ±0.73
M4.Mo.II	12.47	17.32	8.65	295	285	18.10	1.03	12.7	0.70	-	-	240	1.101	15.32		

Table 14: Fracture toughness test data and results for the alloys hardened by following the commercial hardening procedures

Specimen	B mm	W mm	a mm	P_{max} kg	P_Q kg	K_Q $MN/m^{3/2}$	P_{max}/P_Q	K_F $MN/m^{3/2}$	K_F/K_Q	σ_{ys} N/mm^2	Limit. Thick. mm	P_c kg	J (KJ/m^2)	$K_{Q(J)}$ $MN/m^{3/2}$	Hard. Hv30	K_{IC} $MN/m^{3/2}$
4M15.3.I	11.52	17.73	8.70	322	315	20.82	1.02	13.22	0.63	-	-	280	1.630	18.64	780	20.57 ±0.25
4M15.3.II	11.51	17.74	8.84	315	300	20.32	1.05	13.54	0.66	-	-	245	1.287	16.56		
4M. 1Mo.I	11.57	17.67	8.70	325	320	21.20	1.01	13.25	0.62	-	-	255	1.616	18.56	809	20.82 ±0.40
4M.1Mo.II	11.62	17.68	8.61	330	315	20.43	1.04	12.97	0.63	-	-	280	1.289	16.57		
4M.2Mo.I	11.71	17.41	8.51	340	325	2120	1.04	13.04	0.61	-	-	290	1.005	14.63	809	21.87 ±0.67
4M.2Mo.II	11.56	17.42	8.45	360	345	22.53	1.04	13.06	0.57	-	-	305	1.29	16.5		
4M.4Mo.I	12.12	17.72	8.64	310	300	18.67	1.03	12.44	0.66	-	-	245	1.497	17.86	812	18.73 ±0.06
4M.4Mo.II	12.14	17.74	8.51	320	310	18.78	1.03	12.12	0.64	-	-	260	1.552	18.19		

Table 15: Fracture toughness test data and results for the alloys heat treated at 1180°C for 4 hours then commercially hardened

Specimen	B mm	W mm	a mm	P_{max} kg	P_Q kg	K_Q $MN/m^{3/2}$	P_{max}/P_Q	K_F $MN/m^{3/2}$	K_F/K_Q	σ_{ys} N/mm^2	Limit. Thick. mm	P_c kg	J (KJ/m^2)	$K_{Q(J)}$ $MN/m^{3/2}$	Hard. Hv30	K_{IC} $MN/m^{3/2}$
12M15.3.I	12.04	17.24	7.79	380	365	20.80	1.04	11.44	0.54	1346	0.60	325	1.32	16.78	801	20.22
12M15.3.II	12.05	17.22	7.86	355	340	19.64	1.04	11.55	0.58	1346	0.53	285	1.209	16.05		±0.60
12M1.Mo.I	11.30	17.23	7.85	380	355	21.81	1.07	12.28	0.56	-	-	290	1.325	16.80	821	22.03
12M1.Mo.II	11.29	17.23	7.72	395	370	22.25	1.06	12.02	0.54	-	-	315	1.338	16.89		±0.22
12M2.Mo.I	11.55	17.22	7.58	425	395	22.69	1.07	11.49	0.50	1380	0.67	305	1.376	17.13	833	21.63
12M2.Mo.II	11.57	17.23	7.73	377	350	20.57	1.07	11.75	0.57	1380	0.55	285	1.666	18.85		±1.06
12M4.Mo.I	12.19	17.23	8.18	335	325	19.6	1.03	12.06	0.61	1410	0.50	280	1.305	16.68	821	19.06
12M4.Mo.II	12.20	17.28	7.89	345	325	18.52	1.06	11.39	0.61	1410	0.48	290	1.219	16.05		±0.54

Table 16: Fracture toughness test data and results for the alloys heat treated at 1180°C for 12 hours then commercially hardened

Specimen	B mm	W mm	a mm	P_{max} kg	P_Q kg	K_Q $MN/m^{3/2}$	P_{max}/P_Q	K_F $MN/m^{3/2}$	K_F/K_Q	σ_{ys} N/mm^2	Limit. Thick. mm	P_c kg	J (KJ/m^2)	$K_{Q(J)}$ $MN/m^{3/2}$	Hard. Hv30	K_{IC} $MN/m^{3/2}$
72M 15.3 I	10.67	17.32	8.54	312	290	21.09	1.08	14.55	0.68	-	-	275	1.262	16.40	798	22.05 ± 0.96
72M 15.3 II	10.66	17.31	8.55	332	215	23.0	1.04	14.6	0.63	-	-	295	1.394	17.23		
72M1 No I	11.37	17.32	7.71	390	375	22.14	1.04	11.81	0.53	-	-	315	2.086	21.09	821	22.40 ± 0.37
72M1 No II	11.36	17.01	8.06	365	352	22.87	1.03	12.99	0.56	-	-	-	-	-		
72M2 No I	12.09	17.33	7.92	395	370	21.27	1.06	11.49	0.54	-	-	-	-	-	810	21.28 ± 0.01
72M2 No II	12.08	17.30	8.08	375	357	21.18	1.05	11.87	0.56	-	-	285	1.744	19.28		
72M4 No I	12.08	16.42	6.83	405	405	21.26	1.00	10.49	0.49	-	-	385	1.345	16.99	801	21.06 ± 0.86
72M4 No II	12.07	16.40	7.50	360	350	20.74	1.02	11.85	0.57	-	-	-	-	-		

Table (17) Fracture toughness test data and results of the alloys heat treated at 1180°C for 72 hours then commercially hardened.

Specimen	B mm	W mm	a mm	P_{max} kg	P_Q kg	K_Q $MN/m^{3/2}$	P_{max}/P_Q	K_F $MN/m^{3/2}$	K_F/K_Q	σ_{ys} N/mm^2	Limit. thick. mm	P_c kg	J (KJ/m^2)	$K_{Q(J)}$ $MN/m^{3/2}$	Hard. Hv30	K_{IC} $MN/m^{3/2}$
1075/15.3 I	10.77	17.51	8.85	295	285	20.87	1.05	14.9	0.71	-	-	220	20.59	20.95	780	21.75 ± 0.87
1075/15.3 II	10.78	17.41	8.56	330	320	22.61	1.03	14.12	0.62	-	-	245	2.232	21.81		
1075/1 Mo I	11.94	17.51	8.43	427	402	25.25	1.04	14.96	0.59	-	-	290	16.76	18.90	788	24.43 ± 0.82
1075/1 Mo II	11.94	17.51	8.26	425	390	23.61	1.08	14.52	0.61	-	-	275	1.592	18.42		
1075/2 Mo I	12.13	17.41	8.06	450	415	24.15	1.08	13.96	0.57	-	-	360	1.837	19.79	812	24.76 ± 0.61
1075/2 Mo II	12.13	17.42	8.01	480	440	25.36	1.09	13.83	0.54	-	-	340	2.241	21.86		
1075/4 Mo I	17.42	17.42	8.02	465	425	24.64	1.09	13.91	0.56	-	-	355	2.008	20.69	801	24.37 ± 0.27
1075/4 Mo II	12.08	17.41	7.68	470	440	24.10	1.06	13.15	0.54	-	-	-	-	-		

Table (18) Fracture toughness test data and results for the alloys heat-treated at $1075^{o}C$ for 12 hours.

Specimen	B mm	W mm	a mm	P_{max} kg	P_Q kg	K_Q $MN/m^{3/2}$	P_{max}/P_Q	K_F $MN/m^{3/2}$	K_F/K_Q	σ_{ys} N/mm^2	Limit Thick. mm	P_c kg	J (KJ/m^2)	$K_{Q(J)}$ $MN/m^{3/2}$	Hard. Hv30	K_{IC} $MN/m^{3/2}$
1125/15.3 I	11.55	17.55	8.11	350	350	21.25	1.00	12.14	0.57	-	-	320	2.01	20.70	692	20.20 ± 0.95
1125/13.3 II	11.56	17.53	7.72	355	340	19.35	1.04	11.38	0.58	-	-	305	1.467	17.58		
1125/1 Mo I	11.71	17.56	8.01	495	455	26.76	1.08	14.11	0.52	-	-	360	2.416	22.69	614	27.46 ± 0.70
1125/1 Mo II	11.72	17.54	8.05	515	475	28.16	1.08	14.23	0.50	-	-	380	2.171	21.51		
1125/2 Mo I	10.70	17.56	8.03	535	490	31.65	1.09	16.79	0.53	-	-	405	3.614	27.75	590	30.94 ± 0.71
1125/2 Mo II	10.69	17.58	7.49	540	510	30.23	1.05	15.41	0.50	-	-	420	3.620	27.78		
1125/4 Mo I	11.87	17.18	7.48	515	475	26.22	1.08	14.35	0.54	-	-	385	2.259	21.94	609	25.10 ± 1.12
1125/4 Mo II	11.86	17.20	6.81	520	475	23.98	1.07	12.86	0.53	-	-	405	1.880	20.02		

Table (19) Fracture toughness test-date and results for the alloys heat-treated at 1125°C for 12 hours.

ALLOY	B mm	W mm	C mm	ρ mm	K_{IC} $MN/m^{3/2}$	σ_{ys} N/mm^2	P_{max} kg	General Yield limit N/mm^2	Outer Fibre Stress N/mm^2	Plastic zone R_c mm	σ_F N/mm^2	Average σ_F^* N/mm^2	$K_{IC(\rho)}$ $MNM^{3}/_{2}$	K_Q $MNm^{3/2}$	Average $K_{IC(c)}$ $NXMP^{3/2}$
As15.3 1.1	9.48	9.46	1.98	0.279	20.58	1350	430	1843	431	0.03	1487		21.36	22.03	22.39
As15.3 1.2	9.45	9.49	1.80	0.318	"	"	525	1936	524	0.048	1539	1492 ± 29	27.03	25.54	23.17
As15.3 3.1	9.47	9.48	2.05	0.686	"	"	615	1811	656	0.072	1484		33.10	32.09	34.03
As15.3 3.2	9.46	9.44	2.00	0.686	"	"	590	1831	625	0.058	1459		29.71	30.53	34.03
As2 Mo1.1	9.47	9.47	1.82	0.305	24.3	1195	525	1703	552	0.08	1473		30.88	26.89	21.90
As2 Mo1.2	9.48	9.48	2.16	0.292	"	"	395	1556	433	0.04	1348		21.84	21.22	21.42
As2 Mo2.1	9.47	9.49	2.08	0.432	"	"	455	1591	488	0.048	1320	1343 ± 60	23.92	23.70	26.06
As2 Mo2.2	9.46	9.48	2.04	0.432	"	"	455	1607	484	0.046	1315		23.42	23.70	26.06
As2 Mo3.1	9.41	9.49	2.05	0.686	"	"	540	1604	578	0.072	1314		29.30	28.32	32.84
As2 Mo3.2	9.46	9.49	2.05	0.686	"	"	505	1561	553	0.058	1291		27.08	26.30	32.84
As4 Mo1.1	9.46	9.49	1.99	0.292	23.30	1167	440	1591	461	0.052	1358		24.32	22.57	22.16
As4 Mo1.2	9.47	9.49	1.99	0.292	"	"	440	1591	461	0.052	1358	1328 ± 29	24.32	22.55	22.16
As4 Mo3.1	9.47	9.50	2.08	0.686	"	"	555	1554	595	0.088	1307		31.63	29.13	33.97
As4 Mo3.2	9.41	9.49	2.04	0.686	"	"	540	1570	577	0.078	1292		29.78	28.24	33.97

Table (20) Notch bending test data and results for the alloys in as-cast condition

ALLOY	B	W	C	ρ	K_{IC}	σ_{ys}	P_{max}	General Yield limit	Outer Fibre Stress	Plastic zone R_c	σ_F	Average σ_F	$K_{IC(\rho)}$	K_Q	Average $K_{IC(\rho)}$
	mm	mm	mm	mm	$MN/m^{3/2}$	N/mm^2	kg	N/mm^2	N/mm^2	mm	N/mm^2	N/mm^2	$MNM^{3}/2$	$NMm^{3/2}$	$NNM^{3/2}$
8HT.15 3.1.1	9.49	9.54	1.90	0.315	20.0	1071	610	1500	618	0.13	1441		35.29	30.25	32.41
8HT.15 3.1.2	9.54	9.56	2.05	0.305	"	"	590	1443	616	0.13	1451	1391 ± 54	35.29	30.29	31.89
8HT.15 3.3.1	9.49	9.54	2.02	0.711	"	"	690	1453	721	0.196	1331		43.33	35.39	48.70
8HT.15 3.3.2	9.51	9.50	2.01	0.711	"	"	705	1453	738	0.206	1343		44.42	36.14	48.70
8HT. 2Mo 1.1	9.54	9.57	1.84	0.318	30.13	928	590	1322	582	0.154	1294		33.28	28.52	30.74
8HT. 2Mo 1.2	9.53	9.52	1.94	0.318	"	"	590	1284	603	0.164	1313		34.34	29.53	30.74
8HT. 2Mo 2.1	9.52	9.51	2.12	0.432	"	"	565	1223	608	0.174	1242	1249 ± 40	35.37	29.80	35.83
8HT. 2Mo 2.2	9.50	9.55	2.16	0.432	"	"	565	1213	611	0.178	1248		35.78	30.05	35.83
8HT. 2Mo 3.1	9.50	9.55	2.06	0.686	"	"	640	1246	674	0.234	1200		41.02	33.12	45.15
8HT. 2Mo 3.2	9.52	9.54	2.18	0.686	"	"	620	1206	674	0.232	1198		40.84	33.12	45.15
8HT. 4Mo 1.1	9.50	9.53	1.85	0.318	26.34	845	640	1198	640	0.216	1283		35.89	31.29	31.68
8HT. 4Mo 1.2	9.53	9.51	1.90	0.305	"	"	580	1181	588	0.184	1243	1204 ± 60	33.12	28.73	31.02
8HT. 4Mo 3.1	9.47	9.55	2.06	0.686	"	"	655	1135	692	0.300	1151		42.29	34.01	46.53
8HT. 4Mo 3.2	9.52	9.49	2.08	0.686	"	"	635	1125	678	0.286	1139		41.29	33.20	46.53

Table (21) Notch banding test data and results for the alloys heat treated at 1180°C for 8 hours

ALLOY	B mm	W mm	C mm	ρ mm	K_{IC} $MN/m^{3/2}$	σ_{ys} N/mm^2	P_{max} kg	General Yield limit N/mm^2	Outer Fibre Stress N/mm^2	Plastic zone R_c mm	σ_F N/mm^2	Average σ_F* N/mm^2	$K_{IC(\rho)}$ $MNM^{3/2}$	K_Q $NMm^{3/2}$	Average $K_{IC(\rho)}$ $NNM^{3/2}$
72HT 15.3.1.1	9.53	9.56	1.84	0.318	25.78	986	595	1404	589	0.14	1345		33.71	28.82	29.23
72HT 15.3.1.2	9.48	9.51	1.90	0.305	"	"	545	1378	555	0.124	1322	1268	31.73	27.14	28.63
72HT 15.3.3.1	9.50	9.53	2.08	0.711	"	"	590	1316	627	0.17	1197	± 65	37.15	30.77	43.72
72HT 15.3.3.2	9.51	9.52	2.06	0.711	"	"	610	1322	645	0.182	1210		38.44	31.64	43.72
72HT 2Mo 1.1	9.48	9.53	1.94	0.305	26.35	711	610	984	626	0.274	1166		24.01	30.66	31.03
72HT 2Mo 1.2	9.43	9.52	1.96	0.305	"	"	575	979	597	0.254	1141		32.74	29.25	31.03
72HT 2Mo 2.1	9.50	9.51	2.06	0.432	"	"	565	969	657	0.330	1114	1108	37.32	32.30	36.93
72HT 2Mo 2.2	9.48	9.53	2.00	0.432	"	"	630	952	599	0.282	1068	± 36	34.50	29.37	36.93
72HT 2Mo 3.1	9.47	9.51	2.09	0.711	"	"	675	971	724	0.492	1064		43.97	36.77	47.38
72HT 2Mo 3.2	9.48	9.53	2.02	0.686	"	"	740	964	776	0.5	1100		45.94	38.04	46.54
72HT 4Mo 1.1	9.53	9.51	1.96	0.305	23.41	737	585	1014	602	0.242	1167		33.13	29.48	31.01
72HT 4Mo 1.2	9.52	9.54	1.86	0.292	"	"	630	1043	629	0.256	1200	1126	34.07	30.76	30.34
72HT 4Mo 3.1	9.54	9.52	2.05	0.686	"	"	720	991	757	0.46	1115	± 66	45.68	37.13	46.51
72HT 4Mo 3.2	9.51	9.51	2,10	0.686	"	"	590	977	632	0.328	1025		38.57	30.98	46.51

Table (22): Notch Bending test data and results for the alloys heat-treated at 1180°C for 72 hours

ALLOY	B	W	C	ρ	K_{IC}	σ_{ys}	P_{max}	General Yield limit	Outer Fibre Stress	Plastic zone R_c	σ_F	Average σ_F*	$K_{IC(\rho)}$	K_Q	Average $K_{IC(\rho)}$
	mm	mm	mm	mm	$MN/m^{3/2}$	N/mm^2	kg	N/mm^2	N/mm^2	mm	N/mm^2	N/mm^2	$MNM^{3/2}$	$NMm^{3/2}$	$NNM^{3/2}$
M.15.3.1.1	9.50	9.52	2.00	0.305	21.63	1305	520	1778	542	0.06	1539		29.21	26.55	29.79
M.15.3.1.2	9.52	9.51	1.86	0.318	"	"	615	1844	617	0.084	1610	1548	34.56	30.37	30.42
M.15.3.3.1	9.46	9.54	2.10	0.686	"	"	660	1733	707	0.108	1495	± 41	39.19	34.72	44.68
M.15.3.3.2	9.49	9.52	2.10	0.686	"	"	725	1731	777	0.142	1550		44.94	38.10	44.68
M2 Mo 1.1	9.47	9.47	1.90	0.318	21.24	1310	520	1828	533	0.056	1522		28.33	26.49	24.41
M2 Mo 1.2	9.46	9.49	2.00	0.254	"	"	470	1782	494	0.048	1536		26.22	24.18	21.81
M2 Mo 2.1	9.48	9.44	2.18	0.419	"	"	475	1692	528	0.046	1446	1471	25.67	24.52	28.02
M2 Mo 2.2	9.46	9.49	2.16	0.419	"	"	465	1706	510	0.040	1429	± 41	23.94	25.03	28.02
M2 Mo 3.1	9.48	9.49	2.16	0.711	"	"	600	1706	657	0.08	1449		33.86	32.20	36.50
M2 Mo 3.2	9.48	9.43	2.00	0.711	"	"	620	1776	657	0.08	1449		33.86	32.30	36.50

Table (23): Notch bending test data and results of the alloys, commercially hardened

ALLOY	B mm	W mm	C mm	ρ mm	K_{IC} MN/m$^{3/2}$	σ_{ys} N/mm^2	P_{max} kg	General Yield limit N/mm^2	Outer Fibre Stress N/mm^2	Plastic zone R_c mm	σ_F N/mm^2	Average σ_F* N/mm^2	$K_{IC(\rho)}$ MNM$^{3/2}$	K_Q NMm$^{3/2}$	Average $K_{IC(o)}$ NNM$^{3/2}$
12M 15.3L1	9.53	9.54	2.05	0.229	20.22	1346	490	1812	514	0.052	1621		28.05	25.23	25.10
12M 15.3L2	9.53	9.51	1.97	0.229	"	"	460	1847	475	0.040	1562	1571 ± 33	24.60	23.24	25.10
12M 15.3S1	9.50	9.52	2.04	0.686	"	"	675	1814	711	0.10	1529		38.89	34.18	43.45
12M 15.3S2	9.50	9.52	2.04	0.711	"	"	740	1814	779	0.132	1575		44.69	38.21	44.24
12M2 Mo L1	9.48	9.43	1.96	0.305	21.63	1380	520	1891	545	0.052	1597		28.75	26.58	25.99
12M2 Mo L2	9.44	9.50	1.96	0.292	"	"	510	1898	531	0.048	1590		27.63	25.97	25.43
12M2 Mo 2L	9.45	9.45	2.06	0.432	"	"	515	1843	554	0.044	1513	1560 ± 33	26.45	27.01	30.94
12M2 Mo 2S	9.43	9.50	2.03	0.432	"	"	590	1863	626	0.070	1587		33.36	30.67	30.94
12M2 Mo 3L	9.42	9.50	1.95	0.711	"	"	660	1903	687	0.078	1523		35.22	33.59	39.69
12M2 Mo 3S	9.45	9.49	1.94	0.686	"	"	690	1907	715	0.092	1553		38.25	34.95	38.98
12M4 Mo L1	9.53	9.52	2.00	0.229	19.06	1410	470	1925	488	0.038	1629		25.17	23.93	20.58
12M4 Mo L2	9.49	9.54	2.03	0.229	"	"	470	1912	492	0.034	1568	1559 ± 47	23.81	24.17	20.58
12M4 Mo L3	9.49	9.54	2.03	0.229	"	"	605	1952	628	0.044	1497		27.08	30.59	36.27
12M4 Mo 3S	9.53	9.54	2.00	0.711	"	"	655	1927	678	0.068	1542		33.67	32.59	36.27

Table (24): Notch bending test data and results for the alloys heat-treated at 1180°C for 12 hours then commercially hardened

ALLOY	B	W	C	ρ	K_{IC}	σ_{ys}	P_{max}	General Yield limit	Outer Fibre Stress	Plastic zone R_c	σ_F	Average σ_F*	$K_{IC(\rho)}$	K_Q	Average $K_{IC(\rho)}$
	mm	mm	mm	mm	$MN/m^{3/2}$	N/mm^2	kg	N/mm^2	N/mm^2	mm	N/mm^2	N/mm^2	$MNM^{3/2}$	$NMm^{3/2}$	$NNM^{3/2}$
72M2 Mo L1	9.55	9.52	2.01	0.292	21.28	1368	485	1859	504	0.042	1551		25.62	24.70	25.33
72M2 Mo L2	9.49	9.53	2.02	0.305	"	"	520	1855	544	0.054	1590	1548 ± 27	29.05	26.70	25.89
72M2 Mo 21	9.49	9.49	2.05	0.432	"	"	550	1836	584	0.058	1540		30.10	28.60	30.81
72M2 Mo 22	9.50	9.52	2.05	0.432	"	"	525	1839	554	0.048	1512		27.39	27.18	30.81

Table (25): Notch bending test data and results of the alloy heat-treated at 1180°C for 72 hours then commercially hardened

Table 26: Experimental compliance test data for type-I short-bar fracture toughness specimen

a/W	CEB
0.246	42.416
0.256	47.560
0.300	52.000
0.314	48.293
0.343	53.265
0.356	56.328
0.415	70.183
0.434	68.974
0.477	79.501
0.477	78.120
0.553	100.888
0.555	97.587
0.589	110.081
0.623	127.231
0.651	142.439
0.676	156.925
0.708	182.977
0.739	215.990
0.748	227.354
0.794	319.028
0.797	325.130
0.836	476.294
0.839	450.612
0.887	867.821
0.917	1530.509

Table 27: Experimental compliance test data for type-II short-bar fracture toughness specimen

a/W	CEB
0.312	81.574
0.318	79.177
0.322	80.404
0.363	87.132
0.376	89.275
0.390	84.699
0.393	90.630
0.414	94.301
0.483	109.933
0.486	110.428
0.498	113.409
0.522	121.904
0.542	127.614
0.557	131.705
0.566	138.124
0.572	140.249
0.592	152.162
0.619	164.890
0.648	180.825
0.651	182.864
0.667	194.013
0.682	212.615
0.684	211.014
0.702	230.856
0.711	240.975
0.737	267.246

Table 27 (continued)

a/W	CEB
0.746	277.404
0.782	350.650
0.786	355.796
0.812	435.156
0.813	439.850
0.832	516.051
0.843	543.195
0.878	879.754
0.886	970.508

Table 28: Experimental compliance test data for type-III short-bar fracture toughness specimen

a/W	CEB
0.261	67.697
0.270	66.139
0.319	68.059
0.331	70.720
0.334	72.820
0.361	75.920
0.386	80.982
0.425	83.865
0.430	91.137
0.457	92.289
0.475	101.528
0.502	107.316
0.532	122.099
0.546	124.187
0.590	147.335
0.608	152.164
0.647	168.767
0.662	188.930
0.699	213.290
0.731	252.642
0.736	250.890
0.760	290.969
0.791	333.705
0.804	384.754
0.834	485.079
0.868	702.507

Table 29: Comparison of experimentally obtained compliance results with the results obtained analytically from Bluhm's slice model

a/W	CEB (experimental) (Perspex tests)	CEB (analytical) (Bluhm's Model)	% Difference
For type-I short bar specimen geometry			
0.25	44.313	29.297	34
0.30	49.841	34.954	30
0.35	56.316	41.847	26
0.40	64.039	50.177	22
0.45	73.435	60.289	18
0.50	85.119	72.736	15
0.55	100.031	88.466	11
0.60	119.666	109.269	9
0.65	146.552	138.665	5
0.70	185.282	183.802	1
0.75	245.045	260.430	6
0.80	346.862	408.881	18
0.85	549.501	761.367	36
For type-II short bar specimen geometry			
0.35	84.79	67.614	20
0.40	93.182	79.767	14
0.45	103.450	94.36	9
0.50	116.282	112.265	3
0.55	132.732	134.357	1
0.60	154.505	162.337	5
0.65	184.521	199.649	8
0.70	228.188	253.742	11
0.75	296.605	341.302	15
0.80	416.089	503.706	21

Table 29 (continued)

a/W	CEB (experimental) (Perspex tests)	CEB (analytical) (Bluhm's Model)	%Difference
For type-III short bar specimen geometry			
0.30	69.214	52.522	23
0.35	76.415	62.600	17
0.40	84.996	74.732	10
0.45	95.407	89.319	6
0.55	108.313	106.971	
0.55	124.719	128.636	3
0.60	146.229	155.977	7
0.65	175.556	192.369	9
0.70	217.627	245.122	12
0.75	282.828	339.598	17
0.80	392.368	489.372	24
0.85	611.907	844.653	32

Table 30 The curve fitting parameters of the Ryder's exponential solution for the experimental compliance data.

The non-dimensionless experimental compliance data expressed given equation below

$$CEB = \exp(\exp(F/a/W))) - 2.71828$$

$$F(a/W) = e + (v-e)(-\ell n(1-(a/W)))^{1/k}$$

Specimen Type	e	v	k
Type I	1.1748	1.5915	1.3950
Type II	1.3874	1.6387	1.0016
Type III	1.3265	1.6287	1.599

Table 31 Experimentally and analytically (Bluhm's slice model) obtained minimum stress intensity coefficients and corresponding critical crack length ratios.

	Experimental		Analytical	
	a_c/W	Ym*	a_c/W	Ym*
Type I	0.471	17.87	0.470	18.94
Type II	0.512	22.28	0.525	26.82
Type III	0.481	20.33	0.500	24.39

ALLOY	SPECIMEN TYPE	Test No	P_{max} kg	Constant A	K_{ICSB} MN $m^{-3/2}$	Average K_{ICSB} MN $m^{-3/2}$	Average K_{IC} MN $m^{-3/2}$
AS 15.3	Type 1 12 x 12 mm square	1	188	14.93	20.93	21.9 ± 0.6	20.58 ± 1.08
	"	2	195	"	22.05		
	"	3	198	"	22.05		
	"	4	203	"	22.63		
AS 1 Mo	"	1	208	"	23.16	22.6 ± 0.4	23.0 ± 0.24
	"	2	203	"	22.60		
	"	3	198	"	22.64		
AS 3W	"	1	210	"	23.38	24.20 ± 0.7	25.98 ± 0.26
	"	2	225	"	25.06		
24HT 2 Mo	"	1	252	"	28.06	28.5 ± 0.4	27.75 ± 0.70
	"	2	260	"	28.95		
8HT 2Mo	"	1	250	"	27.84	28.95 ± 1.10	30.13 ± 0.18
	"	2	270	"	30.07		
AS 6 Mo	"	1	235	"	26.17	24.7 ± 1.3	23.80 ± 0.36
	"	2	210	"	23.38		

Table 32: Test data and results of short-bar fracture toughness tests

ALLOY	SPECIMEN TYPE	Test No	P_{max} k_g	Constant A	K_{ICSB} MN $m^{-3/2}$	Average K_{ICSB} MN $m^{-3/2}$	Average K_{IC} MN $m^{-3/2}$
8HT 5W	Type I 12 x 12 mm square	1	273	14.93	30.40	30.4 ± 0.9	30.38 ± 0.35
	"	2	260	"	28.95		
	"	3	285	"	31.74		
15.3 + 3 Mo Annealed	"	1	160	"	17.82	18.6 ± 0.6	19.6 ± 0.6
	"	2	170	"	18.93		
	"	3	172	"	19.15		

Table 32 (Continued)

ALLOY	SPECIMEN TYPE	Test No	P_{max} k_g	Constant A	K_{ICSB} MN $m^{-3/2}$	Average K_{ICSB} MN $m^{-3/2}$	Average K_{IC} MN $m^{-3/2}$
15.3 + 3 Mo Annealed	Type I 12 x 12 mm square	1	160	14.93	17.82	18.6 ± 0.6	19.6 ± 0.6
	"	2	170	"	18.93		
	"	3	172	"	19.15		
15.3 + 3 Mo Annealed	Type III 1'rectangular	1	525	16.97	21.58	20.8 ± 0.6	19.6 ± 0.6
	"	2	520	"	21.37		
	"	3	475	"	19.52		
* 15.3 + 3 Mo Annealed	Type II 1'rectanular	1	494	15.0	20.30	19.5 ±0.8	19.6 ±0.6
	"	2	453	15.0	18.79		

* Tested by using fractometer - II

Table 33: The effects of the notch configuration and size of the short-bar specimens on the toughness measurements of high-Cr cast irons

Table 34 : Fatigue-Crack Growth Data of a Series of High-Cr Cast Iron

The crack growth rates were expressed in given equation below which is suggested by Paris - Erdogan (162). The constants in the equation were lists as a table.

$$da/dN = C.(\Delta K)^m$$

ALLOY	C	M
As - Cast Base Alloy	- 11.1367	5.333
As - Cast 1 Mo	- 14.031	7.7661
As - Cast 2 Mo	- 14.004	7.655
As - Cast 4 Mo	- 10.057	4.647
As - Cast 1W	- 11.4786	5.622
As - Cast 3W	- 11.749	5.805
As - Cast 5W	- 10.788	5.113
8 HT 1 Mo	- 13.081	6.559
8 HT 2 Mo	- 11.190	4.923
8 HT 4 Mo	- 11.219	5.262
8 HT 1 W	- 15.606	9.846
8 HT 3 W	- 14.525	7.983
8 HT 5 W	- 10.525	4.531

IX DISCUSSION OF RESULTS

General

The effects of high temperature heat treatments on the break-up and spheroidisation of continuous eutectic-carbide network within the microstructure of 15% Cr and 2.7% C commercial grade high-Cr cast iron were examined. The role of molybdenum, manganese, tungsten and vanadium additions in this process was investigated together with heat treatment variables.

The variations in the fracture characteristics of high-Cr cast irons with these metallurgical variables were evaluated for sharp-cracks and blunt notches. The data obtained from these tests were used in conjunction with metallographic and fractographic studies in order to establish the possible inter-relationship between microstructure and failure mechanism of high-Cr cast irons.

The validity and applicability of short-bar/rod fracture toughness testing for determination of fracture toughness of high-Cr cast irons were discussed. The stress intensity coefficients of different short-bar fracture toughness test specimens were represented with analytical and experimental studies.

9.1 Microstructure of High-Cr Cast Irons and Effects of the Metallurgical Variables on the Eutectic Carbide Morphology

High-Cr cast irons comprise austenite dendrites surrounded by an eutectic with hard M_7C_3 particles constituting 20-40% by volume according to the carbon content. The austenite

may remain or transform to martensite according to chemical composition, cooling rate and heat treatment. The variation in the eutectic-carbide morphology with the Cr and C content of high-Cr cast irons have been described during the construction of Fe-Cr-C ternary system [7-14] and isothermal transformation diagrams of high-Cr cast irons [38]. For a given Cr level, lowering the carbon content of the alloys towards the ferrite primary phase field (A-B line in Fig. 1) causes a decrease in the volume % of the eutectic-carbides. When the carbon level is decreased to less than about 1.5% C at 15% Cr the continuous network of eutectic carbides of high carbon levels changes to isolated particles [53]. The decrease in the carbon content lowers the overall hardness of the alloys consequently the wear resisting properties. For a high-Cr cast iron with 2.0 - 2.5% C content the increase in the Cr content to 25 - 30% Cr produces a fine eutectic carbide distribution [15] but this is also restricted by the shape of the primary austenite field.

The application of conventional spheroidisation heat treatments (850-900^{o}C) has no significant effect on the redistribution of the eutectic carbide phase within the microstructure of high-Cr cast irons. This project investigated the breakdown and spheroidisation of the continuous eutectic carbide network of commercial grade high-Cr cast irons by application of high temperature heat treatments. The role of other common alloying elements besides Cr and C in this process was also studied and four levels (up to

5.5%) of molybdenum, vanadium, tungsten and manganese additions were made 15% Cr and 2.7% C high-Cr cast iron.

Effects of alloying were only considered for the carbide phase since variations in the properties of the matrix phase with these alloying elements have been well established in the literature (see section 2.4)

The solubilities of vanadium, molybdenum and tungsten in the eutectic carbides (M7C3) and matrix phase were studied using an electron micro-probe analyser and results are represented for the carbide phase in Fig. 47. Although the solubility of these three alloying elements exhibited the same trend, the solubility of vanadium in the (M7C3) eutectic carbides was found to be considerably higher than that of molybdenum and tungsten. This might be due to the small difference between the atomic radii of chromium and vanadium. Figure 47 indicates that at least up to 5.5% alloy addition level there is no upper limit in the solubility of these alloys in the (M7C3) eutectic-carbide structure. The carbides which were rich in the added alloying elements were observed together with (M7C3) eutectic-carbides within the microstructure of the alloys. These carbides are shown in plates 4-6 for molybdenum, tungsten and vanadium additions respectively. As can be seen from the plates due to their size, they could not be analysed during the micro-probe studies (necessary particle size should be greater than 4 micron), and no attempt was made to obtain information concerning their

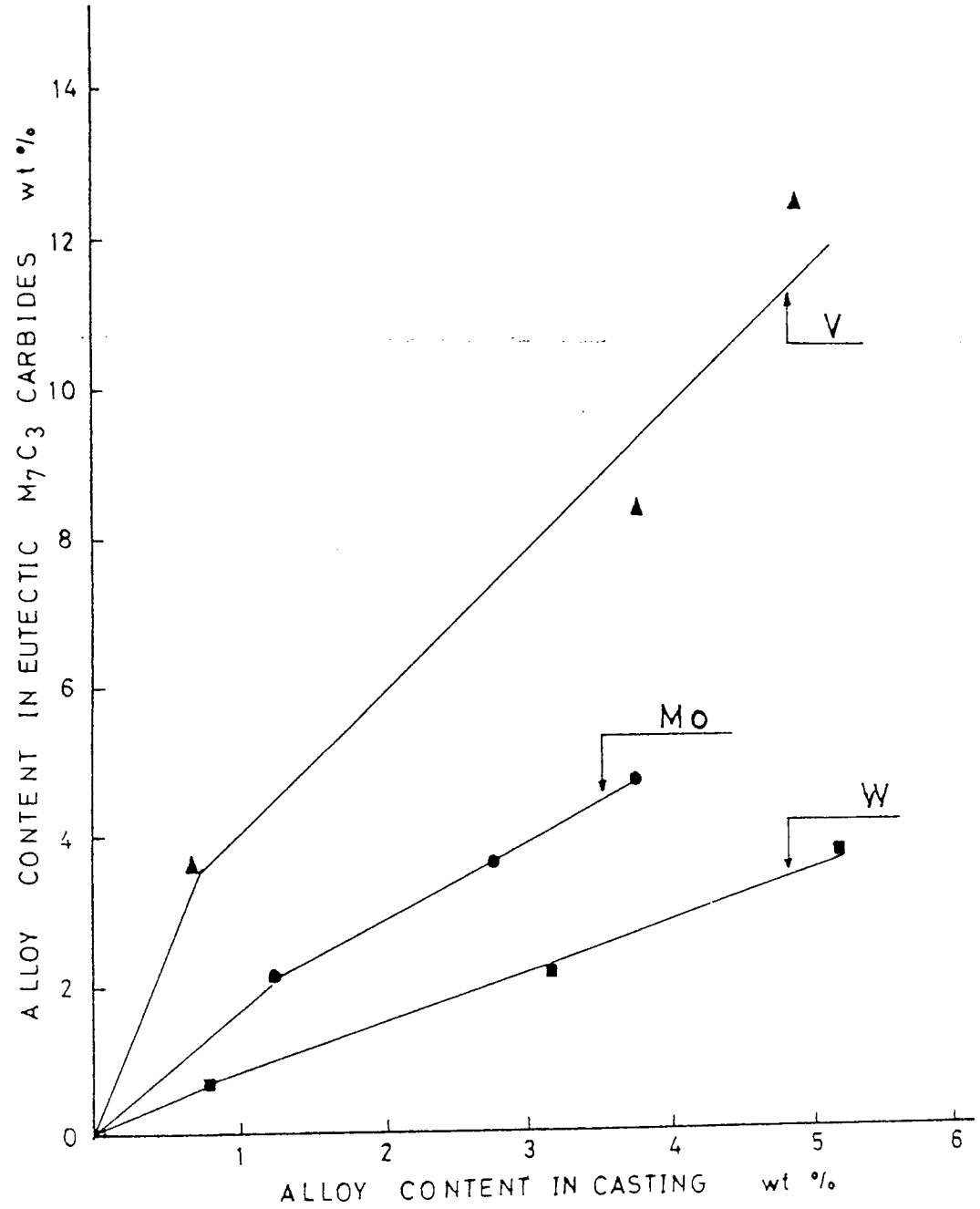

FIGURE 47: Quantity of molybdenum, tungsten and vanadium in the eutectic (M_7C_3) carbides

A - General Appearance

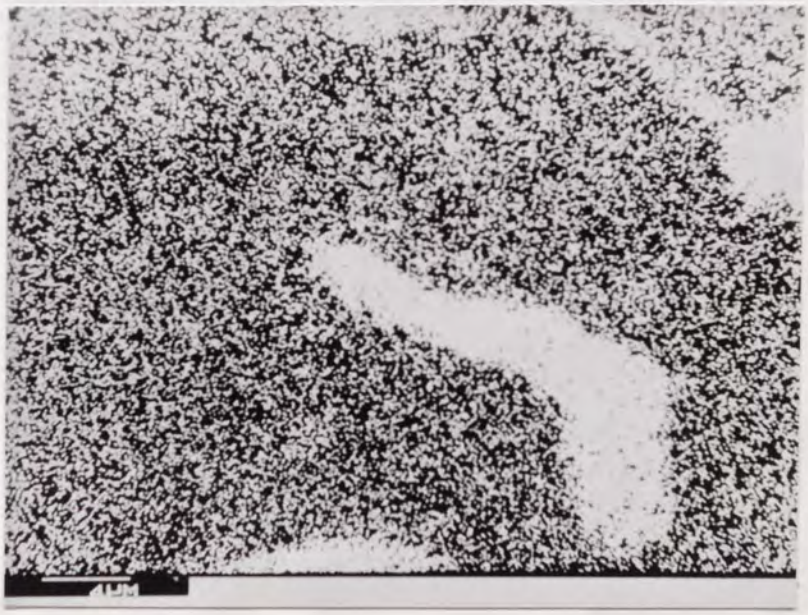

B - Cr X-ray

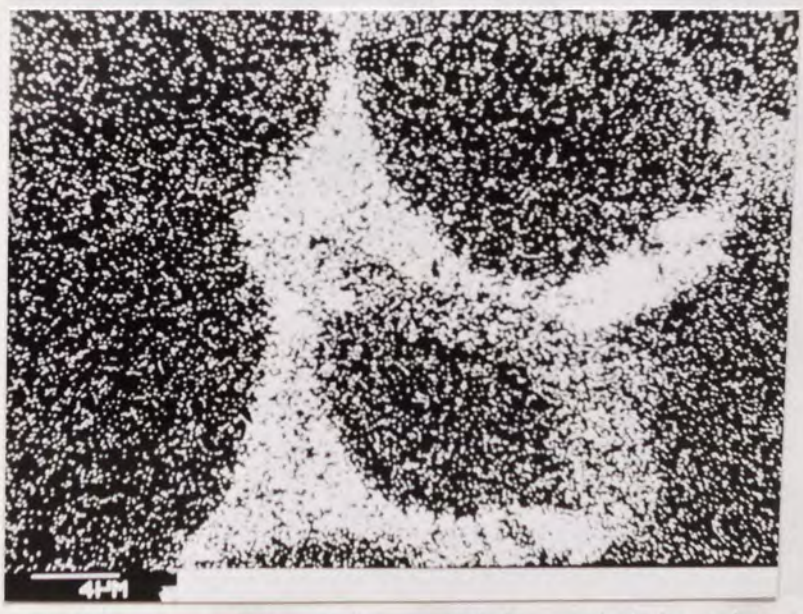

C - Mo X-ray

PLATE 4: Mo-rich carbides within the microstructure of Mo added alloys

A - General appearance

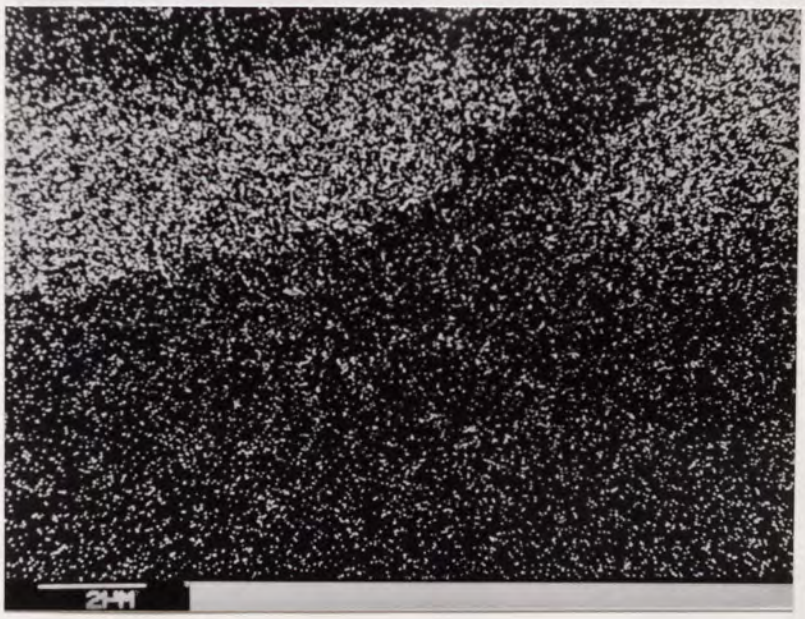

B - Cr X-ray

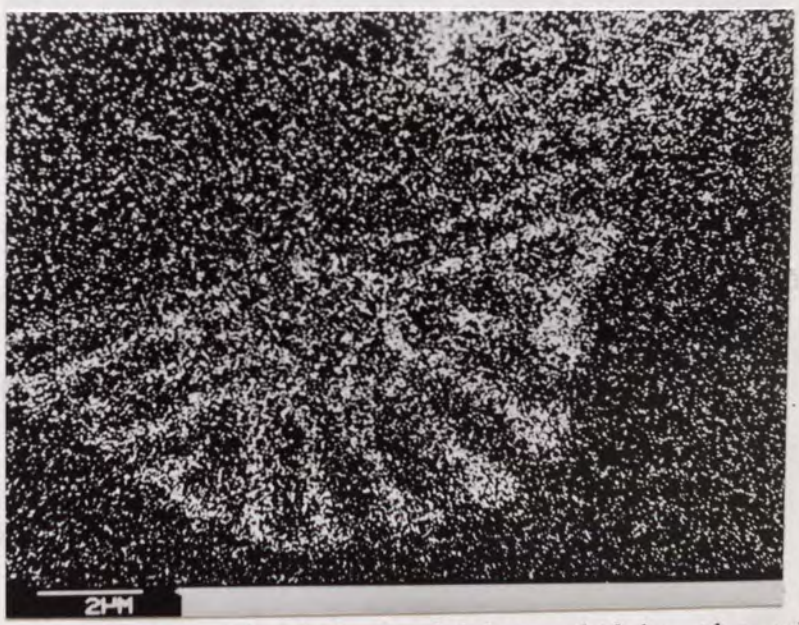

C - Tungsten X-ray

PLATE 5: W-rich carbides within the microstructure of W added alloys

A - General appearance

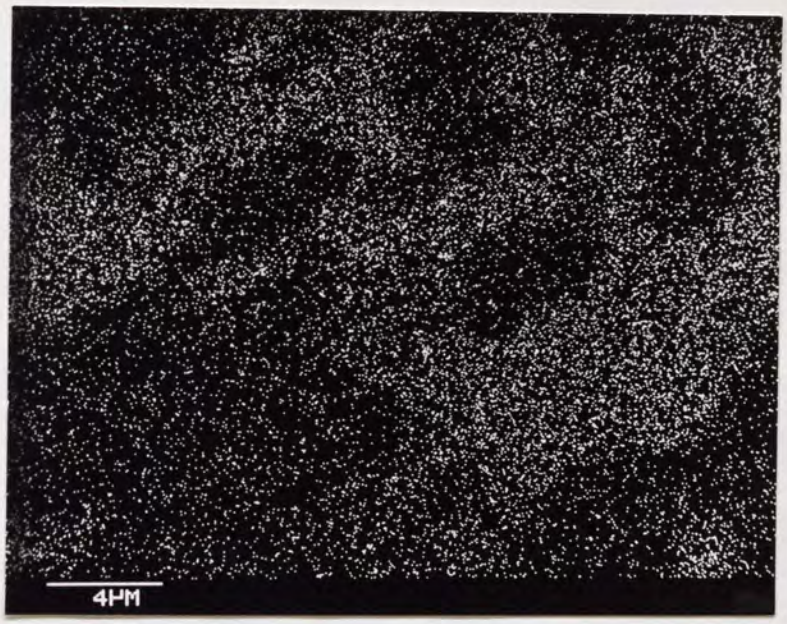

B - Cr X-ray

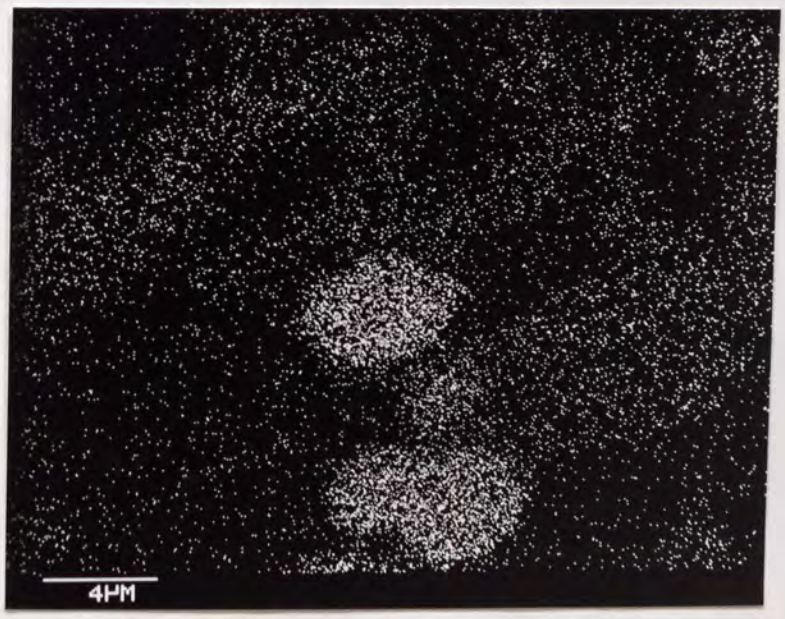

C - Vanadium X-ray

PLATE 6: V-rich carbides within the microstructure of V added alloys

nature by means of X-ray studies. There was an increase in the quantity of these carbides as the addition levels reached the higher levels and this might be explained again in terms of the solubility characteristics, of the alloying elements.

The microstructure of the alloys in the as-cast condition and after application of high-temperature heat treatments are given in plates 7-18, at the end of this section. The given metallographic data for molybdenum and tungsten containing alloys, together with the base alloy were taken from the fracture toughness test specimens, chemical composition of which are given in table 5. The metallographic data for the vanadium and manganese series are only for 5.0% V and 2.7% Mn addition levels which were observed during the preliminary metallographic studies.

For base alloy and lower additions of molybdenum and tungsten, even the cooling rate of $\frac{1}{2}$ inch thick plate in sand moulds was insufficient to prevent the transformation of austenite to ferrite and M23C6 carbides [3]. (Here this transformation and its products were called "pearlitic transformation" and "pealite" respectively.). The observation of lesser amounts of "pearlite" islands within the microstructure of 3% tungsten containing alloy indicated that tungsten has not as strong a delaying effect on this reaction as molybdenum has. When 15% Cr and 2.7% C base metal was alloyed up to 4% molybdenum and 5.5% tungsten levels, in the as-cast condition no marked structural vari-

ation of the eutectic carbides were observed. In the vanadium series by increasing the vanadium content of the alloys, the eutectic carbides become finer and more dense within the microstructure. According to the work of Stephanuscu [64], the reason for this variation is a rise in the eutectic temperature due to increasing vanadium content of the alloys. The quantitative metallographic studies on the molybdenum containing alloys indicated that the as-cast condition did not show any significant variation in the volume % of the (M7C3) eutectic carbides with up to 4% addition of molybdenum (see Fig. 48).

During the high temperature heat treatments the "pearlite transformation" of the base alloy could not be suppressed by the cooling rate provided, therefore except for the base alloy, the others were completely in the autenitic condition after the heat treatments. The application of high temperature heat treatments at 1180°C for different holding periods to these alloys resulted in considerable variations in the eutectic-carbide morphology. The continuous carbide network was broken up and marked spheroidisation of the eutectic carbides was observed within the microstructure of molybdenum and tungsten containing alloys. Vanadium and manganese additions did not play any important role in this aspect although the heat treatment periods at this temperature were extended up to 170 hours (see plates 17, 18).

As can be seen from metallographic plates of tungsten and molybdenum containing alloys, the variation in the carbide morphology is strongly influenced by the addition levels,

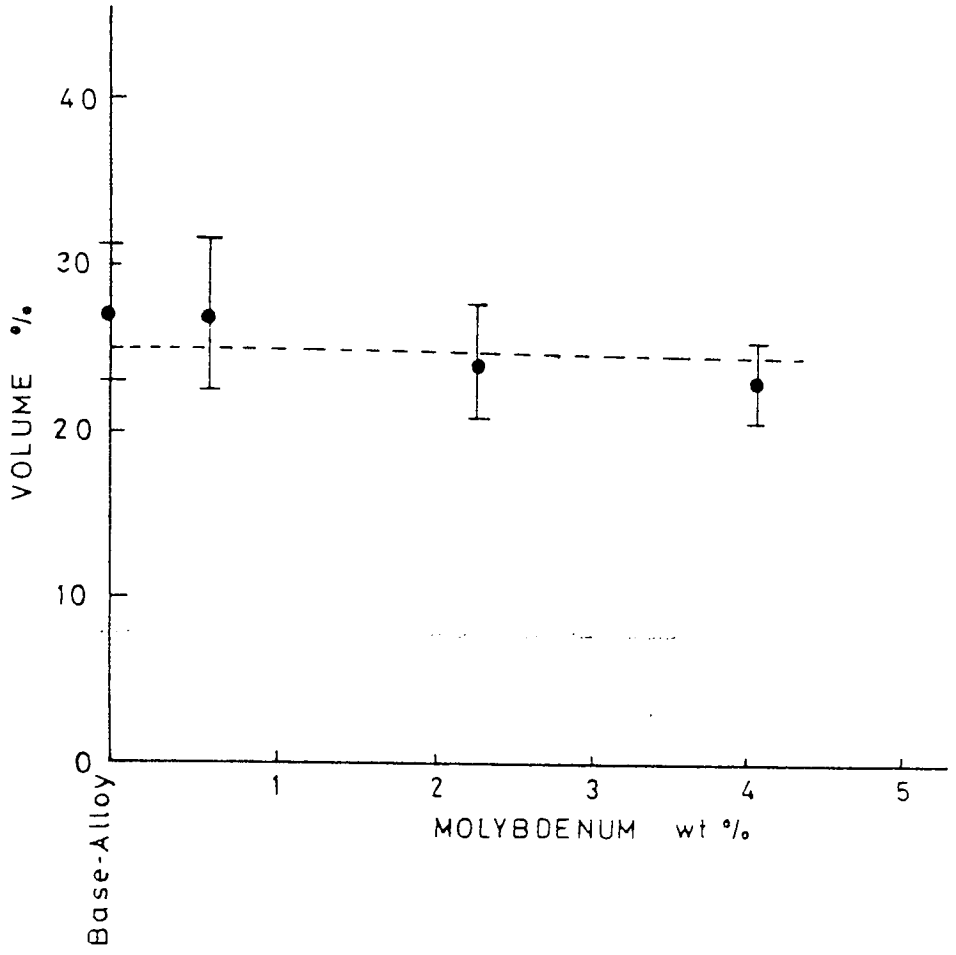

FIGURE 48: Variation of volume % (M7C3) eutectic carbides in as-cast condition with additions of molybdenum

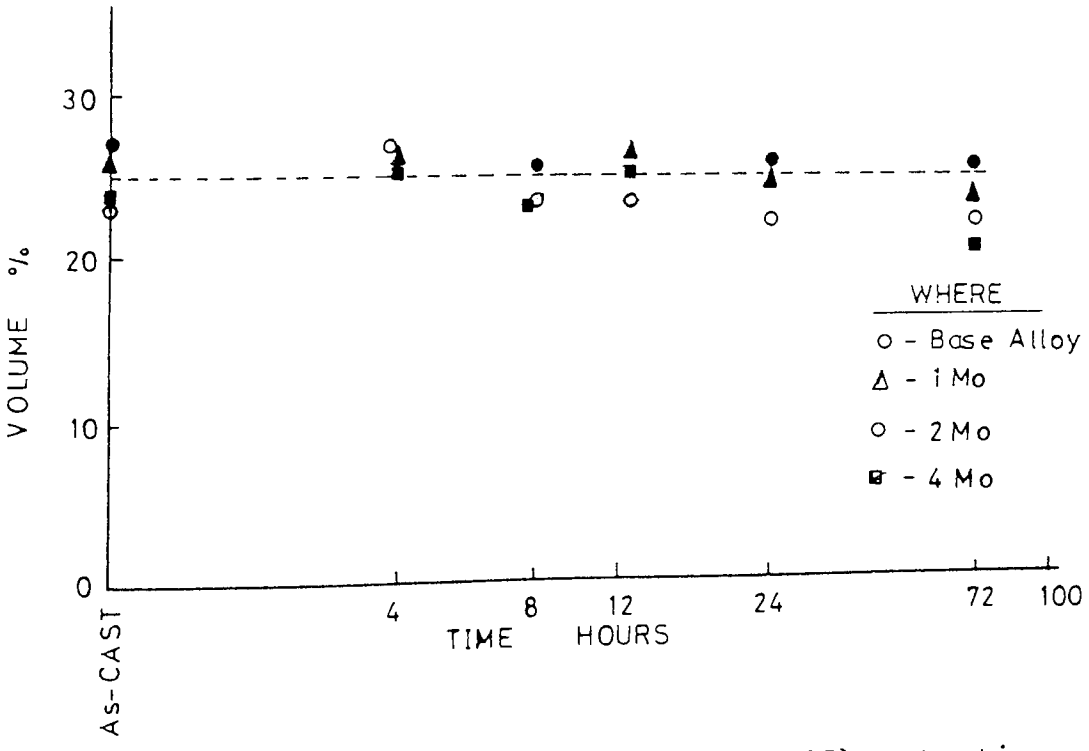

FIGURE 49: Variation of volume % of (M7C3) eutectic carbides within the microstructure of molybdenum containing alloys with holding periods at 1180°C

holding periods at 1180°C and heat treatment temperature. These variations were studied quantitatively for molybdenum containing alloys and for the base alloy. Holding periods at 1180°C, up to 72 hours, did not cause any noticeable dissolution of the eutectic carbides and their volume percent remained almost at the same level within the microstructures (see Fig. 49). The reported almost 50% dissolution of eutectic carbides after application of high temperature heat treatments [53] looks fortuitous and could be a result of possible insufficient application of etching techniques during studies with the quantitative electron microscopy.

If a decrease in the "density" (average number of intercepted eutectic carbides per unit area) is considered as a measure of breaking down of the continuous network or spheroidisation (see Fig- 50) this was achieved rapidly for shorter holding periods at 1180°C with higher addition levels of molybdenum and tungsten, parallel to the metallographic observations. The figure also indicated that there is a slowing down in this process after certain holding periods.

As can be seen from plates 7-15 the high temperature heat treatments, while breaking the continuous eutectic structure into isolated and globular particles, also caused a general coarsening of microstructural features. The average size of the carbides and consequently mean spacing between them was increased, depending on the addition levels and holding periods and these are shown graphically in Fig. 51, and Fig. 52. These Figures are analogous to Fig. 50 which

shows variation in the carbide "density". Considering that the volume % of eutectic carbides remained almost at a constant level these figures suggest that a possible continuous coalescence mechanism is taking place and giving these observed increases in the parameters (carbide spacing and carbide thickness).

Within the microstructure of high temperature heat treated alloys segregation of secondary (M_7C_3) carbides [42] inside the austenite grains was observed. Their distributions were also affected and they become thicker and less pronounced in the volume with increasing holding periods. This could be as a result of either a dissolution or as suggested above a coalescence mechanism.

In order to study the effect of matrix with various carbide distributions on the fracture toughness, the molybdenum containing alloys were subjected to hardening heat treatments by following the commercial heat treatment procedure. As can be seen from plate 16, a hardening heat treatment at 975°C for three hours did not alter the carbide morphology of either the as-cast condition or of those alloys previously subjected to high temperature heat treatments. The only noticeable difference within the microstructures was a considerable increase in the "density" of the precipitated secondary carbides and this has been shown in section 2.3.2 by means of transformation diagrams. The precipitation of secondary carbides with austenisation at this temperature leaves the matrix depleted in carbon and alloying elements and raises

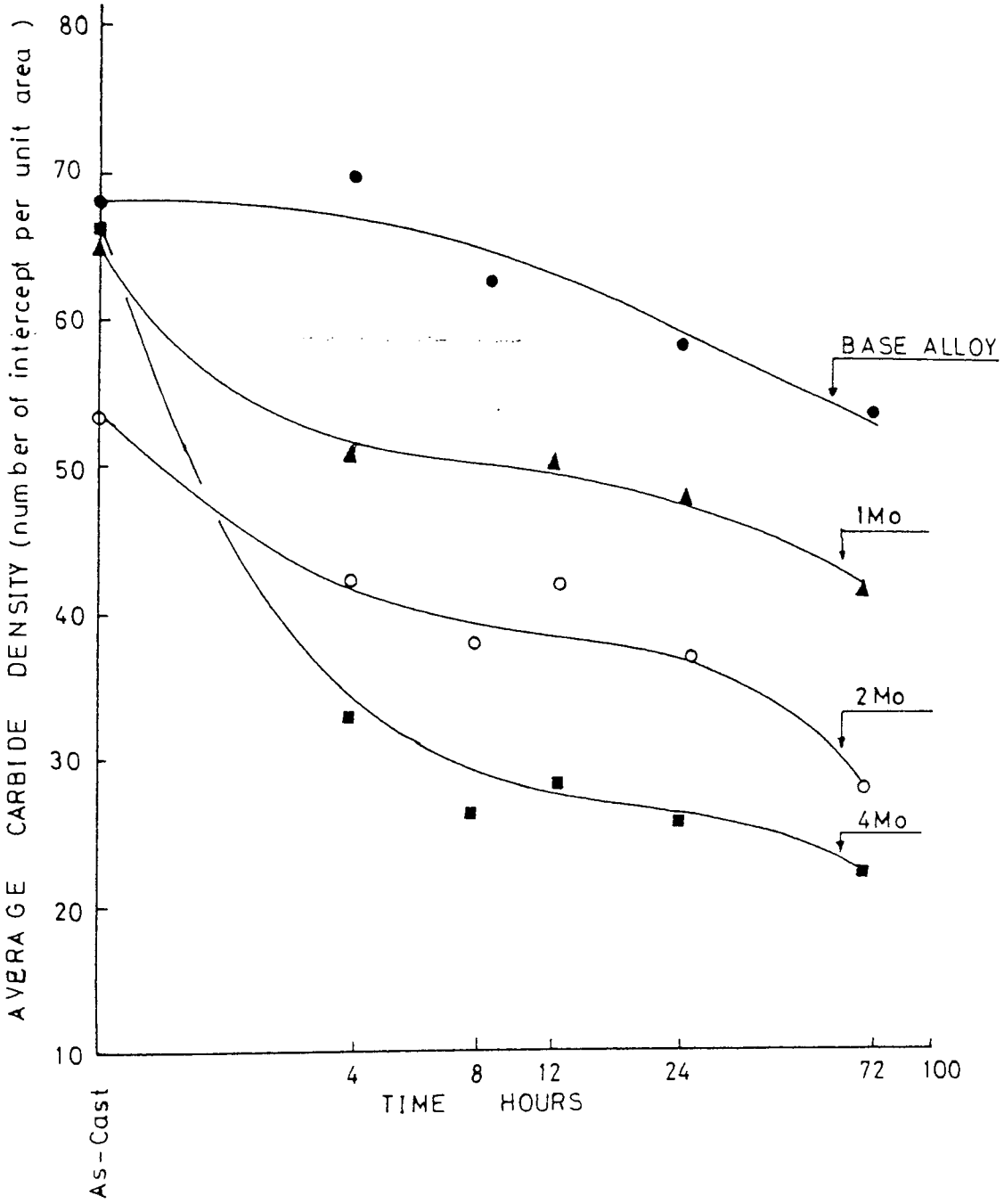

FIGURE 50: Variation in the density (number of intercept per unit area) of the (M7C3) eutectic carbides within the microstructure of molybdenum containing alloys with holding periods at 1180°C

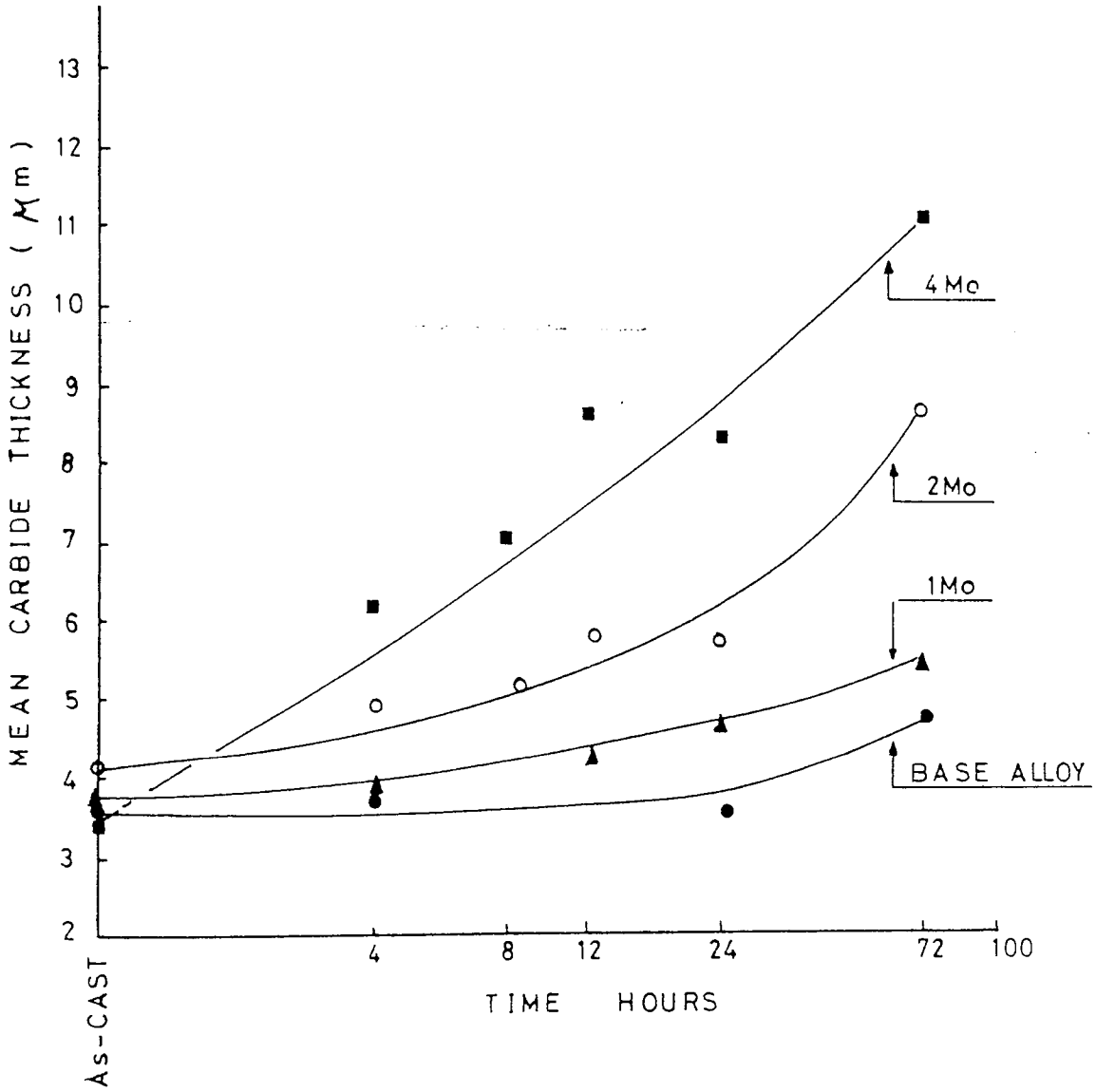

FIGURE 51: Coarsening of (M7C3) eutectic carbides within the microstructure of molybdenum containing alloys with holding periods at 1180°C

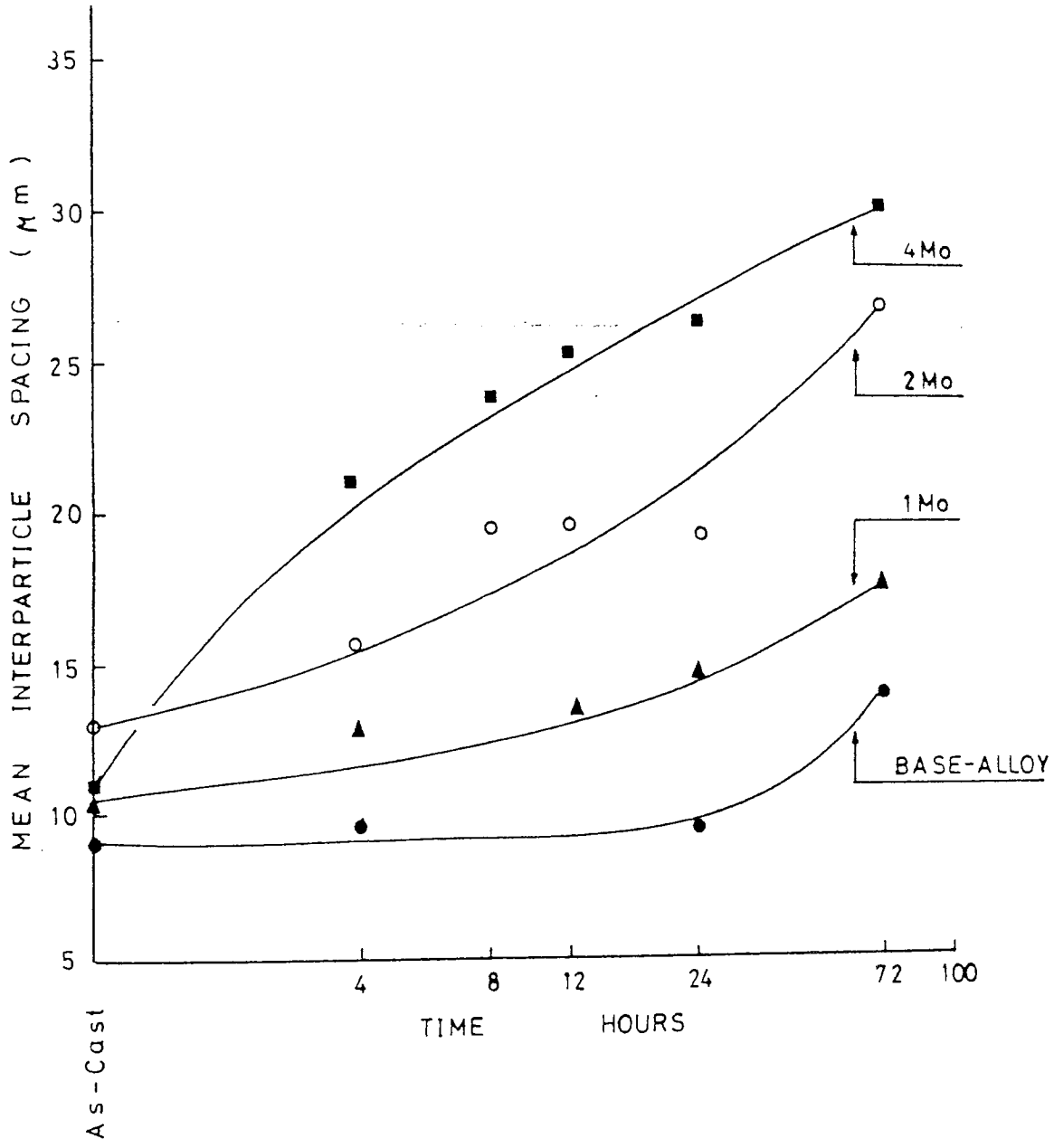

FIGURE 52: Variation in the mean interparticle spacing within the microstructure of molybdenum containing alloys with holding periods at 1180°C

the M_s temperature above room temperature. Subsequent cooling results in transformation of matrix to martensite.

Since hardness is widely accepted as a measure of wear resistance the variation in the hardness values with studied variables were summarised in Figs. 53-55. In the as-cast condition a decrease was observed in the hardness values with increasing alloy content. This could be attributed to a change from a hard autotempered martensitic to a softer austenitic matrix. The alloys exhibited a further decrease in the hardness values after high temperature heat treatments. For martensitic high-Cr cast irons there is an increase in the hardness values with molybdenum additions and the alloys subjected to high temperature heat treatments exhibited slightly lower hardness values than the alloys subjected to only commercial hardening heat treatments directly from as-cast state. The hardness variation of (M7C3) eutectic carbides with studied metallurgical variables could not be determined with available micro-hardness measuring instrument. Even when the heat treatments were carried out at 1010°C a decrease in the hardness values of the eutectic carbides from about 1400 Dph to 1100 Dph was reported [134]. This fact could not be explained with a possible reason, however, the loss in the overall hardness of the alloys was not very significant, favouring the metallurgical variables studied to obtain wear-resistant materials with different carbide distributions.

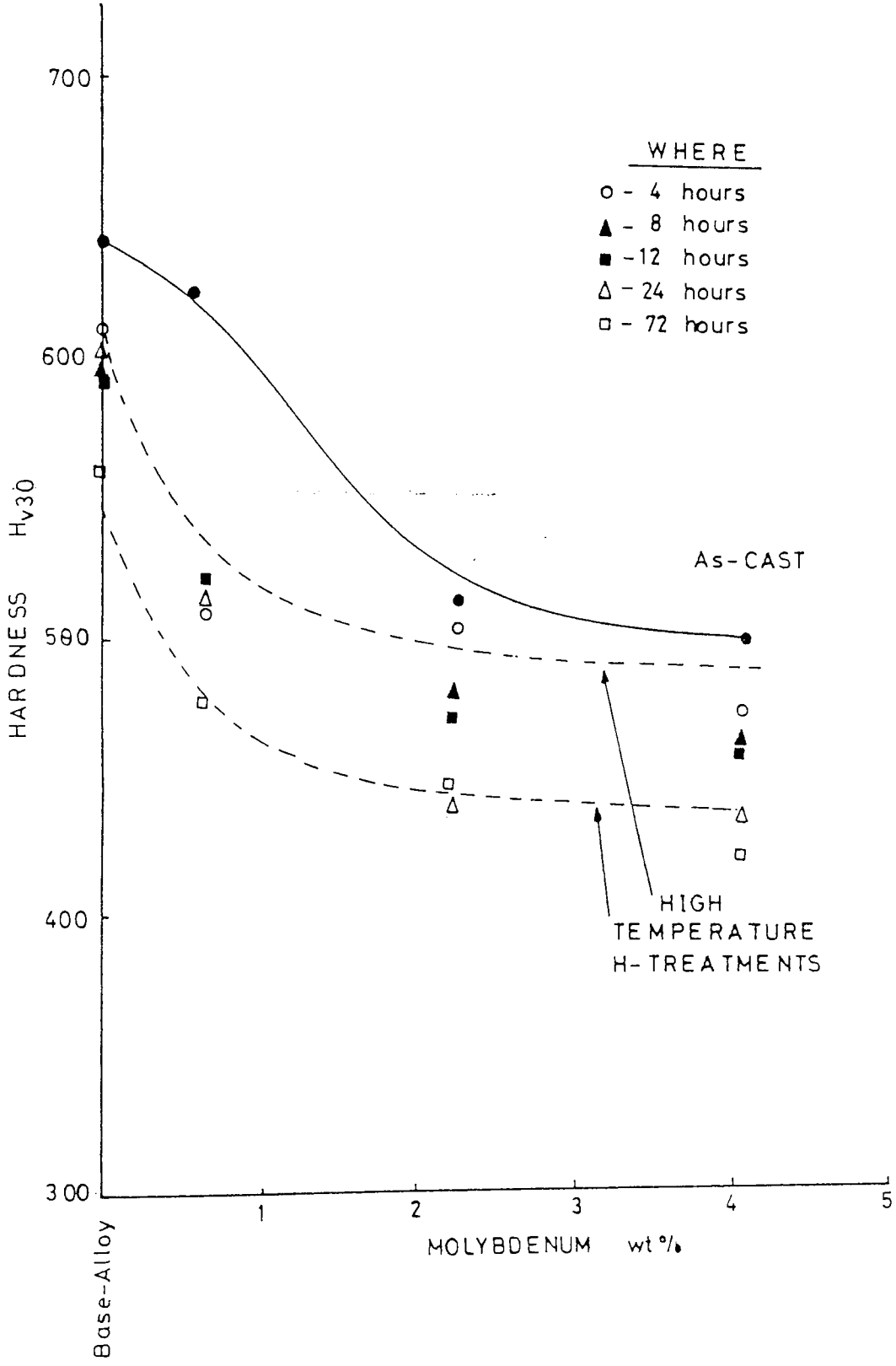

FIGURE 53: Hardness variation of molybdenum containing alloys (heat treatment temperature 1180°C)

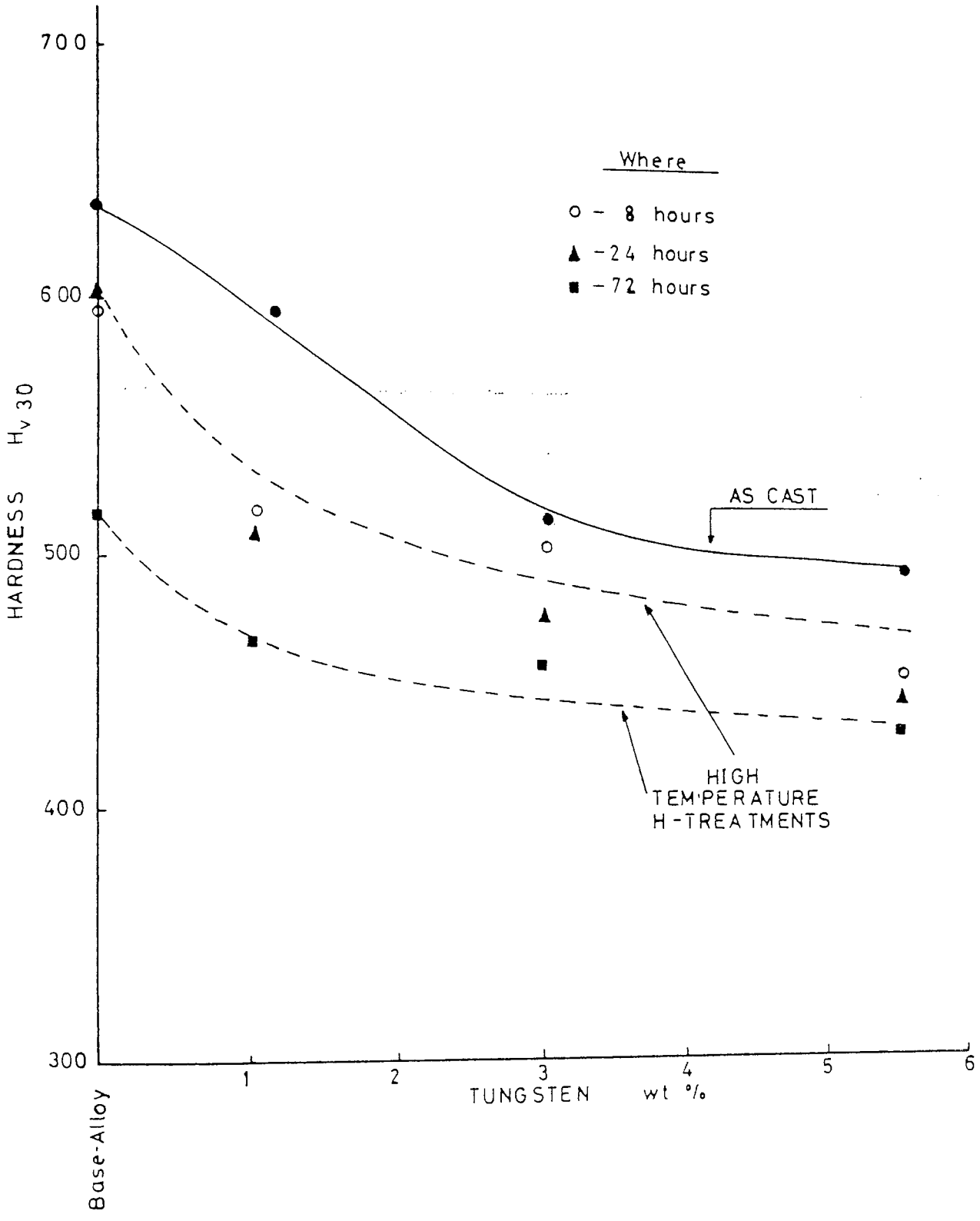

FIGURE 54: Hardness variation of tungsten containing alloys (heat treatment temperature 1180°C)

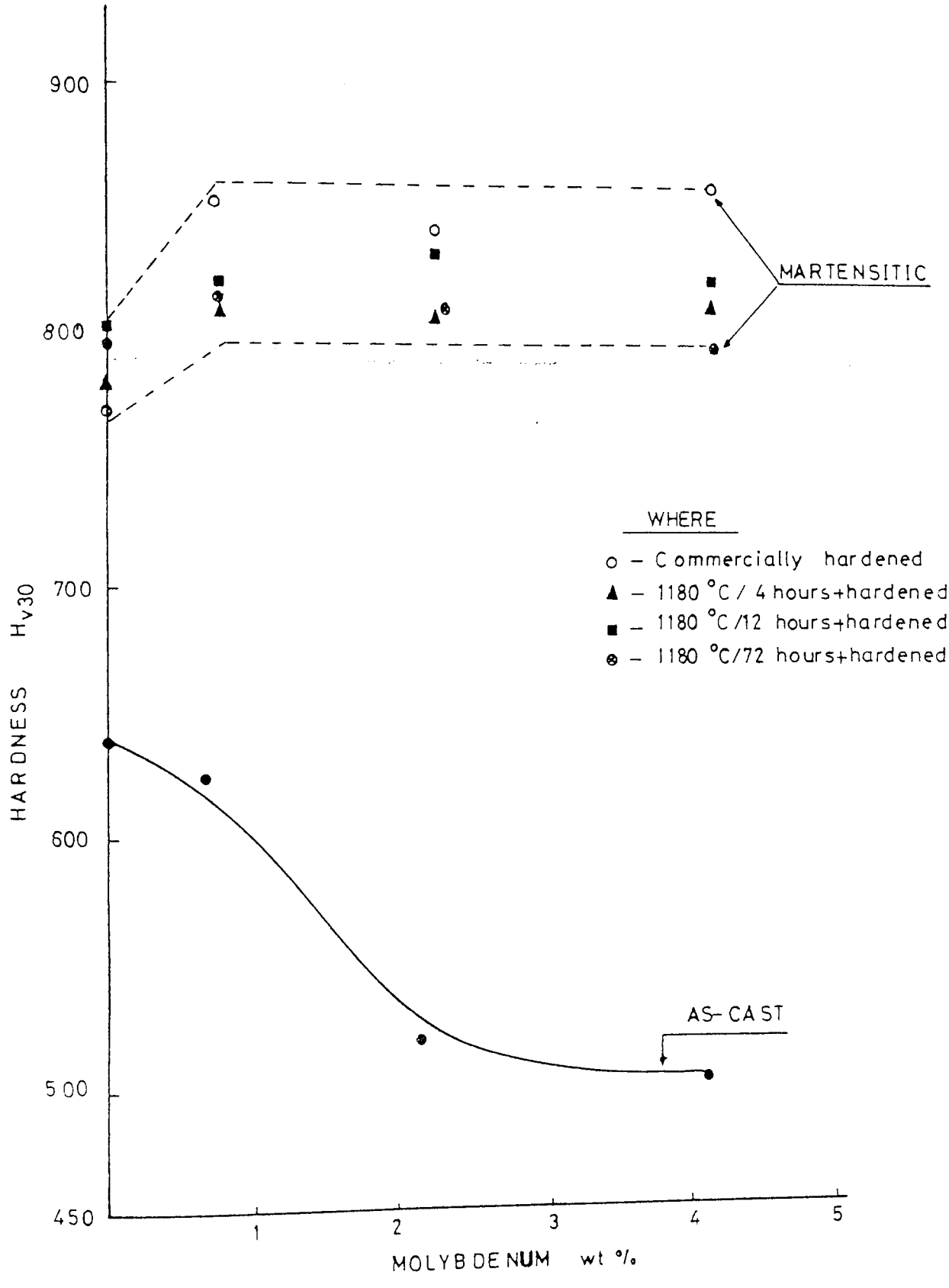

FIGURE 55: Hardness variation of molybdenum containing martensitic high-Cr cast irons

A - Base alloy

K_{IC} : 20.58 $MNm^{-3/2}$

H_{v30} : 637

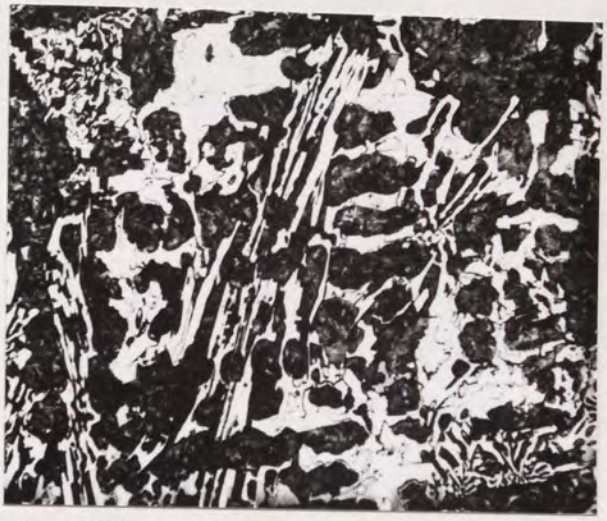

B - 1Mo

K_{IC} : 23.00 $MNm^{-3/2}$

H_{v30} : 625

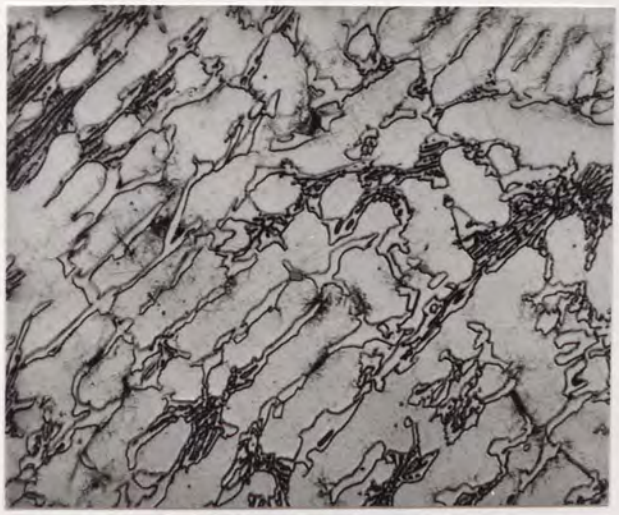

C - 2Mo

K_{IC} : 24.70 $MNm^{-3/2}$

H_{v30} : 518

D - 4Mo

K_{IC} : 23.80 $MNm^{-3/2}$

H_{v30} : 503

PLATE 7: As-cast microstructure of base alloy and molybdenum containing alloy. x140

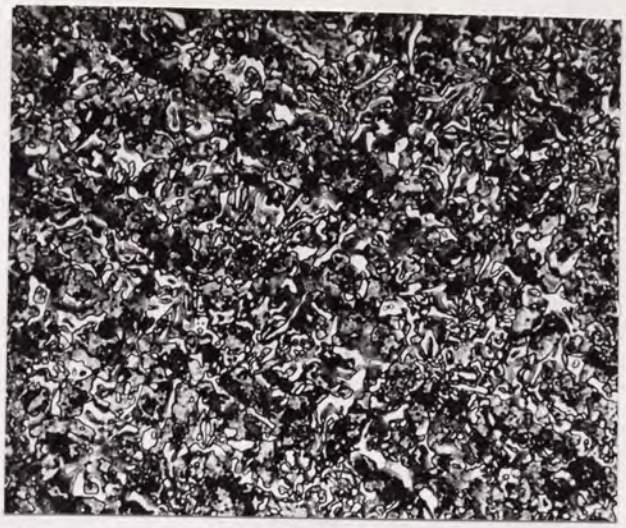

A - Base Alloy

K_{IC} : 19.74 $MNm^{-3/2}$

H_{v30} : 608

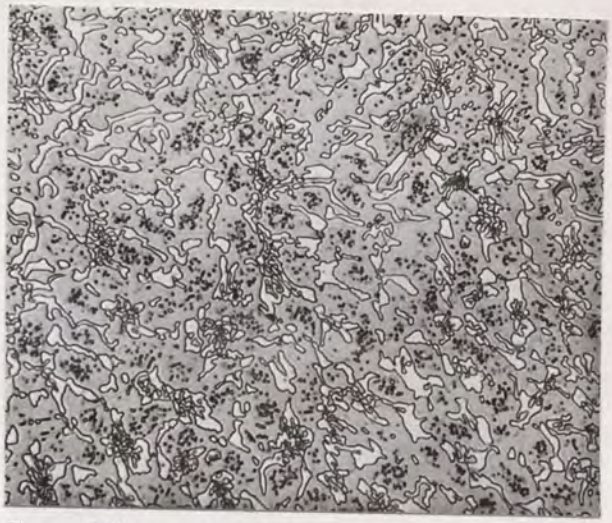

B - 1Mo

K_{IC} : 25.91 $MNm^{-3/2}$

H_{v30} : 507

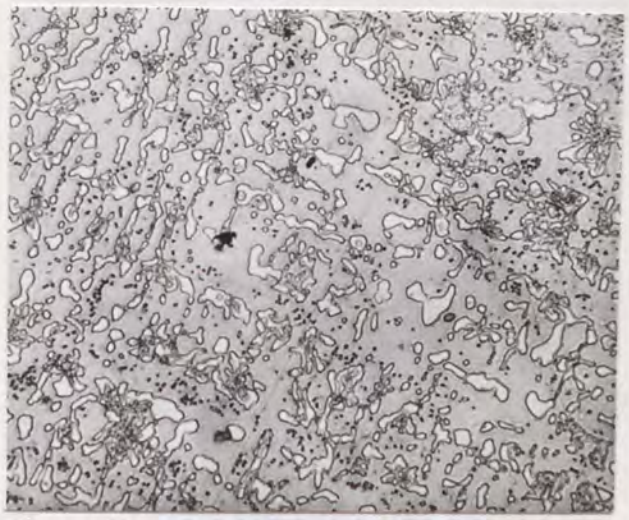

C - 2Mo

K_{IC} : 28.80 $MNm^{-3/2}$

H_{v30} : 505

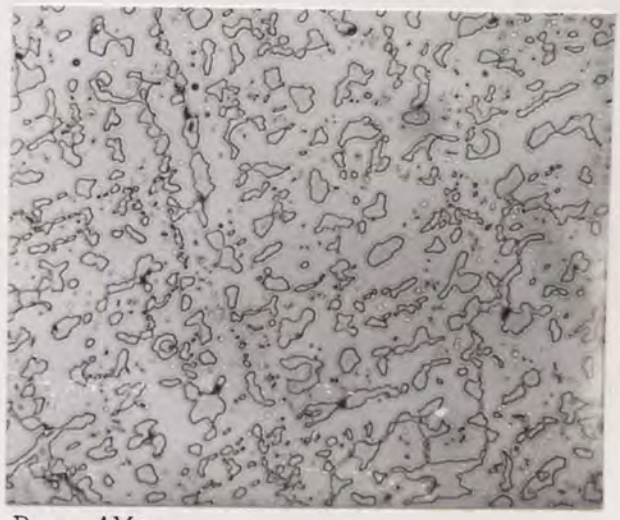

D - 4Mo

K_{IC} : 27.37 $MNm^{-3/2}$

H_{v30} : 474

PLATE 8: Microstructure of base alloy and molybdenum containing alloys after holding for 4 hours at 1180°C x140

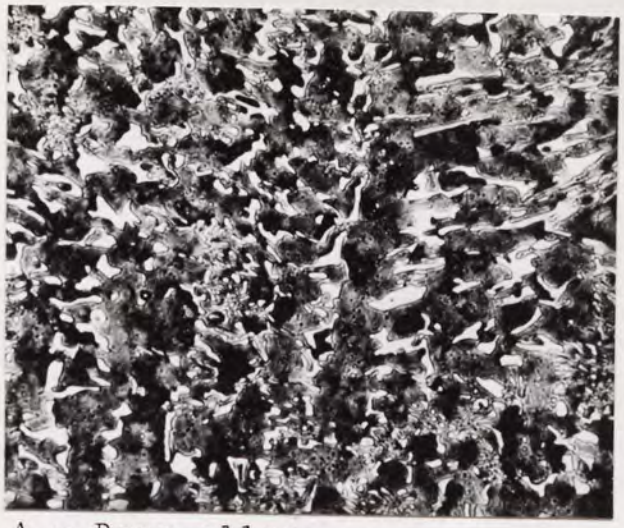

A - Base alloy

K_{IC} : 18.61 $MNm^{-3/2}$

H_{v30} : 596

B - 1Mo

K_{IC} : 25.03 $MNm^{-3/2}$

H_{v30} : 515

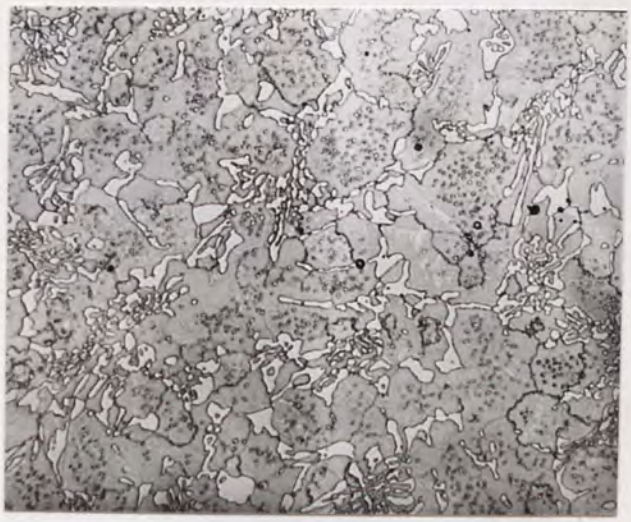

C - 2Mo

K_{IC} : 30.13 $MNm^{-3/2}$

H_{v30} : 478

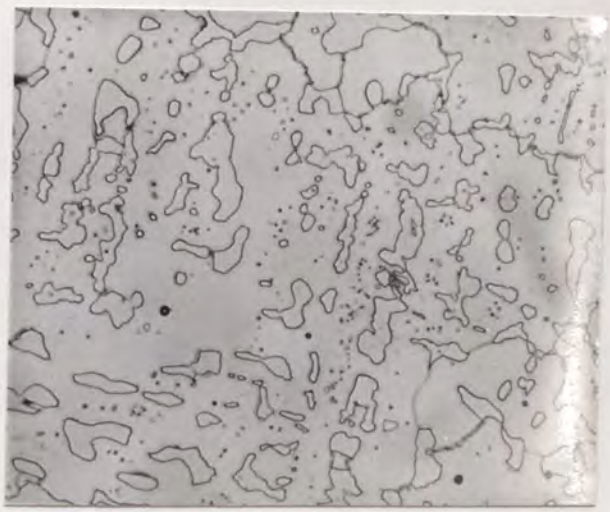

D - 4Mo

K_{IC} : 26.34 $Mnm^{-3/2}$

H_{v30} : 465

PLATE 9: Microstructure of base alloy and molybdenum containing alloys after holding for 8 hours at 1180°C x140

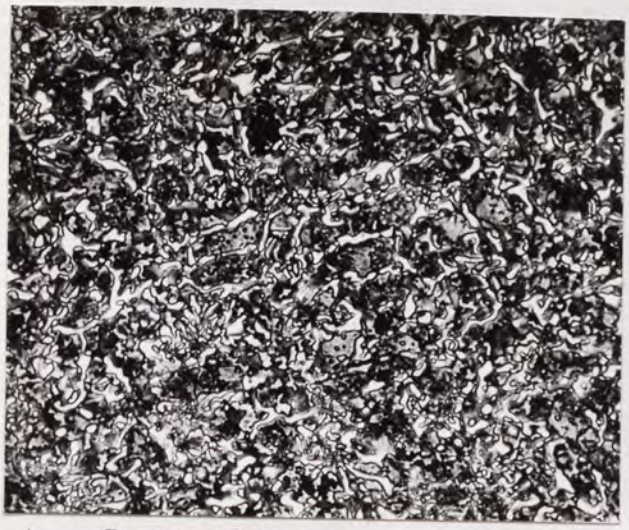

A - Base alloy

K_{IC} : 19.29 $MNm^{-3/2}$

H_{v30} : 602

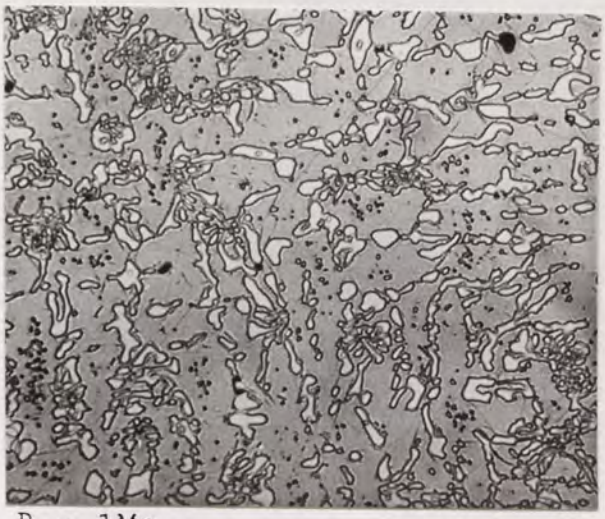

B - 1Mo

K_{IC} : 26.32 $MNm^{-3/2}$

H_{v30} : 515

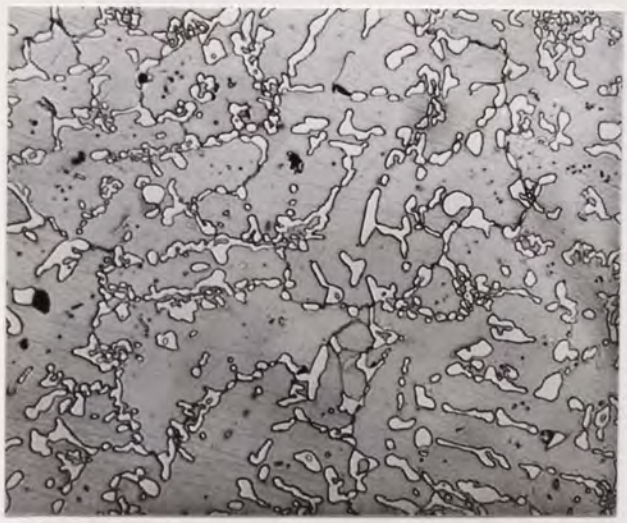

C - 2Mo

K_{IC} : 27.75 $MNm^{-3/2}$

H_{v30} : 441

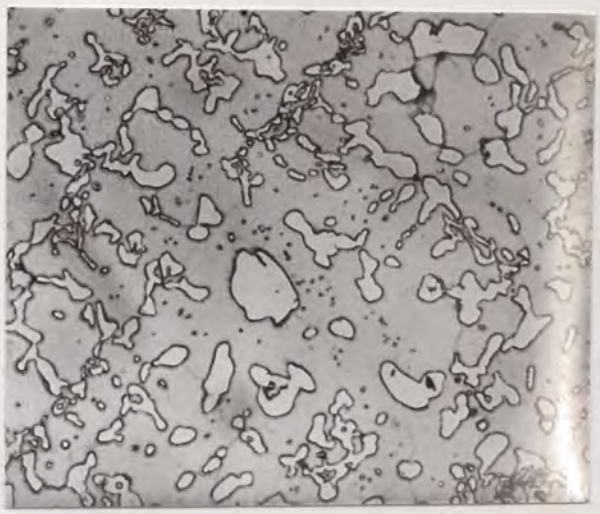

D - 4Mo

K_{IC} : 23.98 $MNm^{-3/2}$

H_{v30} : 438

PLATE 10: Microstructure of base alloy and molybdenum containing alloys after holding for 24 hours at 1180°C x140

A - Base alloy

K_{IC} : 25.78 $MNm^{-3/2}$

H_{v30} : 560

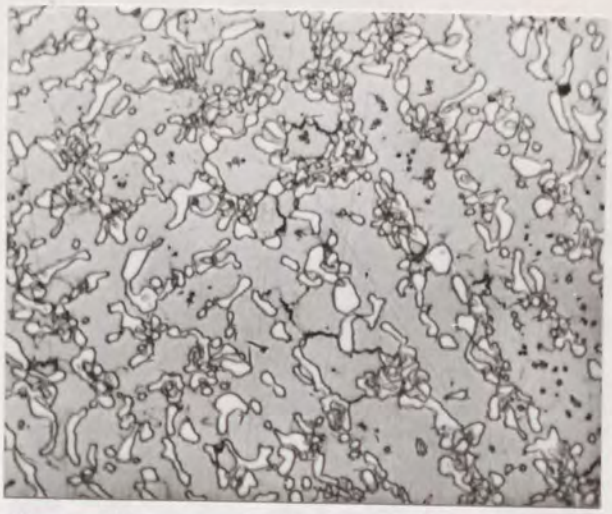

B - 1Mo

K_{IC} : 25.02 $MNm^{-3/2}$

H_{v30} : 475

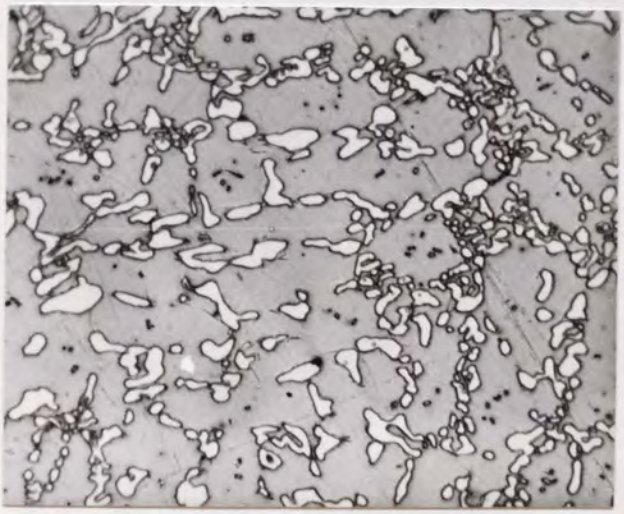

C - 2Mo

K_{IC} : 26.35 $MNm^{-3/2}$

H_{v30} : 442

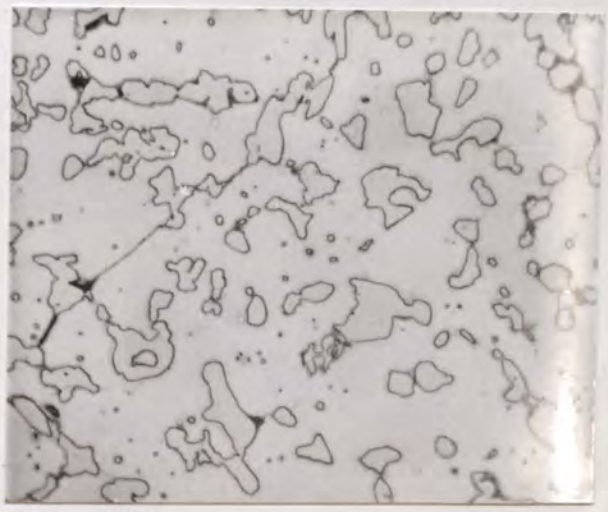

D - 4Mo

K_{IC} : 23.41 $MNm^{-3/2}$

H_{v30} : 422

PLATE 11: Microstructure of base alloy and molybdenum containing alloys after holding for 72 hours at 1180°C x140

A - Base alloy

K_{IC} : 20.58 $MNm^{-3/2}$

H_{v30} : 637

B - 1W

K_{IC} : 22.14 $MNm^{-3/2}$

H_{v30} : 595

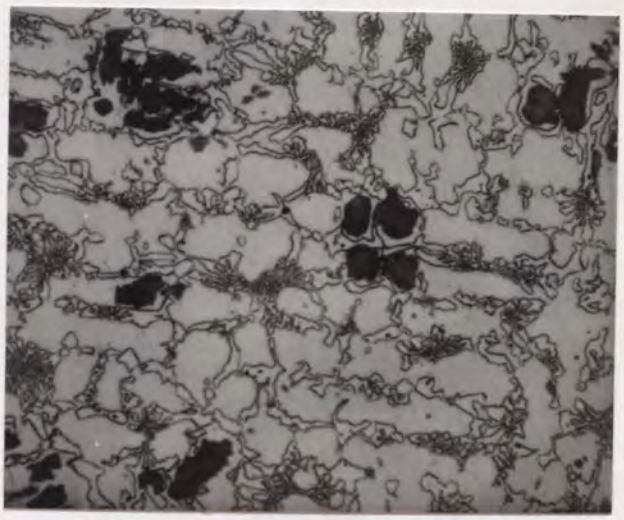

C - 3W

K_{IC} : 25.98 $MNm^{-3/2}$

H_{v30} : 516

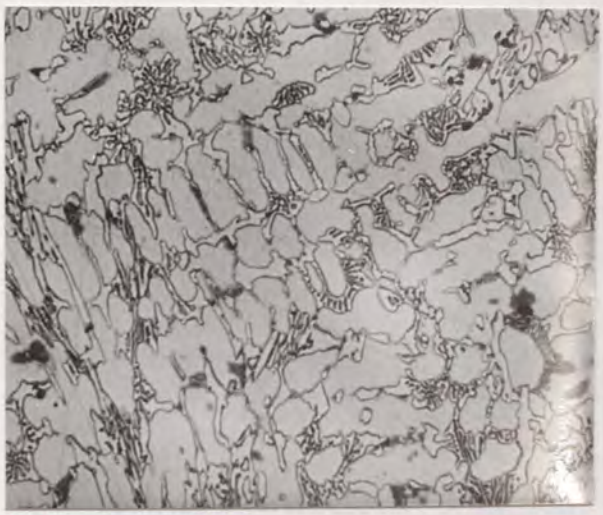

D- 5W

K_{IC} : 23.09 $MNm^{-3/2}$

H_{v30} : 494

PLATE 12: As-cast microstructure of base alloy and tungsten containing high-Cr cast irons x140

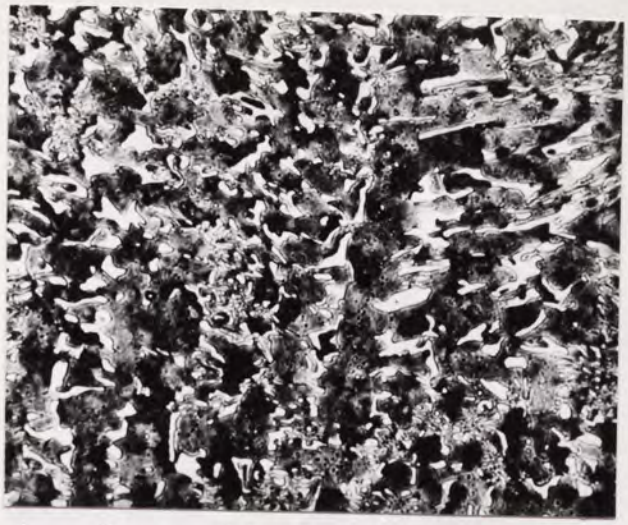

A - Base alloy

K_{IC} : 18.61 $MNm^{-3/2}$

H_{v30} : 592

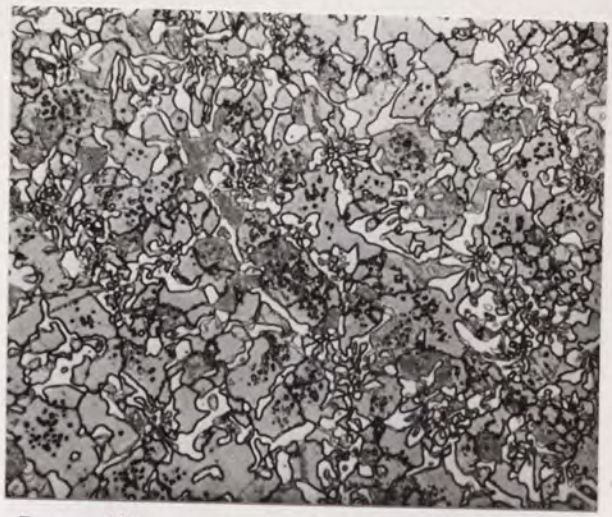

B - 1W

K_{IC} : 24.26 $MNm^{-3/2}$

H_{v30} ; 516

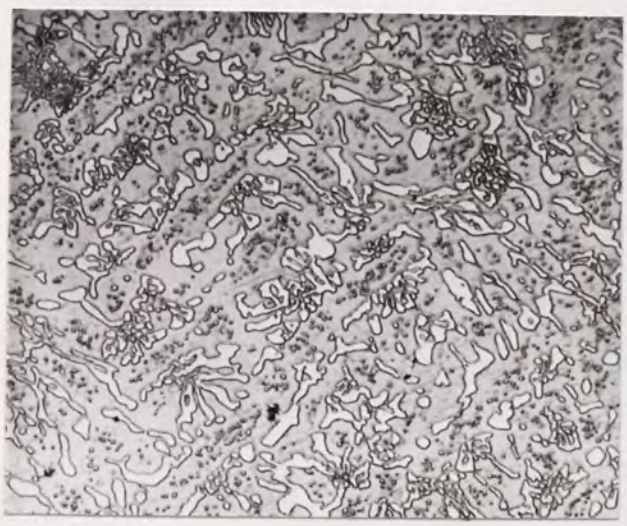

C - 3W

K_{IC} : 27.33 $MNm^{-3/2}$

H_{v30} : 506

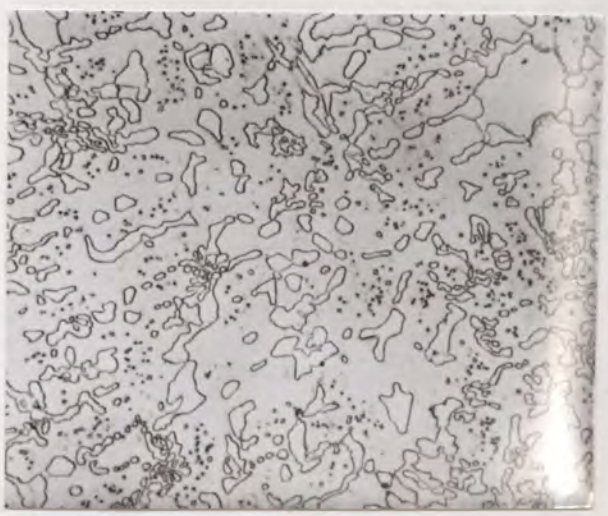

D- 5W

K_{IC} : 30.38 $MNm^{-3/2}$

H_{v30} : 448

PLATE 13: Microstructure of base alloy and tungsten containing high-Cr cast irons after holding for 8 hours at 1180°C x140

A - Base Alloy

K_{IC} : 19.29 $MNm^{-3/2}$

H_{v30} : 602

B - 1W

K_{IC} : 23.06 $MNm^{-3/2}$

H_{v30} : 510

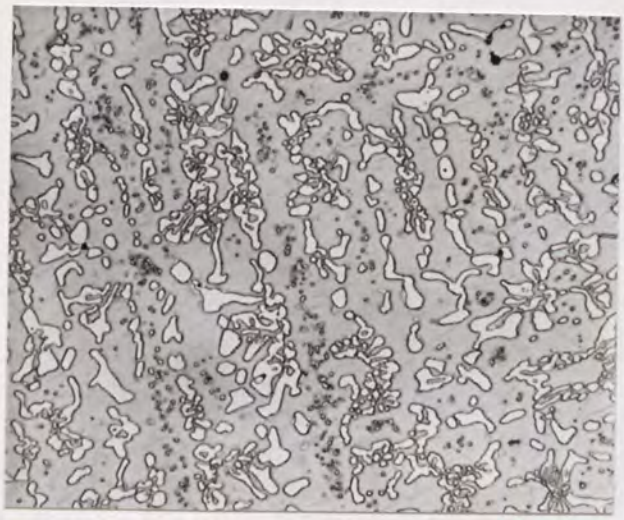

C - 3W

K_{IC} : 25.32 $MNm^{-3/2}$

H_{v30} : 475

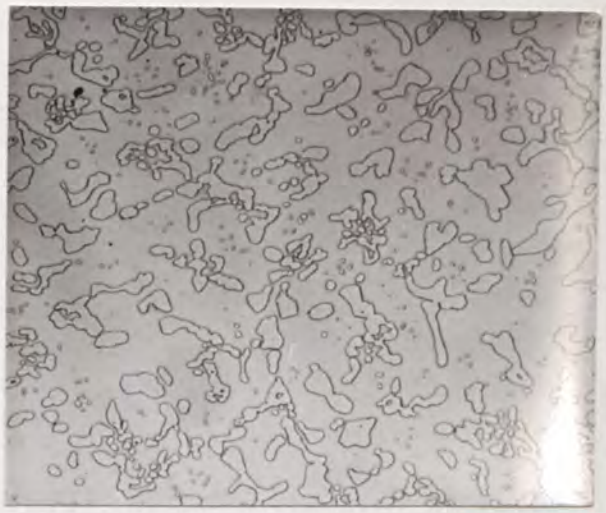

D - 5W

K_{IC} : 27.74 $MNm^{-3/2}$

H_{v30} : 440

PLATE 14: Microstructure of base alloy and tungsten containing high-Cr cast irons after holding for 24 hours at 1180°C x140

A - Base alloy

K_{IC} : 25.78 $MNm^{-3/2}$

H_{v30} : 560

B - 1W

K_{IC} : 25.62 $MNm^{-3/2}$

H_{v30} : 465

C - 3W

K_{IC} : 25.96 $MNm^{-3/2}$

H_{v30} : 454

D - 5W

K_{IC} : 24.28 $MNm^{-3/2}$

H_{v30} : 431

PLATE 15: Microstructure of base alloy and tungsten containing alloys after holding for 72 hours at 1180°C x140

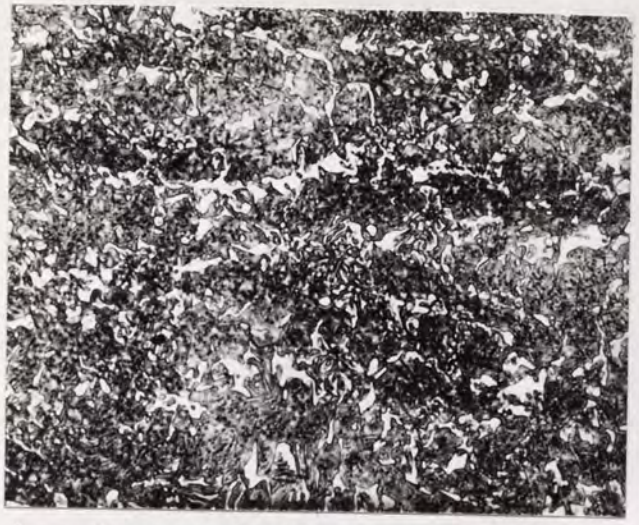

A - Commercially hardened

K_{IC} : 21.24 $MNm^{-3/2}$

H_{v30} : 842

B - 4 hours at 1180°C plus hardened

K_{IC} : 21.87 $MNm^{-3/2}$

H_{v30} : 809

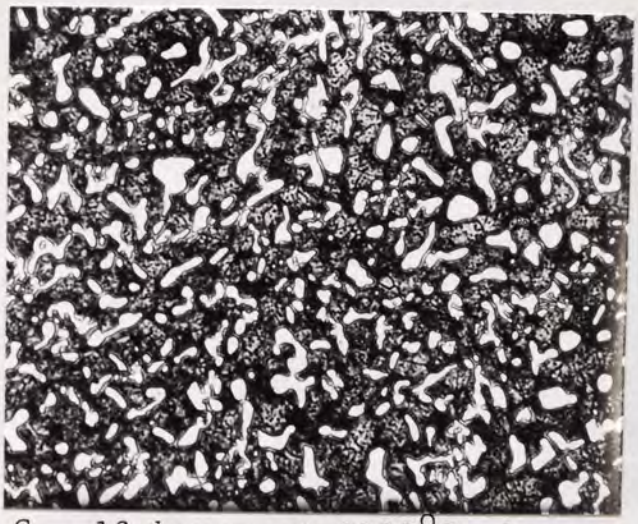

C - 12 hours at 1180°C plus hardened

K_{IC} : 21.63 $MNm^{-3/2}$

H_{v30} : 838

D - 72 hours at 1180°C plus hardened

K_{IC} : 21.28 $MNm^{-3/2}$

H_{v30} : 810

PLATE 16: Martensitic microstructure of 2% molybdenum containing high-Cr cast iron with various eutectic carbide morphologies x140

A - As-Cast microstructure

B - After holding for 16 hours at 1180°C

C - After holding for 40 hours at 1180°C

D - After holding for 170 hours at 1180°C

PLATE 17: Effect of 2.7% manganese addition and various holding periods on the carbide morphology of 15% Cr - 2.7% C containing high-Cr cast iron x140

A - As-cast microstructure

B - After holding for 16 hours at 1180°C

C - After holding for 40 hours at 1180°C

D - After holding for 170 hours at 1180°C

PLATE 18: Effect of 5.0% Vanadium addition and various holding periods at 1180°C on the eutectic carbide morphology of 15% Cr and 2.7% C containing high-Cr cast iron x140

As a summary, additions of molybdenum and tungsten and the application of high temperature heat treatments to these alloys enabled the eutectic carbide morphology to be altered. Additions of vanadium up to 5.0% and manganese up to 2.7% did not show any significant effect in this process.

9.2 Fracture Toughness Testing Methods

Two methods of determining the fracture toughness of the alloys under consideration have been used conjointly throughout the work, these are:

1. The 5% secent L.E.F.M. testing technique which is outlined by Standards [76,77].

2. The J-integral from a single load-load point displacement record, suggested by Rice et al [137].

Except for the measurements of the fatigue crack lengths the recommended K_{IC} testing procedure by ASTM.E399 was adhered throughout the work. It was impossible to distinguish the fatigue crack tip from the fast fracture area in the austenitic alloys. The heat-tinting procedure could not be applied, the nature of the alloys made it necessary to use high temperatures (500-600^{o}C) in order to obtain a reasonable colour change. The first trials carried out had shown that the crack front was almost a straight line (see plate 3). Therefore it was assumed that measurements of the fatigue-crack lengths from polished surfaces were accurate and it is believed that this did not violate the recommended practice

by standards. In the results section the given K_{IC} values are an average of duplicated valid test results. Overall, the maximum variation in results obtained is $\pm$ 1.73 $MNm^{-3/2}$, which indicates good reproducibility of the results.

During the trials the C.O.D. method for determining K_Q gave far higher values than those obtained by the other two methods. The M value in equation (24) for conversion of C.O.D. to K_Q was taken to be 2 for the alloys. As mentioned earlier, the M value is the subject of much controversy. On the other hand, crack opening displacements could be inaccurate because of the very small opening displacements obtained. Therefore during this work, no attempt has been made to determine the critical C.O.D. values of the materials under consideration.

The J values obtained were converted to K_Q values using equation (53). As can be seen from tables 8-20 and Fig. 56, the $K_{Q(J)}$ values were, in some cases, up to 23% less than K_{IC} values obtained using the L.E.F.M. technique for the same test piece, although both methods gave the same trend for the variation of toughness of the alloys by alloy additions and application of high temperature heat treatments. This expected disparity could be due to the following reasons:

In the L.E.F.M. the P_Q (critical load) is determined after the crack has extended, whereas in the J-integral method P_C (critical load) values are determined as a crack initiation load. Therefore $K_{Q(J)}$ values are for instant crack

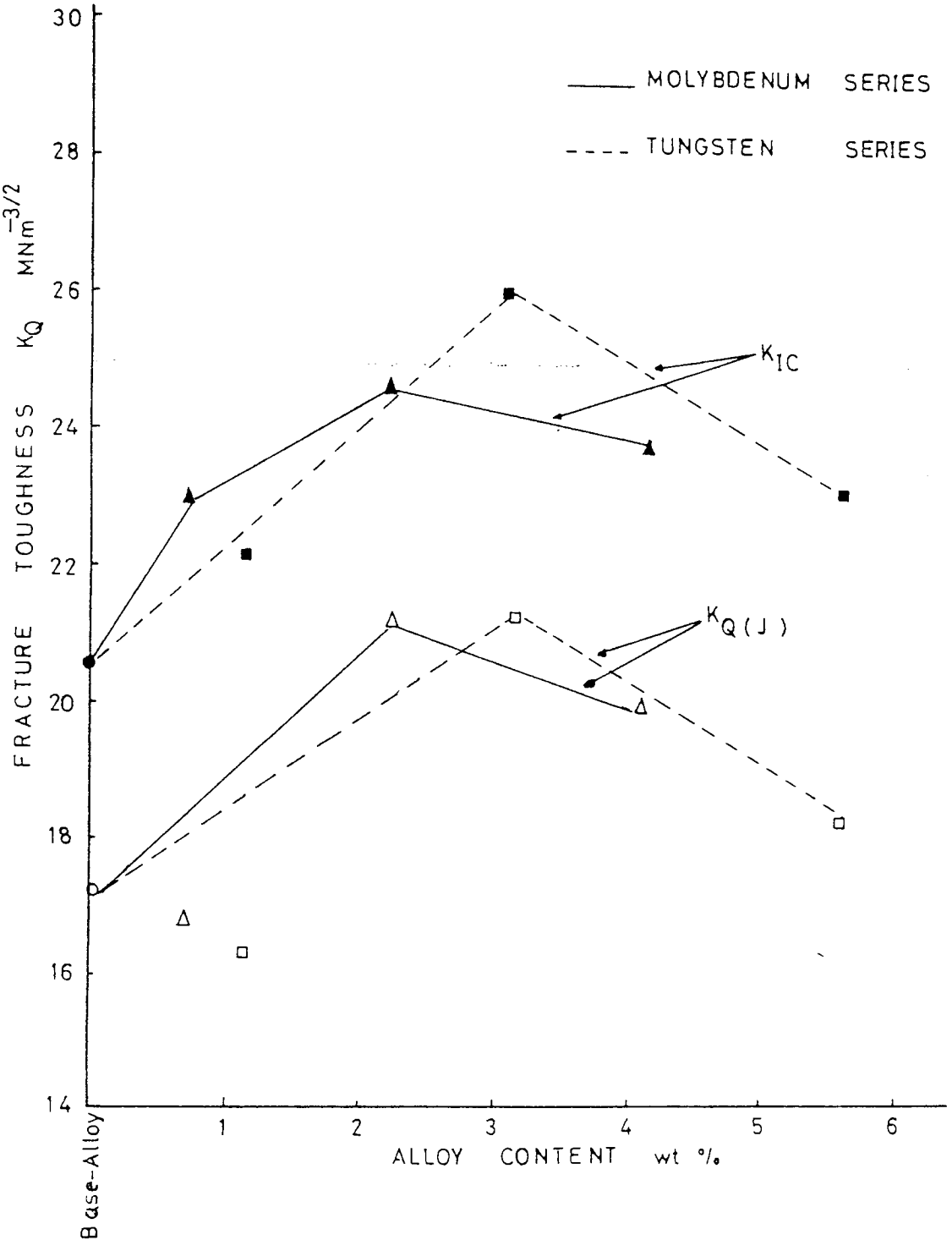

FIGURE 56: Comparison between the L.E.F.M. and yielding fracture mechanics (J-integral) testing techniques on the fracture toughness values of as-cast alloys

initiation whereas K_Q values in L.E.F.M. tests are after the crack has propagated about to 2% of the original crack length. The other possible major source of error in evaluating the J-integral was in the determination of crack initiation point. This point was determined as the point where a deviation from linearity was observed in the potenial drop records (see Fig. 39). It has been proved that it is difficult to distinguish the rise in the electrical resistance caused by plastic deformation and blunting at the crack tip from that caused by crack advancement [143]. As can be seen from the tables the difference between the two test methods is bigger for austenitic high-Cr cast iron, possibly as a result of the reason given above. Due to the limited number of specimens available and the necessary fulfillment of the ASTM.E399 recommendations, no attempt has been made to detect the actual crack initiation point either with compliance measurements by unloading during the testing or by break-open specimens. However, when calculations were carried out taking the crack initiation point after 5 millivolt increase in the potential drop records, the $K_{Q(J)}$ values obtained correlated with the K_{IC} values, but this could not be proved experimentally due to reasons given above. Therefore determinations were carried throughout the work taking the crack initiation point as the point when the first deviation was observed in potential drop records.

When the validity of given $K_{Q(J)}$ or J values is considered, they could be taken as a material property of the studied alloys for very conservative designs.

9.3 Effect of Metallurgical Variables on the Toughness of High-Cr Cast Irons

The scope of the fracture toughness testing programme undertaken was to evaluate the fracture toughness values of high-Cr cast irons with most possible metallurgical variables which gave variations in the eutectic carbide morphology, as discussed previously in section 9.1. In addition to finding out the optimum alloy addition level and heat treatment procedure for maximum toughness combined with adequate hardness, the main aim was also to establish the possible interrelationship between the microstructure and fracture toughness of high-Cr cast irons.

The results obtained from studies were discussed in terms of the effects of alloy additions, heat treatments and hardening variables on the toughness characteristics of austenitic and martensitic high-Cr cast irons. The variation of toughness values with changes in the morphology of microstructural features are discussed in detail in section 9.6.

During the course of the work no attempt was made to investigate the effects of macro-residual stress and directionality since these have been reported as having no significant effect on the toughness characteristics of high-Cr cast irons[53,134,135].

9.3.1 Toughness Variation of Austenitic High-Cr Cast Irons

The variation of toughness with additions of molybdenum and tungsten in the as-cast condition has already been shown in Fig. 56. As can be seen, all alloys with additions of molyb-

denum and tungsten gave higher toughness values than that obtained from the base alloy. They also exhibited a similar toughness trend with variation in addition levels. The retardation of "pearlite transformation" is an important factor when high-Cr cast irons are used in the as-cast condition, since it has been found that the formation of "pearlite" degrades the wear resistance considerably. As mentioned in the literature review, this can often be avoided by certain alloy additions. Molybdenum has been found very attractive and up to 3% additions of molybdenum for this purpose are in very wide application in this aspect. The results indicated that additions of 2% Mo or 3% tungsten to 15% Cr-2.7%C high-Cr cast irons provide maximum toughness in the as-cast condition. Particularly if retardation of "pearlite transformation" is also considered, molybdenum is found to be more favourable than tungsten since "pearlite" colonies were observed in the microstructure of 3% tungsten alloy. Therefore it is concluded that for the as-cast condition an addition of 2% molybdenum provides the best combination of toughness and good wear resistance since a further increase in the addition level has neither a positive effect on the fracture toughness nor on the retardation of of the "pearlite transformation".

As observed in section 9.1, the variation in the carbide morphology within the microstructure of high-Cr cast irons is a result of the combined effects of alloy additions and high temperature heat treatments. Although it is difficult to separate one from another, these two factors were considered as separate variables.

The toughness values obtained from specimens subjected to high temperature heat treatments at 1180°C for various holding periods are plotted against molybdenum and tungsten content of the alloys in Fig. 57 and Fig. 58 respectively. After the high temperature heat treatments an increase of up to 35% was observed in the toughness values of molybdenum and tungsten containing alloys. Except for the very long soaking period (72 hours), a comparison with the fracture toughness of the base alloy shows an increase of about 50%.

As can be seen from the figures the response of the molybdenum and tungsten containing high-Cr cast irons to high temperature heat treatments are not similar, although they have shown the same trend in the as-cast condition. The variation of toughness in tungsten added alloys have exhibited an almost linear increase with increasing tungsten content in the base alloy, whereas for molybdenum additions a maximum at about 2% Mo addition level, decreasing with increasing molybdenum content was observed. The figures also suggest that, in order to reach the similar toughness values, it is necessary to add about 2.5 times more tungsten than molybdenum.

By considering the high temperature holding period as another variable, the obtained toughness values of the alloys were plotted against soaking time at 1180°C in Fig. 59 and Fig. 60 for molybdenum and tungsten added alloys respectively. As can be seen from the figures, there is always a critical holding period for each addition level which gives the maximum fracture toughness at that addition level. Further, longer holding periods have a detrimental effect and lower the

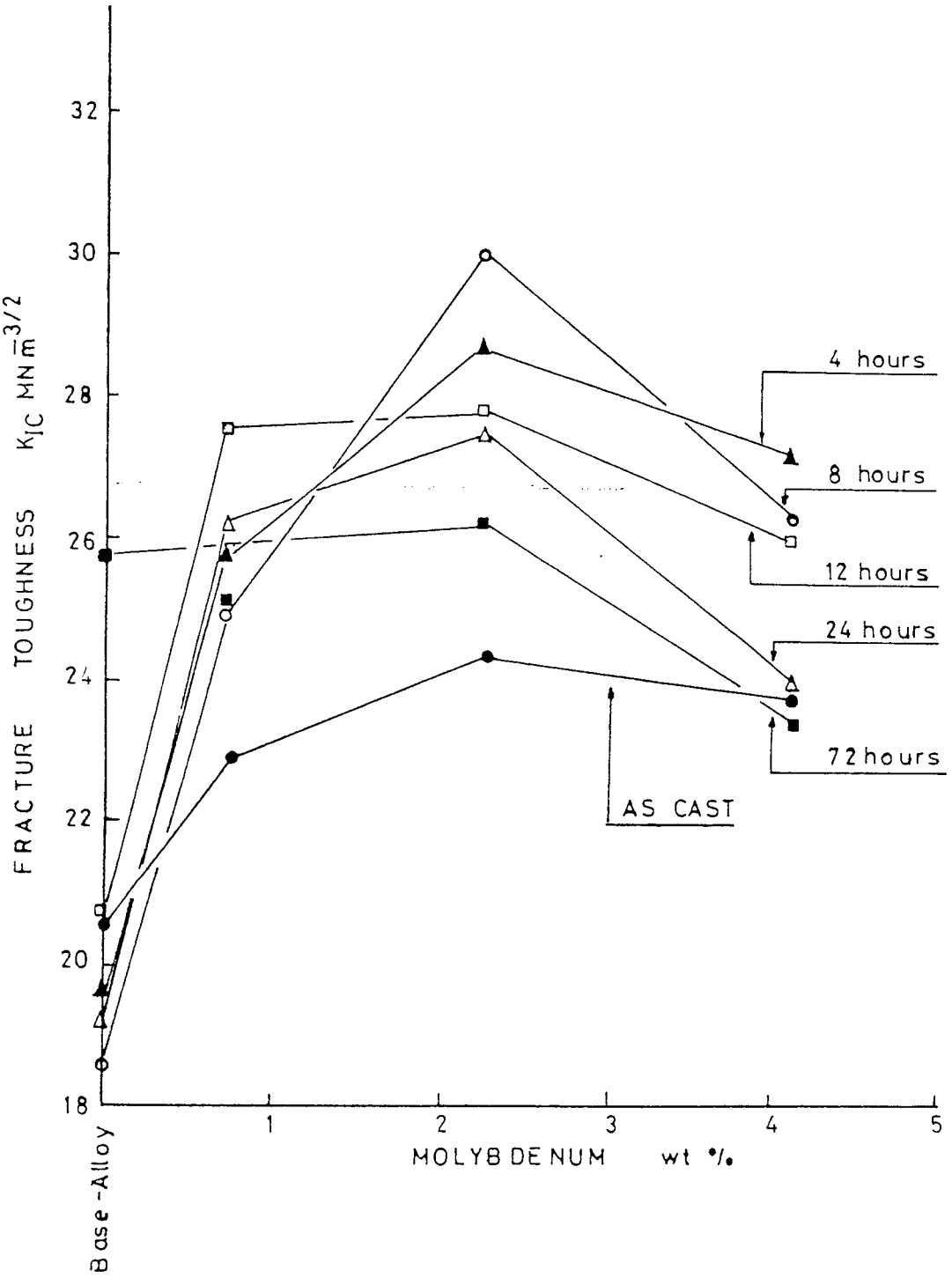

FIGURE 57: Fracture toughness variation of high-Cr cast irons with molybdenum additions

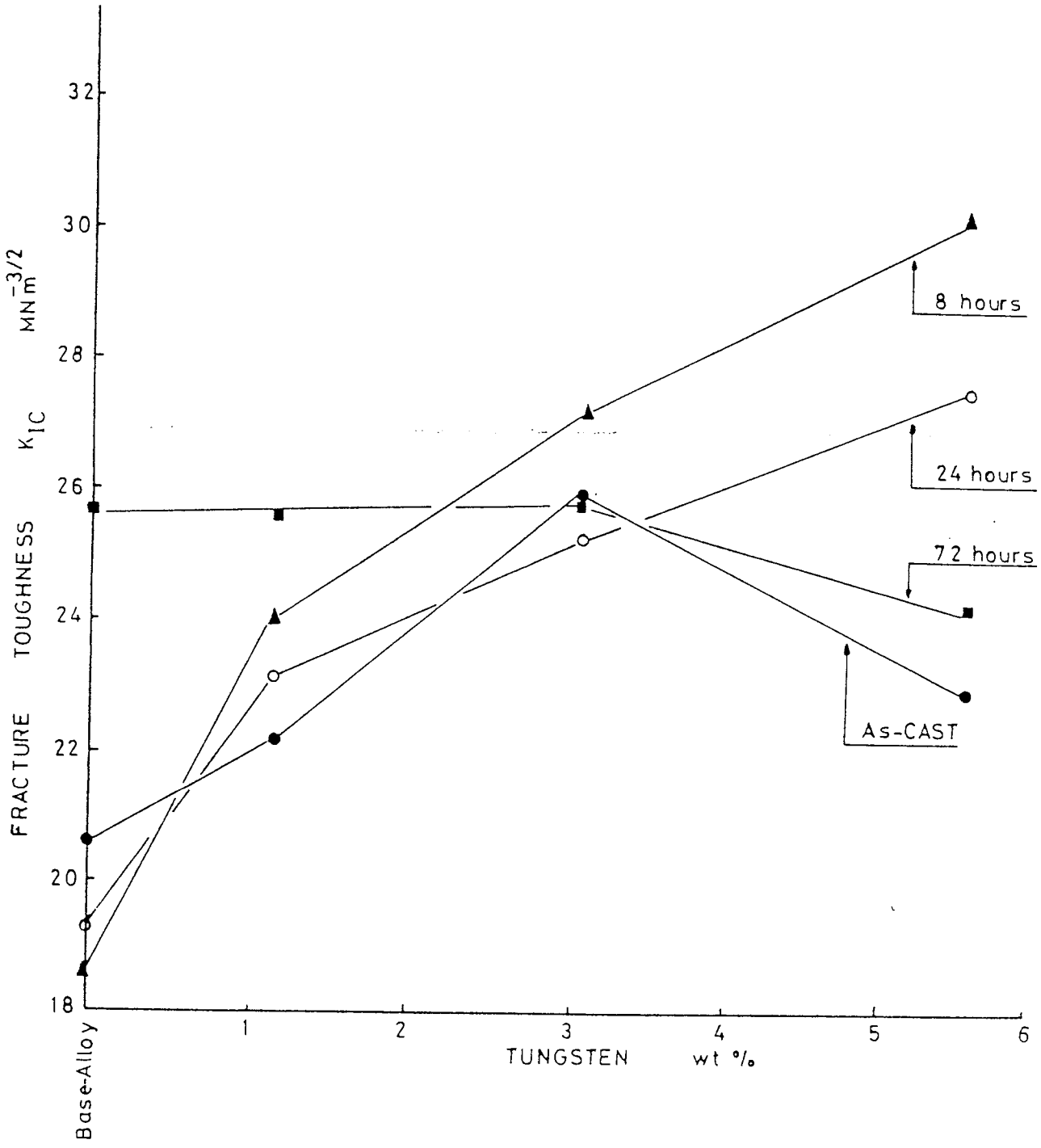

FIGURE 58: Fracture toughness variation of high-Cr cast irons with tungsten additions

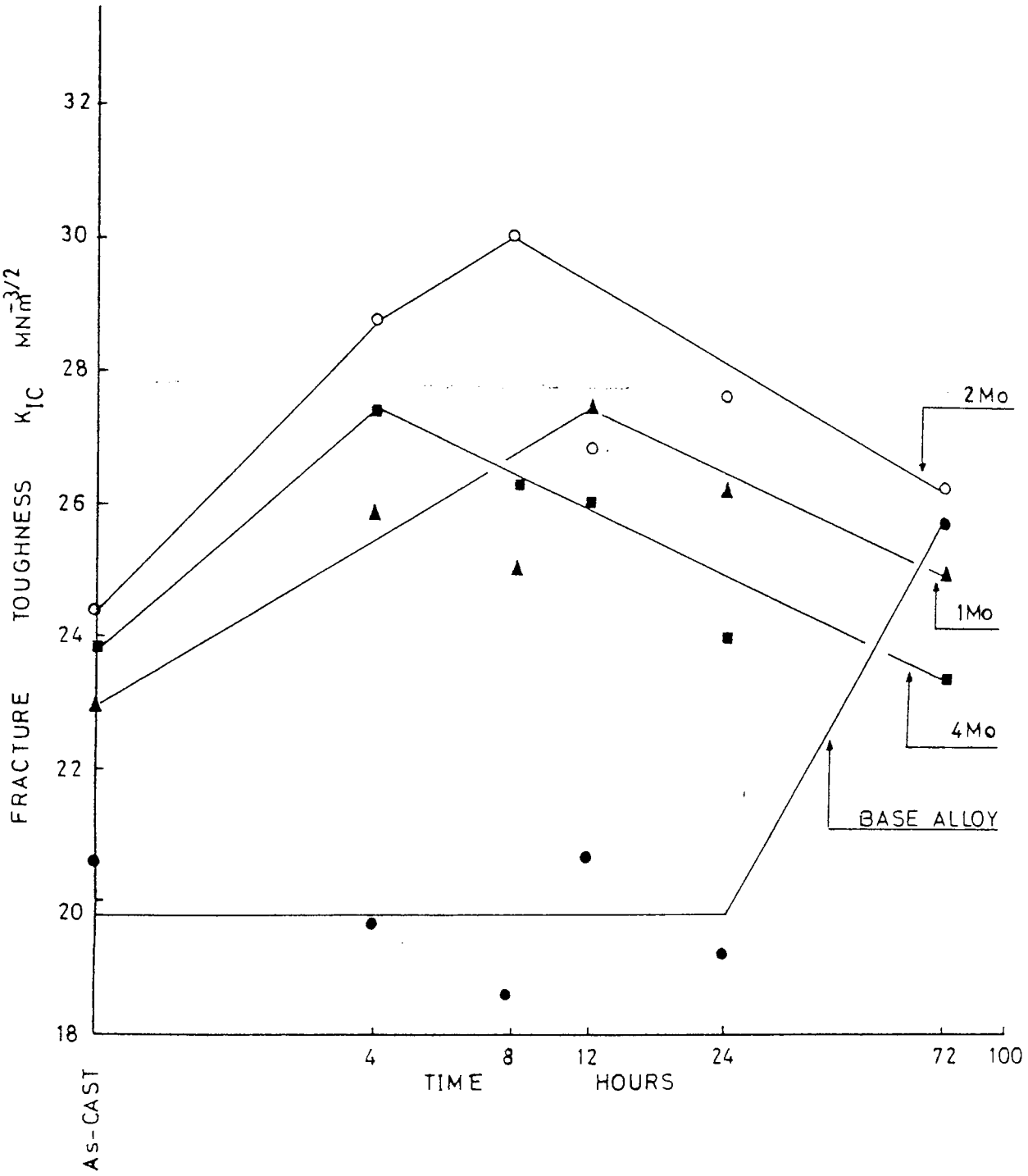

FIGURE 59: Fracture toughness variation of molybdenum containing alloys with holding periods at 1180°C

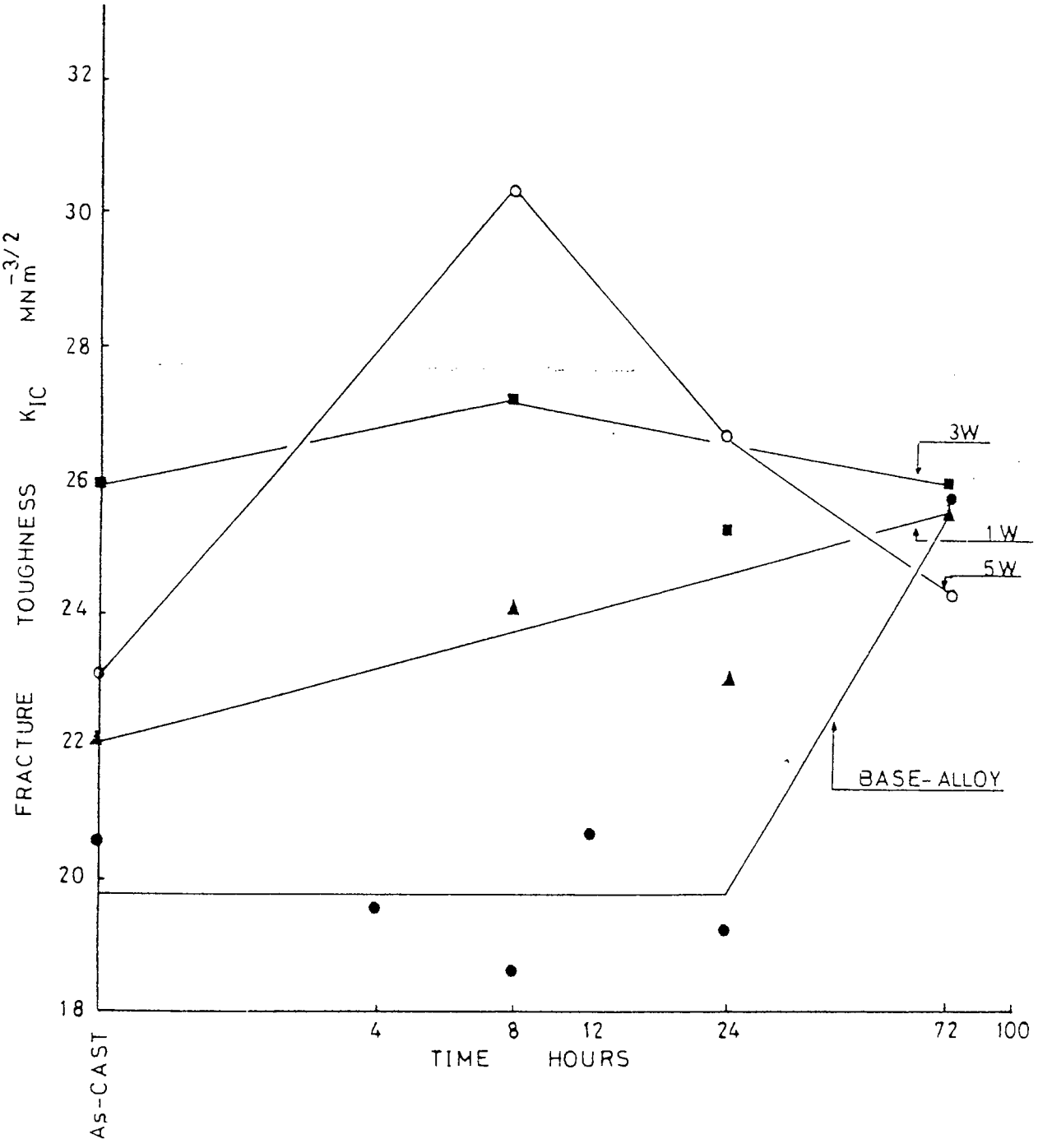

FIGURE 60: Fracture toughness variation of tungsten containing alloys with holding periods at 1180°C

toughness of the alloys to almost their as-cast fracture toughness value.

Another significant trend indicated by the results obtained showed that increase in the toughness values was obtained for shorter holding periods for the alloys which have higher addition levels. A similar trend was also observed from metallographic and quantitative-metallographic studies. If a decrease in the "density" of the eutectic carbides is considered as a measure of spheroidisation or breaking down of the continuous network of eutectic carbide structure, the "density" of the eutectic carbides decreased much more rapidly with increasing alloy content (see Fig. 50).

9.3.2 Toughness Variation of Martensitic High-Cr Cast Irons

In order to obtain martensitic matrix, the alloys were heat treated by following commercial hardening procedures directly from the as-cast state and previously subjected to high temperature heat treatments to alter the eutectic carbide morphology before hardening heat treatments. The determination of the possible variation of toughness with various tempering conditions after hardening heat treatments was not included in the scope of this work.

The obtained fracture toughness values of martensitic high-Cr cast irons are plotted against the molybdenum content of the alloys in Fig. 61 and against the holding periods at 1180^{o}C in Fig. 62, for reasons given earlier. As can be seen from the figures, neither alloy additions nor applica-

tion of high temperature heat treatments have shown any significant effect on the toughness characteristics of martensitic high-Cr cast irons. Almost a constant toughness level was observed with both variables.

A martensitic matrix usually offers better resistance to abrasive wear. Although the high-Cr cast irons responded favourably to hardening heat treatments, the austenite or decomposition products of austenite are retained to room temperature within the microstructure, depending on the section size of the component. Therefore, full hardenability becomes an important consideration, especially for large sectioned components. As mentioned in the literature review, this is achieved by alloy additions. The results obtained here suggested that for martensitic high-Cr cast irons the level of alloy additions to high-Cr cast irons should be considered for particular hardening characteristics rather than toughness properties since additions of up to 4% molybdenum gave no significant variation in the toughness values of the alloys which were hardened directly from the as-cast state.

The other important result is that the variation in the eutectic carbide morphology due to the combined effects of alloying and high temperature heat treatments has shown no significant effect on the toughness characteristics of martensitic high-Cr cast irons. This is opposite behaviour to that observed in austenitic alloys. This indicated that the toughness of martensitic high-Cr cast irons is independent of eutectic carbide morphology (contrary to austenitic

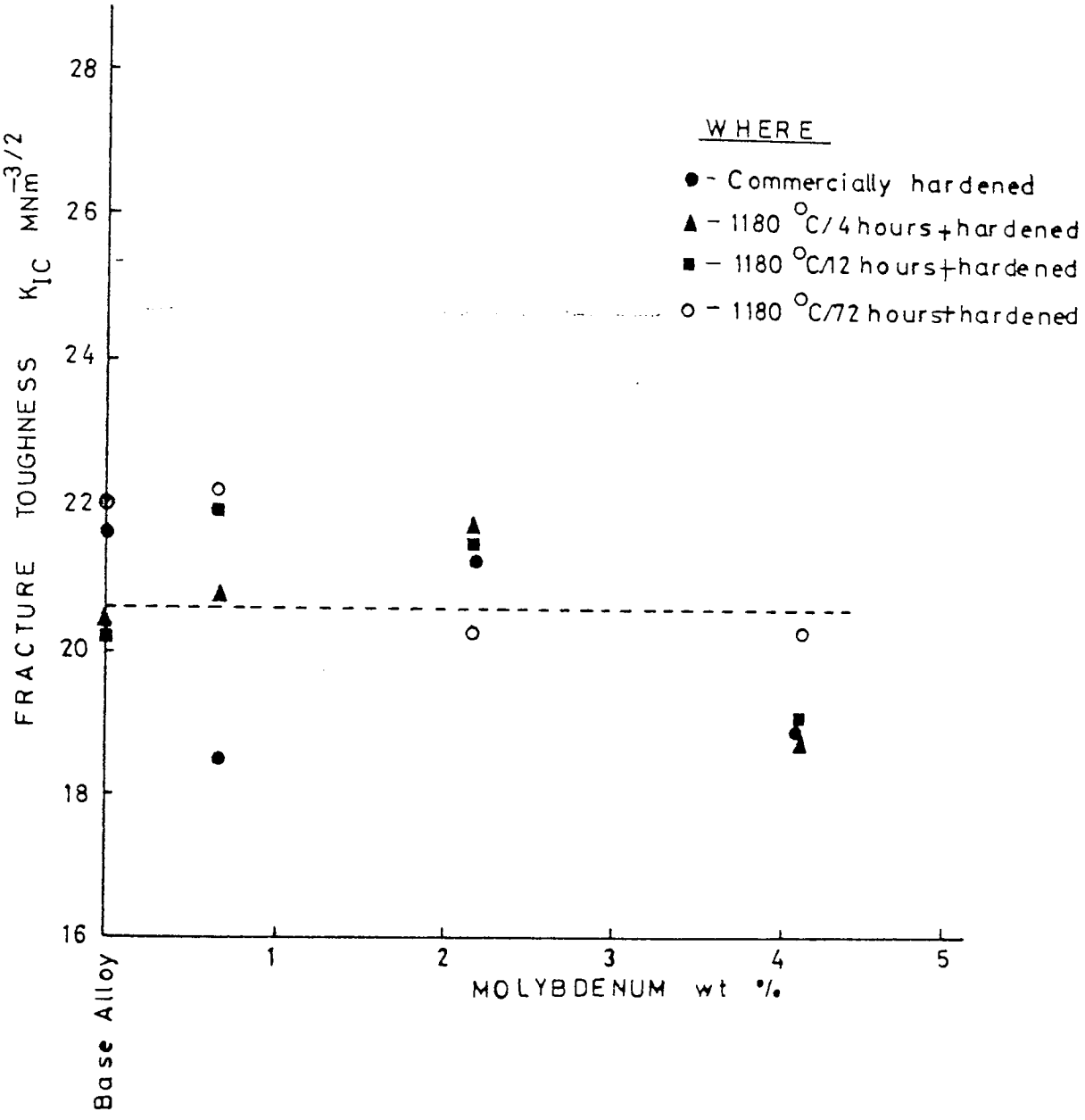

FIGURE 61: Fracture toughness variation of martensitic high-Cr cast irons with molybdenum additions

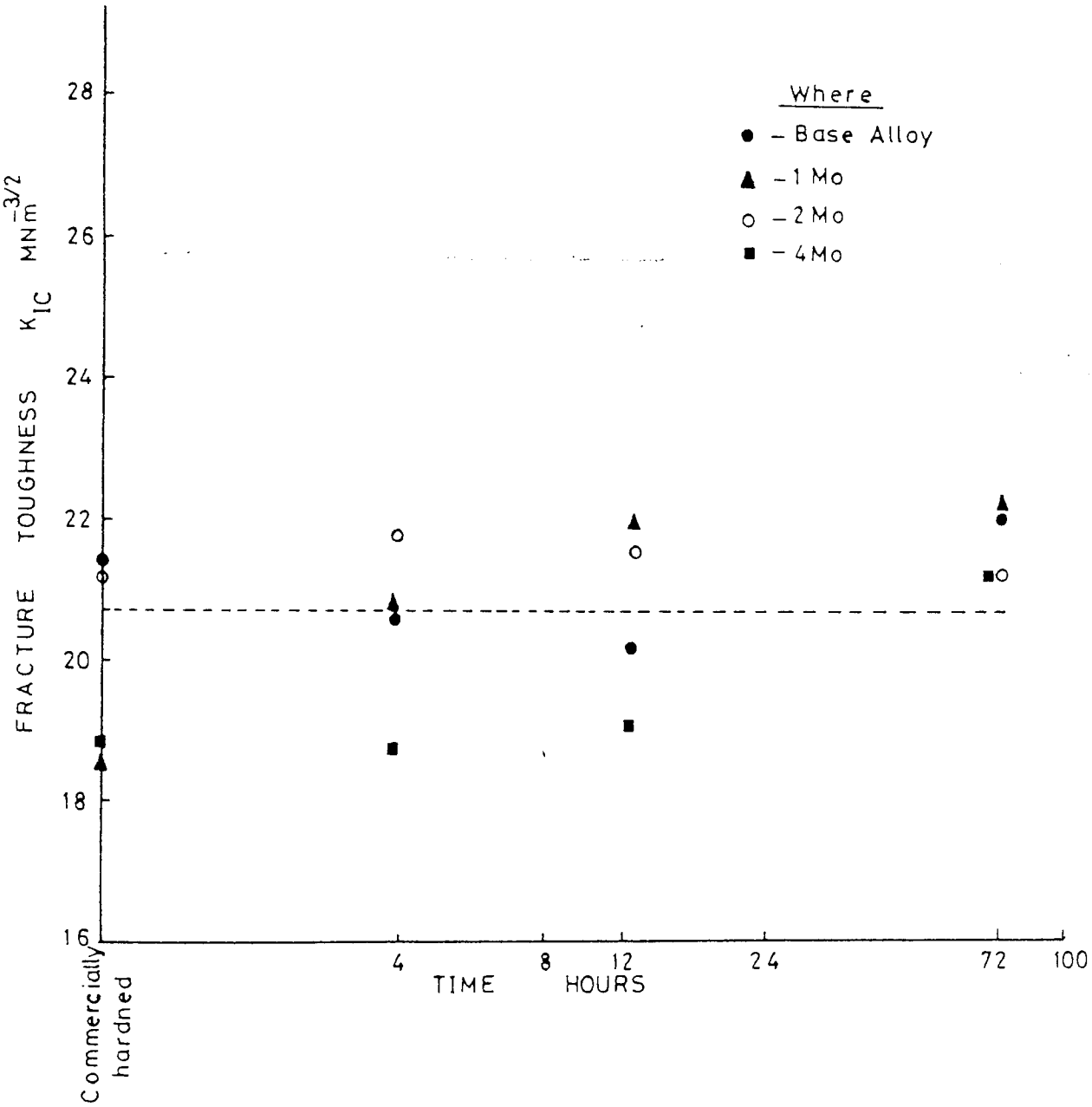

FIGURE 62: Fracture toughness variation of molybdenum containing martensitic high-Cr cast irons with holding periods at 1180°C

high-Cr cast irons) and is influenced by matrix properties.

In order to establish the effect of heat treatment temperature on the toughness, the molybdenum containing alloys together with the base alloy were subjected to heat treatments at temperatures between commercial hardening temperature 975°C and 1180°C for 12 hours. The results are summarised in Fig. 63. As can be seen, the response of molybdenum-containing high-Cr cast irons to heat treatment temperature are distinctly different to the base alloy. The alloy containing 2% Mo gave maximum toughness at 1125°C which was the highest toughness value measured during the studies. These variations in toughness of molybdenum-containing cast irons could be explained by considering the microstructure of the alloys, and variations in the hardness values (see Fig. 64). As can be seen from the plates, the heat treatments at these intermediate temperatures did not alter the eutectic carbide morphology (see plate 19). On the other hand, the matrix of the alloys gradually changed from a fully martensitic structure to a fully austenitic structure. Although no attempt has been made to determine the amount of retained austenite, the decrease in the hardness values in significant levels supported this qualitatively (also apparent from metallography of the alloys in plate 20).

For these intermediate temperatures, it is possible to conclude that fracture toughness is controlled by the matrix, particularly by the amount of retained austenite

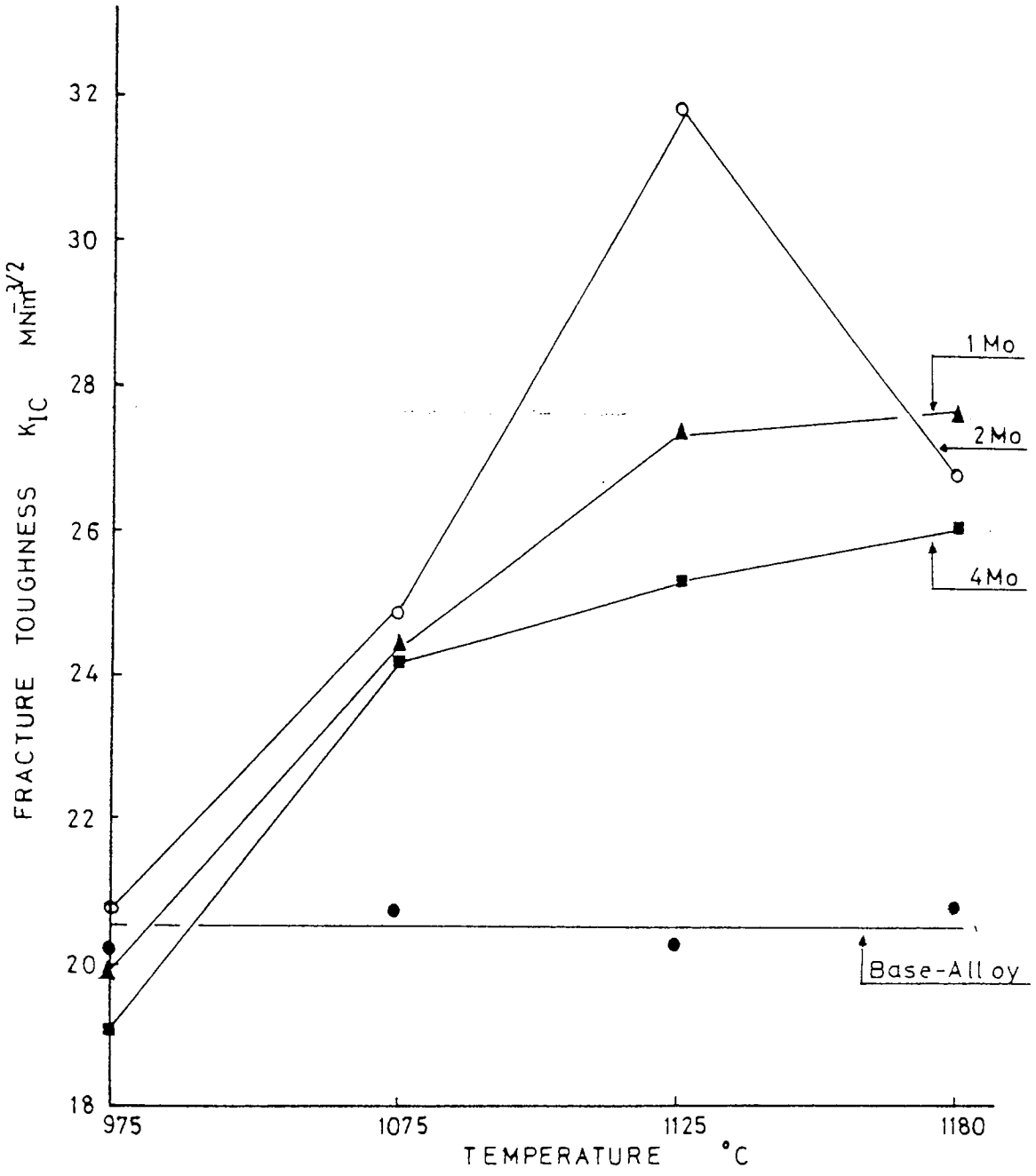

FIGURE 63: Effect of the heat treatment temperature on the fracture toughness of molybdenum containing high-Cr cast irons (holding period 12 hours)

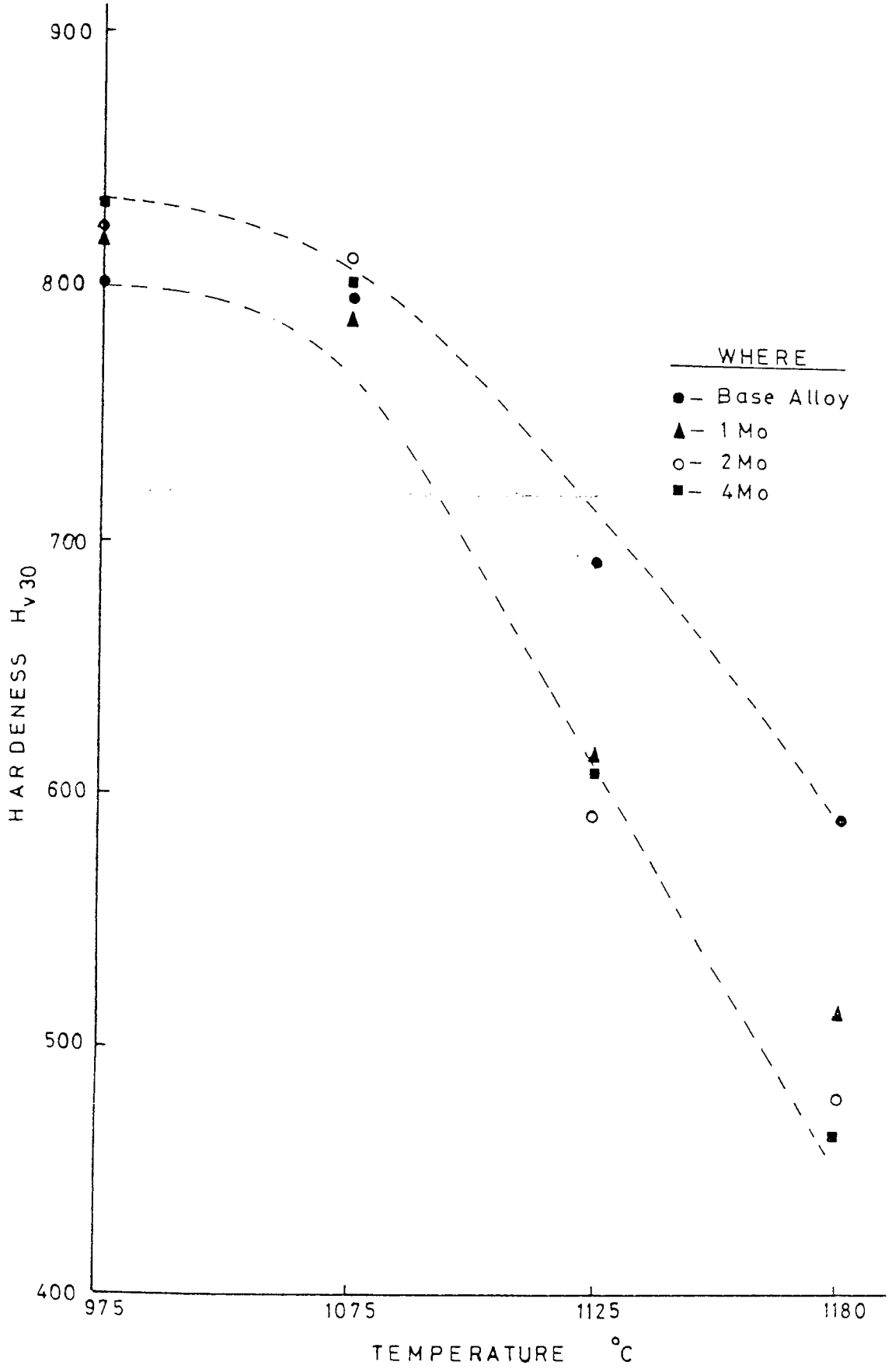

FIGURE 64: Hardness variation of molybdenum containing alloys with heat treatment temperature (holding periods 12 hours)

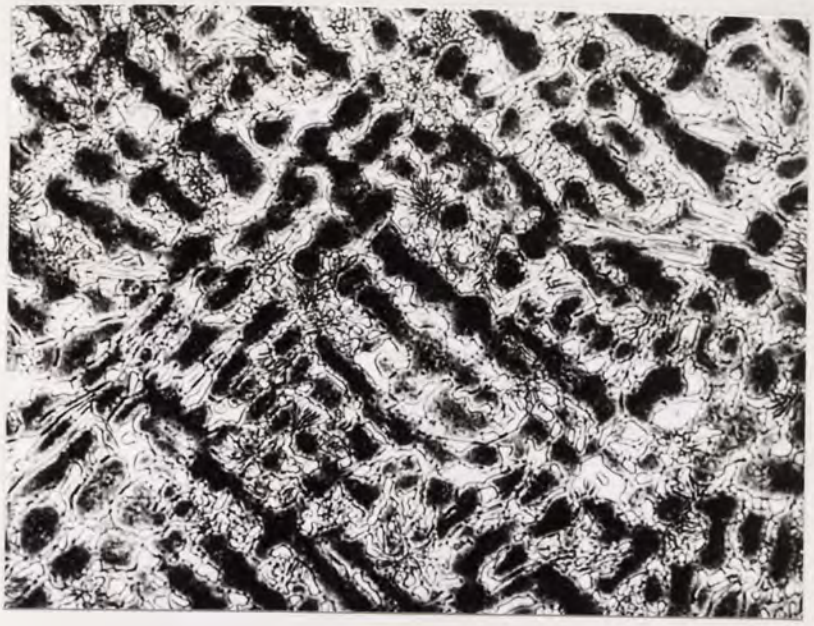

A - Heat treated at 975°C

K_{IC} : 21.24 $MNm^{-3/2}$

H_{v30} : 842

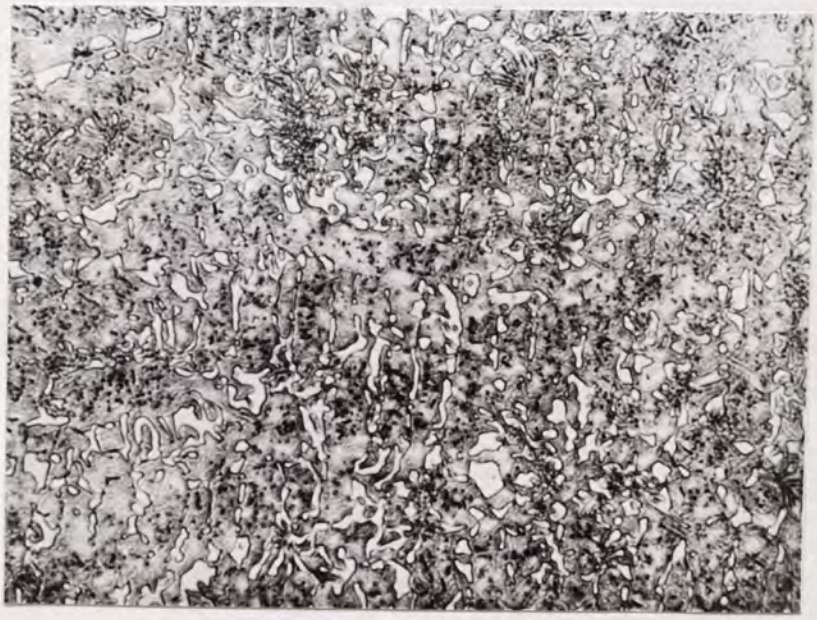

B - Heat treated at 1075°C

K_{IC} : 24.43 $MNm^{-3/2}$

H_{v30} : 812

C - Heat treated at 1125°C

K_{IC} : 30.94 $MNm^{-3/2}$

H_{v30} : 590

PLATE 19: Effects of heat treatment temperature on the microstructure of 2% Mo containing high-Cr cast iron (Holding periods 12 hours).
Note: the variation of eutectic carbide

A - Heat treated at 975°C

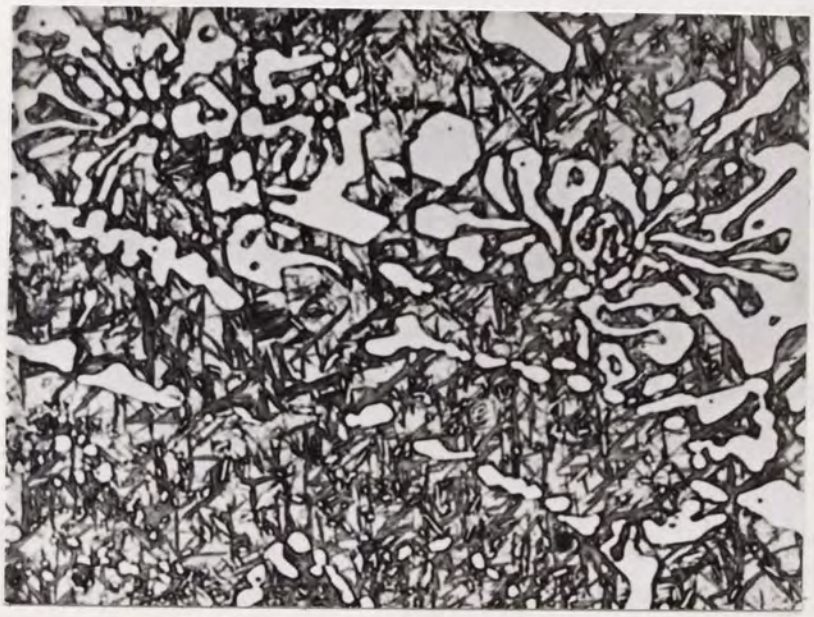

B - Heat treated at 1075°C

C - Heat treated at 1125°C

PLATE 20: Effects of heat treatment temperature on the microstructure of 2% Mo containing high-Cr cast iron (holding periods 12 hours). Note the retention of austenite within the matrix x520

within the matrix, since insignificant variation was observed in the eutectic carbide morphology. It is assumed that when there is a significant increase in the amount of retained austenite and the matrix becomes virtually austenitic, toughness is more likely to be dependent on the eutectic carbide morphology, as observed in section 9.3.1.

The reason for the effect of retained austenite on the observed increase in the toughness values, could be a result of created micro-residual-stresses between the martensite and untransformed austenite. The metallographically observed transformation of austenite to martensite under the applied stresses by the stress-assisted transformation mechanism (see plates 21,22) could also be considered as another possible reason. However, it is assumed that the first approach was most likely taking place in the alloys which have mixed matrix structure, due to the reasons given for stress-assisted martensite formation in section 9.6.2.

9.3.3 Toughness Variation with Hardness in High-Cr Cast Irons

In Fig. 65 the obtained toughness values of the alloys were plotted against their hardness. There is a very broad trend which indicates that fracture toughness increases with decreasing hardness but this is not the controlling parameter of toughness as mentioned in the work of Erickson [144]. Different structures with the same K_{IC} value exhibited large differences in hardness and conversely, at the same hardness, K_{IC} values can vary substantially.

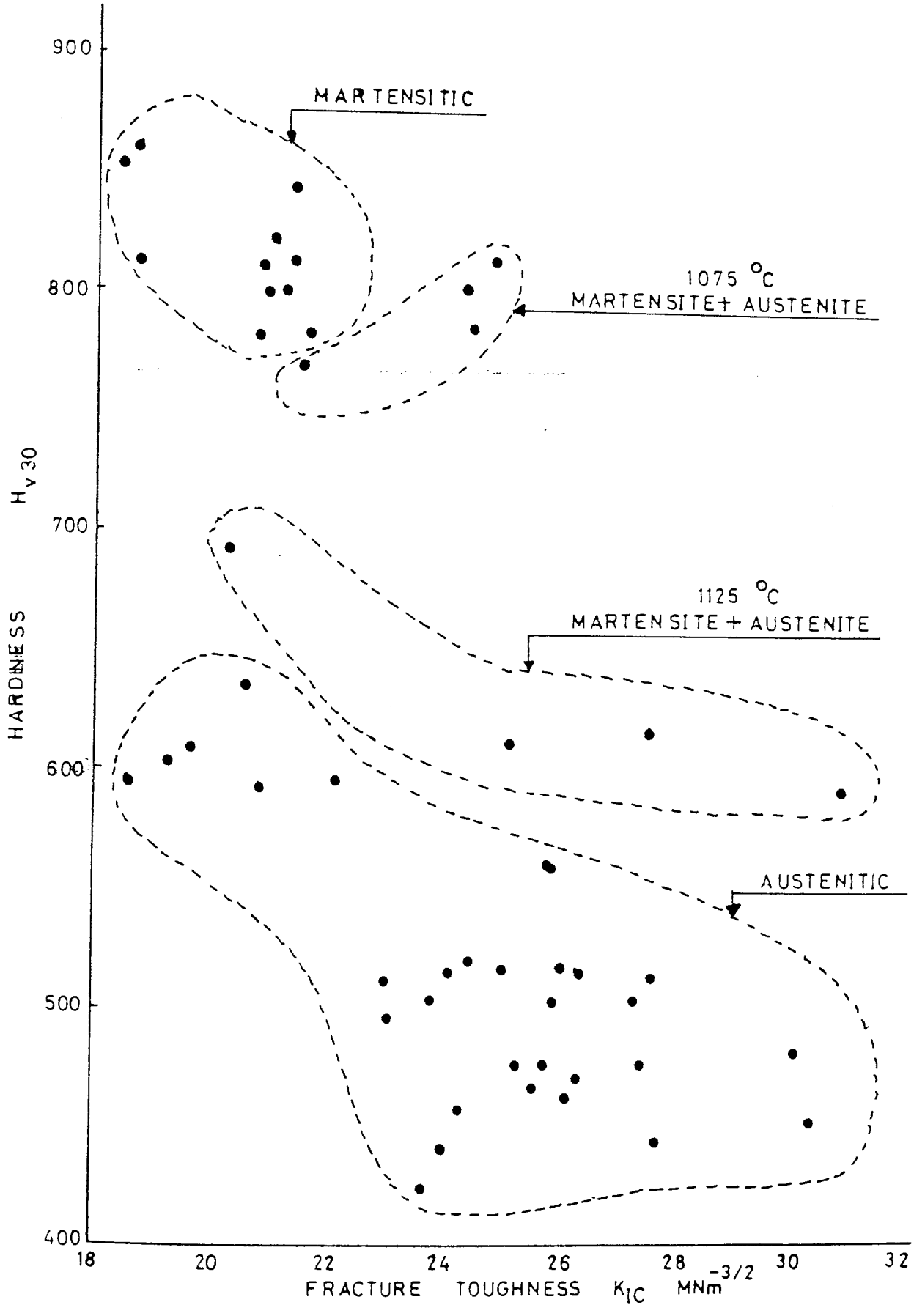

FIGURE 65: Variation of fracture toughness of high-Cr cast irons with hardness of the alloys

As a summary, the addition of 2% molybdenum and heat treatment at 1180°C for 4-8 hours was the best optimisation of the metallurgical variables studied and enabled an increase in the fracture toughness of commercial grade 15% Cr 2.7% C cast iron of almost 50%. It is assumed that these conditions will also provide good wear resistance combined with maximum toughness since the hardness values of the alloys for these holding periods were not much different to the hardness value of the as-cast alloys (see Fig. 53). Also, additions of molybdenum and application of heat treatments at intermediate temperatures which were above the commercial hardening temperature gave similar improvements in the toughness values with hardness values between the hardness of martensitic and austenitic high-Cr cast irons.

Hardness and fracture toughness are material properties. Generally abrasion resistance increases with increasing material hardness but is affected by the wear mechanism. The optimisation of metallurgical variables concluded here was made only by considering the hardness and toughness of the alloys. Therefore they should be accepted as a useful trend rather than absolute conclusions. It is believed that the best optimisation of these given variables can only be achieved with the results obtained from field trials of wear tests, combined with laboratory fracture toughness tests.

9.4 Notch Bending Tests and Variation of Notch-Toughness of High-Cr Cast Irons

In order to establish the possible fracture mechanism of the high-Cr cast irons, notch bending tests were undertaken for selected alloys using charpy sized specimens with various notch radii and a constant notch depth. The test data obtained were processed using the method suggested by Tetelman et al [112], as described in section 7.4. This method, which is based on the slip-line theory, can be criticised by referring to the finite element analysis work of Griffith and Owen [118]. Their work showed that the slip-line theory over estimates the critical fracture stress (σ_F^*) for low loads and also the maximum principal stress $(\sigma_{yy})_{max}$ does not occur at the elastic-plastic interface, as described by slip-line theory, but inside the plastic zone and behind the elastic-plastic interface. However by considering the nominal bending stresses at failure loads of the alloys (see tables 20-25) it can be seen from Figures 26 and 27 the difference between the two methods is very small. Therefore slip-line theory was considered a good approximation for the determination of critical fracture stress of the alloys under investigation.

As can be seen from tables 20-25 the values of σ_F for all notch types, together with the duplicated test results were averaged to find out the critical fracture stress (σ_F^*).

Overall $\pm$ 3% maximum standard error was observed which could be well within the tolerance limits of possible experimental errors. These results led to the conclusion

that there are constant critical fracture stress values of the alloys which are independent of notch root radius, and this is therefore an indication of the stress controlled fracture behaviour of high-Cr cast irons.

According to Tetelman et al [112] stress controlled, unstable fracture occurs in notched bend bars when the maximum principal stress $(\sigma_{yy})_{max}$ below the notch builds up to a critical value of σ_F^*. Since σ_F^* is determined by microstructural parameters, it is therefore a material property, independent of specimen geometry. By equating the critical plastic zone size at fracture in the notch bend specimen (equation 101) with the plastic zone size ahead of a sharp-crack in plane-strain condition (equation 14b) they obtained equation (42).

$$r_{y/\rho} = \left[\exp((\sigma_F^*/\sigma_{ys})-1)\right] \quad \ldots\ldots\ldots(101)$$

$$r_y = \frac{1}{5.6\pi}(K_{IC}/\sigma_{ys})^2 \quad \ldots\ldots\ldots(14b)$$

$$K_{IC(\rho)} = 2.89\,\sigma_{ys}\left[\exp((\sigma_F^*/\sigma_{ys})-1)-1\right]^{\frac{1}{2}}\sqrt{\rho} \quad \ldots(42)$$

They proposed $K_{IC(\rho)}$ (apparent notch toughness) as a material parameter which is a measure of the toughness of materials for blunt stress concentrators. This parameter is geometry dependent and varies linearly with the square root of notch radius. By following the method suggested by Tetelman et al, $K_{IC(\rho)}$ values obtained were plotted against the square root of notch root radii for three

different compositions of high-Cr cast irons in Figs. 66-68 to show variation of apparent notch toughness of high-Cr cast irons with studied metallurgical variables. It was observed in the work of Spink et al [146], that the linearity of the equation (42) suggested by Tetelman et al breaks down for very large root radii. As can be seen from the figures, the studied notch root radii gave a linear relationship. In the as-cast condition, the alloy additions have no significant effect and notch toughness values $K_{IC(\rho)}$ of the alloys are very similar to each other. Although application of high temperature heat treatments to these alloys gave an increase in the $K_{IC(\rho)}$ values, as can be seen from the figures and tables 20-25 there is no straight-forward relationship between $K_{IC(\rho)}$ and K_{IC} values of the alloys. For example, martensitic high-Cr cast irons have the lowest K_{IC} values and they exhibited higher or similar apparent notch toughness values.

In the work of Tetelman et al, equation (42), which leads to determination of the apparent notch toughness, was obtained by equating two plastic zone sizes ahead of the two different stress concentrators (sharp-cracks and notches). The validity of this assumption and consequently validity of equation (42) could be discussed in the following way;

During the studies, the K_Q values were calculated under the assumption that the notches are equivalent length sharp-cracks. As can be seen from tables 20-25, for sharp-notches the $K_{IC(\rho)}$ and K_Q values are comparable but for blunt

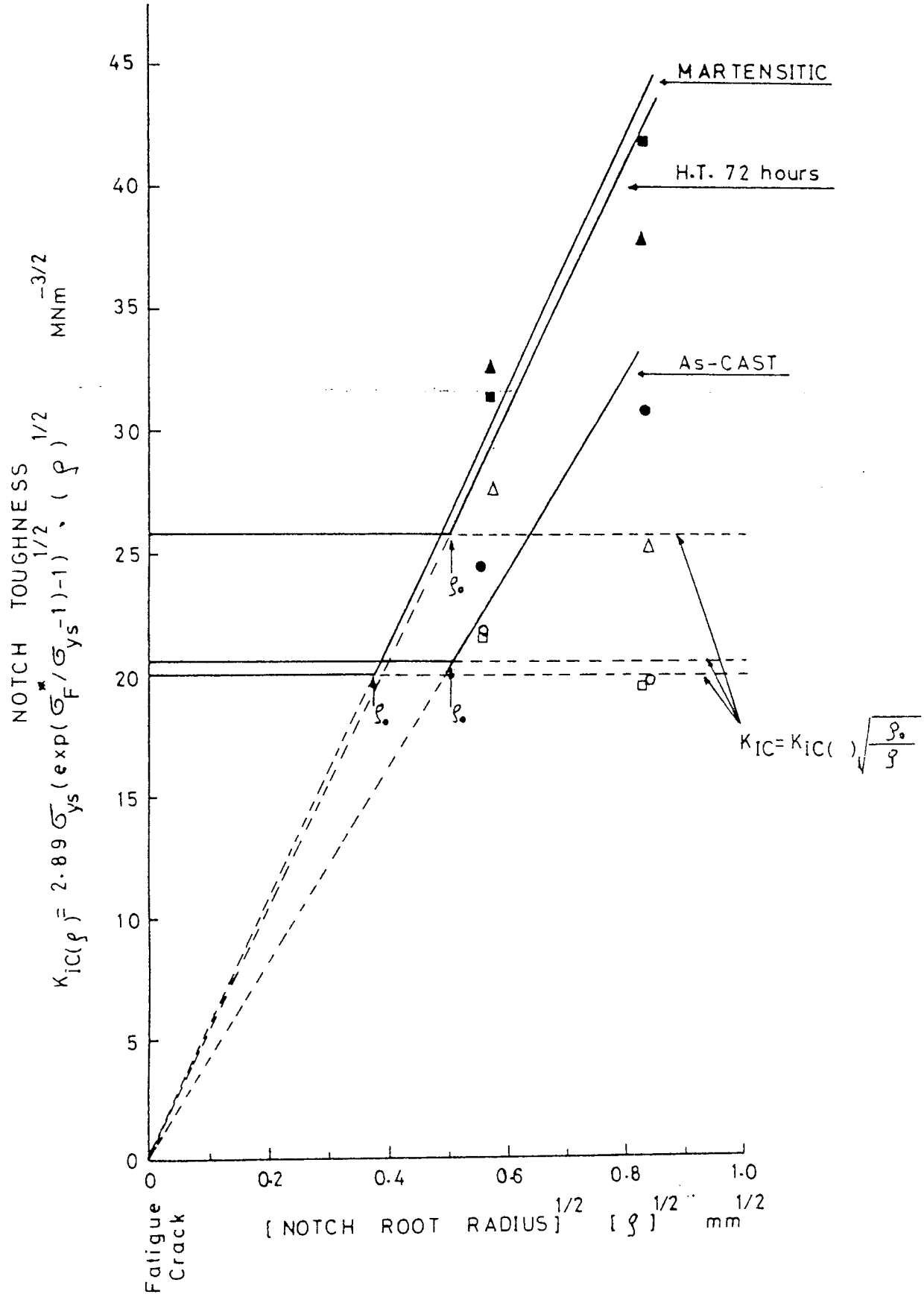

FIGURE 66: Variation of notch toughness $K_{IC(\rho)}$ of base alloy (15%Cr and 2.7%C) for different conditions

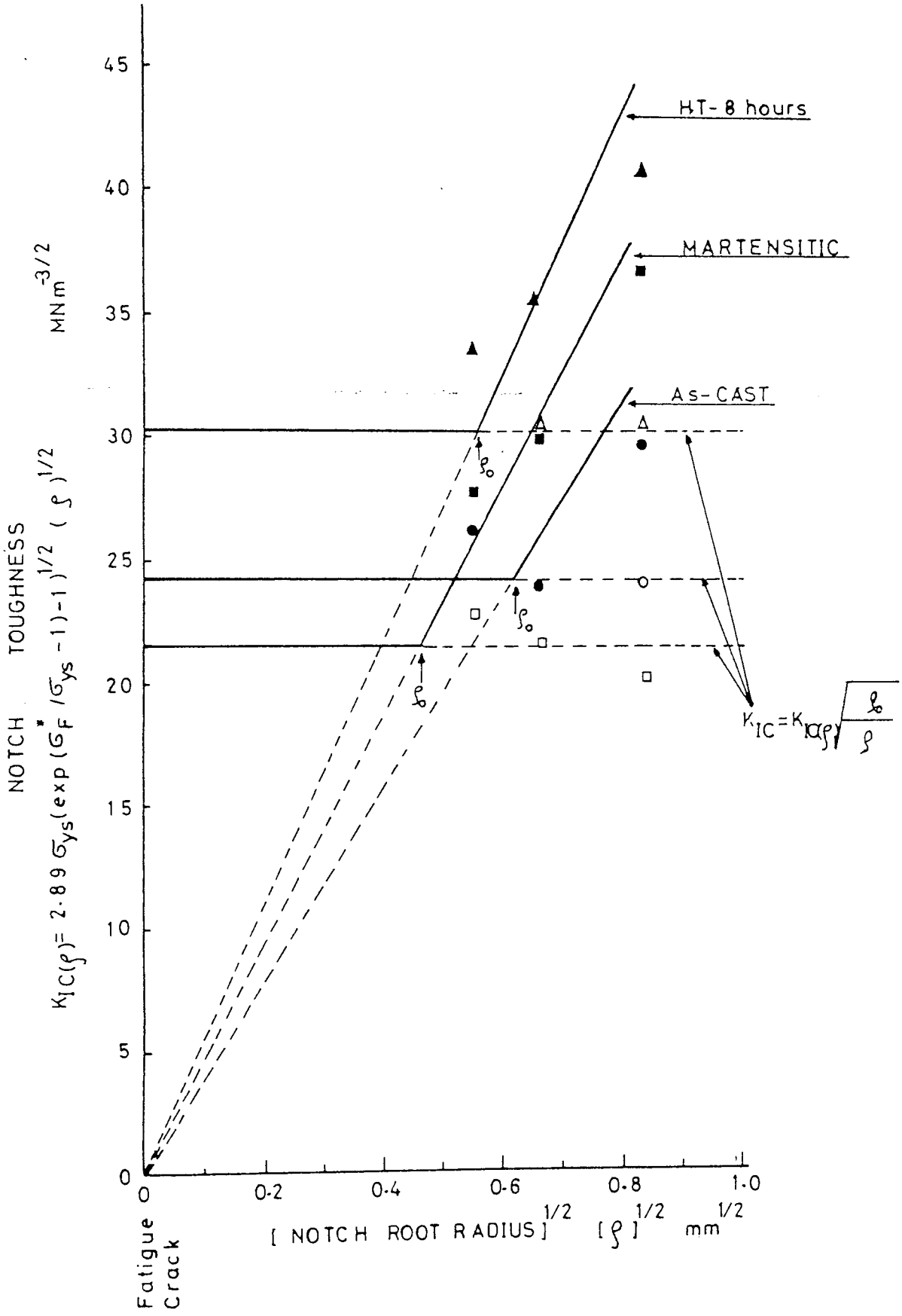

FIGURE 67: Variation of notch toughness $K_{IC(\rho)}$ of 2% molybdenum containing high-Cr cast irons for different conditions

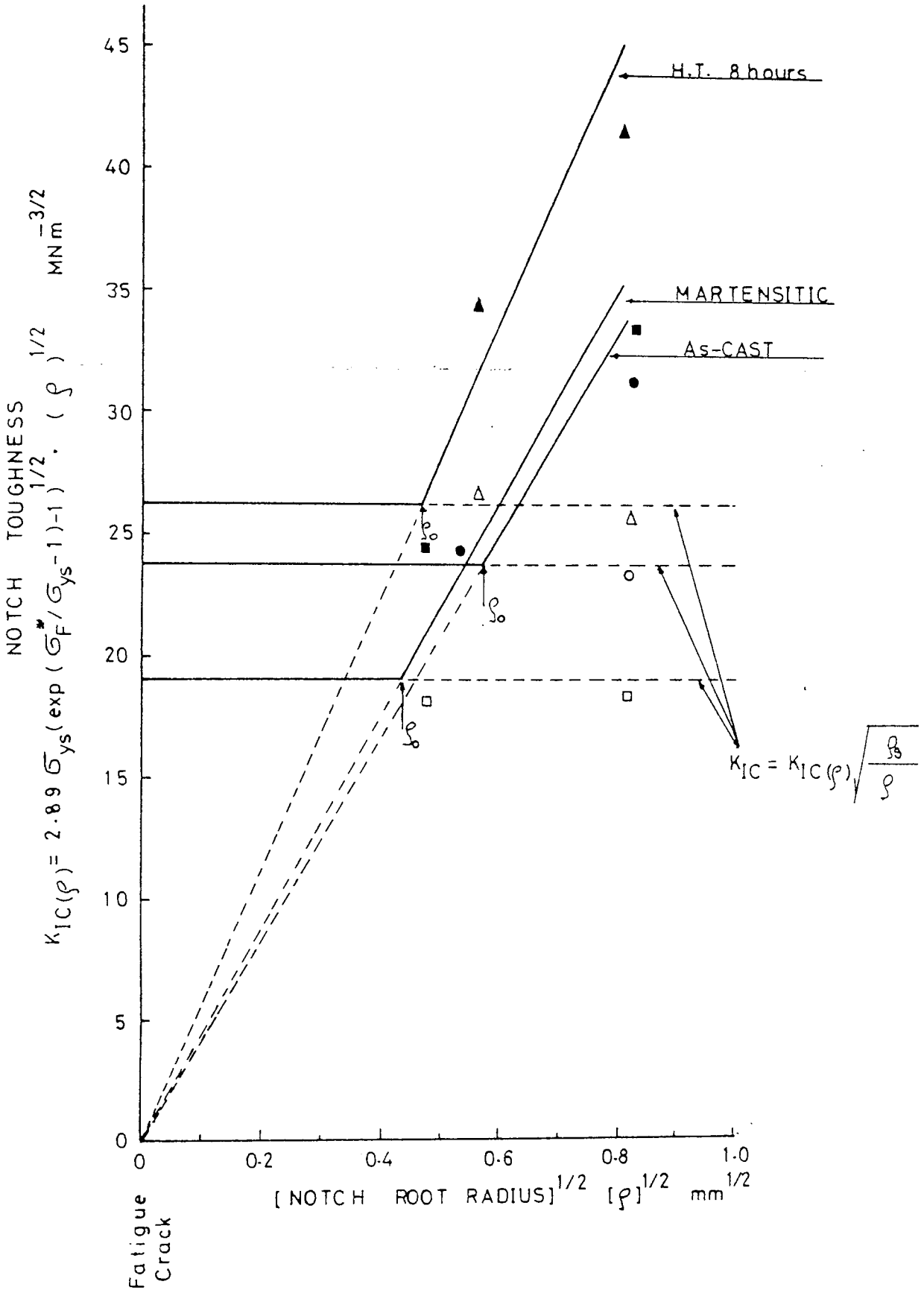

FIGURE 68: Variation of notch toughness $K_{IC(\rho)}$ of 4% molybdenum containing high-Cr cast iron for different conditions

notches, especially those in austenitic alloys, there is a consistent difference between the two values. It was proposed by Wiess [147] that the elastic stress distribution for a sharp-notch of finite root radius differs from that of a sharp-crack only over a very short distance. This could be written as below for fully elastic conditions

$$\sigma_{yy} = \sigma_N \cdot K_\sigma \cdot \left(\frac{1}{(1-2x/a)}\right) \left(1 + (4x/\rho)\right)^{\frac{1}{2}} = \frac{K_Q}{\sqrt{2\pi x}} \quad \ldots\ldots(102)$$

where σ_{yy} : elastic tensile stress acting ahead of the notch or sharp-crack

K_σ : Nueber stress concentration factor (equation 89)

x : distance ahead of the sharp-crack or notch

ρ : root radius of the notch

a : ligament depth

K_Q : stress intensity factor for geometrically equivalent length crack.(equation 44)

The left-hand side of the equation represents the elastic stress distribution of a sharp notch of finite root radius and the right-hand side of the equation represents the elastic stress distribution for a sharp-crack which is a geometrically equivalent length to the notch depth. In fully elastic conditions, the stress distribution in front of a notch is well approximated by the left-hand side of equation (102). However, as the plastic zone develops this relationship will no longer hold. Consider a notched bar under an applied moment which is sufficient to produce a plastic zone of depth R. If the specimen had responded in

a completely elastic manner, then the stress distribution would be given by the dashed line in Fig. 69. However, for the same applied bending moment the real elastic-plastic distribution is represented by the solid curve. In the elastic-plastic case at the elastic-plastic interface the elastic-stresses are always greater than those predicted for the same moment but assuming the specimen is completely elastic. Therefore the stress intensification factor decreases less rapidly for the elastic-plastic one than elastic one. Variation of elastic and elastic-plastic stress intensifications with distance or size of the plastic zone beneath the notch is given in Fig. 70. As can be seen, the difference between two stress intensifications increases as the plastic zone size increases. Therefore it is assumed that the alloys which exhibit small plastic zones at fracture with respect to notch radii, the elastic stress distribution is not very much different in the elastic-plastic case than the fully elastic case. Therefore equation (102) gives a correlation between the two stress concentrators. However, for larger plastic zone sizes equation (102) breaks due to large differences between the two stress intensifications. As can be seen from Fig. 70 for larger plastic zone sizes the elastic stress at the elastic-plastic interface will be very much greater than the fully elastic one. Therefore, for a notch which has a large plastic zone beneath it, the stresses for the elastic-plastic case will be under-

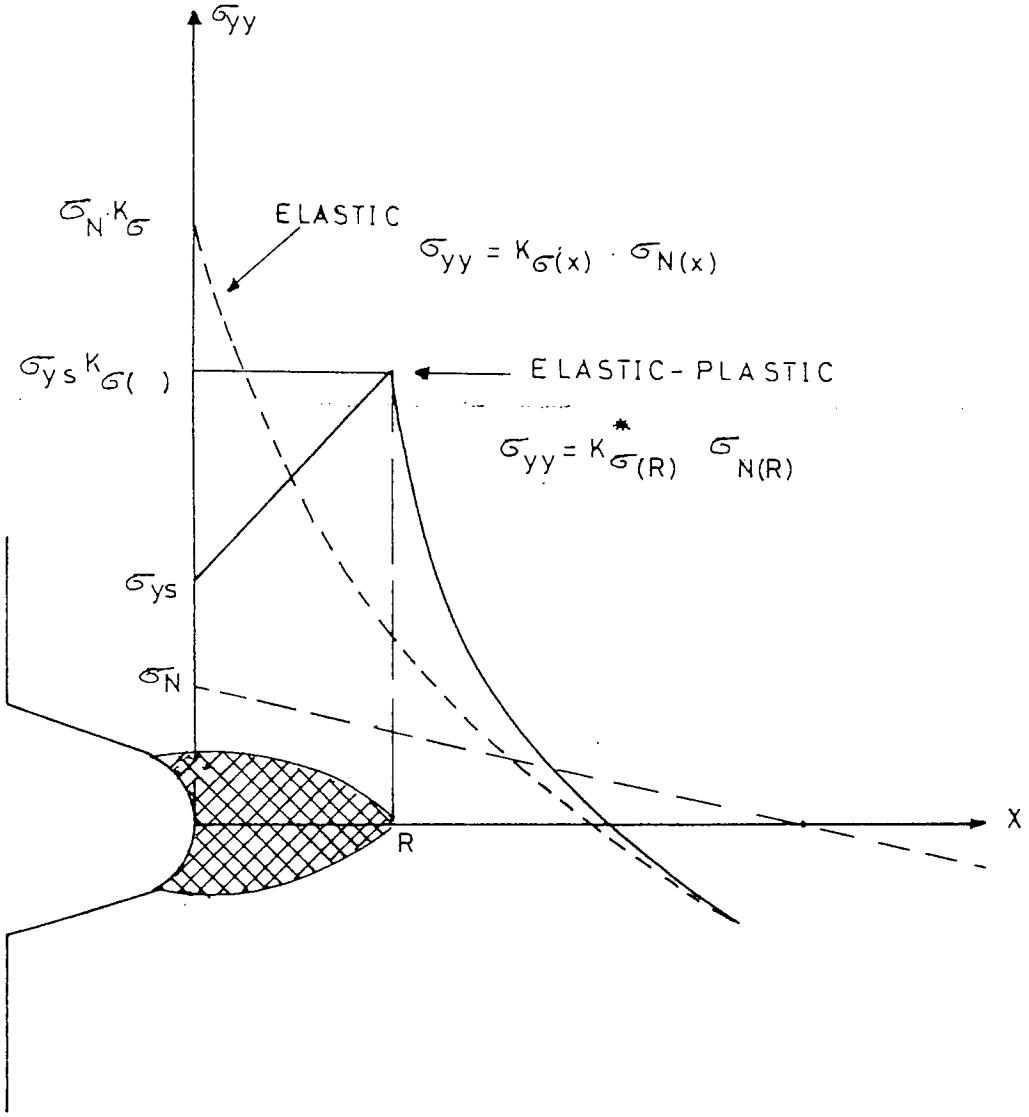

FIGURE 69: Schematic diagram to show the effect of a plastic zone on the elastic stress distribution. The dashed curve represents the completely elastic distribution and solid line the elastic-plastic distribution for the same applied moment (112)

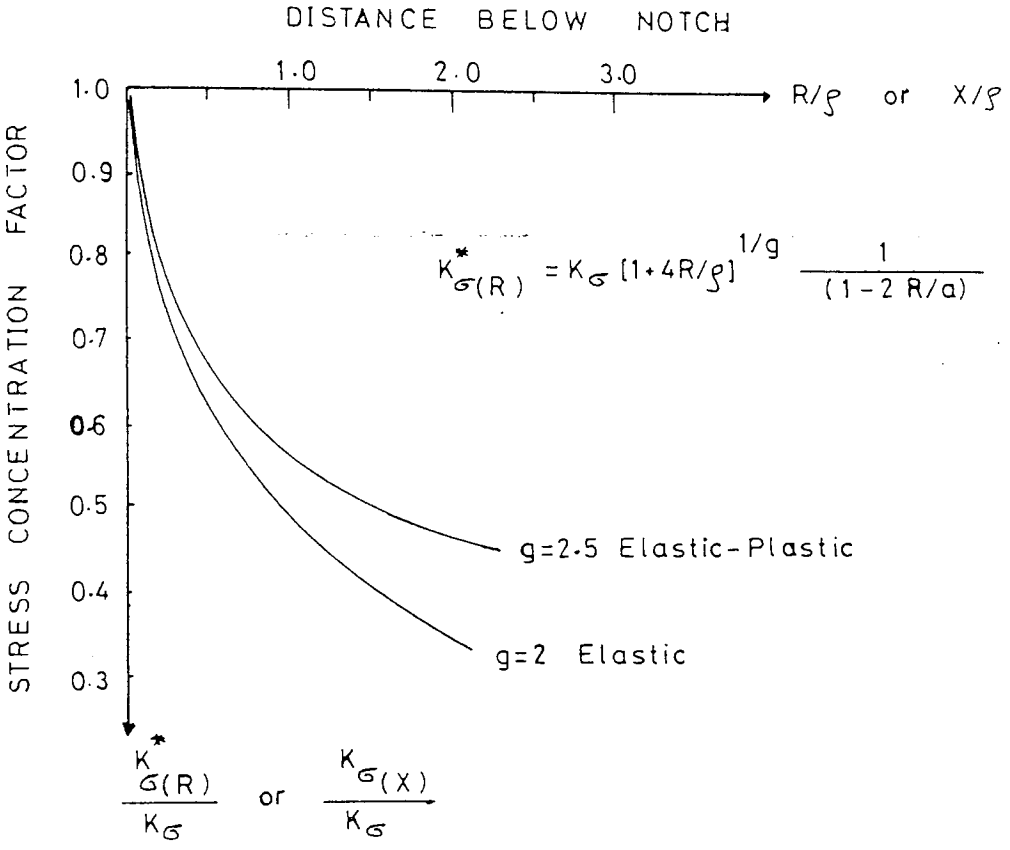

FIGURE 70: Ratio of the effective elastic stress concentration factor as a function of the distance below the notch root. x/ρ (elastic) or R/ρ (elastic-plastic) (112)

estimated with the right-hand side of equation (102) which is the elastic stress distribution for a crack of the same geometric length of the notch. Therefore, the equation (42) will not be strictly valid for unstable fracture. However for the same specimen geometry and loading conditions when the load carrying capacity is considered, a similar distinct variation in the fracture behaviour of the alloys for sharp-cracks and blunt notches would be observed analogous to results obtained from equation (42). This behaviour is discussed in detail in section 9.6.

In the work of Tetelman et al [112] and Ritchie et al [127] it was observed that for notch root radii sharper than a certain radius (ρ_o) (limiting root radius), the $K_{I(\rho)}$ values are equal to K_{IC} values of the materials which are defined normally with fatigue pre-cracked specimens. The value of (ρ_o) can be determined experimentally or empirically as indicated by arrows in the Figures 66-68. Jack and Price [145] proposed that the stress intensity values for blunt notches could be related to those of sharp-cracks by

$$K_{IC} = K_{IC(\rho)} \sqrt{\frac{\rho_o}{\rho}} \qquad \text{.....(103)}$$

The validity of this equation using the empirically obtained ρ_o values is shown with open symbols in the figures. The results indicated that if the value of limiting root radius is known, the K_{IC} values of high-Cr cast irons might be determined directly from notch bending tests without any fatigue pre-cracking or vice-versa. For

the reasons given above again equation (103) will not be strictly valid. However, due to the linear relationship obtained between the $K_{IC(\rho)}$ and $\sqrt{\rho}$, the $K_{IC(\rho)}$ values correlated with K_{IC} values of the alloys.

9.5 Fracture Toughness Determination by Using Non-Standard Short-Bar/Rod Test Specimens

9.5.1 Compliance Studies of Short-Bar Specimen Geometry and Validity of K_{IC}-P_{max} Relationship

In order to find out exact stress intensity coefficients for the short-bar specimen geometries used in this study and also to establish the validity of the K_{IC}-P_{max} relationship, compliance studies were undertaken for three different short-bar geometries. From the experimentally measured values of C.E.B. as a function of a/W a smooth curve can be drawn through the data points, enabling the rate of change of compliance d(CEB)/d(a/W) to be determined. The most common method is polynomial curve fitting. The more terms there are in a polynomial expression, the greater will be the tendency of the differential of the polynomial expression to give maxima and minima and inflection. The method suggested by Ryder et al [139] which is used in this study was proved [148] to be a more satisfactory method for expressing the compliance data, since obtained equations can be differentiated mathematically and also as (a/W) approaches unity C.E.B. values in the equations increase to infinity, consistent with physical reasoning. Processed experimental data and analytically obtained compliance results are given in tabular form in table 31 and graphical form in Figs. 71-73. As can be seen, the experimentally

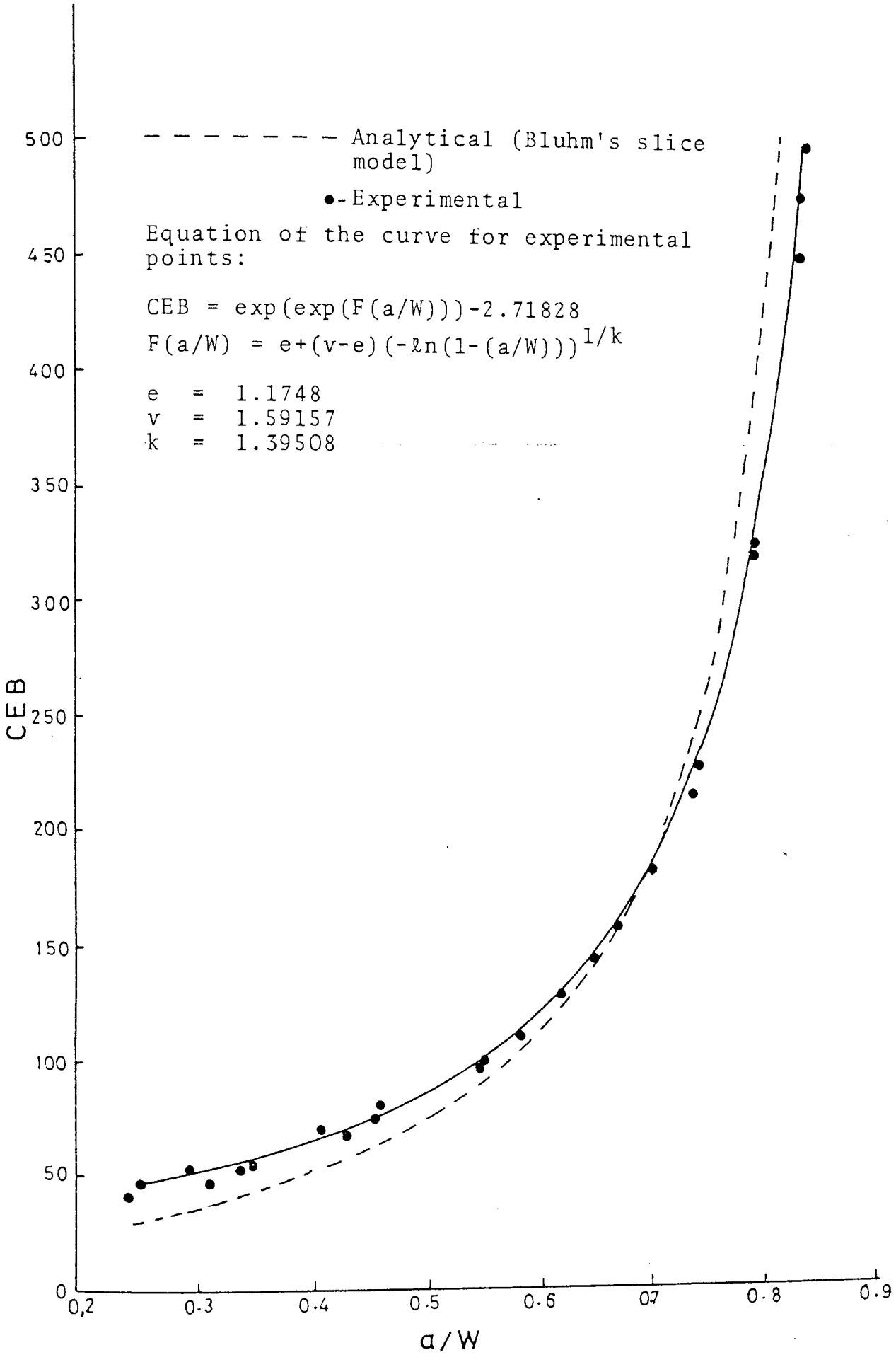

FIGURE 71: Experimentally and analytically obtained non-dimensional compliance (C.E.B) results for TYPE I short-bar specimen geometry

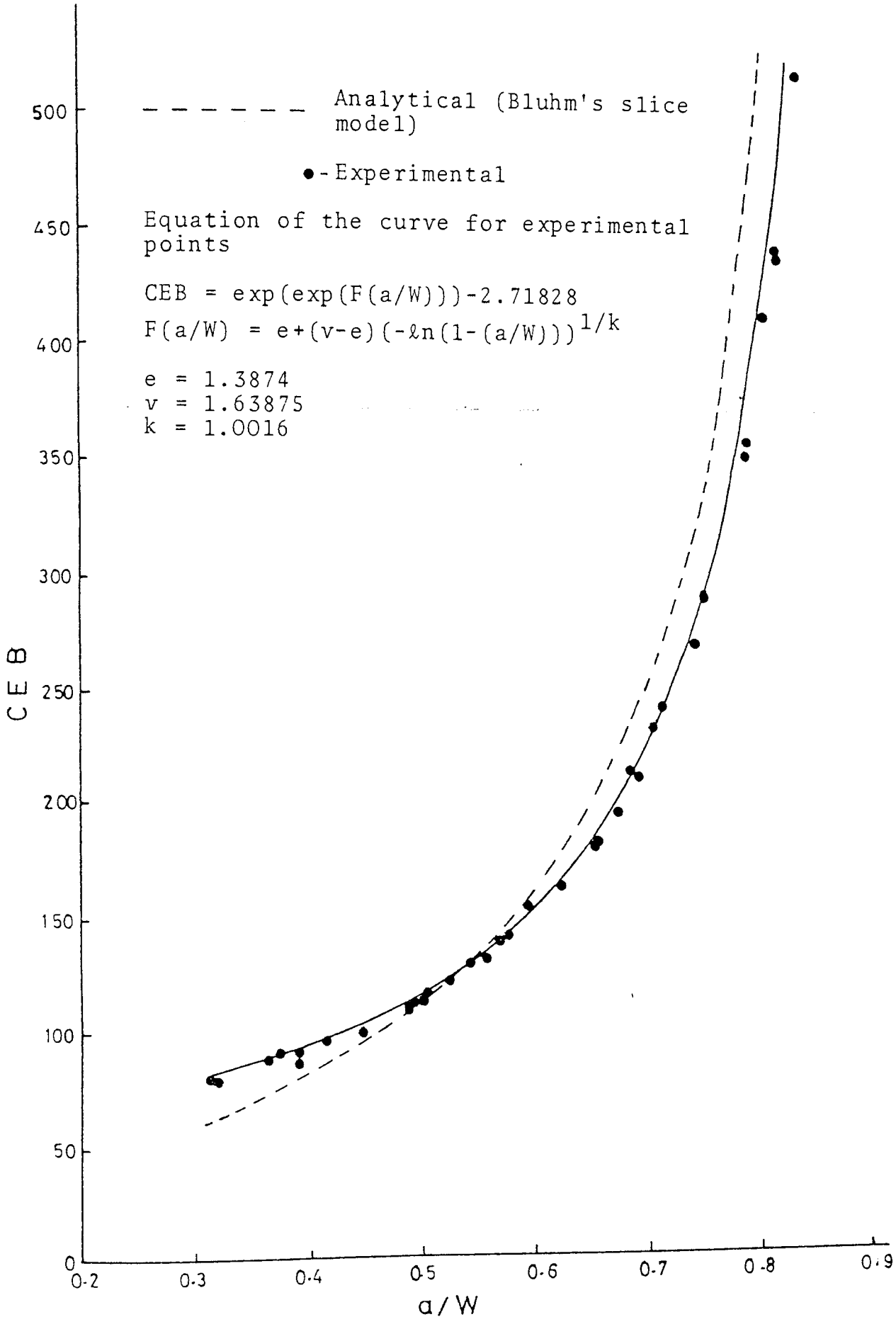

FIGURE 72: Experimentally and analytically obtained non-dimensional compliance (C.E.B.) results for TYPE II short-bar specimen geometry

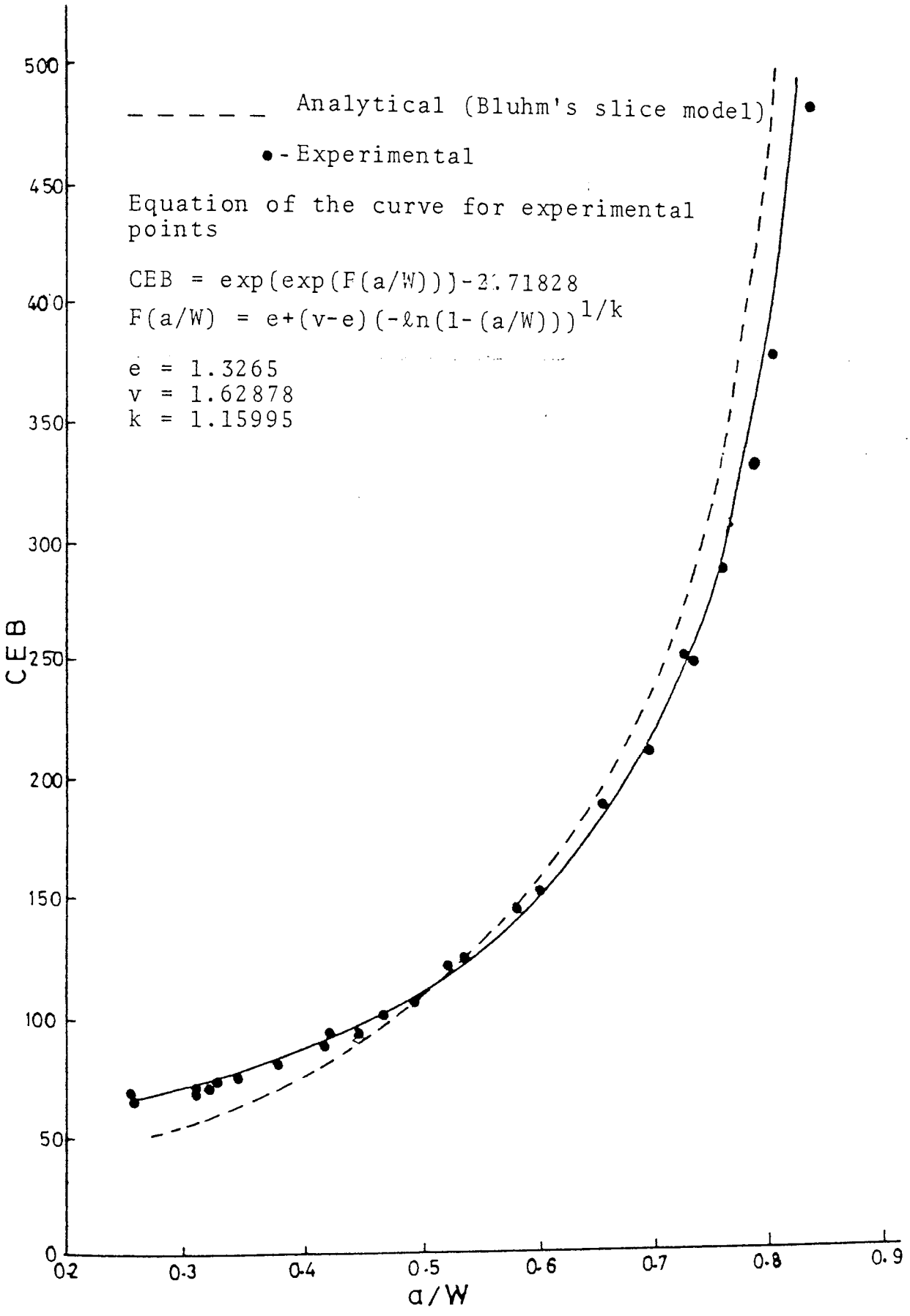

FIGURE 73: Experimentally and analytically obtained non-dimensional compliance (C.E.B.) results for TYPE III short-bar specimen geometry

obtained results were up to $\pm$ 30% different over the range a/W = 0.3 to 0.8, than the results obtained using the analytical Blumh's slice model [138]. This disparity could arise from the following reasons.

In the work of Srawley et al [100], the analytically obtained equation (62) for straight through cracks only gave correlation with experimental results for the range a/W = 0.3 to 0.7. With the present analysis of short-bar specimens with chevron notches the range of a/W to almost the limit value 1.0 and values smaller than 0.3 should be considered. Therefore equation (62) has been used during analytical studies for (a/W) values which are far beyond its limit ranges.

The definition of shear stress transfer coefficient (k) has not yet been fully understood. In the work of Blumh it is recognised as being a function of chevron notch angle (θ) and notch depth (a_o). In the work of Srawley et al it has been found that it varies depending on (a_o) and is independent of (θ). In Fig. 74(k) values obtained by comparing the experimental results with analytical values were plotted against a/W. As can be seen (k) values vary with respect to crack length in increasing order for three short-bar geometries. Therefore it is concluded that Blumh's slice model is a good approximation to study compliance analysis of short-bar type specimens but equation (62) should be improved to cover the chevron notch confirguration. It is also necessary to establish the correct definition of (k).

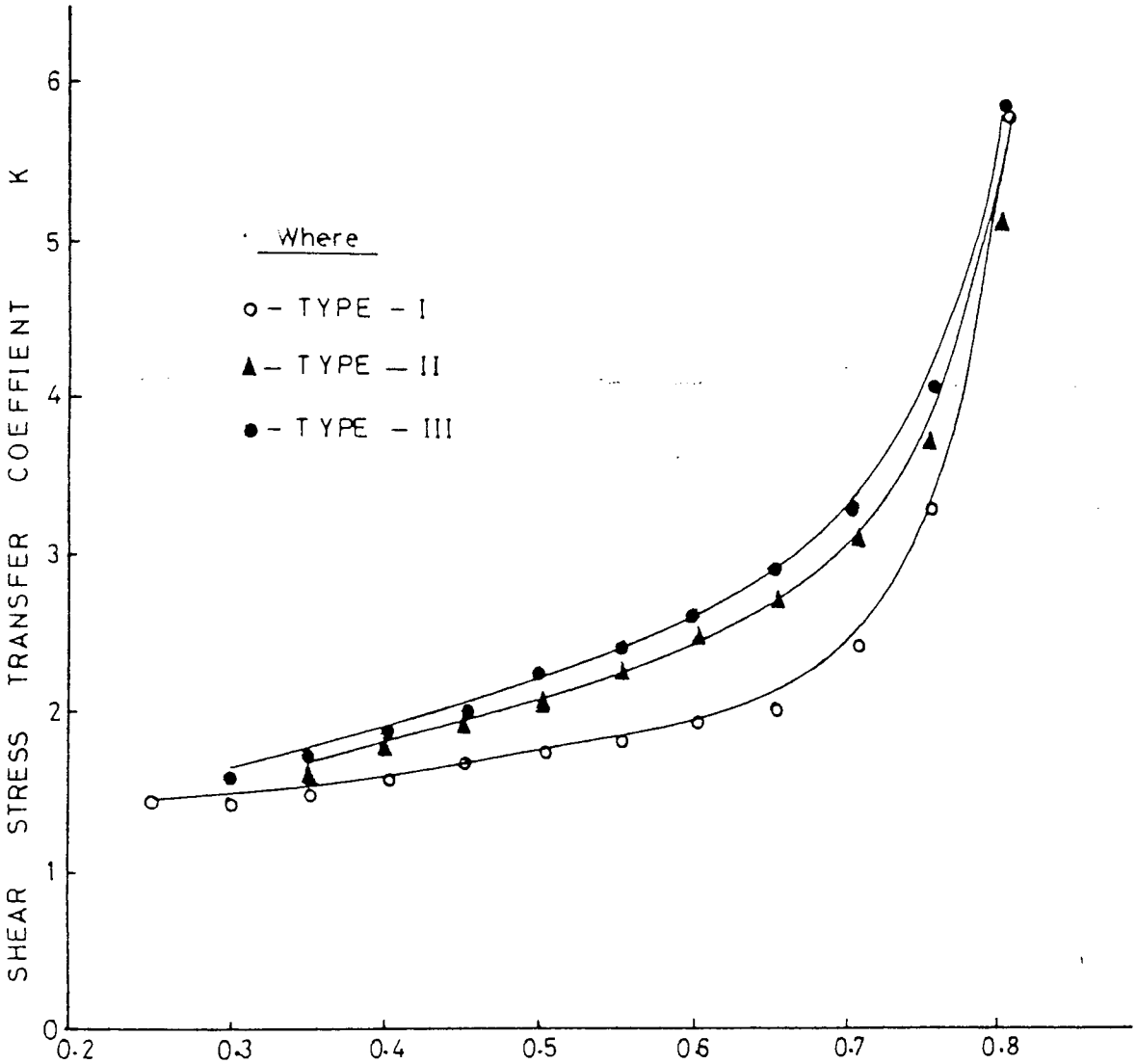

FIGURE 74: Observed variation in the values of shear transfer coefficient (k) with a/W for three different short-bar specimen geometries

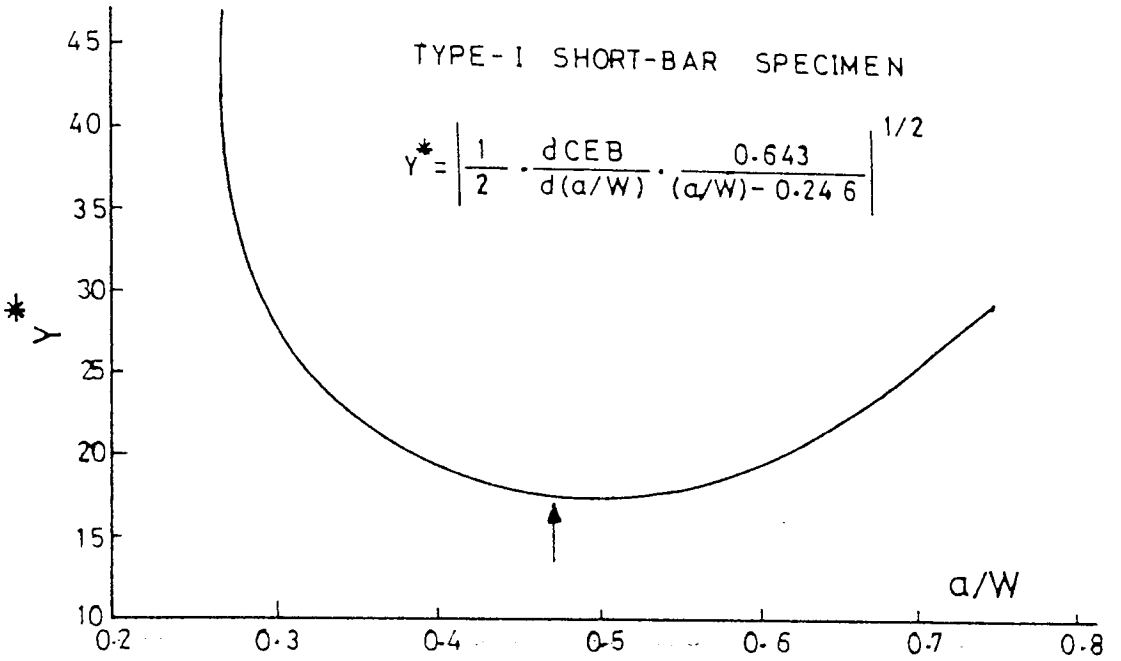

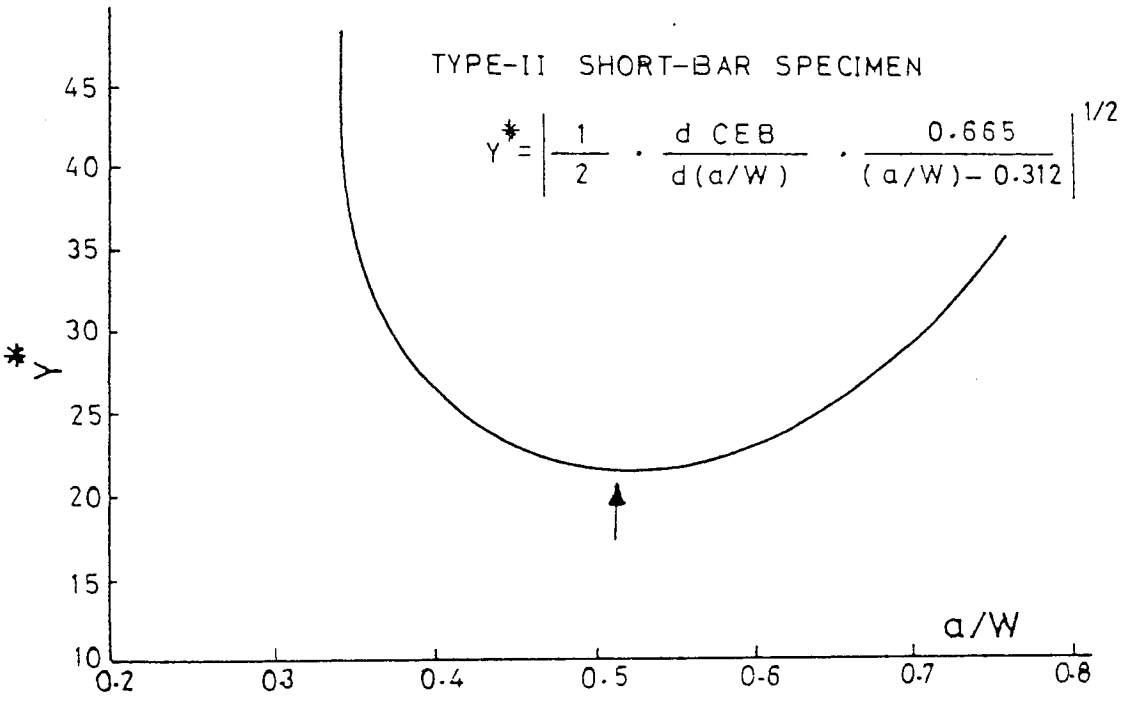

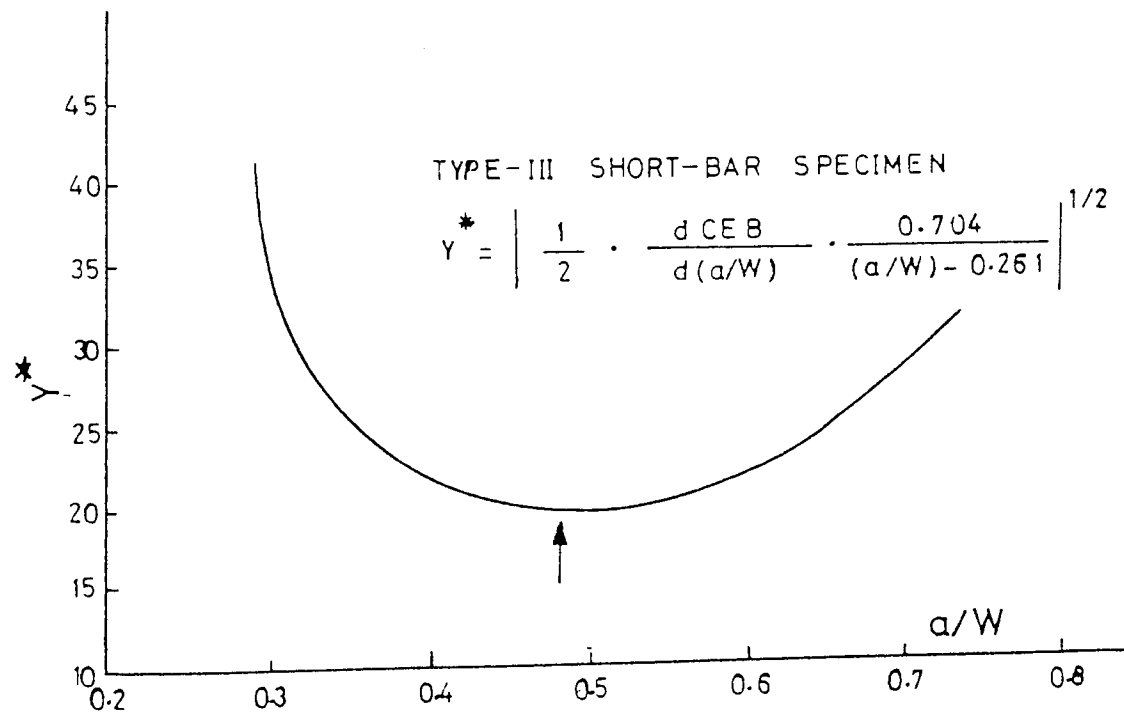

FIGURE 75: Variation of the stress intensity coefficients (Y*) in different short-bar geometries

The stress intensity coefficients (Y*) were determined from equation (78) using the functions obtained from experimental compliance data. The results are shown in Fig. 75 and Y* minimum values with corresponding critical crack length ratios a/W (at the minimum value of Y*) are given in table 31. As can be seen from Fig. 75, each type of short-bar specimen geometry has a minimum stress intensity coefficient. Therefore as defined in equation (77) the K_{IC} and P_{max} relationship exists. For fully L.E.F.M. conditions fracture toughness can be determined using short-bar/rod type specimens only by measuring the maximum load without measuring the critical crack lengths. Since short-bar/rod fracture toughness testing is material independent and geometry dependent, the results indicated that very small variations in either specimen geometry or in the chevron notch geometry for a given specimen geometry cause considerable variation in the stress-intensity coefficients. In order to use the stress intensity coefficients given in table 31, the scaled short-bar specimen dimensions should be in accordance with the given calibrated specimen dimensions in Fig. 36.

9.5.2 Toughness Determination of High-Cr Cast Irons by Using Non-Standard Short-Bar Fracture Tests

To compare the toughness values obtained using the two methods data were plotted as $K_{IC(\text{three point bending})}$ versus $K_{ICSB\ (\text{short-bar})}$ in Fig. 76. As can be seen from the figure and table (32,33) very good correlation is observed between the two test methods. The difference between the results of two test methods never exceeded

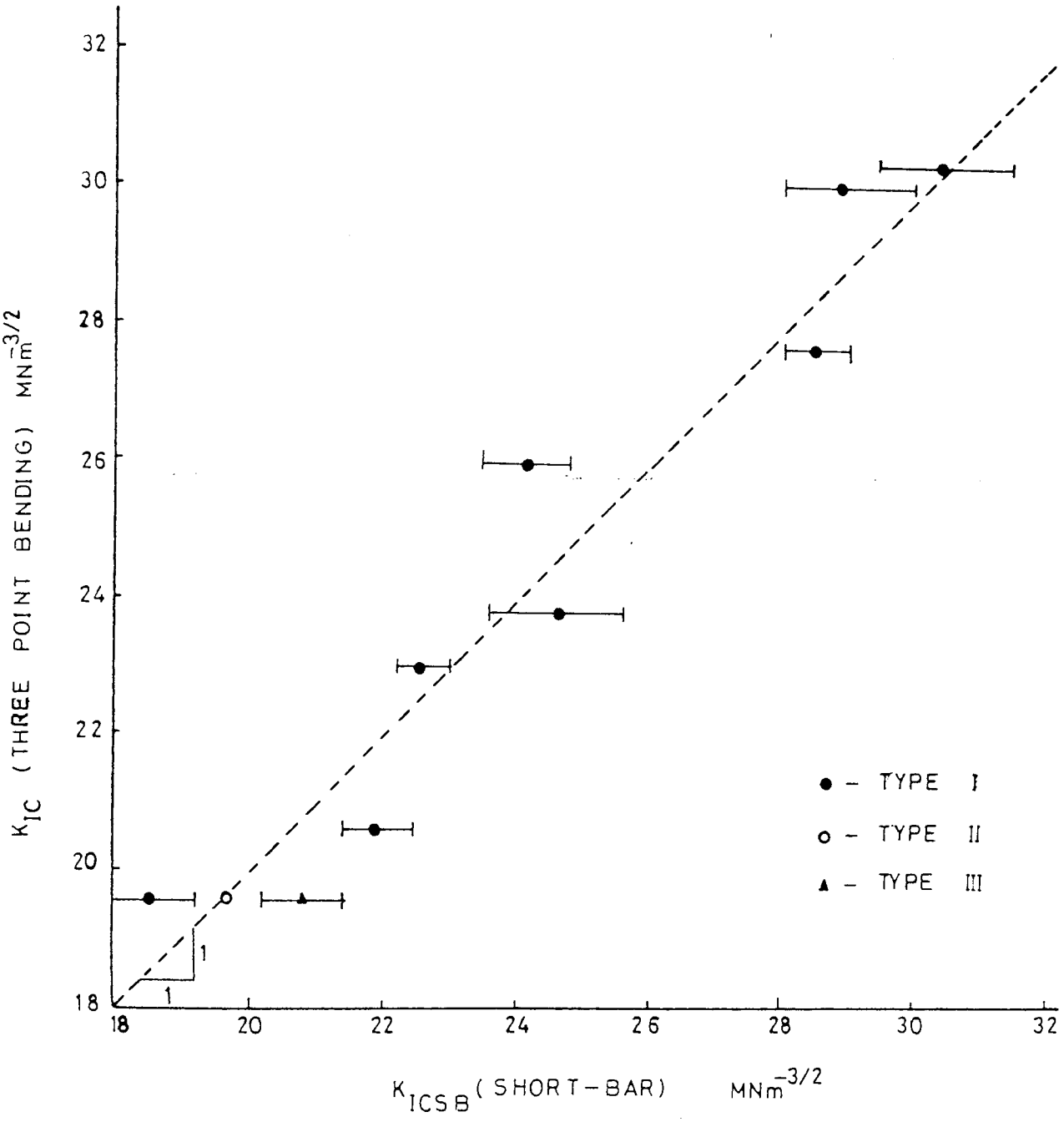

FIGURE 76: Comparison of the fracture toughness values of high-Cr cast irons obtained from short-bar fracture toughness technique with the valid K_{IC} values obtained from recommended standard test by ASTM E-399

1.3 $MNm^{-3/2}$ over the range of toughness values. It is also worthwhile to mention that, as can be seen from tables 32 and 33, excellent reproducibility is observed in the short-bar fracture tests.

In Fig. 37 the type I specimen geometry is scaled to 12 x 12 x 18 mm version of type I specimen geometry in Fig. 36, which was used during the compliance studies. In order to establish size and geometry effects on the toughness measurements the results obtained from three different short-bar specimen geometry are summarised in table 33. However, the specimens which were tested using the Fractometer II gave high values when calculations were carried out using A = 18.62 in equation (30). This disparity could arise from the load-cell calibration of the fractometer II or from the stiffness of the machine (see also appendix I). Nevertheless, the results from this table indicated that, as stated above, when L.E.F.M. conditions are fulfilled the fracture toughness of metallic materials can be obtained from equation (30) and for this, scaled specimen geometries should be in accordance with the calibrated short-bar/rod fracture toughness specimen geometries.

The short-bar/rod fracture toughness testing technique has certain advantages in that a sharp-crack is produced during loading, therefore neither fatigue-precracking nor measurements of crack length is required. This makes it necessary only to determine the maximum load. Therefore

the difficulties which were faced during the toughness measurements of high-Cr cast irons by following the procedures outlined by standards will be eliminated. On the other hand, the short-bar technique has advantages over the other alternative test methods which were suggested to determine the toughness of brittle metallic materials in section 3.5, since for L.E.F.M. conditions K_{IC}-P_{max} relation is obtained analytically by an energy approach and its validity has been proved analytically and experimentally. (Most of the suggested alternative methods give correlation with fracture toughness empirically rather than analytically.)

The short-bar/rod technique is a very new method for measuring the toughness of materials, but it is gaining popularity due to its simplicity. Although the theoretical and experimental studies have not been fully established there are some studies [97-99] which indicate that it can also be applied for elastic-plastic cases (see appendix I). The results obtained here suggest that, due to the nature of high-Cr cast irons, the L.E.F.M. conditions are always fulfilled even when using very small scale short-bar specimens. Therefore it is concluded that the short-bar/rod fracture toughness technique can be successfully used as a simple and quick method to determine the fracture toughness of high-Cr cast irons or similar hard steels.

The other significance of the short-bar fracture test results is that they indicate the accuracy of the stress intensity coefficients which were obtained from compliance

studies. Almost identical A values were obtained when the known valid fracture toughness values (K_{IC}) were equated to equation (30) by inserting the experimental P_{max} values.

9.6 Theoretical Considerations

The studied metallurgical variables (additions of molybdenum and tungsten, application of high temperature heat treatments and hardening variables) alter the microstructure of high-Cr cast irons significantly. These variations within the microstructure resulted in considerable improvement in the toughness characteristics of the alloys. In order to find out any possible relationship between the microstructure and fracture toughness of high-Cr cast irons the following points were considered.

9.6.1 Grain Size Effect

The toughness of materials generally varies inversely with grain size. This variation of toughness with grain size for high-Cr cast irons was also shown in the work of Durman [53] (see Fig. 30). The alloys examined here exhibited massive grain growth after homogenisation at elevated temperatures for long holding periods. If the grain size is the controlling mechanism of the alloys, the heat treated materials should have exhibited lower toughness values than as-cast condition, due to massive grain growth. In contradiction to the above conclusion, all austenitic high-Cr cast irons exhibited some increase

in the toughness values. Therefore the grain size dependence of the toughness of high-Cr cast irons might be eliminated as a controlling factor. This observed variation of toughness in the work of Durman [53] could be a result of variation in the volume % of the eutectic carbides or size of the eutectic carbides, since these variables are controlled by diffusion mechanism and could easily be altered by variations in cooling rates during solidification.

9.6.2 Stress-Assisted Martensite Formation

In the high temperature heat treated austenitic alloys the formation of martensite in the crack path and ahead of the crack tip could be considered as a reason for the improvement in the toughness values similar to that in the well-known TRIP STEELS (see plates 21-22). A comprehensive study on the light microscope did not give any evidence of martensite formation. As suggested by Zekay et al [18] and Channi et al [19], the reason for this could be the secondary carbide precipitation observed after the heat treatments resulting in a depletion of carbon and alloying elements in the surrounding austenite and presumably causing a local elevation of the M_s and M_d temperature of the alloys.

The high M_s temperature and low ductility of the alloys studied here and also the observation of plate-like martensite in the areas immediately adjacent to the fracture path and in the very short distance ahead of the crack tip, suggested that formation of martensite is stress-assisted as described in section 2.2.2.

PLATE 21: Observed stress-assisted martensite formation in heat treated and alloy added high-Cr irons. x1200

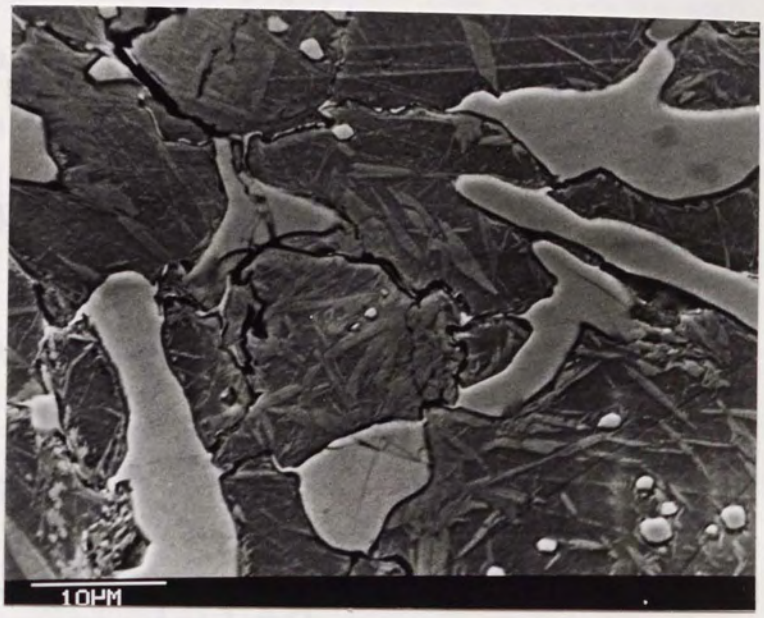

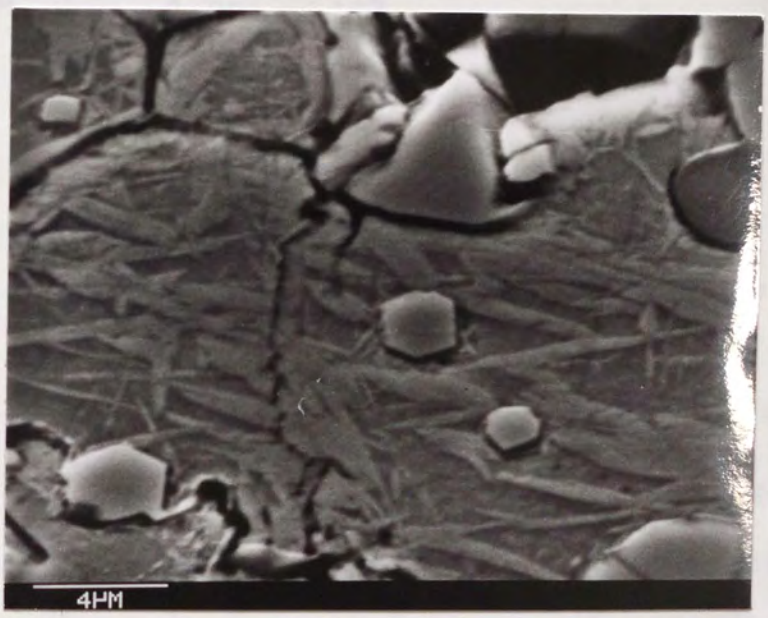

PLATE 22: Stress-assisted martensite formation ahead of the crack tip

The volume % martensite formation within the plastic zone ahead of the crack tip needed to give the increase in the toughness values observed was calculated from equation (1) given by Atolovich and Singh [33] (as described in section 2.2.2). The calculations were carried out for a 2% molybdenum containing alloy after 8 hours heat treatment with the following values

$$\Delta G^{A\rightarrow M} : \frac{e_{IS}\cdot\pi\cdot \bar{V}_M\cdot\beta\cdot\alpha^2\cdot P^4}{\sqrt{3}\ \bar{\sigma}_M^{\,3}\ t^4\ W^4}\ c.f.(a/W) \quad .....(2)$$

where $$\Delta G^{A\rightarrow M} : \frac{(K_{ICHT8}) - (K_{ICASCAST})^2}{E}\ (1-\nu^2)$$

e_{IS} : 0.34 (33)

β : 0.5

α : $(2/5.6\pi)$

c : 9 mm

$f(a/W)$: 7.905×10^4

t : 12 mm

W : 18 mm

$\bar{\sigma}_M = \sigma_F^* = 1245\ N/mm^2$

$\bar{V}_M$: Volume % martensite within the plastic zone at fracture

The calculations have shown that about 33% in volume martensite formation is necessary within the plastic zone ahead of the crack tip in order to give this observed increase in the toughness values by the energy dissipation mechanism. As can be seen qualitatively from the plates the amount of martensite produced ahead of the crack tip is very much lower than this value. Therefore it is assumed that the stress level required to produce the

martensite could also be sufficient to initiate the failure, and formation of martensite under these circumstances might not play an important factor in the fracture mechanism of high-Cr cast irons. Formation of stress-assisted martensite within the microstructure of those alloyed and high temperature heat treated cast irons could be considered another improvement besides their high toughness values, since, under working conditions, development of a hardening surface layer means further resistance against abrasive wear.

9.6.3 Effects of Eutectic Carbide Morphology

In Fig. 77, the fracture toughness values of a series of austenitic high-Cr cast irons was plotted against $[L_o/C_o]^{\frac{1}{2}}$ (the square root of the ratio of mean interparticle spacing to mean carbide thickness) for the alloys. As can be seen, a good correlation was observed. This result indicated that there is an apparent relationship between the fracture behaviour of austenitic alloys and their eutectic carbide morphology. It was also possible to conclude that the fracture toughness of austenitic high-Cr cast irons is not only influenced simply by the volume % of the eutectic carbides as reported [53,134,135] but the distribution of the eutectic carbides also plays an important role, considering the volume % of eutectic carbides at almost the same level with studied metallurgical variables. As can be seen from figure 77, the fracture toughness of austenitic alloys can be increased considerably by increasing this parameter (i.e. $[L_o/C_o]^{\frac{1}{2}}$), as shown in section 9.3,

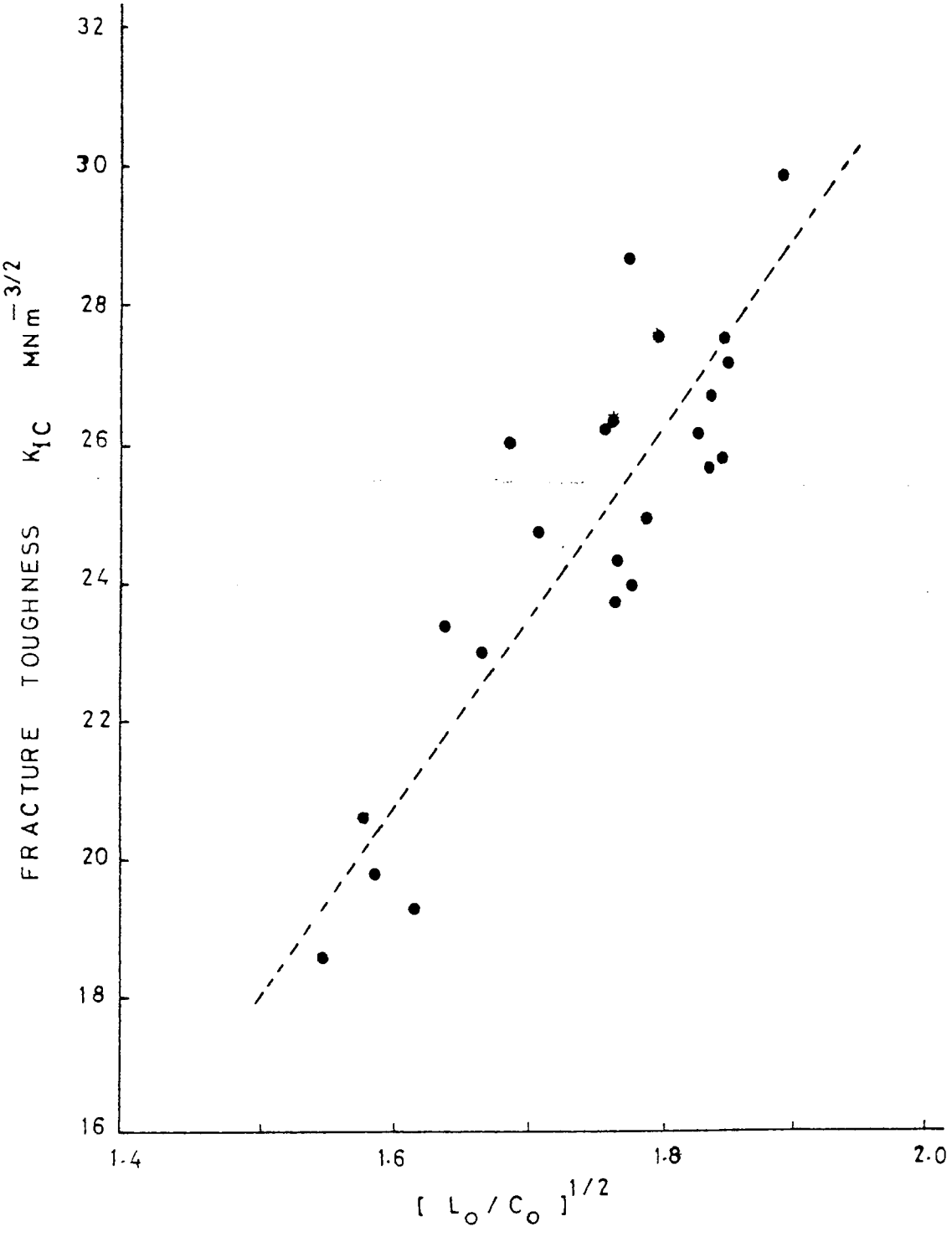

FIGURE 77: Variation of fracture toughness of the austenitic alloys with observed microstructural parameters

L_o : Mean interparticle spacing

C_o : Mean carbide thickness

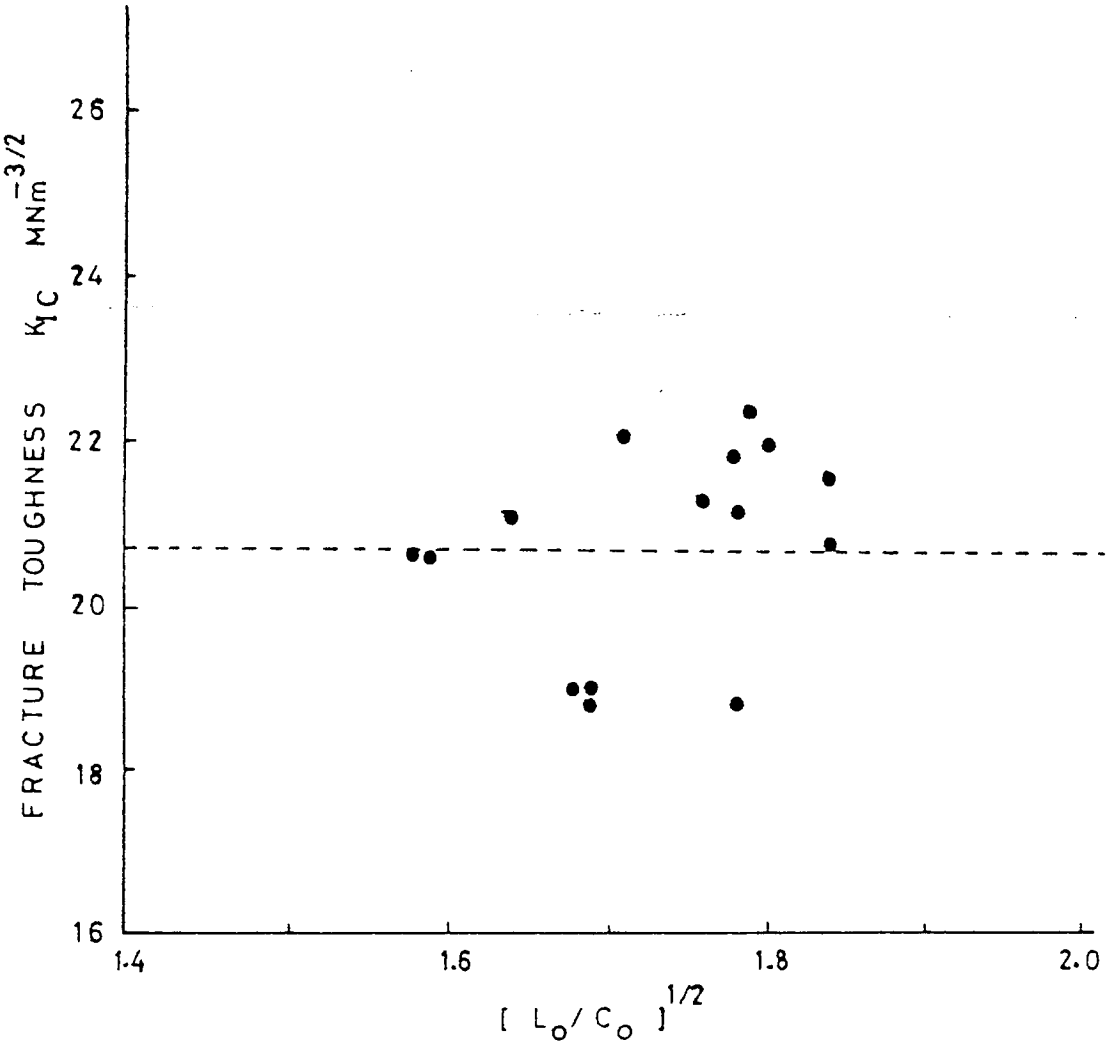

FIGURE 78: Variation of fracture toughness of martensitic high-Cr cast irons with observed microstructural parameters

L_o : Mean interparticle spacing

C_o : Mean eutectic carbide thickness

this can be achieved by means of additions of molybdenum or tungsten and application of high temperature heat treatments.

For martensitic high-Cr cast irons, although this parameter varied with the mentioned metallurgical conditions, as can be seen from figure 78, opposite behaviour to austenite alloys was observed and the fracture toughness of martensitic high-Cr cast irons independent of the eutectic carbide morphology. In this aspect constant levelling of toughness has also been reported for a wide range of variations in the volume % of eutectic carbides in the published literature [53, 134, 135] (see Fig. 31).

9.6.4 Microscopic Examination of Fracture in High-Cr Cast Irons

Extensive fractographic examination of the studied alloys was undertaken using a Cambridge Stereoscan and light microscopical techniques. In order to make a comparison the fracture surfaces of the alloys for various conditions are given in plates 23-25. Analogous to the metallographic plates in section 9.1, the variation of the eutectic carbide morphology was easily distinguished on the fracture surfaces. Although eutectic carbide morphology changed significantly, the fracture surfaces of the austenitic alloys remained dominated by cleavage cracking of the eutectic carbides. Although no attempt has been made to study this quantitatively, it was reported in the work of Gahr et al [149] that for austenitic alloys the amount of eutectic carbides on fracture surfaces is substantially higher than the carbide volume measured by quantitative metallography on polished surfaces. This was supported

qualitatively in plates 26 and 27 which were obtained from notch bend specimens by polishing the surfaces before commencing the fracture tests. As can be seen, the number of carbides which had interacted with crack paths is considerably higher than the number of carbides on the drawn random straight lines. The crack paths preferentially followed the eutectic carbides.

The observed flat facets and river marking of typical cleavage fracture behaviour of eutectic carbides are illustrated in plates 28 and 29. The micro-cracks and river patterns indicate the initiation of cleavage fracture on different planes of the eutectic carbides which run into each other to give a micro-crack the length of an entire carbide.

The remaining fracture surfaces exhibited the dimpled ductile failure of the austenitic matrix which is given in detail in plates 30, 35 and 36. As can be seen from the plates, neither apparent necking around the secondary carbides nor extensive void growth were distinguished. Coarse overlapping tongues were observed. These are presumably produced by a ductile tearing mechanism and immediately preceded formation of voids around the secondary carbides at later stages of fracture.

The fracture surfaces of martensitic high-Cr cast irons exhibited almost similar characteristics to those which were observed in the austenitic alloys. The failure of

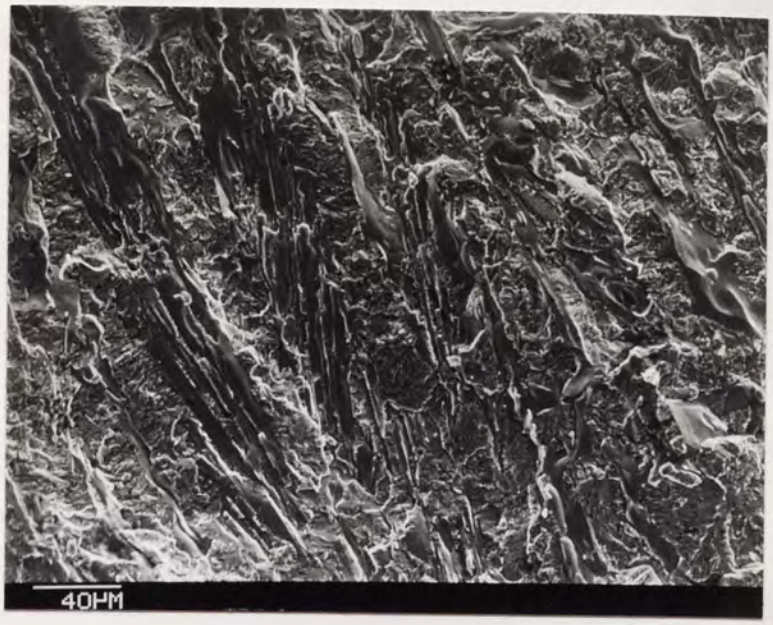

A - As-cast case alloy

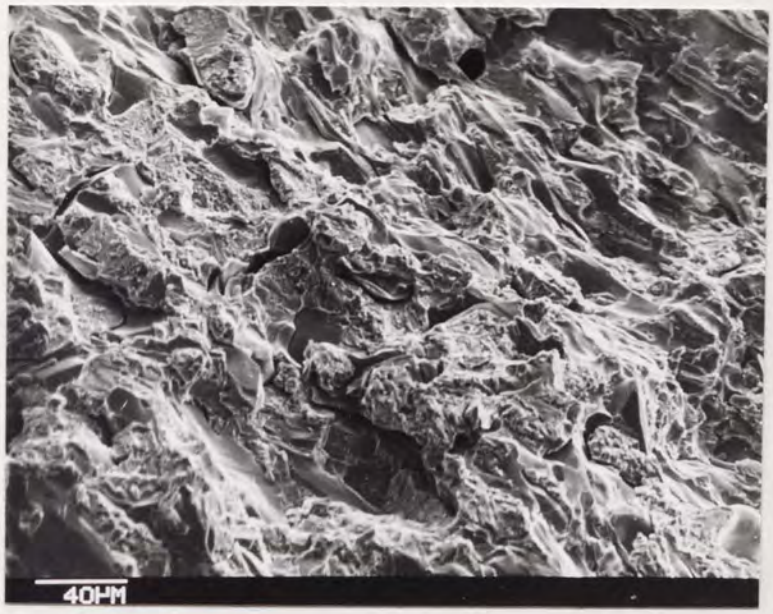

B - Alloy 8HT 4Mo

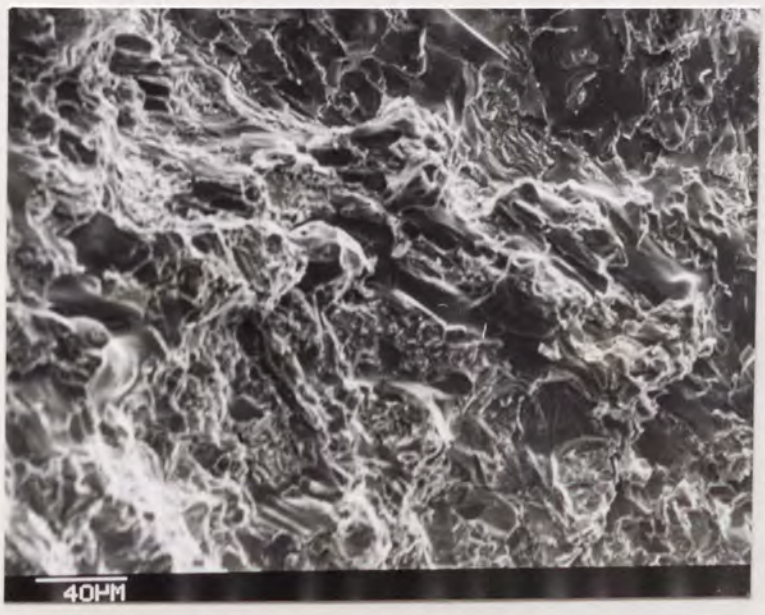

C - Alloy 8HT 5W

PLATE 23: Fracture appearance of various alloys in as-cast condition and after high temperature heat treatments

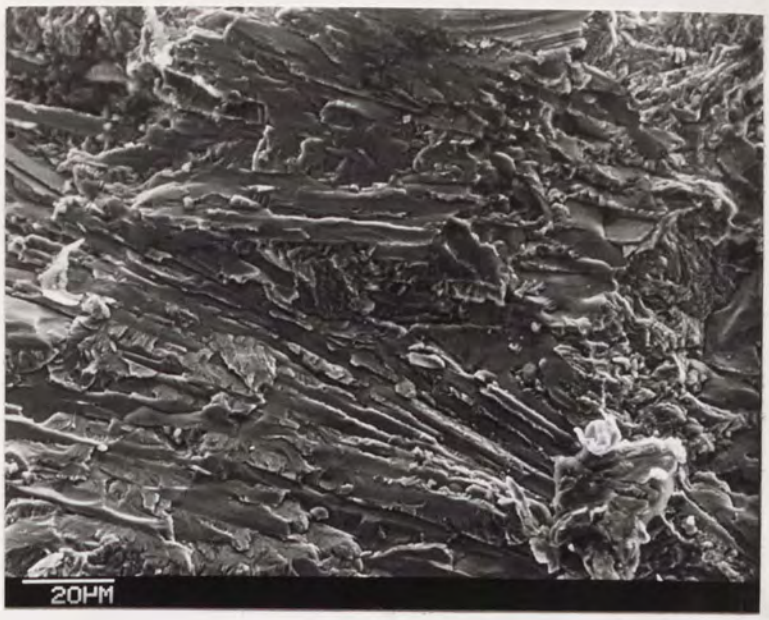

A - As-cast

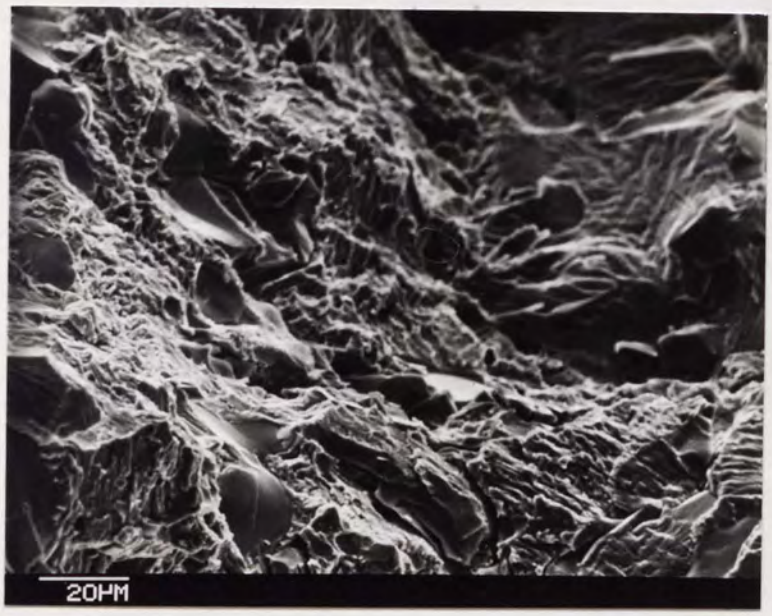

B - After 24 hours

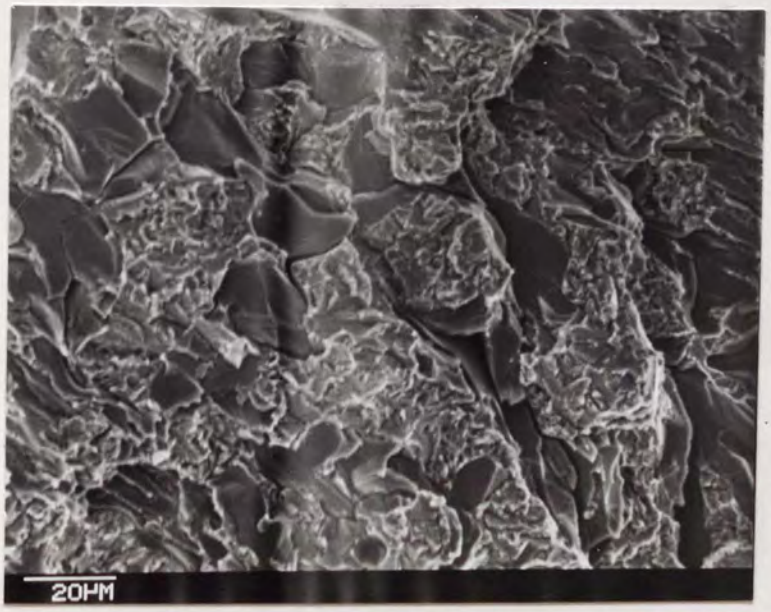

C - After 72 hours

PLATE 24: Fracture appearance of 2% Mo containing high-Cr cast iron after various holding periods at 1180°C (austenitic)

A - As-cast

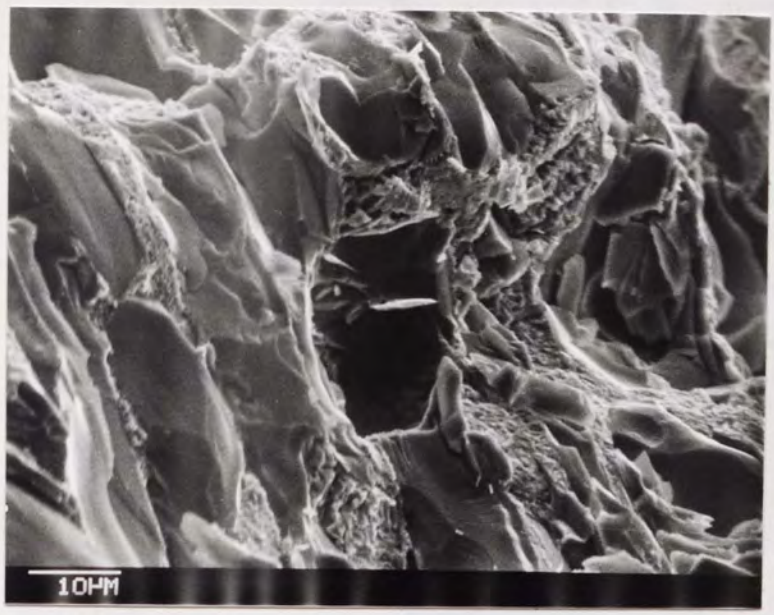

B - After 8 hours

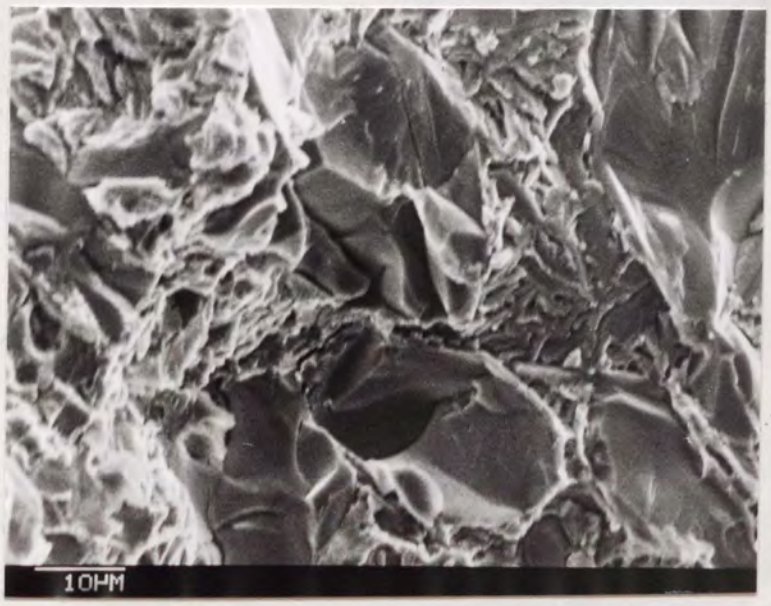

C - After 24 hours

PLATE 25: Fracture appearance of 4% Mo containing alloy after various holding periods at 1180°C (austenitic)

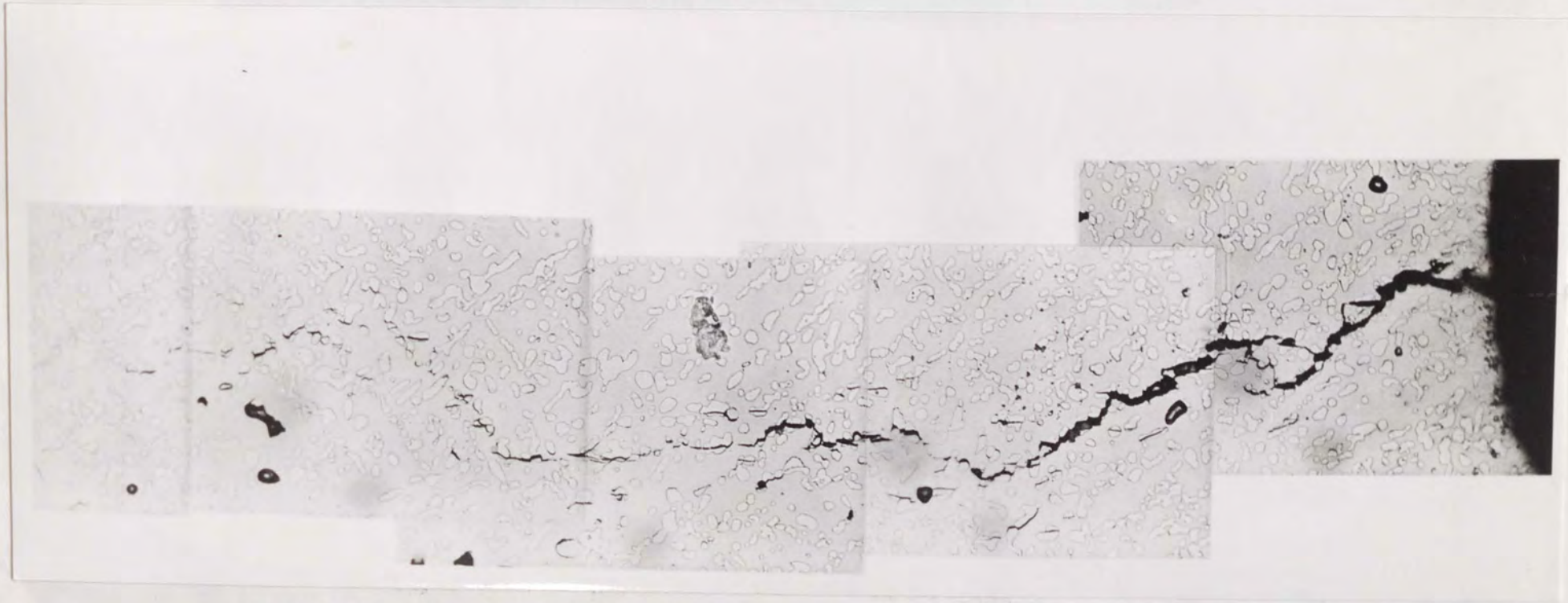

PLATE 26: Crack path in notch bend specimens
Alloy : 72 HT.2Mo
Notch radius : 0.686 mm

PLATE 27: Crack path in notch bend specimens
Alloy : 8HT 4Mo
Notch radius : 0.686 mm

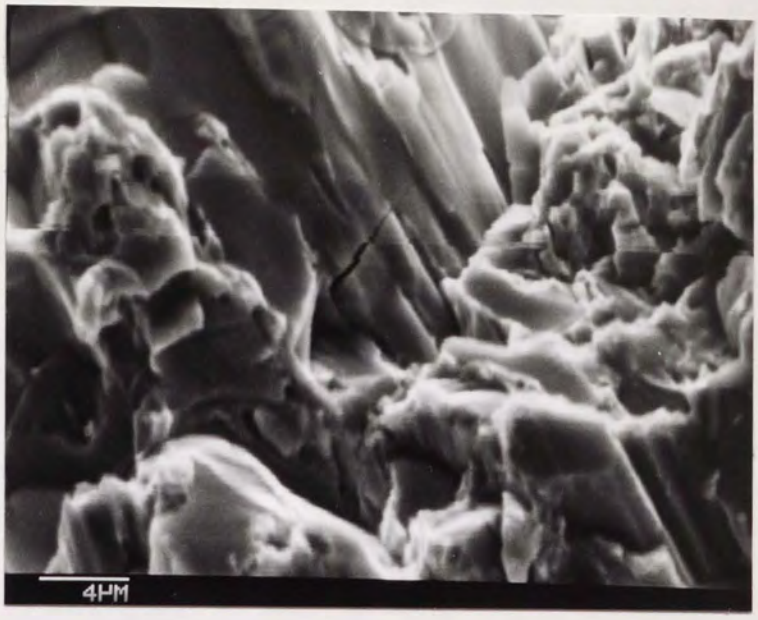

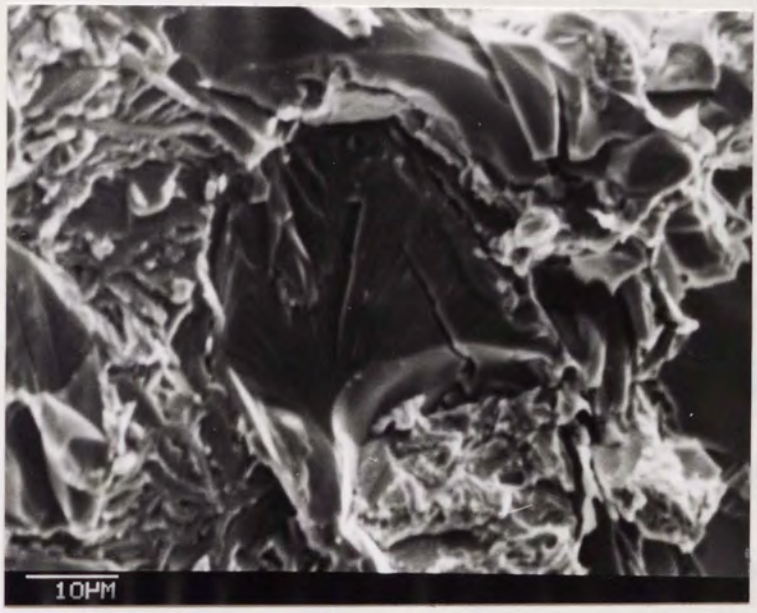

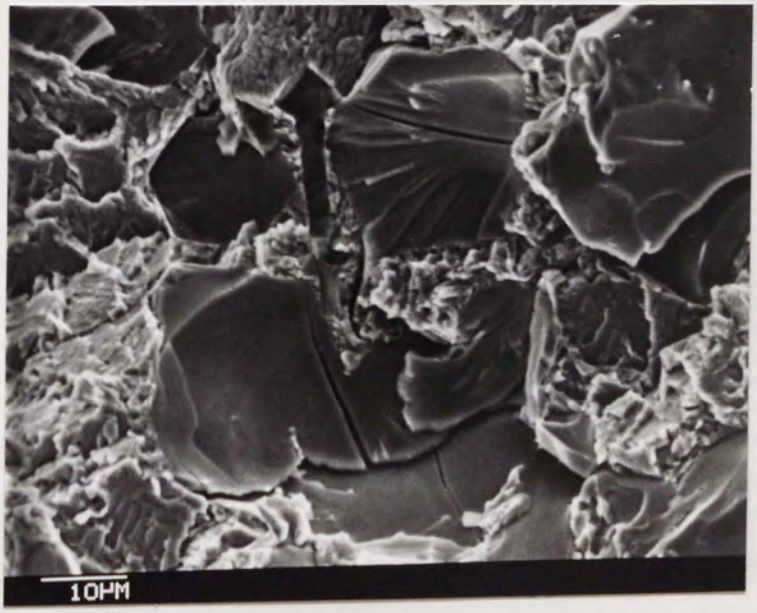

PLATE 28: Cleavage failure of eutectic carbides in the fracture process of high-Cr cast irons

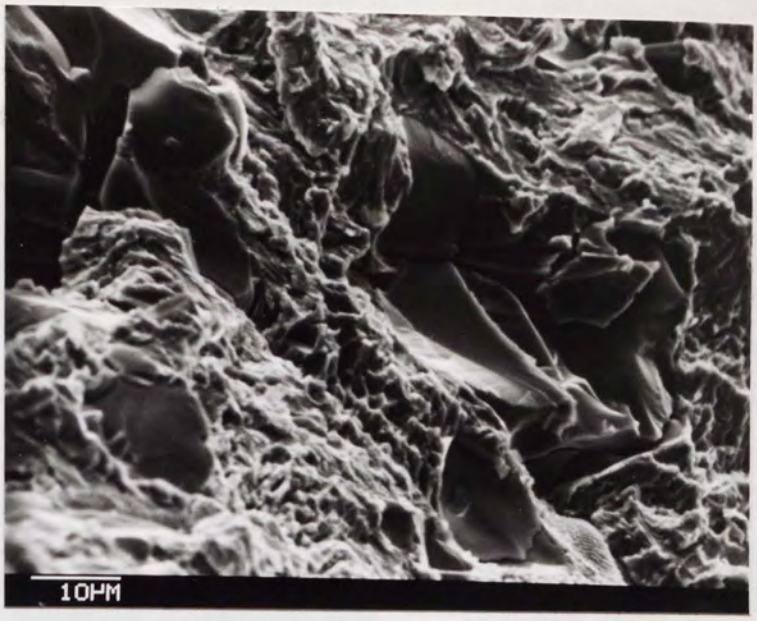

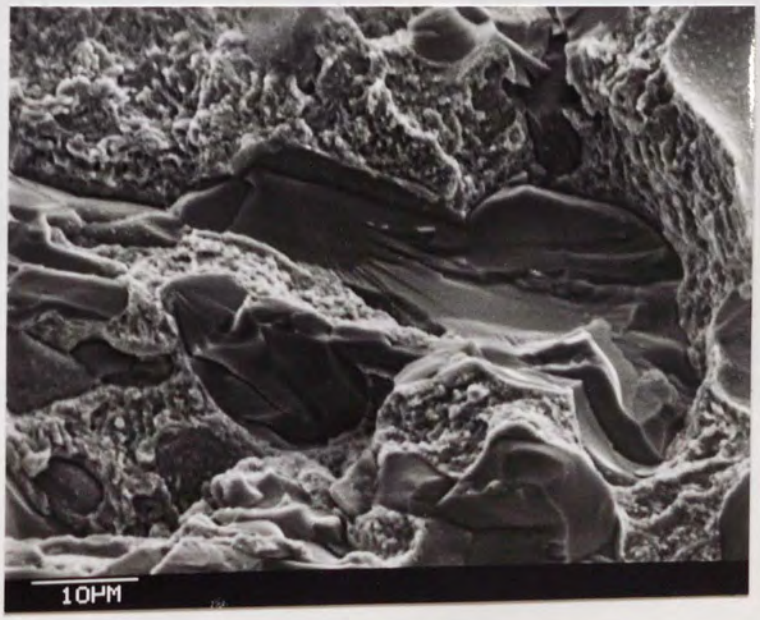

PLATE 29: Cleavage failure of eutectic carbides in the fracture process of various high-Cr cast irons

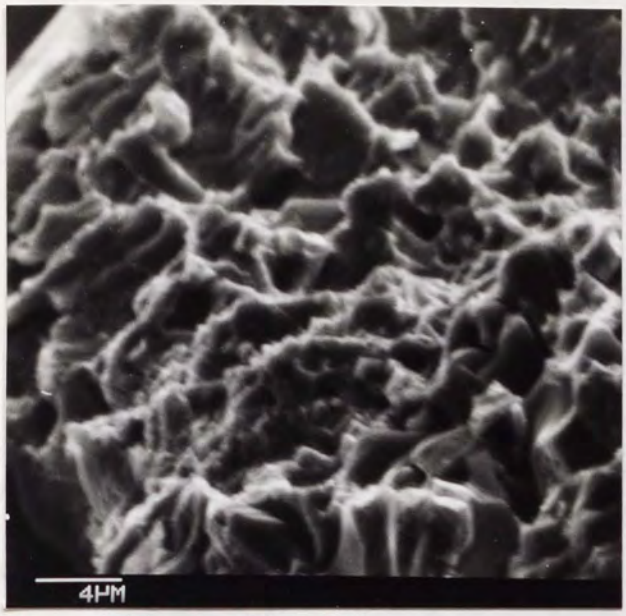

A - Alloy: 8HT 4Mo

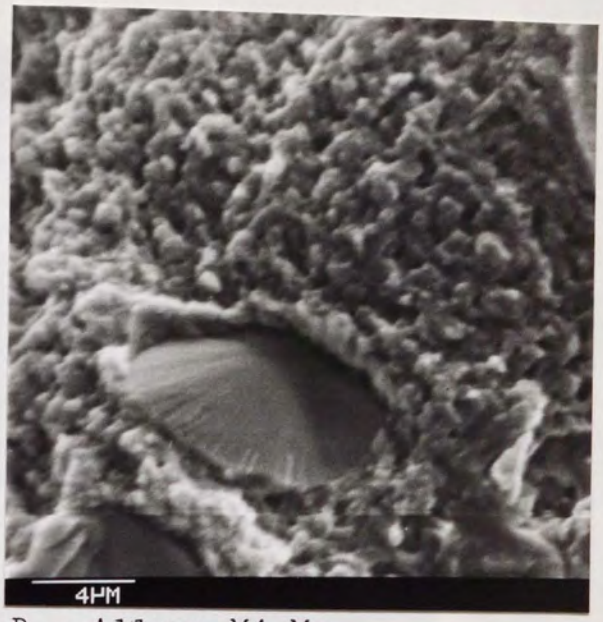

B - Alloy: M4 Mo

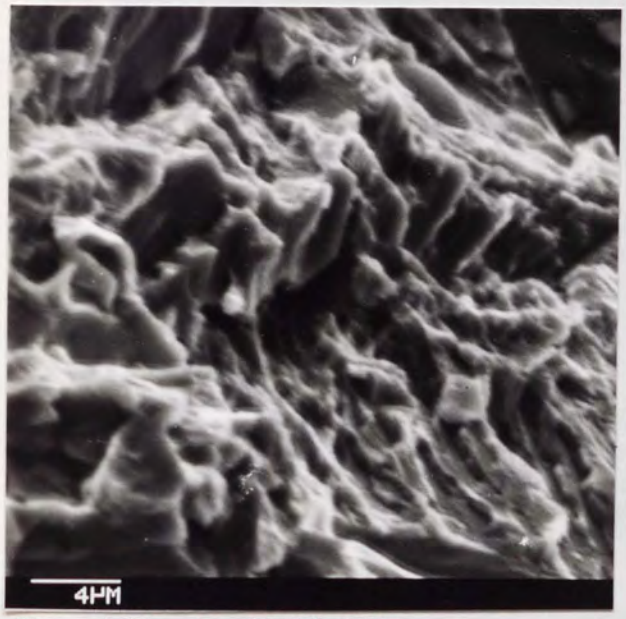

C - Alloy: 12HT 2Mo

D - Alloy: 12M 2Mo

PLATE 30: Ductile failure of austenitic and martensitic matrix in the fracture process of high-Cr cast irons

PLATE 31: General appearance of fracture in an austenitic alloy. Note the increase in the fraction of eutectic carbides at the fracture surface. Alloy: 8HT 2Mo

PLATE 32: General appearance of fracture in a martensitic alloy. Note the lower area %age of eutectic carbide on surface compared with austenitic alloys. Alloy: 12M 2Mo

A - General appearance of fatigue zone Alloy: As.15.3

B - Detail of fracture behaviour in fatigue zone Alloy: 2Mo AsCAST

C - Detail of fracture behaviour at fatigue zone Alloy: 12HT 2Mo

PLATE 33: Fracture appearance in the fatigue zone of fracture samples of austenitic alloys

A - General Appearance of fatigue zone Alloy: M.15.3

B - General Appearance of fatigue zone. Note: spark machined notch Alloy: 4M2Mo

C - Fracture detail in fatigue zone Alloy: 72M2Mo

PLATE 34: Fracture appearance in the fatigue zone of fracture of martensitic alloys

the eutectic carbides, however, occurred to a lesser extent than in the austenitic alloys, in agreement with the work of Gahr [149]. For a qualitative comparison the fracture surfaces of two types of high-Cr cast irons are given in plates 31 and 32. Due to the large amount of secondary carbide precipitation in martensitic alloys, a finer and higher density of dimpled failure of the martensitic matrix was observed (see plate 30). The formation of dimples in martensitic alloys was very similar to austenitic alloys and, as mentioned above, neither formation of necking nor extensive void growth and coalescence was observed (see plates 37 and 38). The observations in conjunction with Fig. 78 indicated that two different failure mechanisms were operating in the fracture process of austenitic and martensitic high-Cr cast irons.

As shown in plate 3, it was very difficult to distinguish the fatigue crack tip from the fast fracture area in the austenitic alloys. It was not possible to observe any fatigue-striations and the fracture characteristics were identical in fatigue-crack zones with the fast fracture areas (i.e. cleavage failure of eutectic carbides and dimpled ductile failure of matrix). (See plates 33 and 34).

9.6.5 Micromechanism of Fracture in High-Cr Cast Irons

In the micromechanism of fracture, it is assumed that fracture takes place when the critical fracture stress (σ_F^*) (for cleavage brittle fracture) or critical strain (ε_F)

(for ductile failure) is attained at a crack tip. As mentioned above the products of two failure mechanisms were observed together on the fracture surfaces of high-Cr cast irons. Therefore to determine the controlling mechanism slow notch bending tests were carried out using charpy sizes specimens with constant notch depth and various notch radii. It was mentioned in section 4.2.1 that for strain controlled fracture the longitudinal strain at fracture initiation (ε_F) is independent of notch geometry while the maximum local stress [$\sigma_{yy(max)} = \sigma_F$] is dependent on notch geometry. Therefore if the failure mechanism of high-Cr cast irons was the attainment of the critical strains the obtained σ_F values for each notch type should have been different, as observed in the work of Tetelman et al[115] and Goldenberg et al [117]. As can be seen from tables 20-25, the results obtained from different notch geometries together with duplicated test results gave the same fracture stress (σ_F^*) of the alloys with maximum $\pm$ 3% standard error. This is a strong evidence that failure of the alloys occurs by attainment of the critical stress values which were independent from notch geometry (stress controlled fracture).

McClintock[150] has developed an approximate criterion for ductile failure which was based on the assumption that the growth of cylindrical holes and critical strain for fracture was approximated with the given equation

$$\varepsilon_F = \frac{(1-n)\ln(\ell_2^o/2r_2^o)}{\sinh[(1-n)(\sigma_{xx}+\sigma_{yy}/2\bar{\sigma}/\sqrt{3})]} \quad \ldots\ldots\ldots(104)$$

where $2r_2^o$ and ℓ_2^o : initial diameter and spacing respectively, n : work hardening exponent and $(\sigma_{xx} + \sigma_{yy})/2$ represents the hydrostatic stress for plane-strain conditions. The variation of strain ahead of the notch in bending is described in the figure 25.

The critical strains for void growth, coalescence and consequent fracture in a ductile manner would be more readily achieved at the notch root or a very short distance ahead of the notch root as observed experimentally in the reported literature [115,117]. The areas very close to the notch root on the fracture surfaces of bend specimens were studied using stereoscan electron-microscopy and detailed pictures are given in plates 35-38. As can be seen, neither austenitic nor martensitic high-Cr cast irons exhibited any indication of a full mechanism of ductile fracture (i.e. necking around secondary carbides, extensive void growth and coalescence) at the bottom of the notch where the conditions are fulfilled for the strain controlled fracture mechanism described above. These observations led to the conclusion that the failure mechanism of high-Cr cast irons is stress-controlled and fracture takes place by attainment of critical fracture stress of the alloys (σ_F^*) ahead of the sharp cracks.

Although martensitic high-Cr cast irons obey the critical fracture stress criterion by given constant (σ_F^*) values independent of notch geometries (see tables 20-25)

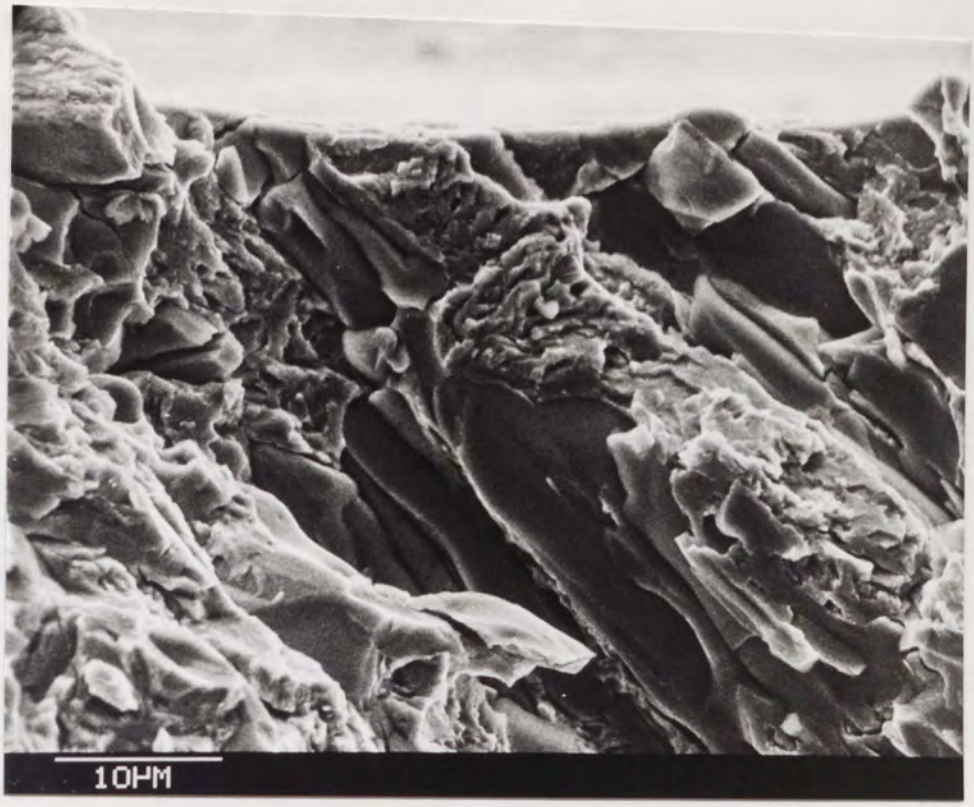

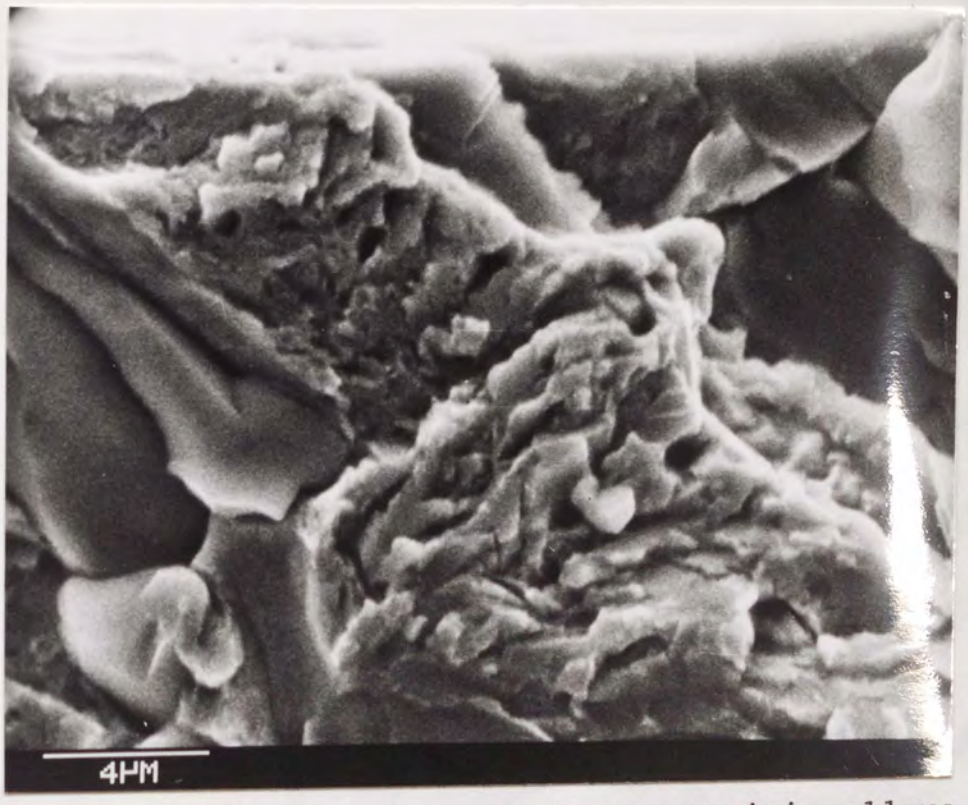

PLATE 35: Fracture appearance in the austenitic alloys at the notch root. Note the appearance of the austenitic matrix.
Alloy: 8HT4Mo
Notch Root Radius: 0.686 mm

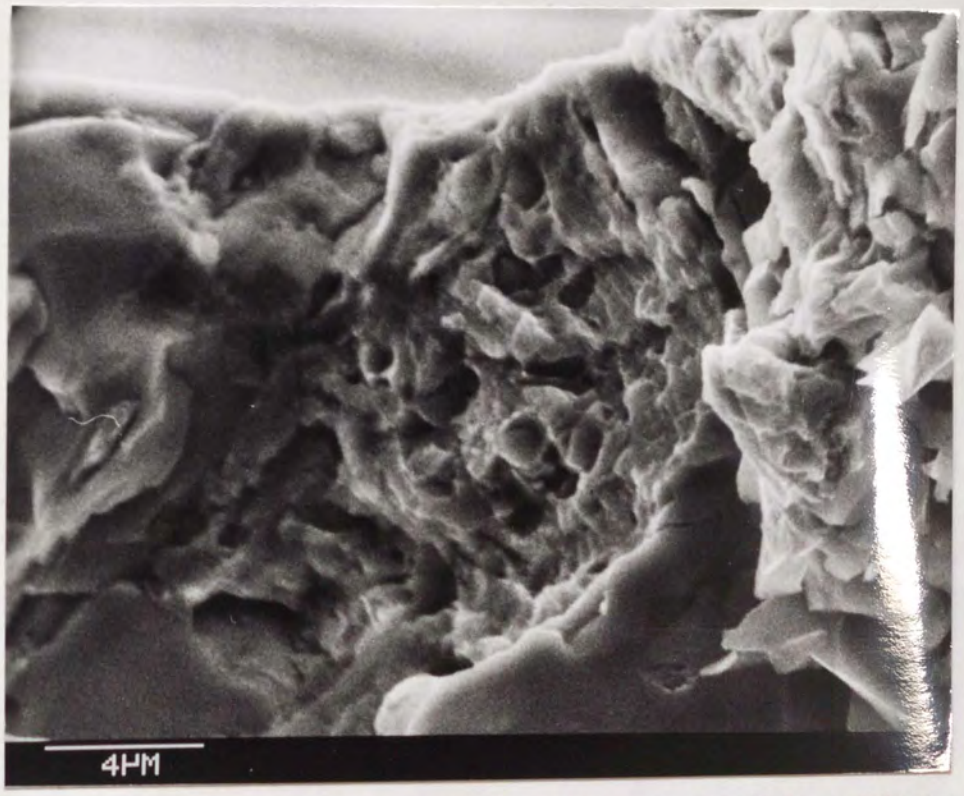

PLATE 36: Fracture appearance in the austenitic alloys at the notch root. Note the appearance of the austenitic matrix.
Alloy: 72HT2Mo
Notch Root Radius: 0.686 mm

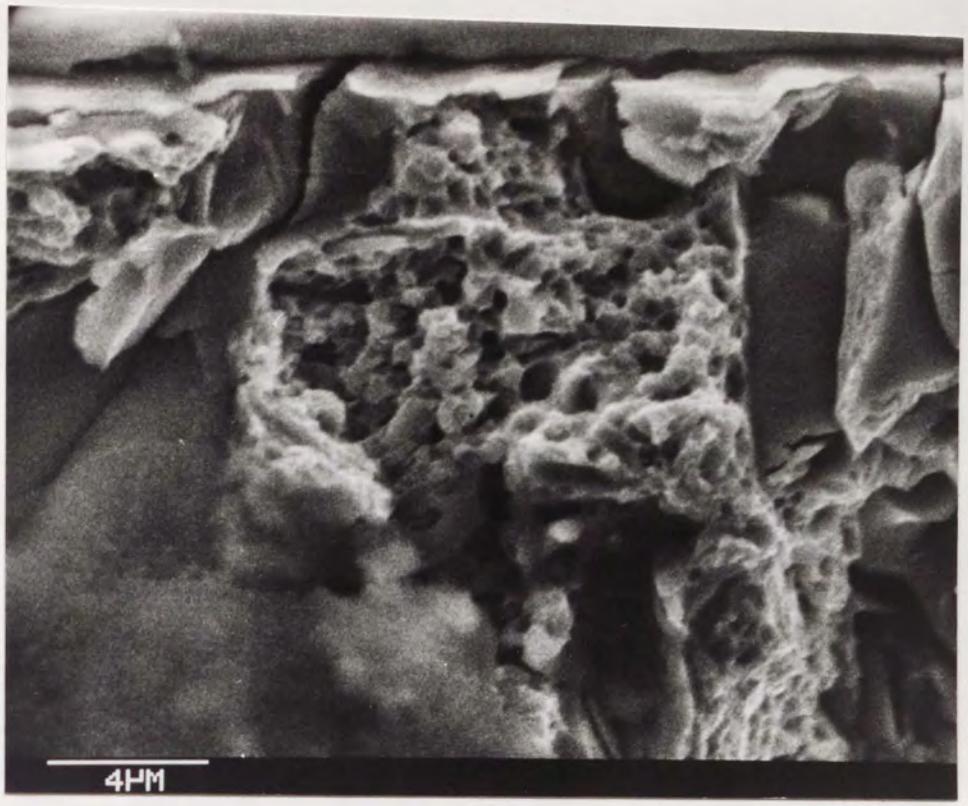

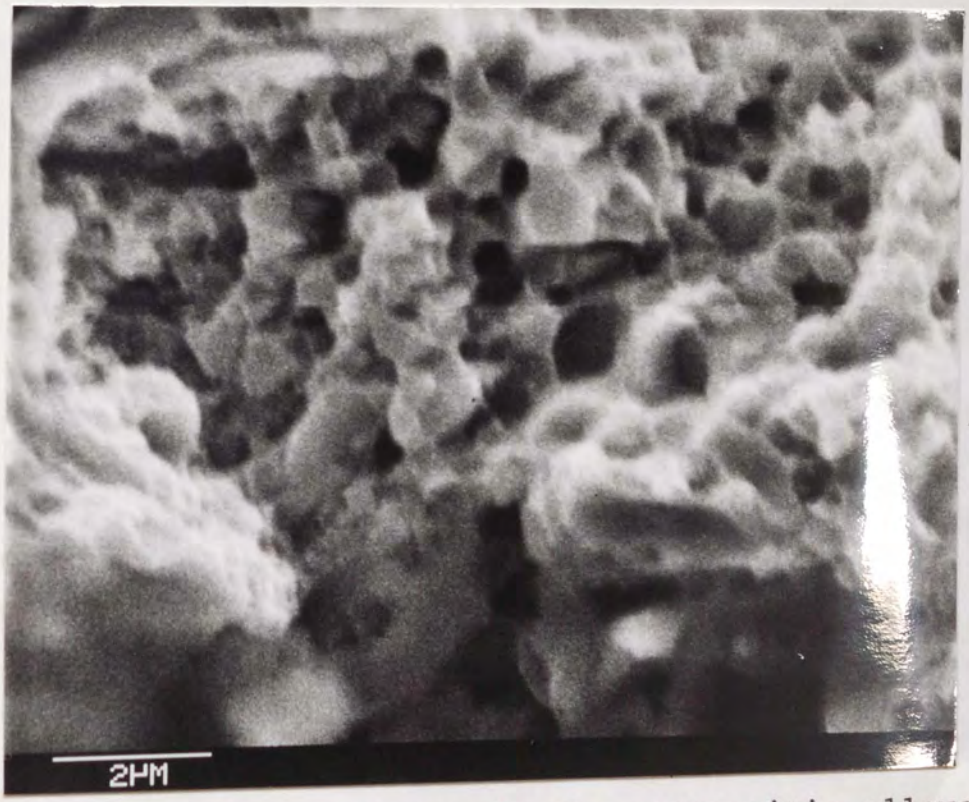

PLATE 37: Fracture appearance in the martensitic alloys at the notch root. Note the appearance of the martensitic matrix
Alloy: M72M2Mo
Notch Root Radius: 0.432 mm

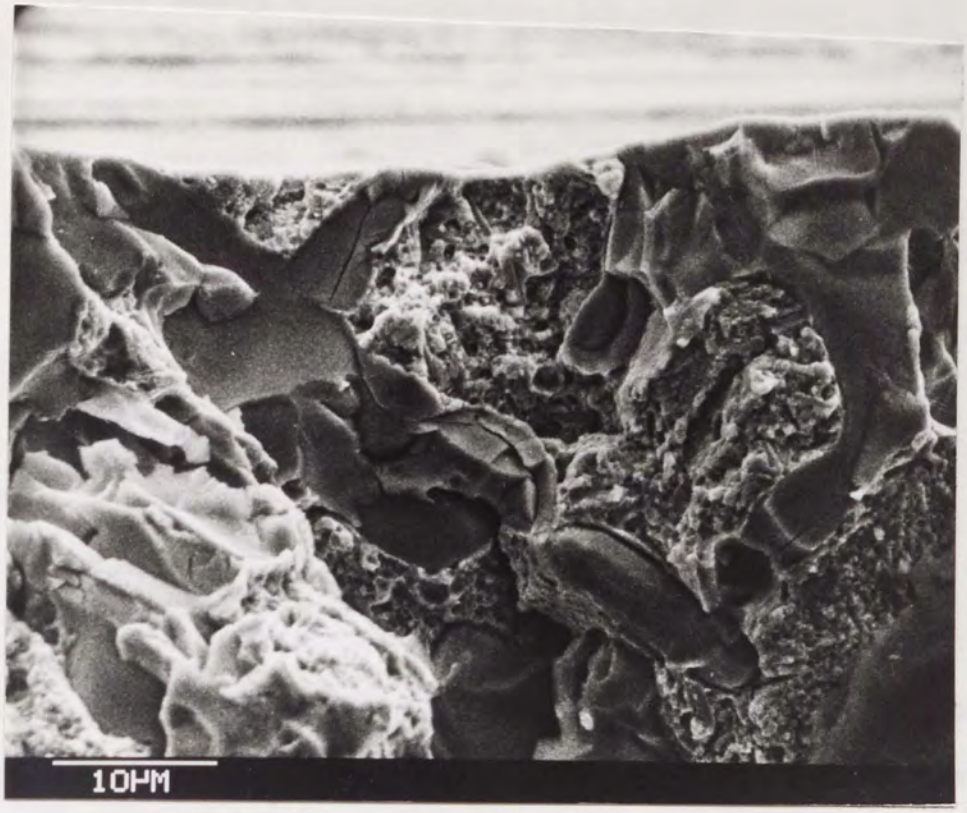

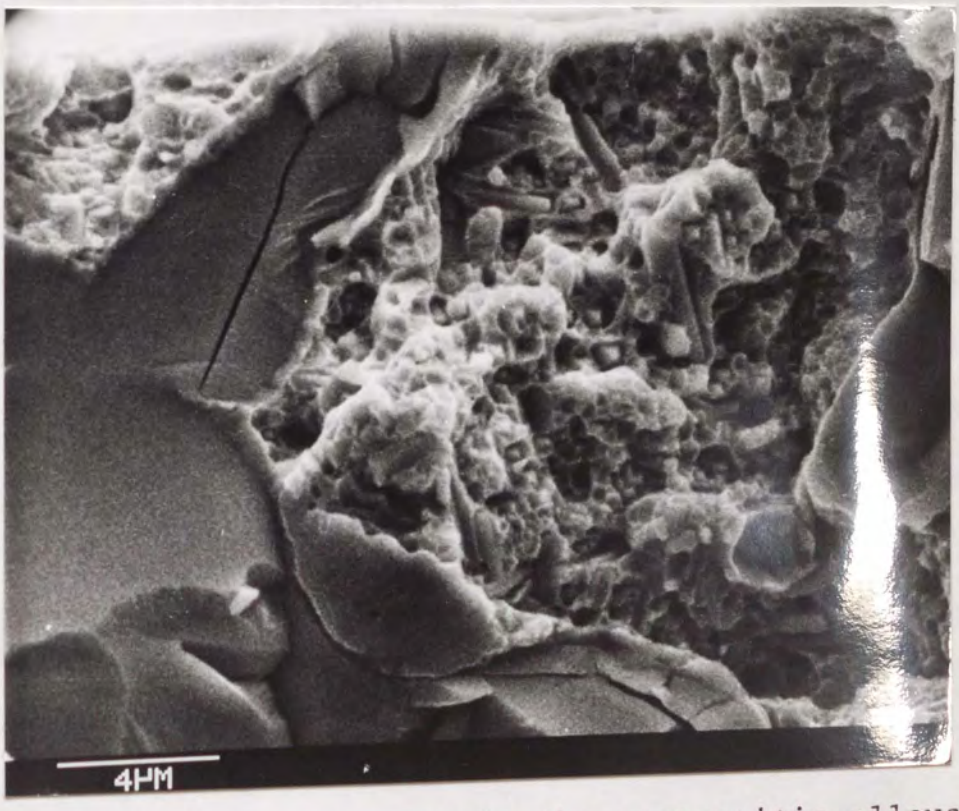

PLATE 38: Fracture appearance in the martensitic alloys at the notch root. Note the appearance of the martensitic matrix.
Alloy: 12M2Mo
Notch Root Radius: 0.711 mm

similar to austenitic alloys, for convenience the failure mechanisms of these two different high-Cr cast irons were discussed separately.

9.6.5.1 Failure Mechanism of Austenitic High-Cr Cast Irons

It was observed that fracture toughness of austenitic alloys varies with changes in the eutectic carbide morphology (see Fig. 77). As can be seen from plates 23-25, fracture surfaces were dominated by cleavage cracking of the eutectic carbides and preferential orientation of the crack path through eutectic carbides was observed (see plates 26-27). Although the remaining matrix failed in a ductile manner, the analyses of notch bending tests have shown that the failure mechanism is controlled by attainment of the critical fracture stress (σ_F^*) of the alloys (stress controlled fracture).

The observed failure of the eutectic-carbides ahead of the fatigue-cracks and running cracks (but inside their stress-field) (see plates 26 and 27) can be best explained by the model suggested by Barnby and Smith [105] which is based on the dislocation pile-up mechanism (see section 4.1). The necessary shear stress level to break the carbides is approximated by equation (31). The stress levels to break the carbides obtained from this equation by replacing the grain size parameter with mean inter-particle spacing of the alloys were well below the observed critical fracture stress of the alloys (i.e. $2\tau_{eff} \lesssim \sigma_F^*$). Therefore σ_F^* value of the alloys was defined as the necessary tensile stress level to initiate the

propagation of micro-cracks within the eutectic carbides into surrounding matrix and it is expected that its magnitude depends on the nucleated micro-crack size and shear stress contribution from slip bands. The obtained (σ_F^*) values of the austenitic alloys are therefore plotted against mean-carbide thickness of the alloys in Fig. 79. As can be seen the σ_F^* values of the alloys decrease with increasing carbide thickness in accordance with equation (38) which is suggested as a model for cleavage brittle fracture by Smith [111] (see section 4.2). According to this model, the fracture of high-Cr cast irons could be described as the spreading of a micro-crack from an eutectic carbide by at least one inter-particle spacing, in otherwords breaking of the remaining ligament between the two eutectic particles. Although this model suggested by Smith [111] is for cleavage-failure, due to initiation of voids around secondary carbides (as described in further section) inside the stress fields of initiated micro-cracks could easily provide the propagation of the cracks in the austenitic matrix with observed ductile tearing or void-sheet mechanism which is controlled by the stress-state [151] similar to cleavage brittle fracture.

As can be seen from tables 8-20 the increase in the holding periods caused a continuous decrease in the yield stress of the alloys. This could be explained by the dislocation mechanism suggested by Orowan [152] by considering the metallographically observed increase in the mean inter-particle spacing of both secondary and eutectic carbides (see Fig. 52 and plate 40). The drop in the yield stress

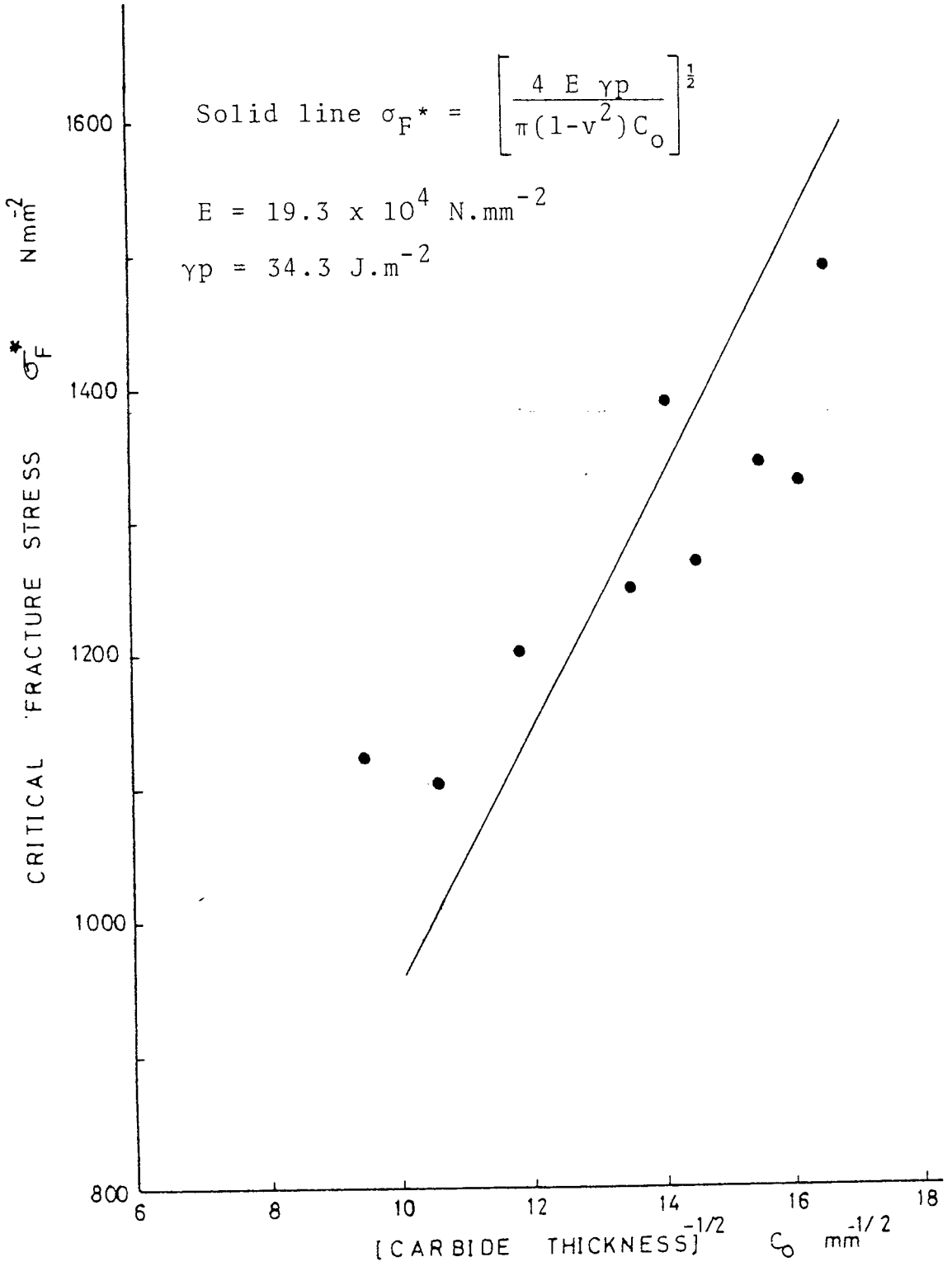

FIGURE 79: Variation of critical fracture stress σ_F^* of austenitic alloys with eutectic carbide thickness

values implies that in micro-scale there is a decrease in internal stress concentration and consequently a decrease in enhancement of the triaxiality. The loss of triaxiality lowers the stress intensification at the loaded crack tip so that a higher applied stress intensity is necessary to satisfy the fracture conditions.

The role of eutectic carbide morphology in the fracture process of austenitic high-Cr cast irons could be described in the following way:

1. As observed experimentally and as described above, eutectic carbides fracture at lower stress levels. An increase in the carbide thickness gives an increase in the size of the initiated micro-crack which consequently lowers the necessary stress level for initiation of propagation by simply considering the Griffith approach.

2. An increase in the interparticle spacing between the eutectic carbides causes an elevation of the stress level necessary to propagate the crack between the two eutectic carbides. This is due to a decrease in the triaxiality as described above and also due to an increase in the ligament length through which the crack should pass.

Therefore toughness increases with increasing interparticle spacing and decreases with increasing carbide size. For a given eutectic carbide distribution within a microstructure, the toughness of austenitic high-Cr cast irons will be governed by the magnitude of these

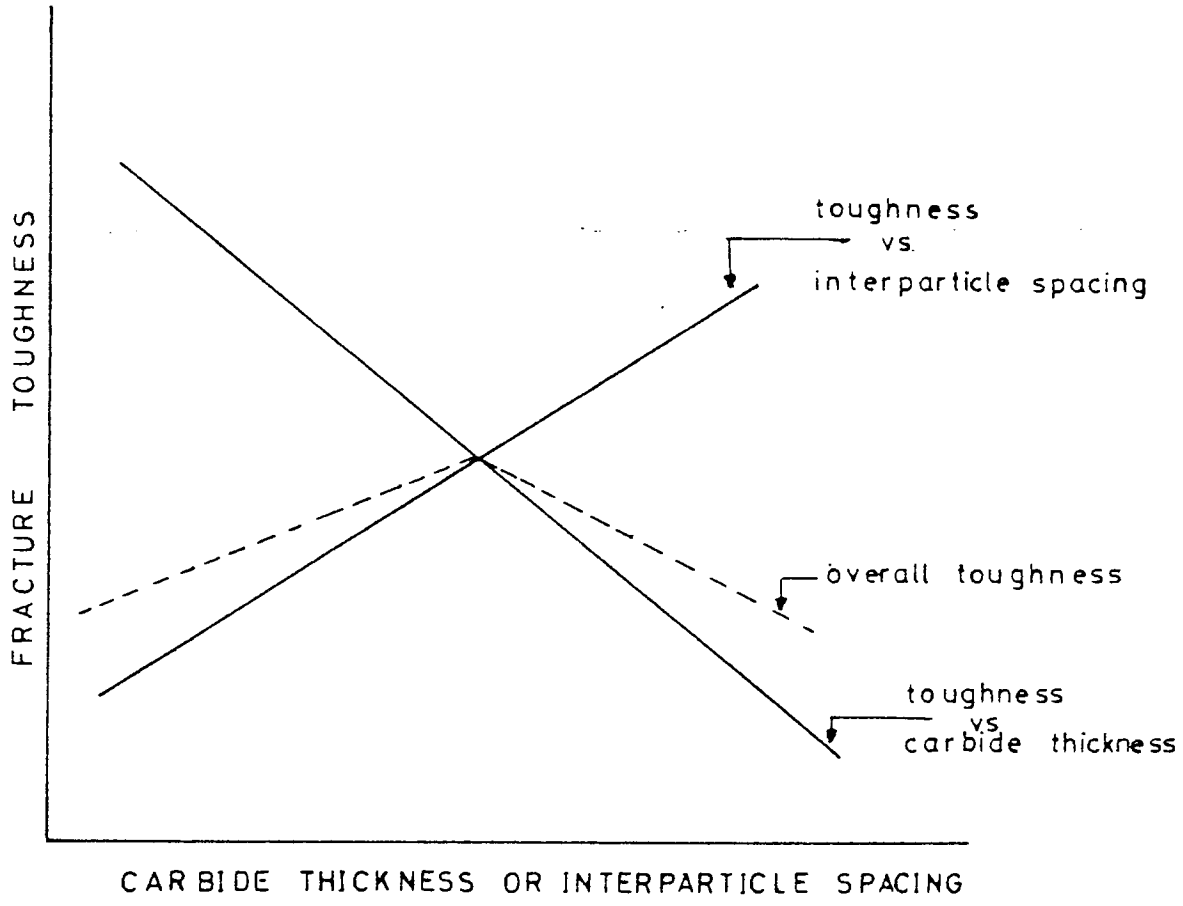

FIGURE 80: Schematic representation of role of eutectic carbide morphology on the fracture toughness of high-Cr cast irons

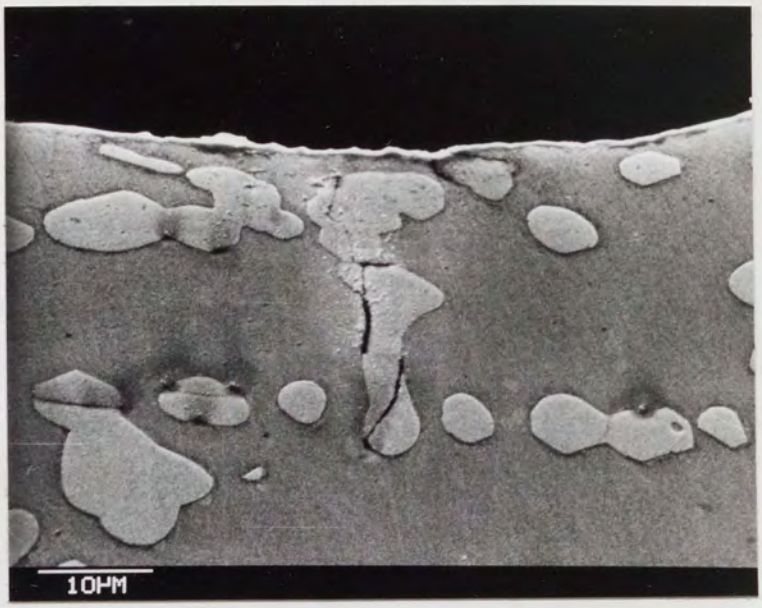

PLATE 39A: Initiation of microcracks at the eutectic carbides in the austenitic alloys

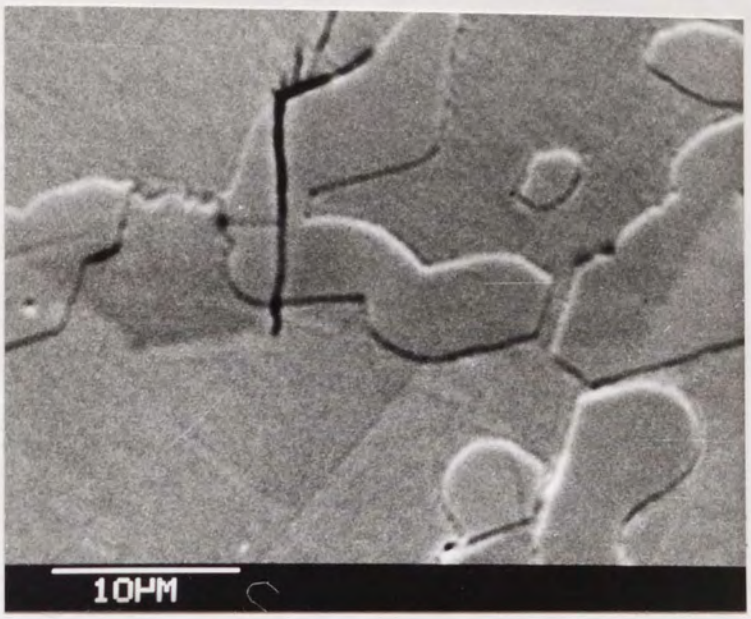

PLATE 39B: Propagation of initiated micro-cracks from the eutectic carbides to surrounding austenitic matrix

two opposite signed effects of carbide distribution. The decrease in the toughness values of the alloys after certain holding periods (see Figs. 59 and 60) was assumed to be due to an increase in carbide size if the toughness is considered to be controlled simply by the sum of these two opposite signed effects. This is shown schematically in Fig. 80. The defined physical events in the failure mechanism of austenitic alloys is summarised in plate 39 with observations.

9.6.5.2 Failure Mechanism of Martensitic High-Cr Cast Irons

As can be seen from Fig. 78, there is no significant correlation between toughness and the parameters of eutectic carbide morphology and for various carbide distributions almost similar toughness values were observed. This differs from the behaviour of austenitic high-Cr cast irons. On the other hand, the slow notch bending tests indicated that fracture is stress controlled similar to austenitic alloys.

The eutectic carbide morphology of the martensitic alloys was identical to the austenitic alloys for given conditions (i.e. alloy additions, high temperature heat treatments). The only exception was that, as mentioned in section 9.1, the hardening heat treatments at 975^{o}C caused a considerable amount of precipitation of secondary (M_7C_3) carbides within the microstructures. In order to make a qualitative comparison the distributions of the secondary carbides in austenitic and martensitic high-Cr cast irons are given in plates 40 and 41. These were obtained from two stage carbon replicas using transmission electron microscopy.

A - After holding for 4 hours x15.000

B - After holding for 24 hours x15.000

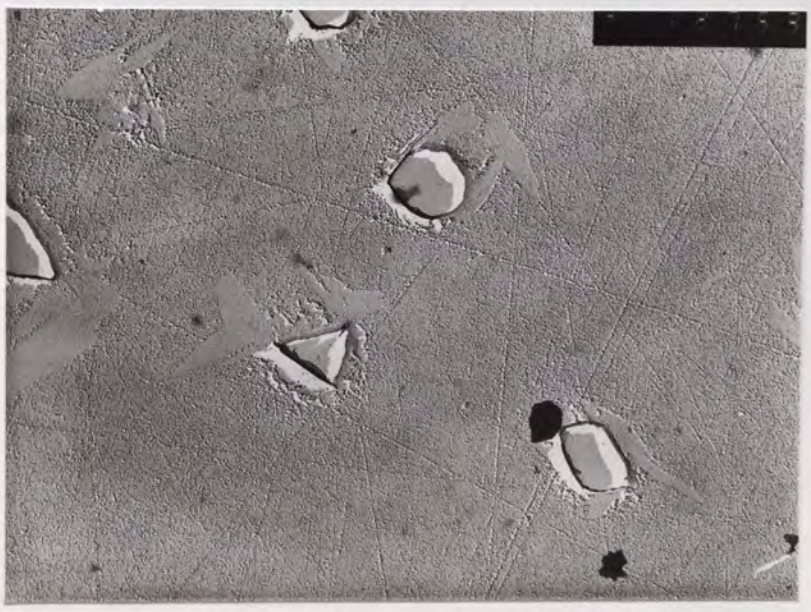

C - After holding for 72 hours x 12.000

PLATE 40: Variation in the morphology of precipitated secondary carbides by holding periods at 1180°C (alloy 2Mo - austenitic)

A - Alloy 4M2Mo
x 12.000

B - Alloy 12M2Mo
x 25.000

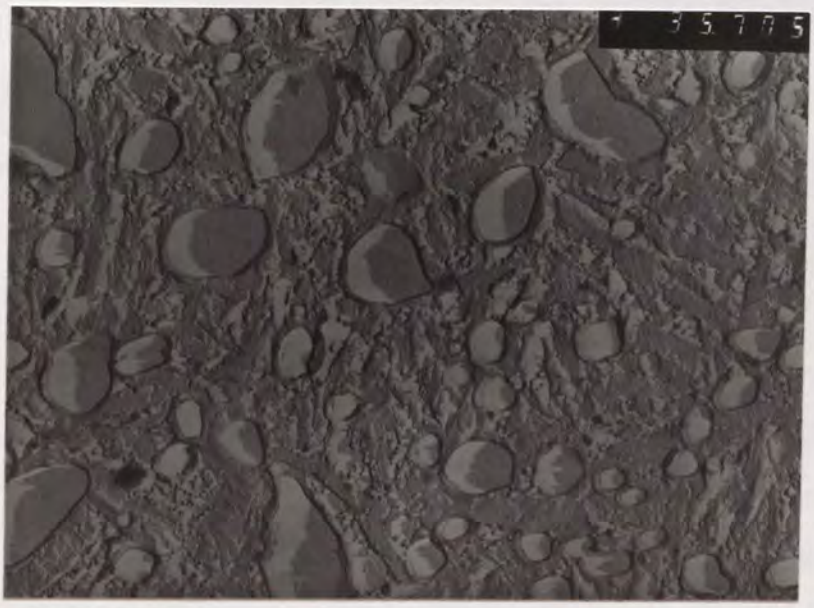

C - Alloy 4M2Mo
x 35.000

PLATE 41: The secondary carbide morphology in martensitic alloys in high-Cr cast irons. Note greater carbide density than in Plate 40.

It is proposed that independency of fracture toughness of martensitic alloys from eutectic carbide morphology is a result of secondary carbides and they alter the observed failure mechanism of austenitic high-Cr cast irons in the following way.

Formation of voids and failure of matrix in martensitic High-Cr cast irons

When a particle-strengthened material is stressed the matrix material undergoes plastic deformation while the particles generally deform only elastically. Nucleation of voids around the particles results from this inhomogeneous deformation of matrix and particles. There have been conflicting observations on whether the voids form immediately on yielding or after large values of strain. Also formation of voids has been reported as causing both particle cracking and separation of particle-matrix interface. On the other hand several theoretical studies have been proposed based on the release of stored elastic energy which is a product of high stresses caused by impingement of dislocation pile-ups (Gurland [153] Goods and Brown [154] and others [155,156]). According to these models, void nucleation cannot take place unless the elastic energy released by removing the stress from the particles is at least equal to the surface energy created (critical energy criterion). The model suggested by Argon et al [157], takes into account the interaction between the plastic fields of neighbouring particles to provide a stress concentration at the non-deforming particles. This model incorporates a dislocation mechanism proposed by Ashby [158] (critical stress criterion).

As can be seen from plates 40 and 41 the mean inter-particle spacing between the secondary carbides in martensitic alloys decreased significantly due to the considerable amount of precipitation, when compared with the austenitic high-Cr cast irons. In the work of Durman [53] for 1.4% carbon containing martensitic high-Cr cast iron, the average mean interparticle spacing of secondary carbides was reported as 0.7 μm. For the alloys studied this value is expected to be lower, due to higher carbon levels. According to the method suggested by Argon et al [157] plastic fields of closely spaced particles easily overlapped to give maximum plastic incompatability stresses at particles and such effects favour easy void formation under a low level of applied stresses. Although their model could not be treated numerically due to uncertainties in local-stresses, the observed events and implications discussed below suggested that this model could easily operate in martensitic alloys.

By considering the high density of secondary carbides, the dislocation loops around the particles can easily develop by the mechanism suggested by Orowan [152]. This could cause a decrease in the stress concentration created around the eutectic carbides since the number of dislocations available to break the eutectic carbides are left in the dislocation loops around the secondary carbides. Although martensitic materials have a higher density of dislocations than austenitic alloys [159], the lower amount of cleavage cracking of the eutectic carbides in the martensitic alloys observed is strong evidence that this event happens (see

plates 31 and 32). These created dislocation loops exert back stress in the slip plane which opposes further slip and the lattice requires higher stress levels to overcome the average back stresses from the loops. The dislocation punching out mechanism suggested by Asby [158] could become operative and this raises the normal interfacial stress around the particles and ultimately either the particle-matrix interface or the particles fracture. According to Argon et al [157] the interaction between the plastic fields of closely spaced particles enhances the interfacial stress, facilitating void formation. Consequently void formation is achieved at low levels of applied stresses.

According to Goods and Brown [154], the carbide particles are bonded to the surrounding matrix strongly. On the other hand carbides are relatively brittle and, like ceramic materials, their fracture strength is sensitive to surface flaws. As the size of the particle increases so does the probability that the particle contains flaws of a sufficient length to increase brittle fracture below the cohesive strength of the interface. The event leading to formation of voids around secondary carbides in the martensitic alloys could not be observed clearly (i.e. the result of particle cracking or breaking-up of the particle-matrix interface). However it is assumed that the experimentally observed stress controlled final failure mechanism takes place just after initiation of voids giving a direct void-sheet formation due to the very close spacing of secondary carbides which create high triaxiality, as described by Hancock and Mackanzii [151], which is markedly dependent upon stress-state.

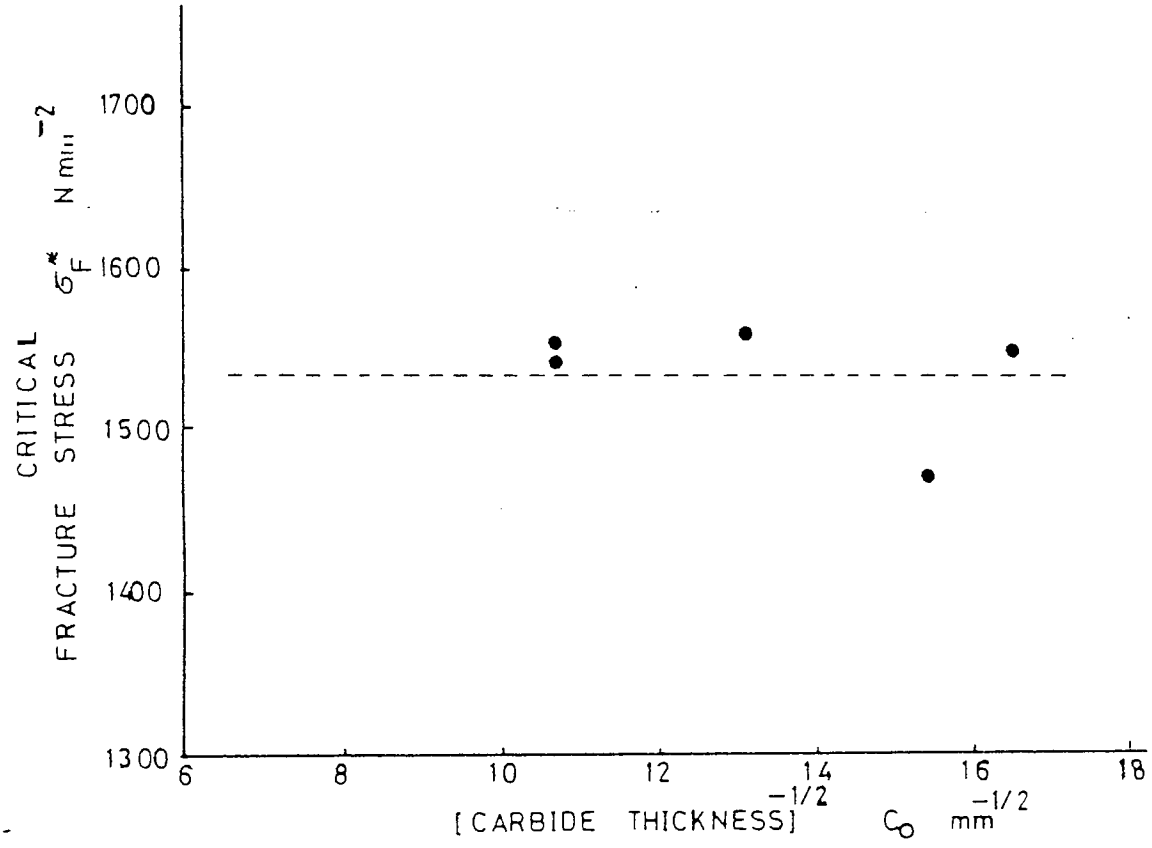

FIGURE 81: Variation of critical fracture stress σ_F^* of martensitic high-Cr cast irons with eutectic carbide thickness

According to the phenomena described, the cleavage cracking of the eutectic carbides in martensitic high-Cr cast irons could be a result of initiated micro-cracks within the matrix. The observed constant critical fracture stresses of martensitic high-Cr cast irons for different carbide thicknesses supports this phenomenon (see Fig. 81), otherwise if the propagation of the nucleated micro-cracks from eutectic carbides is considered, critical fracture stress of martensitic alloys should have been different, as observed in austenitic alloys (see Fig. 79).

According to this fracture mode described, the fracture toughness of martensitic high-Cr cast irons is controlled by secondary carbide distributions. By considering the almost insignificant variation in the secondary carbide morphology of the alloys after hardening heat treatments, it is possible to explain the constant levelling of toughness of martensitic alloys which have different eutectic carbide distributions.

9.6.5.3 The Validity of Proposed Models and their Application for the Assessment of Fracture Toughness of High-Cr cast irons

The stress distribution ahead of a loaded crack tip differs in two important ways from that in the notched bend specimens used to determine the critical fracture stress (σ_F^*) values. Firstly the maximum tensile stress elevation is higher ahead of the crack tip. Secondly the maximum stress varies rapidly with distance ahead of the crack tip whereas it varies gradually below the notch root. Dimensional consid-

erations have shown that if the fracture from a sharp-crack is to occur at a critical stress intensity factor K_{IC} than the attainment of a critical local tensile stress (σ_F^*) is not a sufficient fracture criterion, a distance requirement must also be satisfied. Ritchie et al [124] postulated that critical fracture stress (σ_F^*) had to be exceeded over some microstructurally determined characteristic distance ahead of the crack tip before fracture could occur. This concept is widely accepted for both stress controlled and strain controlled fracture mechanisms and it is generally defined as a distance which represents the minimum amount of material which is characteristic of the scale of physical events involved in fracture (i.e. such as cleavage cracking of carbides, formation of voids, etc.).

According to the above assumption the failure of a body containing a sharp-crack by a stress controlled fracture mechanism requires that the critical fracture stress (σ_F^*) should be exceeded ahead of the crack tip and this stress level extends over a characteristic size scale (X_o). After considering the failure of the alloys well below the general yielding, this assumption was approximated to Westergaard solutions [74] with the equation given below

$$K_{IC} = \sigma_F^* \sqrt{2\pi X_o} \qquad \text{.....(104)}$$

The components of this equation (σ_F^* and X_o) are both defined by microstructural parameters, therefore they are both properties of the alloys. By inserting the values of

experimental critical fracture values, their carbide thickness (C_o) and 19.3 x 10^4 N/mm^2 as a constant value of Young's modulus into equation (105), the value of the plastic term of austenite (γ_p) for high-Cr cast irons was found to be 34.3 $\pm$ 7 J/m^2

$$\sigma_F^* = \left[\frac{4E\gamma_p}{\pi(1-\nu^2)C_o}\right]^{\frac{1}{2}} \qquad \ldots\ldots\ldots(105)$$

This equation is analogous to equation (38) which was suggested by Smith [111], only the contribution of dislocation pile-up was omitted and according to Gurland et al [125] this causes an error of only 2-3%. This enabled calculations of the critical fracture stress of the alloys which were not tested in notch bending tests using their carbide thickness from metallographic studies. The value of the critical distance (X_o) in equation (104) was taken as equal to 3.5 times that of the interparticle spacing. The theoretically obtained fracture toughness of austenitic high-Cr cast irons calculated with these assumptions from equation (104) were compared with the experimentally obtained valid K_{IC} values of the alloys in Fig. 82. As can be seen, the agreement between the calculated and experimentally determined K_{IC} values of austenitic high-Cr cast irons is quite good. The difficulty was the somewhat arbitrary choice of characteristic distance as 3 or 4 times the interparticle spacing. In order to use only a single value and to match all experimental points the characteristic distance was accepted as an average value, i.e. 3.5 times the interparticle spacing. In the work of Tetelman et al [131] the limiting root radius values (ρ_o) were assumed that the measure of characteristic distance (X_o) and related tomicrostructural parameters such as

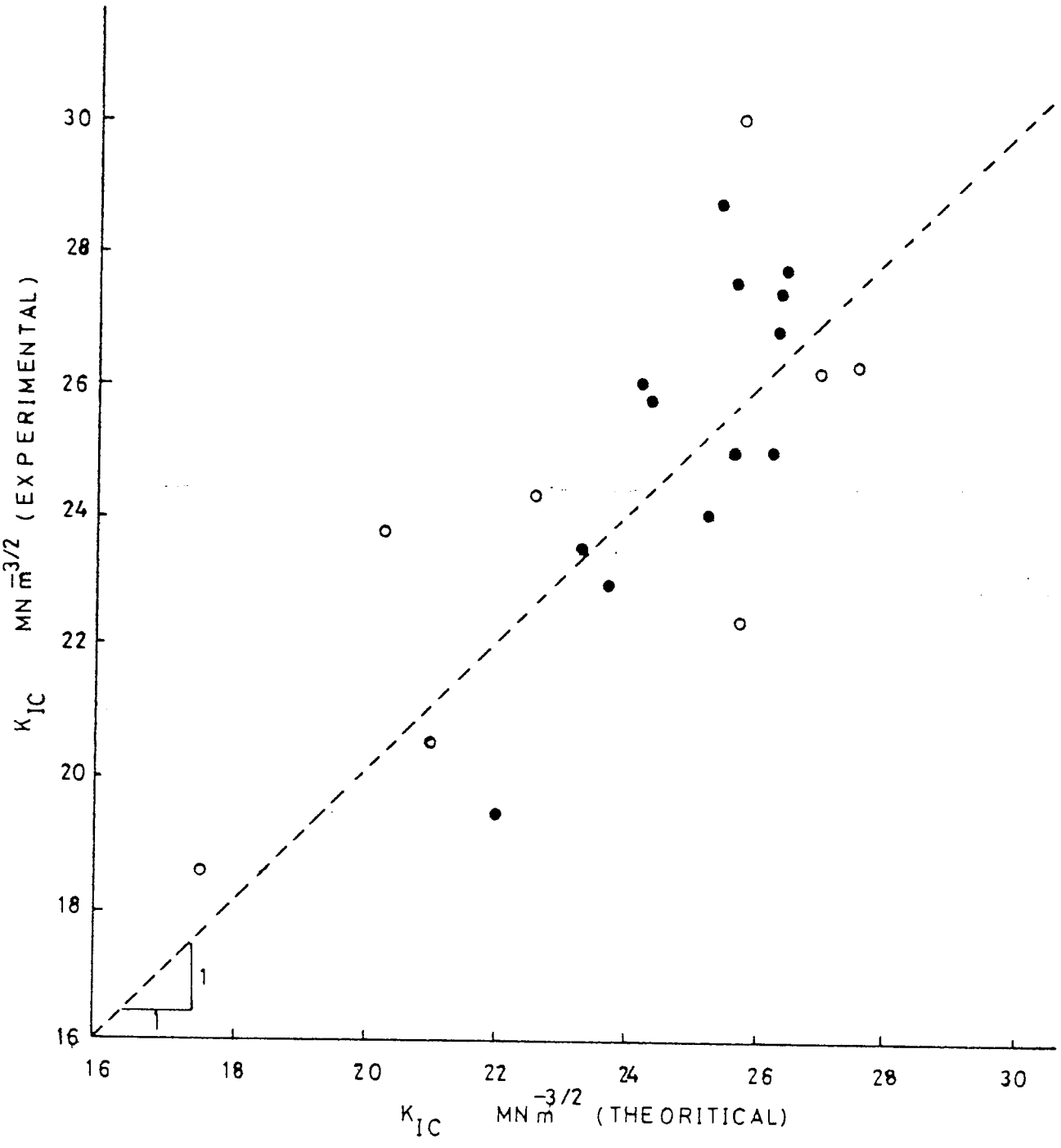

FIGURE 82: Comparison of experimentally and theoretically obtained fracture toughness values of the high-Cr cast irons

$$K_{IC(theoretical)} = \sigma_F^* \sqrt{2\pi X_o}$$

where $\sigma_F^* = \left[\frac{4\ E\gamma_p}{\pi(1-\nu^2)C_o}\right]^{\frac{1}{2}}$

X_o = 3.5 times mean interparticle spacing

The open symbols determined by using the experimentally obtained σ_F^* values from notch bend tests

slip or twin band spacing, grain size, etc. Although good correlation was observed between the experimental and calculated K_{IC} values as described above, the present analysis of interparticle spacing did not relate numerically with the values of (ρ_o) which were obtained from Figs 66-68. A similar disparity is also observed in the work of Ritchie et al [127].

When similar calculations were carried out using experimental (σ_F^*) values of martensitic high-Cr cast irons in equation (104) with experimental K_{IC} values, the value of ($X_o/3.5$) was found to be about 7 μm. When this parameter was compared with microstructural parameters it did not match either the interparticle spacing of eutectic carbides or the interparticle spacing of secondary carbides which were assumed to be less than 0.7 μm. Similarly in the work of Kotilainen et al [160], the characteristic distance could not be related with any microstructural parameters for stress controlled failure of bainitic steels. The failure mechanism of martensitic high-Cr cast irons was described as a void-sheet failure which is controlled by stress-state. The approximately constant value of 7 μm obtained indicated that in order for this mechanism to operate a certain amount or critical amount of formation of voids is necessary and not simply failure of the remaining matrix between the two dimples.

During the assessment of macroscopic fracture behaviour from micro-mechanistic fracture, it appears that for stress controlled fracture, the values of (σ_F^*) can be correctly

determined as a material property from the notch analyses. However, the magnitude of the characteristic distance is arbitrary although it includes material properties such as grain size, interparticle spacing, etc. In the literature the multiplication factor of these microstructural parameters has been reported as varying from 1.3 to 5.5 for stress controlled failure of different steels (Gurland et al [125], Ritchie et al [124], Parks [126], and Ritchie et al [128]).

Although this suggested model brings uncertainty into the magnitude of the characteristic distance, this approach does however correlate well with the experimentally determined valid K_{IC} values of austenitic alloys using the theoretically and experimentally determined critical fracture stress (σ_F^*) values of the alloys from notch analyses and taking the characteristic distance as an average 3.5 times of the interparticle spacing. These results clearly show the validity of the proposed failure mechanism of the alloys by demonstrating that the role of eutectic-carbide morphology in the failure mechanism of austenitic alloys and constant levelling of toughness in martensitic alloys is due to the uniformity of the secondary carbide distribution. Therefore it could be satisfactorily used for close estimation of fracture behaviour of high-Cr cast irons from their microstructure.

As mentioned in section 9.4, the alloys having lower K_{IC} values exhibited higher or similar notch toughness values to those alloys having higher K_{IC} values. This observed

discrepancy could be explained by considering the fracture criteria of two stress concentrators, as given in Fig. 83. The failure criterion for a blunt notch is that the maximum tensile stress (σ_{yy}) below the notch builds up to a critical value (σ_F^*) (since σ_F^* is a material property) at the elastic-plastic interface. By considering equation (83) (Hill's solutions) the magnitude of tensile stress at the elastic-plastic interface is governed by the size of the plastic zone, yield stress and root radius. Therefore fracture does not occur until the plastic zone size spreads to a critical value which equals tensile stress $(\sigma_{yy})_{max}$ to critical fracture stress. Therefore fracture can be described for a blunt notch as the attainment of the critical plastic-zone size, the magnitude of which is governed by critical fracture stress, yield stress and notch geometry, as given in equation (83). Whereas in the case of sharp-crack the failure point is situated at a fixed distance (X_o) as discussed earlier. As can be seen from figures 66-68 the martensitic alloys exhibited lower toughness values with sharp-cracks but they are comparable or superior for blunt notches. This may suggest that the toughness evaluation of high-Cr cast irons includes a measure of resistance to fracture ahead of both sharp-cracks and blunt notches. Similar observations were also made by Ritchie et al [127] on the toughness evaluation of ASISI 4340 alloy.

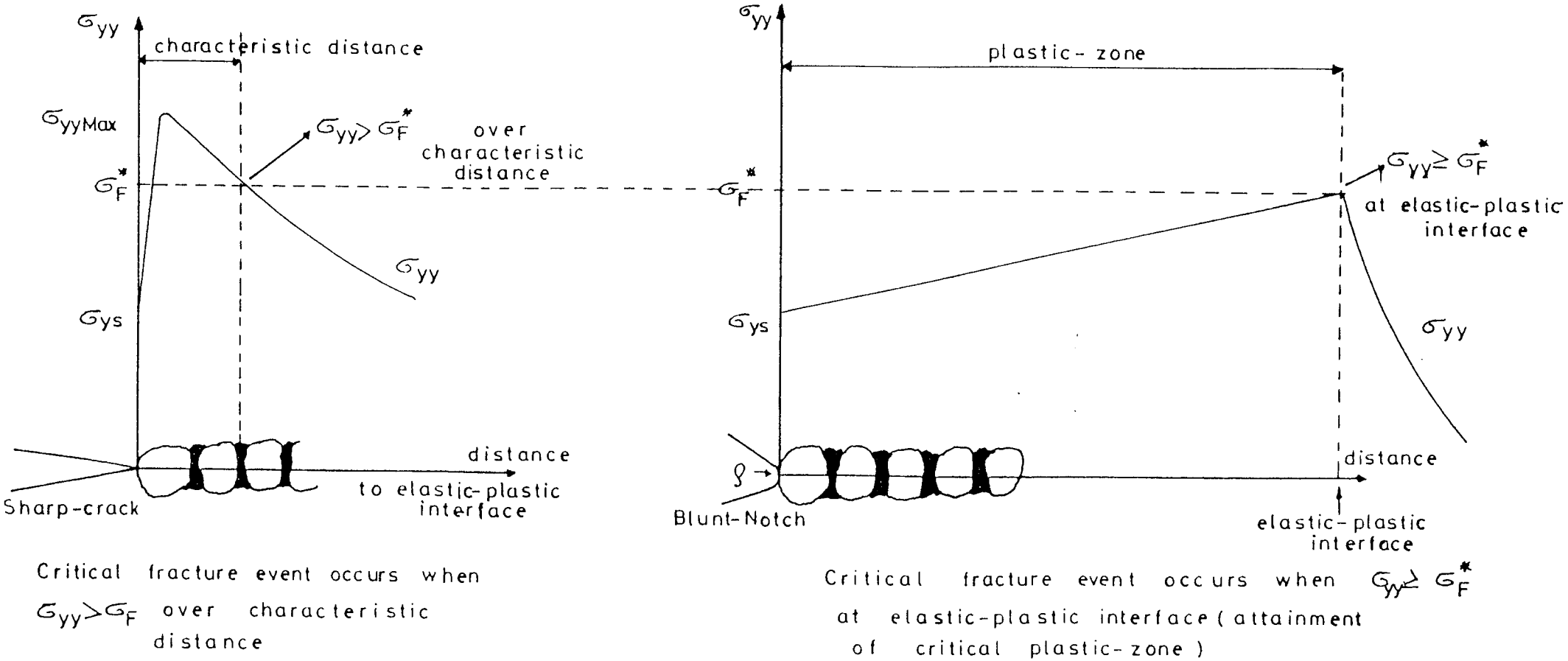

FIGURE 83: Schematic representation of failure criteria ahead of the sharp-cracks and blunt notches

9.7 Application of Fracture Toughness Data

One of the major advantages in knowing the fracture toughness of a material is the ability to predict accurately the critical defect sizes for a given certain level of applied stress. The ASTM-E24 committee has categorised the types of defects likely to be encountered as surface, embedded and through thickness cracks. Casting is almost the only production method for the alloys studied. It is very common in practice to accept a certain amount of shrinkage defects especially when producing thick sectioned components. The runner and feeder systems used are usually removed by knock-out or abrasive-cutting processes which give a big possibility for the creation of tiny surface cracks. Therefore the determination of critical defect sizes for embedded and surface cracks were considered the most appropriate way of comparing the relative toughness of the alloys which were obtained with different metallurgical variables. The calculations were carried out using equation (106) and equation (107) for embedded and surface cracks respectively. The value of the shape factor which appears in the equations was obtained from the work of Barnby [161] as $\Phi = 1.15$ for an eliptical crack $a/b = 0.4$ (a length of minor axis, b length of major axis). The results are summarised in Figs. 84-85.

$$a_c = \frac{K_{IC}^2}{\sigma_w^2 \pi} \left[\Phi^2 - \frac{\sigma_w^2}{4(2)^{\frac{1}{2}} \sigma_{ys}^2} \right] \quad \text{.....(106)}$$

$$a_c = \frac{K_{IC}^2}{\sigma_w^2 \pi} \left[\frac{\Phi^2 - 0.212(\sigma_w/\sigma_{ys})^2}{1.2} \right] \quad \text{.....(107)}$$

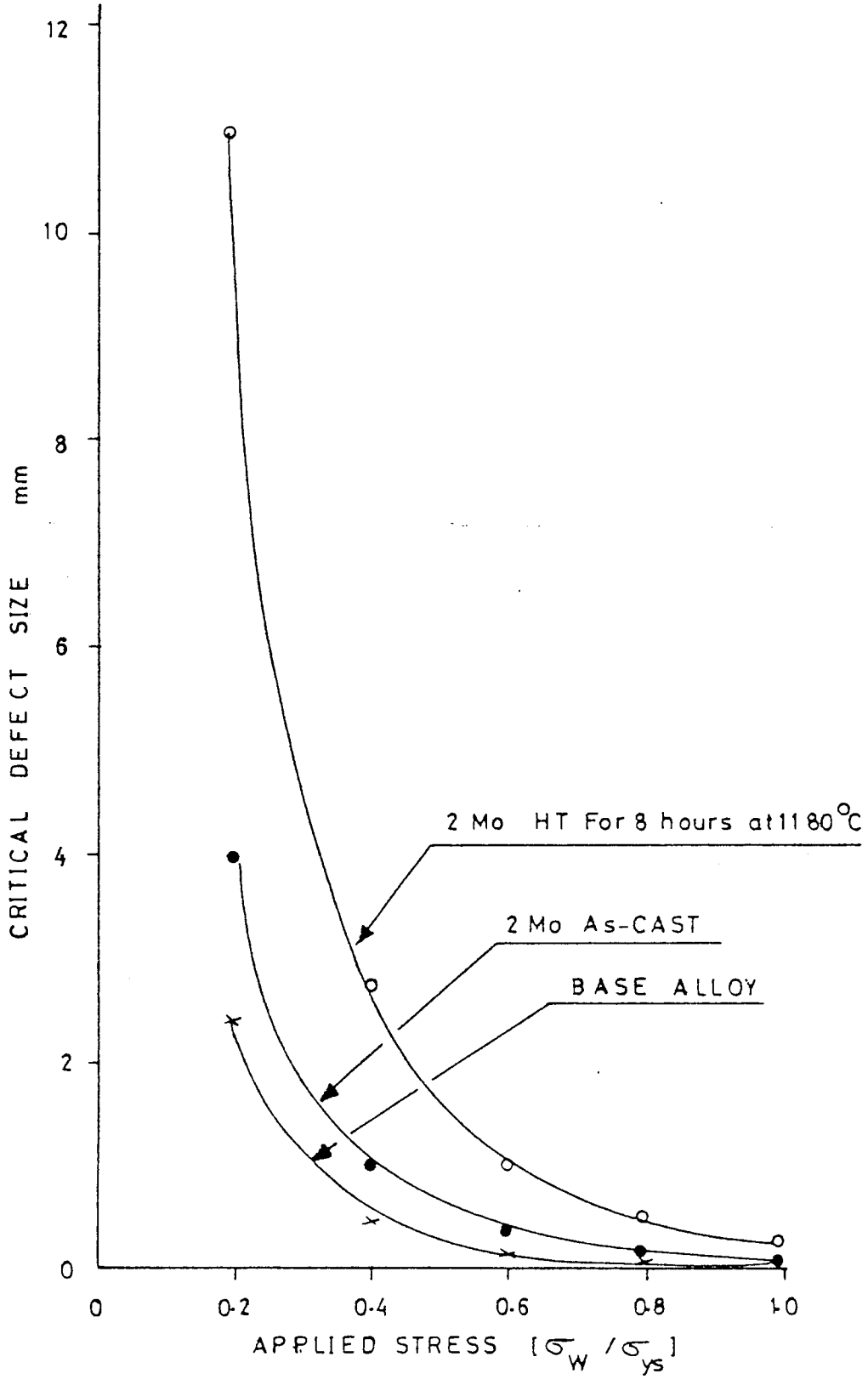

FIGURE 84: Critical Defect size for various high-Cr cast irons as a function of applied stress for totally embedded elliptical defects

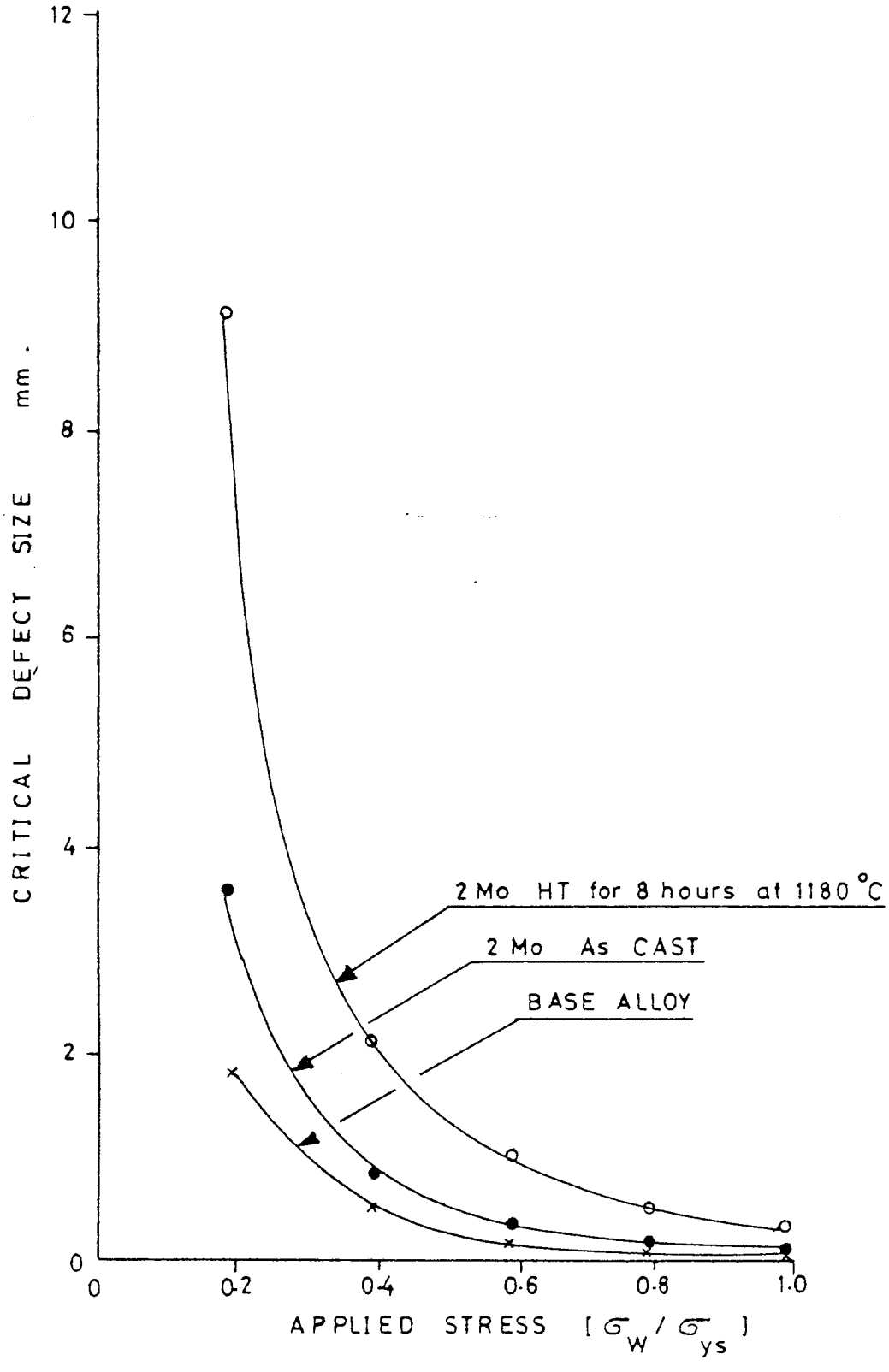

FIGURE 85: Critical defect size for various high-Cr cast irons as a function of applied stress for elliptical side defects

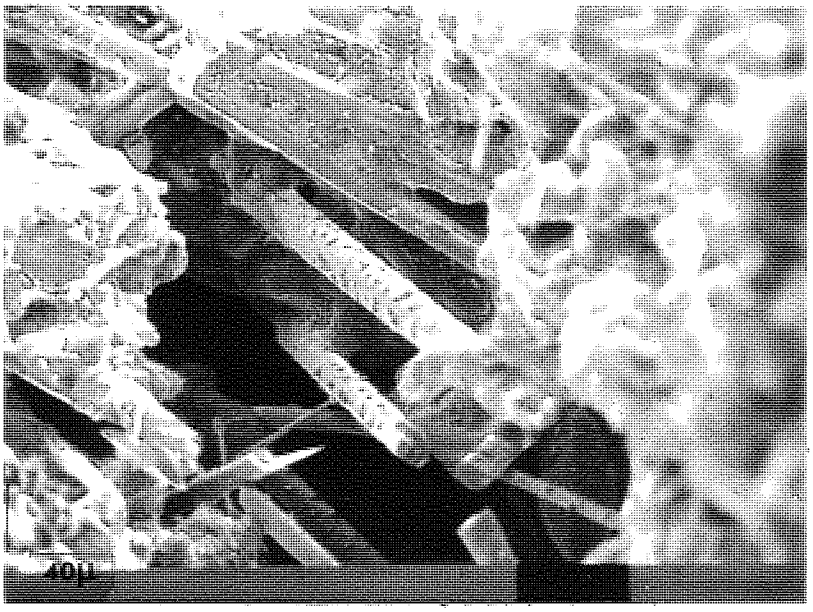

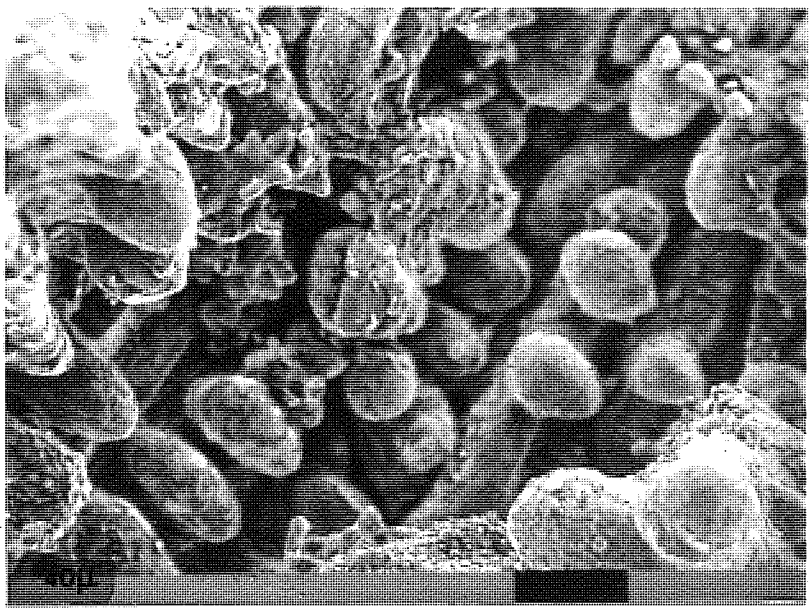

PLATE 42: Shrinkage porosity in high-Cr cast irons (primary castings)

9.8 Fatigue Properties of High-Cr Cast Irons

Although the main objective of the work was to determine the toughness characteristics, some very limited information relating to fatigue behaviour of the studied alloys (only as-cast and those heat treated for 8 hours) was gleaned during the fatigue pre-cracking process of fracture toughness test specimens.

The fatigue life of structural components is determined by the sum of the cycles required to initiate a fatigue crack and the number of cycles to propagate from subcritical dimensions to the critical size. Consequently the fatigue life of structural components may be considered to be composed of two stages

1. Fatigue-crack initiation
2. Fatigue-crack propagation

During the studies most of the notches were produced by spark machining which leaves micro-cracks, therefore no attempt has been made to obtain information which concerns the stage I (crack initiation life and threshold values). But it is worthwhile to mention that the as-cast condition in the base alloy and for low addition levels (0.6% Mo and 1% W) cracks were initiated and grown under stress intensity $(\Delta K)_{max} = 10.3\ MNm^{-3/2}$ (assuming the notch to be a sharp-crack). For higher additions of Mo and W in the as-cast condition no crack initiation or non-propagating cracks were observed up to 1×10^6 cycles with this stress intensity

level. Therefore fatigue loads were increased to give a stress intensity of 12.7 $MNm^{-3/2}$. The same trend was observed after 8 hours high temperature heat treatment, this time with the former loads the crack either did not initiate or did not propagate although tests were carried out up to 1 x 10^6 cycles, and the load was increased to give 14.3 $MNm^{-3/2}$ stress intensity. These results are inadequate to reach any certain conclusion regarding the behaviour of the alloys for crack initiation, but indicate that there is a certain improvement in the fatigue threshold and crack initiation properties of the high-Cr cast irons by alloy additions and the application of high temperature heat treatments.

The dependence of fatigue crack growth rate (da/dN) on the alternating stress intensity $\Delta K = (K_{max}) - K_{(min)}$ were expressed by the wellknown Paris-Erdoğan [162] equation (108) and results are given in table 34 and Figs. 86-87.

$$da/dN = C(\Delta K)^m \quad \text{..... 108}$$

As can be seen from the figures, in the as-cast condition the fatigue propagation rate of the alloys exhibited almost the same trend and there is no significant effect of alloy additions. Homogenisation at 1180°C for 8 hours reduced the crack growth rates of the high-Cr cast irons for all addition levels except for the base alloy. The slowest crack propagation rate was observed for the 2% Mo and 5% W addition level. As can be seen for the given stress intensity level there is almost a 70% decrease in the crack propagation rate when compared with the as-cast condition.

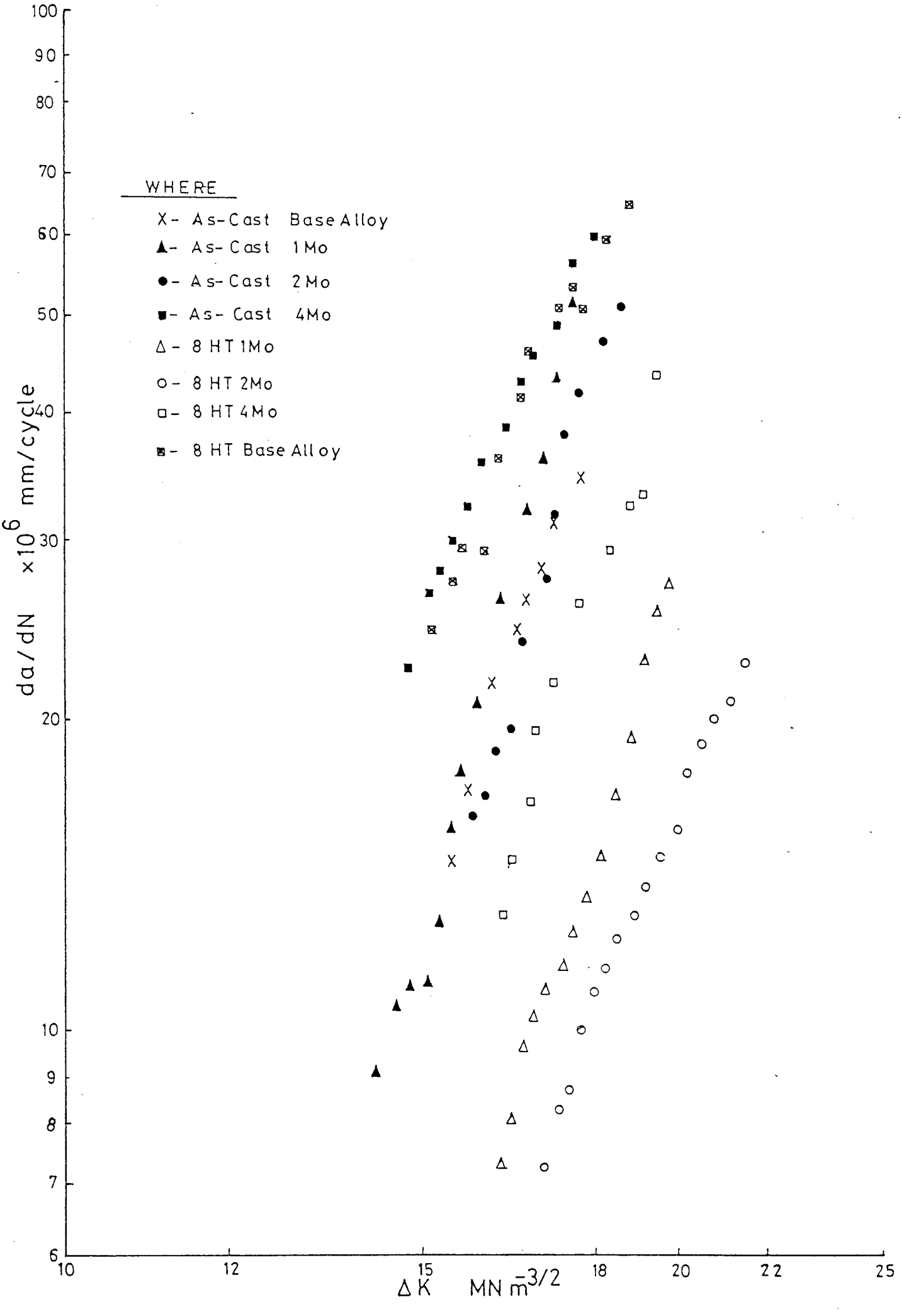

FIGURE 86: Fatigue-crack growth data of molybdenum containing high-Cr cast irons

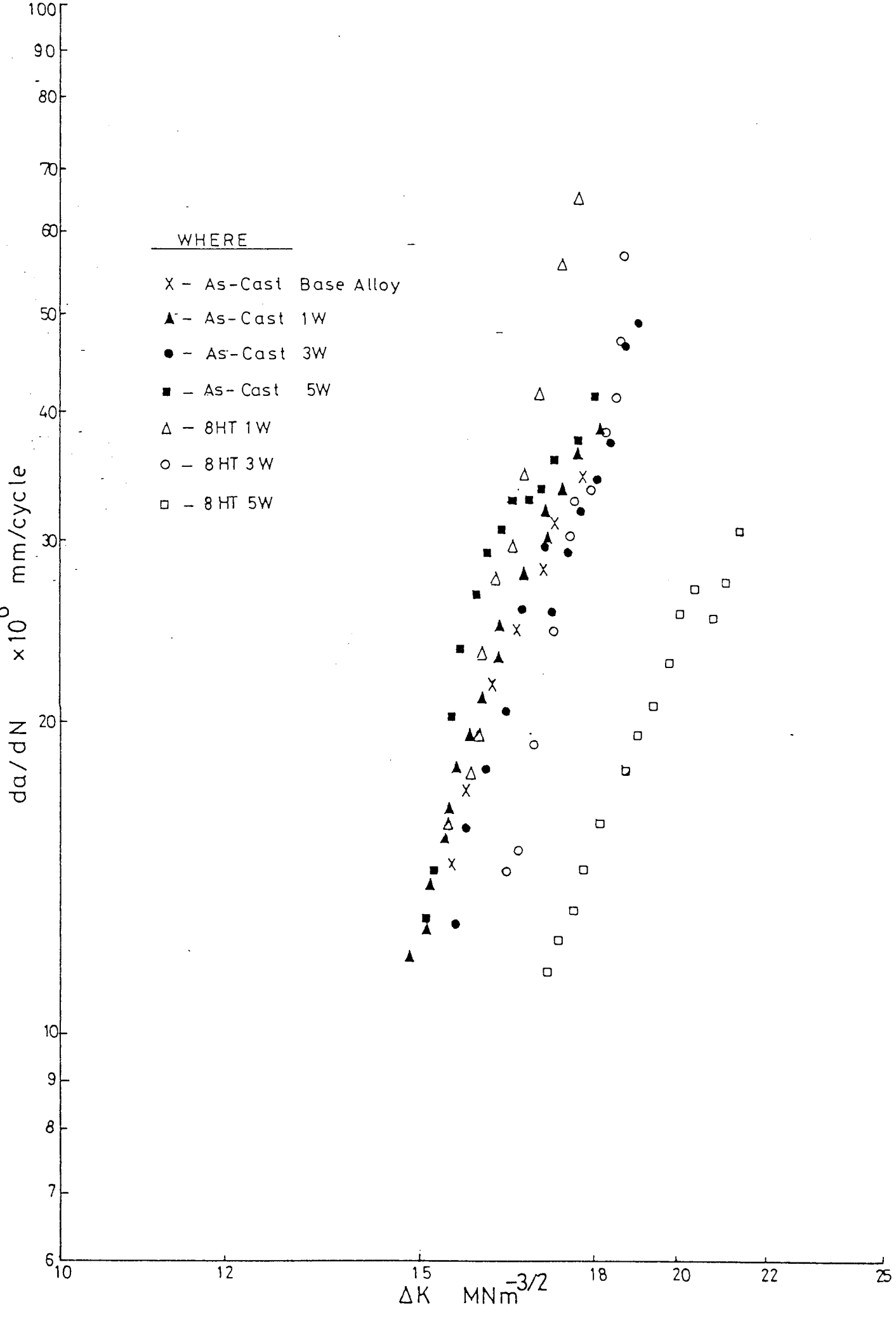

FIGURE 87: Fatigue crack growth data of tungsten containing alloys

9.9 Commercial Significance of Results

High-Cr cast irons are frequently used for abrasive wear resistance, as in crushing, grinding and mineral handling operations. The chemical composition is generally in the range 12-25% Cr and 1-3% C, a typical composition being 15% Cr and 2.5-3% C. The advantage of this composition in the whole high-Cr series is due to economic reasons. Besides the saving in Cr, the high carbon content of the alloys enables the use of high-carbon steel scrap and high-carbon ferro-alloys in the electric melted charges in place of more expensive low carbon steel scrap and low carbon ferro-alloys. With this composition, austenitic structure can be maintained by alloy additions and it is possible to obtain a martensitic product of the same composition by application of hardening heat treatments.

Although these alloys exhibited very good resistance to abrasive wear, their low fracture toughness properties restrict the usage of these alloys for a wide range of applications. The metallurgical variables investigated in here have shown that the fracture and fatigue properties of these conventional alloys can be improved by almost 50% without any significant loss in the hardness. The fracture toughness values of the alloys investigated were almost the same level as the fracture toughness of very competitive alloys in this field, such as 12% manganese steels[53]. The low initial hardness and yield stress of this latter material makes the high-Cr cast irons an attractive alternative with better wear resistance.

Overall 2% addition of molybdenum and heat treatment of this alloy for 4-8 hours at 1180°C was the optimum condition for achieving the maximum toughness for austenitic high-Cr cast irons. The results obtained here have shown that the 2% molybdenum addition was also optimum level for the as-cast condition and further additions have no significant effect on either fracture or the retardation of "pearlite transformation". Since the addition of 2% molybdenum is necessary to obtain a "pearlite" free as-cast structure, for further improvement in the toughness values up to 50%, the extra cost of high temperature heat treatments will be the dominating factor for the applicability of the results in practice. Due to the nature of the alloys and heat treatment temperature, the furnace atmosphere should be protective to avoid any de-carburisation. This can be achieved with very slight positive pressure by introducing relatively cheap nitrogen gas into a well sealed furnace. For the production of a small component, such as hammer heads, cement mill balls, heat treatments can be easily carried out in salt bath furnaces. Although the increase in the cost per ton of product due to heat treatment would not be considerably high, it needs investment for those establishments already in production and this needs a great deal of analysis.

The results indicated that similar methods to improve the toughness of martensitic high-Cr cast irons are negative. Therefore the alloy addition for production of martensitic

alloys should be considered, particularly hardening characteristics rather than toughness properties. It appears that the general practice of costly additions of molybdenum up to 3% for full hardenability could be replaced at least partially with other cheaper alloying elements such as manganese, and this could lower the production cost. On the other hand retardation of a certain amount of austenite within the martensitic matrix by increasing the hardening temperature resulted in a considerable increase in the fracture toughness values. Although during the studies the holding period at 1125^{o}C was 12 hours, it might be possible to obtain high toughness values in shorter holding periods since for this type of microstructure it is believed that the toughness is controlled by the amount of retained austenite. Due to the simplicity of the heat treatment and the combination of very high toughness values with very high hardness levels, this type of microstructure could be very competitive for applications where no repeated impact is involved.

The wear loss due to abrasion also depends very strongly on the wear system. The underlined optimum conditions here were made by considering only the toughness and hardness values of the alloys, therefore they should be regarded as a useful trend rather than absolute values. It is believed that these suggested metallurgical variables which appeared to be the only way to improve the toughness of high-Cr cast irons at the present can be best optimised with results obtained from field trials of wear tests combined with

laboratory fracture tests. It is hoped that, in this aspect, the new fracture toughness testing (short-bar/rod) of which validity has been shown will be a useful tool. It appears that, due to its simplicity, the cost of testing gives almost comparable prices with ordinary tensile testing.

X CONCLUSIONS

This project attempted to achieve improvements in the fracture toughness characteristics of relatively brittle high-Cr cast irons by refining their microstructure without losing their excellent resistance to abrasive wear. The results obtained were concluded as follows.

1. The addition of molybdenum or tungsten to high-Cr cast irons and the application of homogenisation heat treatments to these alloys at 1180^{o}C enabled alteration of the continuous eutectic-carbide structure into an isolated and globular eutectic-carbide morphology. The application of high temperature heat treatments in the absence of these alloying elements or replacing them with vanadium or manganese additions did not show any significant effect and continuous eutectic-carbide morphology remained the same.

2. The variation in the eutectic carbide morphology were found to be strongly affected by the levels of molybdenum or tungsten additions, heat treatment temperatures and holding periods. The higher addition levels of these alloying elements enabled marked variation to be attained in a short period of time.

3. Above variables which alter the eutectic-carbide morphology also gave up to 50 percent increase in the fracture and fatigue properties of austenitic alloys without any significant loss in the hardness values. For the martensitic alloys, consistant fracture toughness values were observed with these variables. Their toughness characteristics could be improved as much as austenitic alloys by introduction of a certain amount of retained austenite into the matrix.

4. The analysis of notch bending tests together with evidence from fractographic examinations at the notch roots have indicated that failure mechanism of austenitic and martensitic high-Cr cast irons are stress controlled despite the fact that the fracture surfaces reveal a partial dimpled ductile failure mechanism.

5. The critical fracture stress of the austenitic alloys decreases as the mean eutectic-carbide thickness increases. This is analogous to the model for cleavage-brittle fracture suggested by Smith. The fracture mechanism of austenitic alloys was found to be controlled not simply by the volume percent but also to a great extent by the size and distribution of the eutectic-carbides. The toughness of these alloys increases as the square root of the ratio of interparticle spacing to mean carbide thickness increases. The approximate analysis and metallo-

graphic observations have indicated that formation of stress-assisted martensite ahead of the crack tip and along the crack path in these alloys is in insufficient levels to account for the observed increase in the toughness values by an energy dissipation mechanism.

6. The fracture mechanism in the martensitic alloys was found to be independent of eutectic carbide morphology. The fracture mechanism of these alloys was defined as void-sheet failure mechanism which is controlled by the stress-state as described by Hancock and McKenie. The uniformity of secondary carbide precipitation during hardening heat treatments was given as a reason for the consistent values of fracture toughness of these alloys with studied metallurgical variables.

7. The fracture toughness of austenitic and martensitic high-Cr cast irons were approximated by the equation given below. This equation incorporates the microstructural parameters as described in the test.

$$K_{IC} = \sigma_F^* \sqrt{2\pi X_o}$$

where σ_F^* = critical fracture stress

X_o = characteristic distance (3.5 times of interparticle spacing)

Although the choice of characteristic distance (X_o) is arbitrary, the correlation observed between theoretical and experimentally obtained valid fracture toughness values is good and clearly demonstrates the role of microstructural parameters. Therefore it could be used satisfactorily for reasonable estimation of fracture behaviour of the high-Cr cast irons from their microstructure.

8. For the analytical determination of stress intensity coefficients of test pieces with chevron notches, the model suggested by Bluhm is a good approximation. However correct definitions of shear stress correction factor (k) and improved solutions of stress intensity coefficients of straight through cracks are necessary.

9. The method suggested by Ryder et al to study with experimentally determined compliance data yields better results than polynomial curve fitting procedures.

10. The results obtained from compliance studies have shown that for truly L.E.F.M. conditions the K_{IC}-P_{max} relationship exists and fracture toughness of metallic materials can be determined using the short-bar/rod type of specimens by determining only the maximum load without measuring any crack lengths. Since this relationship is material independent geometry dependent very small variations either in the specimen geometry or in the chevron notch config-

uration alter the stress intensity coefficients considerably. Therefore the scaled specimens should be in accordance with calibrated specimen geometries and dimensions.

11. Excellent agreement was obtained between this non-standard short-bar/rod fracture toughness test results and the valid K_{IC} results obtained from recommended testing techniques by standards. Therefore fracture toughness of high-Cr cast irons can be determined very accurately and in a reproducible manner with the application of this testing technique.

XI SUGGESTED FURTHER WORK

1. The physical reasons which give the variation in the eutectic carbide morphology with certain alloying elements should be established. The outcome from this study could help the replacement of the usage of costly alloying elements in this process such as molybdenum and tungsten.

2. The studied metallurgical variables might also be applied for lower and higher chromium containing high-Cr cast irons as regards to simplification of high temperature heat treatments and further improvements in the toughness properties.

3. The fatigue-crack initiation characteristics of the high-Cr cast irons were needed to be established with studied metallurgical variables. As can be seen from Figs. 84 and 85, due to the nature of the alloys at high working stresses the critical defect sizes are small and crack propagation rates are relatively high. Therefore it is assumed that crack initiation by alternative stresses are very important in the life of the components. The data obtained from these studies could be useful as fracture toughness data in the selection of the alloys for various applications of wear.

4. As mentioned in the discussion the short-bar/rod fracture toughness testing is completely geometry dependent. The small variations in the scaled test pieces causes considerable variation in the stress intensity coefficients consequently evaluation of the misleading results. Therefore the minimum stress intensity (Y*) coefficients might be evaluated in relation with geometrical parameters of the short-bar/rod fracture toughness testing specimen similar to K calibration functions of standard compact tension or bending fracture toughness testing specimens.

XII REFERENCES

1. H.S. Avery, "Handbook of Mechanical Wear", Univ. of Mich. Press

2. R.W. Durman, Foundry Trade Journal, 1973, May 24, p. 645

3. R.S. Jackson and J. Dodd, Metallurgia, 1967, Vol. 76, p. 107

4. Murakami, Oka and Nishigari, Tech. rep. Tokuku Univ., 1950, Vol. 3, p. 59

5. W. Tofaute, A. Sponheuer and H. Bennek, Arch. Eisenhuttenw, 1936, Vol. 9, p. 607

6. Kinzel and Craft, "Alloys of Iron and Chromium", Vol. I, McGraw-Hill, 1940

7. K. Bungardt, E. Kunze and E. Horn, Arch. Eisenhuttenw, 1958, Vol. 29, p. 193

8. N.R. Griffing, W.D. Forgeng and G.W. Healy, Trans. A.I.M.E. 1962, Vol. 224, p. 148

9. R.S. Jackson, J.I.S.I., 1970, Vol. 208, p. 163

10. L.R. Woodyatt and G. Krauss, Met. Trans., 1976, Vol. 7A, p. 983

11. R. Beng, J.F. Elliott and J. Chipman, Met. Trans., 1974, Vol. 5A, p. 2235

12. Mats, Weldenstrom and B. Uhrenius, Scand. J. Met., 1977, Vol. 6, p. 202

13. T. Nishizava and B. Uhrenius, Scand. J. Met., 1977, Vol. 6, p. 67

14. K.V. Gorev and L.A. Sevcuck, Izevd. Akad. Nauk. Belerus, U.S.S.R., 1973, (Fizk-Tekhn), Vol. 2, p. 40

15. H. Frederikson and B. Remaus, 44th Int. Foundry Con. Frenge, p. 7

16. H.J. Goldschmidt, J.I.S.I., 1948, Vol. 160, p. 345

17. W. Hume Rothery, "The structure of alloys of Iron" Pergamon Press

18. V.F. Zackay, E.R. Parker, D. Fahr and R. Buch, Trans. ASM 1967, Vol. 60, p. 252

19. G.R. Chanani, V.F. Zackay and E.R. Parker, Met. Trans., 1971, Vol. 2, p. 133

20. W.W. Gerberich, P.L. Hemmings and V.F. Zackay, Met. Trans. 1971, Vol. 2, p. 2243

21. D. Bhandakar, V.F. Zackay and E.R. Parker, Met. Trans. 1972, Vol. 3, p. 2619

22. D. Fahr, Met. Trans., 1971, Vol. 2, p. 1883

23. J.P. Bressanalli and A. Moskowitz, Trans. ASM, 1966, Vol. 59, p. 223

24. F. Lecroisey and A. Pineau, Met. Trans., 1972, Vol. 3, p. 387

25. P.L. Manganon and G. Thomas, Met. Trans., 1970, Vol. 1, p. 1577

26. T. Angel, J.I.S.I., 1954, Vol. 117, p. 165

27. W.W. Garberich, G. Thomas, E.R. Parker and V.F. Zackay, "Proc. Second Int. Conf. on the Strength of Metals", California, 1970, p. 894

28. G.B. Olson and M. Cohen, Met. Trans., 1975, Vol. 6A, p. 791

29. G.F. Bolling and R.H. Richman, Scripta Met. 1970, Vol. 4, p. 539

30. G.F. Bolling and R.H. Richman, Phil. Mag., 1969, Vol. 19, p. 247

31. G.F. Bolling and G.F. Richman, Met. Trans., 1971, Vol. 2, p. 2451

32. G.F. Bolling and G.F. Richman, Acta Met. 1970, Vol. 8, p. 673

33. S.D. Antolovich and B. Singh, Met. Trans., 1971, Vol. 2, p. 2135

34. S.D. Antolovich, T.R. Risbeck and A. Saxena, Eng. Fracture Mech., 1980, Vol. 13, p. 717

35. A. Rosen, R. Jago and T. Kjer, J. Met. Sci., 1972, Vol. 7, p. 870

36. E. Hornbogen, Acta Met., Vol. 26, p. 147

37. G. Chan and S.D. Antolovich, Met. Trans., 1974, Vol. 5, p. 217

38. F. Maratray and U. Nanot, "Transformation Characteristics of Cr and Cr-Mo Cast Irons", Climax-Molybdenum Brochure

39. F. Maratray and U. Nanot, "Factors effecting the structure of Cr and Cr-Mo white cast irons", Climax-Molybdenum Brochure

40. D. Dyson and K. Andrews, J.I.S.I., 1969, Vol. 193, p. 208

41. K.W. Buluft, M. Cohen and B. Averbach, Trans. ASM., 1951, Vol. 43, p. 497

42. A. Inoue, S. Arakawa, and T. Masumoto, Trans. J.I.M., 1978, Vol. 19, p. 11

43. E.I. Kolosova, V.I. Syrecyschikova and G.M. Goldsythehyen, Phys. Met. and Metalog., 1976, Vol. 41, p. 196

44. S.D. Japrie, A.G. Martin, R.A. Avarney and C.M. Sellors, J.I.S.I., 1973, Vol. 211, p. 515

45. G.R. Keeg and J.M. Silcok, Met. Sci. J., 1972, Vol. 6, p. 47

46. G.R. Keeg and J.M. Silcok, Scripta Met., 1972, Vol. 6, p. 1083

47. L.K. Singhae and J.W. Main, Met. Trans., A.I.W.E., 1968, Vol. p. 814

48. F.R. Beksit and B.R. Clark, Acta. Met., 1967, Vol. 15, p. 113

49. W. Fairshurst and K. Rohrig, Foundry Trade J. 1974, Vol. 136, p. 685

50. E.V. Rozhova, M.E. Garber and I. Tyspin, Metal Sci. H. Treatment, 1977, Vol. 19, p. 273

51. R.W. Durman, British Foundryman, 1976, Vol. 69, p. 141

52. J.M. Boyes, B.C.I.R.A., 1963, Vol. 11, p. 461

53. R.W. Durman, Ph.D. Thesis, University of Aston 1970

54. G.I. Silman and F.S. Frolstov, Met. Sci. H. Treatment, 1977, Vol. 19, p. 121

55. W.W. Ciass, AFS Trans., 1974, Vol. 82, p. 317

56. T.E. Norman, A. Soloman, and D.V. Doane, AFS Trans., 1959, Vol. 67, p. 242

57. N.I. Kitaigore, Met. Sci. H. Treatment, 1975, Vol. 17, p. 417

58. M. Waldenstrom, Met. Trans., 1977, Vol. 8A, p. 1963

59. J.C. Farge, P. Chollet and Y. Ernex, Foundry Trade J., 1971, Vol. 130, p. 319

60. R.B. Gurlach, AFS Trans., 1974, Vol. 82, p. 304

61. I. Levi, M.E. Garber and E.V. Roghova, Russian Casting Prod., 1970, p. 54

62. I. Tyspin, M.E. Garber and E.V. Roghova, Met. Sci. H. Treatment, 1970, Vol. 12, p. 612

63. G.J. Cox, Foundry Trade J., 1974, Vol. 136, p. 31

64. D.M. Stepfanuscu, 42th Int. Foundry Conf., Lizbon, 1973

65. S. Parrent, England and J. Margerie, AFS Trans., 1974, Vol. 82, p. 393

66. I.E. Lev, A.I. Yatsenko, G.E. Belai and T.I. Gerasimova, Russian Casting Prod., 1969, p. 337

67. M.F. Baranov and Y. Babro, Liteinov Prozv U.S.S.R., 1974, Vol. 1, p. 16

68. A. Ryabstev, A.I. Gdovashonuk and I.I. Framin, Metal Sci. H. Treatment, 1974, Vol. 16, p. 46

69. A.A. Griffith, Phil. Trans. Soc., 1921, A.221, p. 163

70. G.R. Irwin, "Fracturing of Metals", ASM, Cleaveland, 1948

71. E. Orowan, Prop. Phys., 1949, Vol. 4, p. 185

72. G.R. Irwin, J.App. Mech., 1957, Vol. 24, p. 361

73. G.R. Irwin, 9th Int. Conf. App. Mech., Brussells, 1957

74. H.M. Westergaard, J. App. Mech., 1939, Vol. 61, p. 49

75. J.T. Barnby, Non-Destructive Testing, 1971, Vol. 4, p. 385

76. A.S.T.M.-E.399, 1974

77. B.S. 5447, 1977

78. D.S. Dugdale, J. Mech. Phys. Solids, 1960, Vol. 8, p. 100

79. G.I. Barenblatt, Adv. Appl. Mech. 1962, Vol. 7, p. 75

80. B.A. Bilbly, A.H. Cottrell and K.H. Swinden, Proc. Roy. Soc., 1963, A.272, p. 304

81. A.A. Wells, Crack Propagation Syp. Cranfield, 1961

82. F.M. Burdekin and D.E.W. Stone, J. Strain Analysis, 1966, Vol. 1, p. 145

83. J. Eftis and H. Liebowitz, Eng. Fracture Mech., 1975, Vol. 7, p. 101

84. J.R. Rice, J. App. Mech., 1968, Vol. 35, p. 379

85. J.W. Hutchinson, J. Mech. and Phys. Solids, 1968, Vol. 16, p. 13

86. J.R. Rice and G.F. Rosengreen, J. Mech. and Phys. Solids, 1968, Vol. 16, p. 1

87. J.R. Rice, "Fracture Vol. 2" Academic Press, New York, 1968

88. J.A. Begley and J.D. Landes, A.S.T.M. STP-514, Philadelphia, 1972, p. 1

89. C.E. Turner, J. of Strain Analys. 1975, Vol. 10, p. 207

90. A.S.T.M. Task Group. E-24.01.09, Proc. A.S.T.M. 1977, Vol. 77, p. 451

91. R.W. Judy and R.J. Goode, A.S.T.M. STP-527, Philadelphia, 1973, p. 48

92. B.S. Draft and Development 19, 1972

93. J. Nakajama, J. Am. Ceramic Soc., 1965, Vol. 48, p. 583

94. H.G. Tattersall and G. Tappin, J. Met. Sci., 1966, Vol. 1, p. 296

95. L.A. Simpon, J. Am. Ceramic Soc., 1973, Vol. 56, p. 1

96. R.W. Davidge and G. Tappin, J. Mater. Sci., 1968, Vol. 3, p. 165

97. L.M. Barker, Eng. Fracture Mech., 1977, Vol. 9, p. 361

98. L.M. Barker, "Theory of Determining K_{IC} from Small non-L.E.F.M. specimens, supported by experiment on Aluminium", TR-78-6R, 1978, Terra-Tek Inc.

99. L.M. Barker, A.S.T.M. STP-678, 1979, Philadelphia, p. 73

100. D. Munz, R.T. Bubsey and J.E. Srawley, Int. J. of Fracture, 1980, Vol. 16, p. 359

101. L.M. Barker and F.I. Barratta, "Comparison of K_{IC} measurements by the short rod and A.S.T.M. E-399 methods", TR-79/3, 1979, Terra-Tek Inc.

102. A.S.T.M. E-24 B 09.06, Subcommittee Fracture Toughness of Brittle non-metallic Materials

103. J.T. Barnby, ACTA Met., 1967, Vol. 15, p. 903

104. J.T. Barnby and M.R. Johnson, Met. Sci. J. 1969, Vol. 3, p. 155

105. J.T. Barnby, and E. Smith, Met. Sci. J. 1967, Vol. 1, p. 1

106. A.N. Stroh, R. Soc., 1954, A224, p. 404 and Adv. Phys. 1957, Vol. 6, p. 418

107. T.C. Lindely, G. Oates and C.E. Richards, Acta Met. 1970, Vol. 19, p. 1127

108. J.T. Barnby and E. Smith, Met. Sci. J., 1967, Vol. 1, p. 56

109. A.H. Cottrell, Trans. Am. Inst. Min. Met and Pet. Engineering, 1958, Vol. 212; p. 192

110. G.J. McMahon and M. Cohen, Acta Met., 1965, Vol. 13, p. 591

111. E. Smith "Proc. Conf. Physical Basis of Yield and Fracture" 36 Int. Phys. Soc. Oxford

112. T.R. Wilshaw, C.A. Rau and A.S. Tetelman, Eng. Fracture Mech., 1968, Vol. 1, p. 191

113. H. Nuber, A.E.C. Tech. Rep. No. 45-47, 1958

114. R. Hill, "Mathematical theory of plasticity" Oxford Univ. Press, London, 1950

115. S.A. Mohamed and A.S. Tetelman, Eng. Fracture Mech., 1975, Vol. 7, p. 631

116. M.L. Wilkins, "Proc. of the Conf. on Fracture Mechanics and Technology", Hong Kong, 1977

117. T. Goldenberg, T.D. Lee and J.P. Hirt, Met. Trans. 1978, Vol. 9A, p. 1663

118. J.R. Griffith and D.R.S. Owen, J. Mech. and Phys. Solids, 1971, Vol. 19, p. 419

119. J.F. Knott "Fracture 1977 Vol. I", ICF Waterloo, Canada, June 1977

120. D.A. Curry and J.F. Knott, Met. Sci. J. 1978, Vol. 12, p. 511

121. J.W. Hutchinson, J. Mech and Phys. Solids, 1968, Vol. 16, p. 13

122. J.R. Rice and G.F. Rosengren, J.Mech. and Phys. Solids, 1968, Vol. 16, p. 1

123. J.R. Rice and D.M. Tracey, J. Mech. and Phys. Solids, 1969, Vol. 17, p. 201

124. R.O. Ritchie, J.F. Knott and J.R. Rice, J. Mech. and Phys. Solids, 1973, Vol. 21, p. 395

125. S.P. Rawal and J. Gurland, Met. Trans., 1977, Vol. 8A, p. 691

126. D.M. Parks, J. Eng. Mater. Technol. Ser. H., 1976, Vol. 98, p.30

127. R.O. Ritchie, B. Franchis and W.L. Server, Met. Trans. 1976, Vol. 7A, p. 834

128. R.O. Ritchie, W.L. Server and R.A. Wullaert, Met. Trans. 1979, Vol. 10A, p. 1557

129. D.A. Curry and J.F. Knott, Met. Sci. J., 1979, Vol. 13, p. 341

130. D.A. Curry, Met. Sci., 1980, Vol. 14, p. 78

131. A.S. Tetelman and J. Malkin, Eng. Fracture Mech., 1971, Vol. 3, p. 151

132. D.E. Diesburg, A.S.T.M. STP-559, 1973, Philadelphia, p. 3

133. D.E. Diesburg, A.N. Arber and K. Rohrig, "Giesseria", 1976, Vol. 3, p. 25

134. D.E. Diesburg "Toughness of As-Cast and H.Treated White Cast Irons", Climax-Molybdenum Internal Report L-212-113, Jan. 1973

135. D.E. Diesburg, "Effect of Carbon on the Toughness of High-Cr Cast Irons" Climax-Molybdenum Internal Report L-212-114, May 1973

136. J.T. Barnby and Daimalani, J. Mat. Sci., 1976, Vol. 11, p. 1979

137. J.R. Rice, D.C. Paris and J.G. Murkle, A.S.T.M. STP-536, 1973, Philadelphia, p. 231

138. J.I. Blumh, Eng. Fracture Mech., 1975, Vol. 5, p. 593

139. J.T. Ryder, G.F. Bowie and D.E. Pettit, Eng. Fracture Mech., 1977, Vol. 9, p. 901

140. D. Gilbey and S. Pearson, RAE Technical Report 66402, 1966

141. R.O. Ritchie, G.C. Garret and J.F. Knott, Int. Fracture Mech., 1971, Vol. 7, p. 462

142. T. Nakona, H. Kawatani and S. Kinoskita, Trans. I.S.I.J., 1977, Vol. 17, p. 110

143. K. Erikson, Scand. J. Met., 1973, Vol. 2, p. 197

145. A.R. Jack and A.T. Price, Int. J. Fracture Mech., 1970, Vol. 6, p. 401

146. G.M. Spink, P.J. Worthington and P.T. Heald, Met. Sci. Eng., 1973, Vol. 11, p. 113

147. V. Weiss, A.S.M.E. - Paper 62 Wa-270, 1962

148. T.V. Duggan, M.W. Procter and L.J. Spance, Int. J. Fatigue, 1979, p. 37

149. Karl H.Z. Gahr and D.V. Doane, Met. Trans. 1980, Vol. 11A, p. 613

150. F.A. McClintock, J. App. Mech., 1968, Vol. 35, p. 353

151. J.W. Hancock and A.C. Mackenzie, J. Mech. Phys. Solids, 1976, Vol. 24, p. 147

152. E. Orowan- "Symp. on Internal Stress in Metals", Inst. of Metals, London

153. J. Gurland, Acta Met. 1972, Vol. 20, p. 735

154. S.H. Goods and L.M. Brown, Acta Met. 1979, Vol. 27 p. 1

155. L.M. Brown and W.M. Stoobs, Phil. Mag., 1976, Vol. 34, p. 351

156. K. Tanaka, T. Mori and T. Nakamura, Phil. Mag. 1970, Vol. 21, p. 267

157. A.S. Argon, J. Im and R. Safoglu, Met. Trans. 1975, Vol. 6A, p. 825

158. M.F. Ashby, Phil. Mag., 1966, Vol. 14, p. 1157

159. R.W.K. Honeycombe, "Some Strengthening Mechanisms in Alloys Steels", Climax-Molybdenum Brochure

160. H. Koitalainer and K. Torronen, "Fracture 1977, Vol. 2A" ICF, Waterloo, Canada, June 1977

161. J.T. Barnby, Non-Destructive testing, 1972, Vol. 5, p. 32

162. P.C. Paris and F. Erdogan, J. Basic Eng. (Trans. A.S.M. Series D), 1963, Vol. 85, p. 528

APPENDIX I

Determination of fracture toughness of high-strength cast aluminium alloy AUWE-224 by using non-standard short-bar/rod fracture toughness test method.

Summary

The applicability of short-bar/rod fracture toughness testing technique to the determination of fracture toughness of metallic materials which exhibit non-linear elastic behaviour was investigated.

I.1 Introduction

The method, which was suggested by Barker [1], enables the determination of fracture toughness of brittle metallic materials using calibrated specimens requiring neither fatigue pre-cracking nor measurements of critical crack length which cause failure of the specimen in an unstable manner. Thus the fracture toughness of the materials can be determined from equation (1) by measuring only the maximum load, as long as the scaled specimen dimensions are in accordance with calibrated specimens

$$K_{IC} = \frac{P_{max}A}{B^{3}/2} \qquad \ldots\ldots\ldots(1)$$

This equation is only valid for material which behave in a truly linear elastic fashion, in other words for materials which have a flat crack-growth resistance curve .

For materials which exhibit non-linear elastic behaviour or a rising crack resistance curve during testing due to extensive plastic deformation ahead of the crack tip

Barker [3] suggested a plasticity correction factor (p) which can be determined during the testing. Thus equation (1) might be re-written in the following way

$$K_{ICSB} = \frac{Fc.A}{B^{3}/2} \left[\frac{1+p}{1-p}\right]^{\frac{1}{2}} \quad \ldots\ldots\ldots (2)$$

where Fc : average load between two unloading and re-loading cycles

A : constant

p : plasticity correction factor

B : specimen width or diameter

As can be seen from section 9.5 in the text of the thesis, for high-Cr cast irons, very good correlation is observed between the results obtained from the short-bar and standard tests. The aim of this study was to show the material independency of the short-bar fracture toughness specimen and also to study the applicability of this testing method to metallic materials which exhibit non-linear elastic behaviour.

I.2 Experimental Procedures

The chemical composition of the cast aluminium alloy used in this study is given below. The material was homogenised at 535°C for 48 hours and then quenched in water at 70°C and aged for 24 hours at 170°C then air cooled.

I.2.1 Chemical Composition of the alloy

Cu	Ag	Mg	Si	Ti	Zn	Fe	Sn	Zr	Ni	V
4.69	0.01	0.33	0.08	0.11	0.05	0.1	-	0.01	-	0.10

Al - remainder

I.2.2 Three point bend fracture toughness tests

The fracture toughness tests of the fatigue pre-cracked 22 x 22 mm square sectioned specimens were carried out in three point bending with span length 4 times the width, in accordance with the standards described in text of the thesis. Crack initiation was detected by potential-drop technique, for this purpose 60 amp D.C. current was passed along the specimen and no heating was observed during testing.

I.2.3 Short-Bar/Rod fracture toughness tests

The dimensions and chevron notch configurations of the short-bar/rod specimens are given in Fig. 1. The specimens were obtained from the same block from which the three point bend specimens were prepared.

The chevron notches and grip slots were machined either by using an electric discharge machine or by using a 0.012 inch thick miller cutter. In order to avoid any question of directionality, chevron notches in short-bar/rod specimens were in the same direction as the notches in three point bend specimens. The specimens were pulled in tension as described in the text.

I.3 Data Analysis

I.3.1 Data analysis of the three point bend fracture toughness tests

The K_Q and $K_{Q(J)}$ values were determined by following the procedures in section 7.1. and 7.2 from load vs. C.O.D. and load-L.P.D. records respectively. The crack length measurements were taken from the fracture surfaces using a travelling microscope and for J-integral analysis, the

FIGURE 1: Dimensions of short-bar/rod fracture toughness test specimens

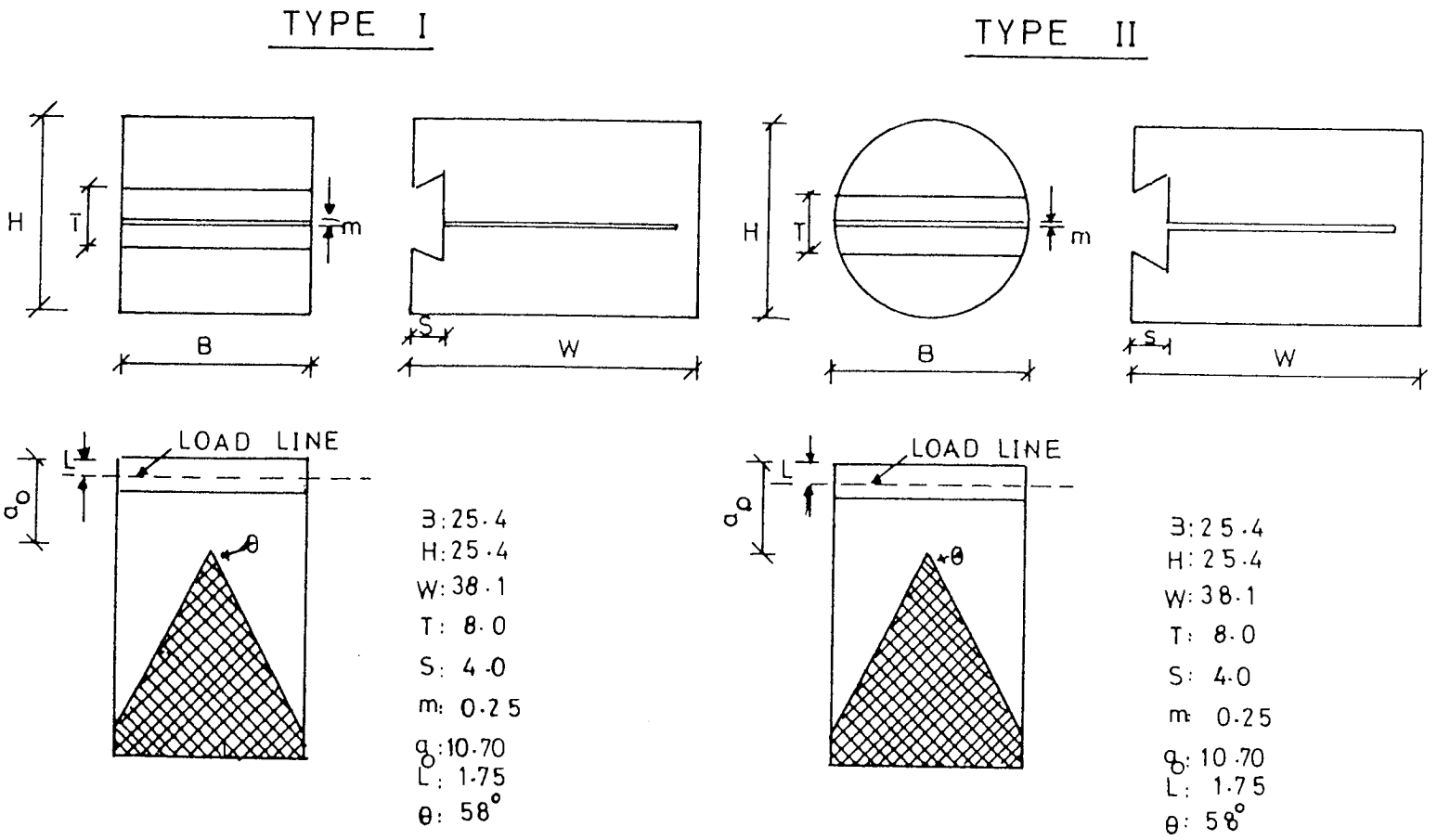

ALL DIMENSIONS IN mm

(not scale)

Continued from Figure 1

TYPE III

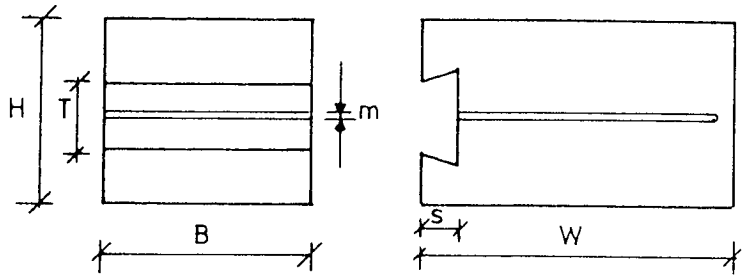

B : 25.4
W : 38.1
H : 22.0
T : 8.0
S : 4.0
m : 0.25
a_o : 11.30

L : 1.75
θ : 55.0°

TYPE IV

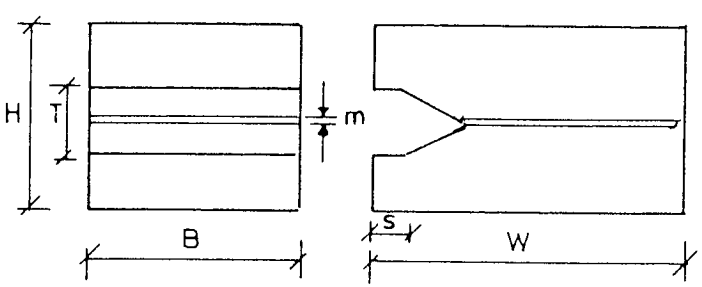

B : 25.4
W : 38.1
H : 22.0
T : 8.0
S : 4.0
m : 0.25
a_o : 11.30

L : 1.25
θ : 55.0°

ALL DIMENSIONS IN mm

(not scale)

crack initiation point was taken as the first observed deviation from linearity in the potential-drop vs. load records.

I.3.2 Data analysis of short-bar/rod fracture toughness tests

The data analysis of short-bar/rod test records was performed by the procedure outlined by Barker [4]. A typical obtained load versus mouth opening displacement is given in Fig. 2.

The plasticity correction factor and critical load determined in the following way:

1. The high and low points on each unloading-reloading cycle were determined. (H and L points in the figure (2). A high point is the point at which the grips started moving together to relax the load on the specimen, and the corresponding low point is on the reloading part of the unloading path at half of the high point).

2. An ideal elastic release path which passes through the H and L points was drawn for each unloading and reloading cycle.

3. The average load line, which represents the average load between the two unloading-reloading cycles which are just before and just after the maximum load, was drawn.

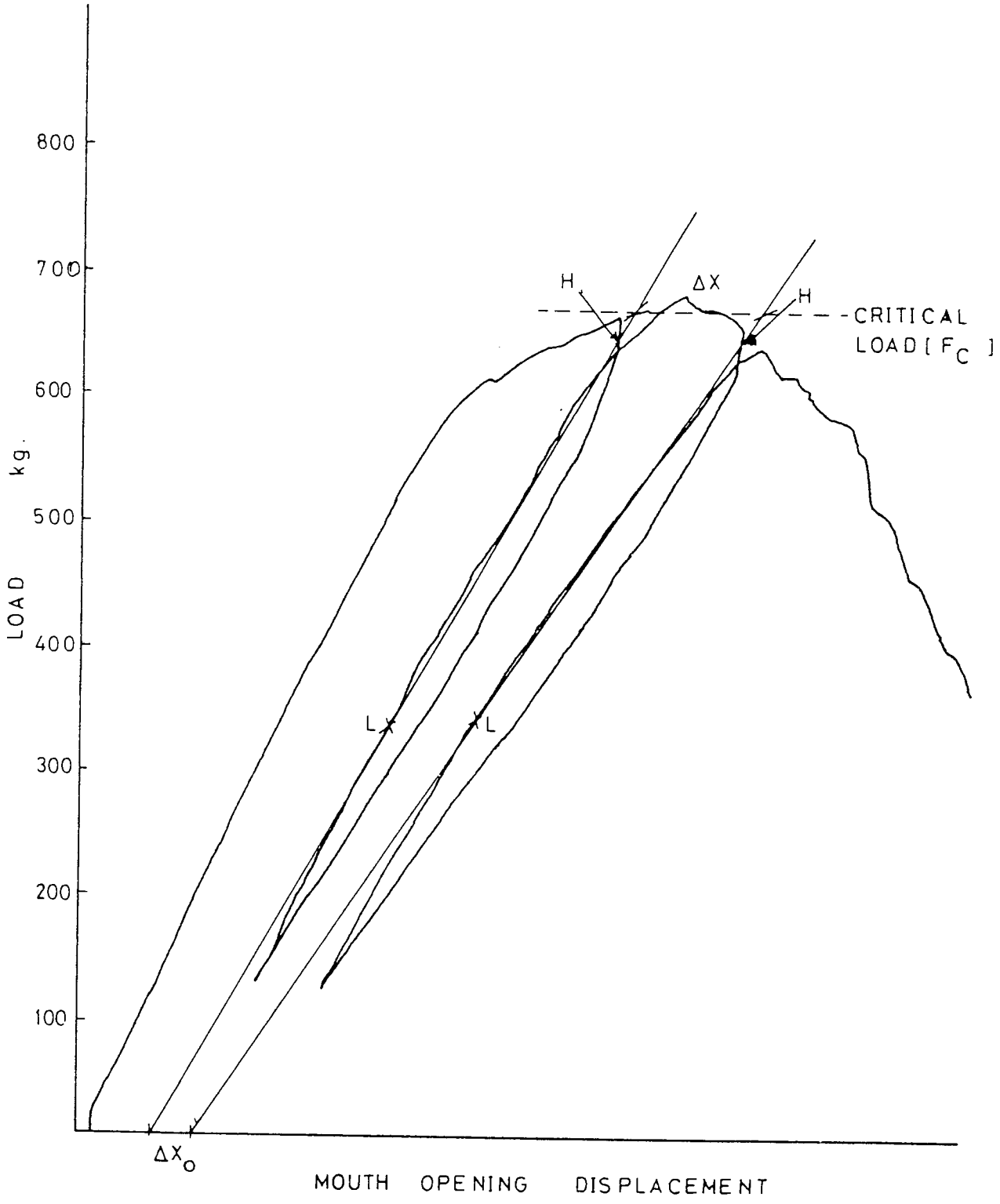

FIGURE 2: Typical load vs mouth opening displacement record from short-bar fracture toughness testing of Al-224 alloys and determination of plasticity correction factor (p) from loading and unloading lines

4. The Δx (the distance between the release path approximations at average load line) and Δx_o (the distance between the release path approximations at zero load line) were measured.

The value of the plasticity correction factor (p) was determined from the equation given below:

$$p = \frac{\Delta x_o}{\Delta x}$$

5. The K_{ICSB} values were obtained using equation (2) by determining the value of A from stress intensity coefficient studies for the same specimen configuration in the following way

$$A = \frac{Y_M^*}{\sqrt{W}/B}$$

where Y_M^* = minimum stress intensity coefficient

B = specimen width

W = specimen length (from loading line)

The value of A = 22 is given by Barker for fractometer II tests.

I.4 Results

The test results obtained are summarised in table 1 for three point bend fracture toughness tests and in table 2 for short-bar/rod tests. Also the general appearance of the test specimens is shown in plate 1 and plate 2 for bend and short-bar/rod tests respectively.

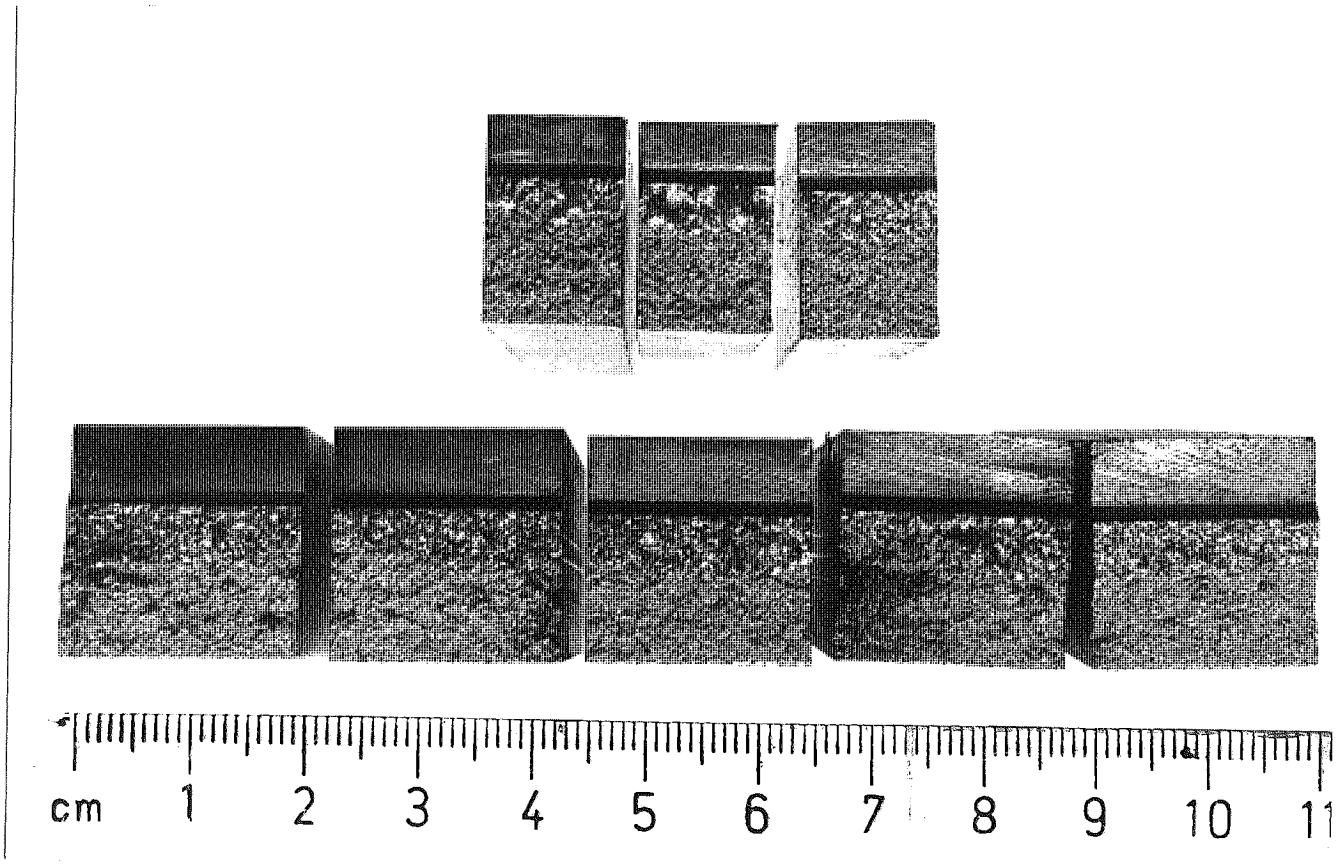

PLATE 1: General fracture appearance of three point bend specimens

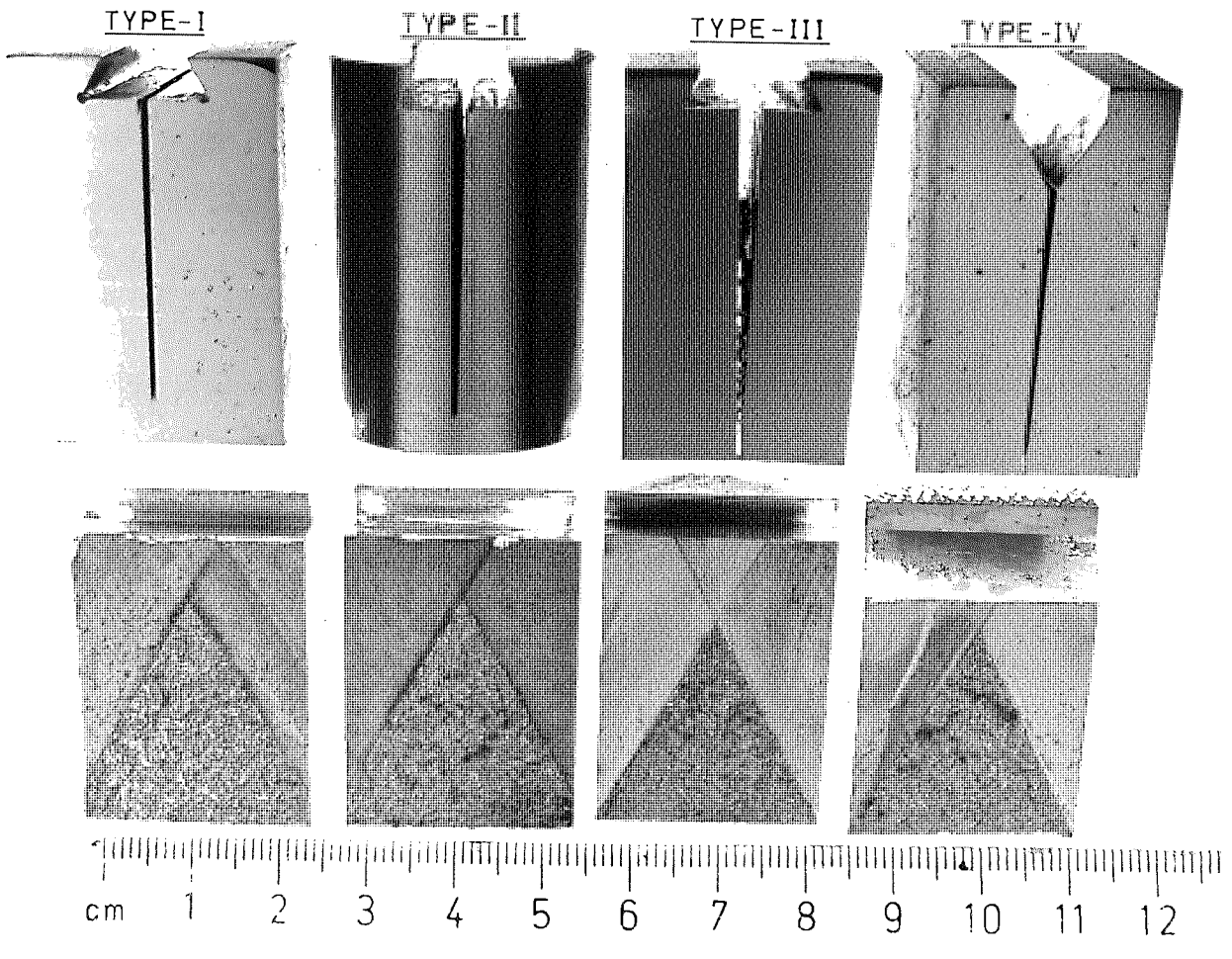

PLATE 2: General fracture appearance of short-bar/rod specimens

Specimen	Breadth B mm	Width W mm	Crack Depth mm	P_Q kg	PC kg	P_{max} kρ	P_{max}/P_Q	K_F $MNm^{-3/2}$	K_Q $MNm^{-3/2}$	$K_{Q(J)}$ $MNm^{-3/2}$
1	19.66	19.67	11.37	365	440	460	1.26	10.28	17.91	31.81
3	20.00	19.95	11.51	375	460	475	1.26	10.57	17.96	29.46
4	19.65	20.05	11.67	430	480	535	1.24	10.73	21.36	28.61
5	19.69	19.81	11.63	540	570	600	1.11	11.24	27.32	32.32
6	19.98	19.90	11.44	420	500	525	1.25	10.41	20.02	31.30
1	11.44	18.19	9.73	310	360	370	1.19	13.61	23.44	29.37
2	12.05	18.64	10.61	285	350	360	1.19	14.48	22.08	29.21
3	11.75	17.89	9.59	290	340	360	1.24	13.47	21.71	29.25

TABLE 1: Three-point fracture toughness test results

Specn. Type	Test No	Constant A	Critical Load kg	Plasticity Correction Factor P	K_{ICSB} $MNm^{-3/2}$	Average K_{ICSB} $MNm^{-3/2}$
Type I	1	14.93	720	0.22	32.56	31.32 ±1.25
	2	14.93	740	0.13	30.50	
	3	14.93	650	0.23	29.71	
	4	14.93	750	0.18	32.54	
Type II	1	16.00	675	0.20	31.90	31.55 ±0.90
	2	16.00	680	0.13	31.89	
	3	16.00	685	0.19	30.04	
	4	16.00	685	0.20	32.39	
Type III	1	18.60	650	0.16	34.41	33.9 ±0.82
	2	18.60	605	0.22	33.80	
	3	18.60	600	0.21	33.25	
	4	18.60	630	0.25	35.48	
Type IV *	1	15.00	711	0.25	33.34	32.99 ±1.20
	2	15.00	690	0.22	31.37	
	3	15.00	773	0.20	34.27	

* Tested by using fractometer II

TABLE:2 Test results of short-bar/rod fracture toughness tests

I.5 Discussion

The correct and valid determination of K_{IC} values was very necessary for this study since the validity of the short-bar/rod fracture toughness testing method and useage of the results in an engineering sense can only be decided by a comparison with results obtained from well established standard test methods.

K_{IC} values of the aluminium alloy AUWE-224 used in this study could not be obtained by following the procedures outlined by ASTM-E399. The P_Q/P_{max} ratios were always higher than 1.10 for the specimens of 22 x 22 mm cross-section (see fig. 3). Although results are not reported here, even when 42 x 42 mm sectioned thick three-point test pieces were used the validity criterion were still violated due to very large fatigue-crack tip bowing. Therefore stress intensity values were evaluated from J-integral values since the J-integral method was suggested as the best method for assessment of fracture toughness of this alloy [5].

As can be seen from the tables, the difference between the results obtained from short-bar/rod tests and three point bending tests are less than $\pm$ 3 $MNm^{-3/2}$, therefore it can be concluded that there is good correlation between the two fracture toughness test methods. It also appears that short-bar/rod specimens are independent of the specimen material since by using the same value of the stress intensity factor of a given geometry good correlations were obtained for different materials.

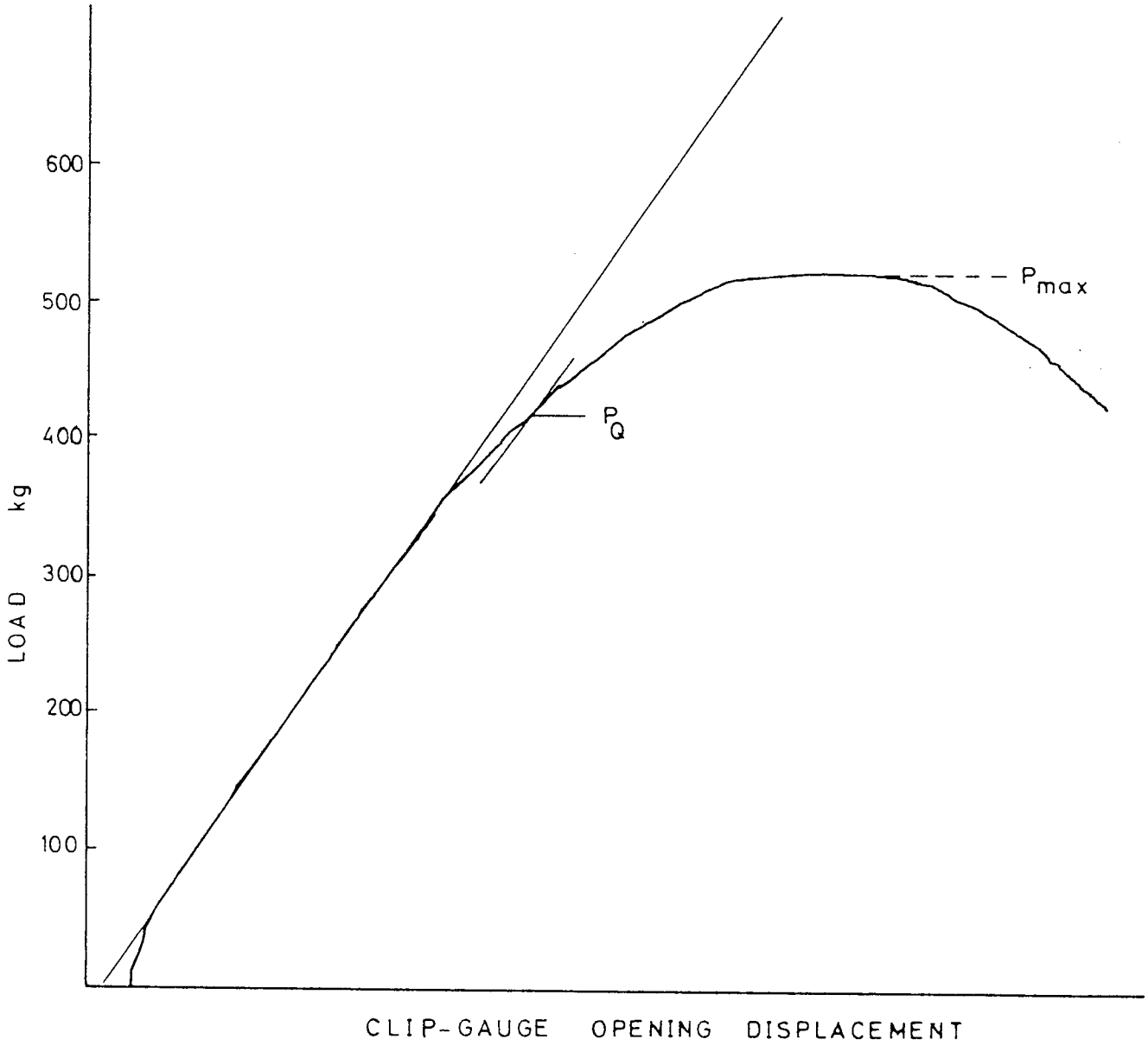

FIGURE 3: Typical load vs clip-gauge opening displacement record from fracture toughness tests of Al-224 alloys

The plasticity correction factor values which were used during the calculations of K_{ICSB} are also given in table 2. Although, according to Barker [4], the p values should not exceed 0.2 and above this value, the K_{ICSB} values obtained are regarded as invalid for the short-bar/rod test, as can be seen from the table, values as high as p = 0.25 still gave comparable results with $K_{Q(J)}$ values.

The specimens were prepared exactly in accordance with Barker's specifications and when tested in the fractometer gave higher values when calculations were carried out using the constant A = 22, as in the case of high-Cr tests. As mentioned in the text, although the compliance analysis of this type of specimen gave A ≅ 20, this disparity could be attributed to the load-cell calibration of the test machine or stiffness of the machine.

I.6 Conclusions

The applicability of the short-bar/rod fracture toughness technique to the toughness measurements of high-strength cast aluminium alloy AUWE-224 were investigated and the following conclusions can be drawn:

1. The results obtained from short-bar/rod tests gave good correlation with the $K_{Q(J)}$ values which were obtained using the J-integral technique. Therefore short-bar/rod fracture toughness testing techniques can be applied to determine the fracture toughness of AUWE-224 aluminium alloys.

2. With plasticity correction factor p as high as 0.25 comparable results were still obtained. However, it is felt that more studies are necessary in the definition and limitation in the usage of the plasticity correction factor.

I.7 References

1. L.M. Barker, Engineering Fracture Mechanics, 1977, vol. 9, p. 361

2. D. Munz, R.T. Bubsey and J.E. Srawley, Int. J. Fracture, 1980, vol. 16, pp. 359

3. L.M. Barker, Theory for determining K_{IC} from small non-LEFM specimens, supported by experiments on aluminium, TR.78-62, 1978, Terra Tek. Inc.

4. L.M. Barker, Data analysis methods for short-bar/rod fracture toughness of metallic materials, TR.80-12, 1980, Terra Tek. Inc.

5. P.E. Holden, Ph.D. thesis, 1979, University of Aston.

Pages removed due to Confidentiality reasons